CIVIL ENGINEERING STUDIES
Illinois Center for Transportation Series No. 24-013
UILU-ENG-2024-2013
ISSN: 0197-9191

Cone Penetration Testing for Illinois Subsurface Characterization and Geotechnical Design

Prepared By
Jorge Macedo
Paul Mayne
Sheng Dai
Paola Torres
Cody Arnold
Luis Vergaray
Yumeng Zhao
Georgia Institute of Technology

Research Report No. FHWA-ICT-24-011

A report of the findings of

ICT PROJECT R27-210
Cone Penetration Testing (CPT) for Illinois Subsurface Characterization and Geotechnical Design

https://doi.org/10.36501/0197-9191/24-013

Illinois Center for Transportation

May 2024

TECHNICAL REPORT DOCUMENTATION PAGE

1. Report No. FHWA-ICT-24-011	2. Government Accession No. N/A	3. Recipient's Catalog No. N/A
4. Title and Subtitle Cone Penetration Testing for Illinois Subsurface Characterization and Geotechnical Design		**5. Report Date** May 2024 **6. Performing Organization Code** N/A
7. Authors Jorge Macedo (https://orcid.org/0000-0002-0457-4824), Paul Mayne, Sheng Dai, Paola Torres, Cody Arnold, Luis Vergaray, Yumeng Zhao		**8. Performing Organization Report No.** ICT-24-013 UILU-2024-2013
9. Performing Organization Name and Address Illinois Center for Transportation Department of Civil and Environmental Engineering University of Illinois at Urbana-Champaign 205 North Mathews Avenue, MC-250 Urbana, IL 61801		**10. Work Unit No.** N/A **11. Contract or Grant No.** R27-210
12. Sponsoring Agency Name and Address Illinois Department of Transportation (SPR) Bureau of Research 126 East Ash Street Springfield, IL 62704		**13. Type of Report and Period Covered** Final Report 8/16/19–5/31/24 **14. Sponsoring Agency Code**

15. Supplementary Notes

Conducted in cooperation with the U.S. Department of Transportation, Federal Highway Administration.
https://doi.org/10.36501/0197-9191/24-013

16. Abstract

This project sets the stage for implementing a cone penetration testing (CPT) practice in the state of Illinois, providing recommendations for using and interpreting CPT soundings in subsurface investigations. This study also contributes to modernizing Illinois Department of Transportation (IDOT) policy to current CPT-related practices adopted in other departments of transportation, which is consistent with recommendations from the Federal Highway Administration. Toward the goals of this project, CPT soundings across the nine districts of the state of Illinois have been conducted, and available CPT data at IDOT have been evaluated. The generated data have been uniformly processed, generating a database of 156 CPTs distributed across the nine districts. The database also includes shear wave velocity profiles at 28 locations and pore pressure dissipation tests at 45 locations. In addition, information (editable and non-editable) provided by IDOT has been carefully examined. The provided information consisted of boreholes with standard penetration test (SPT) data and laboratory tests on collected Shelby tubes. This information has been used to develop SPT-CPT correlations that can be applied in the state of Illinois and to provide examples of interpreting seismic piezocone test (SCPTu) data in the context of laboratory testing. Due to the several independent, fast, and reliable measurements that can be conducted in a CPT sounding and the fact that they can be done cost-effectively, CPT soundings are increasingly being preferred for in situ testing, and their adoption at IDOT is a positive step forward and consistent with the best practices at other U.S. departments of transportation.

17. Key Words	18. Distribution Statement
Cone Penetration Testing, Subsurface Investigations, Piezocone, Seismic Piezocone, Dissipation Tests, Illinois Soils	No restrictions. This document is available through the National Technical Information Service, Springfield, VA 22161.

19. Security Classif. (of this report)	20. Security Classif. (of this page)	21. No. of Pages	22. Price
Unclassified	Unclassified	155 + appendices	N/A

Form DOT F 1700.7 (8-72) **Reproduction of completed page authorized**

ACKNOWLEDGMENT, DISCLAIMER, MANUFACTURERS' NAMES

This publication is based on the results of **ICT-R27-210: Cone Penetration Testing (CPT) for Illinois Subsurface Characterization and Geotechnical Design**. ICT-R27-210 was conducted in cooperation with the Illinois Center for Transportation; the Illinois Department of Transportation; and the U.S. Department of Transportation, Federal Highway Administration.

Members of the Technical Review Panel (TRP) were the following:

- Brian Laningham, TRP Chair, Illinois Department of Transportation
- Brad Hessing, TRP Co-Chair, Illinois Department of Transportation
- Jeremy Brown, Illinois Department of Transportation
- Giancarlo Gierbolini, Illinois Department of Transportation
- Aaron Hayes, Illinois Department of Transportation
- Scott Kassel, Illinois Department of Transportation
- Rustin Keys, Illinois Department of Transportation
- Nick Lombardi, Federal Highway Administration
- Veniecy Pearman-Green, Illinois Department of Transportation
- John Senger, Illinois Department of Transportation
- Michael Short, Illinois Department of Transportation
- Heather Shoup, Illinois Department of Transportation
- Nathan White, Illinois Department of Transportation

EXECUTIVE SUMMARY

Cone penetration testing with pore pressure measurements (CPTu, or piezocone test) is a widely-used in situ exploratory test method that allows the expedient and direct characterization of soil deposits by collecting three continuous readings with depth (typically every 2 cm [0.79 in.]) including (a) cone tip resistance, q_t; (b) sleeve friction, f_s; and (c) porewater pressure, u_2. Pore pressure dissipation tests can also be conducted during the CPTu sounding to provide additional subsurface information. With the addition of geophone sensors, it is also easy to collect shear wave velocity data, termed a seismic piezocone test (SCPTu). All data are available immediately to the geoengineer for review, examination, and analysis, instead of requiring days or weeks for boring log preparation and laboratory testing to be completed.

This research study sets the stage for implementing a CPTu/SCPTu practice in the state of Illinois and provides recommendations for using and interpreting SCPTu tests in subsurface investigations. In this context, one of the main motivations for this project is to contribute to modernizing Illinois Department of Transportation (IDOT) policy to current CPTu-related practices adopted in other departments of transportation, which is consistent with recommendations from the Federal Highway Administration to the A-Game (Advanced Geotechnical Methods in Exploration), a current and major initiative.

This report is divided into seven chapters, distributed as follows:

- Chapter 1 provides an introduction to the study, discussing the CPTu/SCPTu history, CPTu/SCPTu testing, field equipment, Illinois geology, and the CPTu/SCPTu practice at other state transportation agencies.
- Chapter 2 presents the CPTu/SCPTu soundings for this project and the generated CPTu/SCPTu data. In this context, the chapter presents the CPTu/SCPTu systems used, the testing procedures, and data exploratory analyses on the generated data.
- Chapter 3 discusses the recommended procedures by the researchers for interpreting CPTu/SCPTu data in the context of subsurface characterization. This chapter also discusses CPTu/SCPTu-based design procedures.
- Chapter 4 presents the processing of the collected CPT/CPTu data.
- Chapter 5 presents the processing of the historical standard penetration test (SPT) data from information facilitated by IDOT and proposes new SPT-CPT correlations based on the processed data.
- Chapter 6 presents case studies of CPT data interpretation in the context of laboratory testing data generated by soil laboratories at IDOT and Georgia Tech using available undisturbed samples collected in Shelby tubes.
- Chapter 7 closes the study by highlighting the key project outcomes and providing recommendations to implement and expand the CPTu/SCPTu practice at IDOT.

TABLE OF CONTENTS

CHAPTER 1: INTRODUCTION 1

HISTORY OF CONE PENETROMETER FOR IN SITU TESTING 1

PIEZOCONE TESTING 2

FIELD EQUIPMENT 4

PRACTICES OF OTHER STATE TRANSPORTATION AGENCIES USING CPT-BASED TESTING AND DESIGN 6

ILLINOIS GEOLOGY 7

CHAPTER 2: FIELD TESTING AND GENERATED SCPTU/CPT DATA 12

CONE PENETROMETER EQUIPMENT 13

SCPTU TESTING PROCEDURES 16

INFORMATION GENERATED ON THIS PROJECT 19

CHAPTER 3: RECOMMENDED PROCEDURES FOR INTERPRETING CPT/SCPTU DATA AND CPT/SCPTU-BASED DESIGN PROCEDURES 22

BASIC DEFINITIONS OF IN SITU STRESSES 22

Hydrostatic Pore Water Pressure 22

Total and Effective Stress 22

PIEZOCONE PARAMETERS 23

Corrected Tip Resistance and Sleeve Friction 23

Normalized Piezocone Parameters 24

CORRELATIONS FOR UNIT WEIGHT 25

CORRELATIONS AND INTERPRETATION FOR SOIL BEHAVIOR 27

Soil Behavior Type Index 27

CPT Charts for Soil Behavior Classification 29

CORRELATIONS FOR RELATIVE DENSITY OF SANDS 34

CORRELATIONS FOR SOIL STRENGTH 38

Effective Friction Angle 38

Undrained Shear Strength 41

Clay Sensitivity 43

CORRELATIONS FOR IN SITU STATE AND STRESS HISTORY PARAMETERS 44

Pre-consolidation Stress ($\boldsymbol{\sigma p}$) and Yield Stress Ratio (YSR) 44

At-Rest Coefficient (K_0) 48
Soil Compressibility ($\lambda 10$) 48
State Parameter (ψ) 49
CORRELATIONS FOR SOIL STIFFNESS AND SOIL MODULI 50
Shear Wave Velocity Estimation with CPT 51
Maximum Shear Modulus 52
Drained Young's Modulus 52
Constrained Modulus 53
Rigidity Index 53
CORRELATIONS FOR FINES CONTENT 55
POREWATER PRESSURE DISSIPATION TESTING 55
On the Assessment of t_{50} 56
Coefficient of Consolidation 58
Correlations for Hydraulic Conductivity 59
SEISMIC CONE PENETRATION TESTING 60
Non-Continuous Profile Methods 61
Continuous Profile Methods 63
Soil Parameters from Shear Wave Velocity 64
CPT-BASED LIQUEFACTION TRIGGERING PROCEDURES 66
CPT-BASED GEOTECHNICAL DESIGNS 67
Shallow Foundations 68
Deep Foundations 74
CHAPTER 4: PROCESSING OF GENERATED CPT DATA 86
DISTRICT 1 86
District 1: Site 1 (Deer Creek) 87
DISTRICT 2 89
District 2: Site 2 90
DISTRICT 3 92
District 3: Site 4 (IL 47) 93
DISTRICT 4 95
District 4: Site 1 (SN 029-0074) 96
DISTRICT 5 97

District 5: Site 4 (SN 010-0180) 98
DISTRICT 6 100
District 6: Site 1 (IL River Bridge at Florence) 102
DISTRICT 7 104
District 7: Site 1 (SN 013-0010) 105
DISTRICT 8 106
District 8: Site 1 (SN 060-0143) 107
DISTRICT 9 109
District 9: Site 1 (SN 028-0037) 110

CHAPTER 5: SPT-CPT CORRELATIONS 112
EXISTING SPT-CPT CORRELATIONS 112
SELECTION OF SPT-CPT PAIRS 120
Screening of Data Pairs 120
Processing of Illinois Data 121
SPT-CPT CORRELATIONS FOR ILLINOIS 123

CHAPTER 6: CASE STUDIES FOR CPT DATA INTERPRETATION WITH LABORATORY TESTING FROM SHELBY TUBES 126
FLORENCE SITE—DISTRICT 6 126
Shelby Tube Information and Laboratory Testing 126
Data Interpretation 129
TESTING AT NORTHWESTERN UNIVERSITY SITE 138

CHAPTER 7: CONCLUSIONS AND RECOMMENDATIONS 142

REFERENCES 144

APPENDIX A 156

APPENDIX B 157

APPENDIX C 158

LIST OF FIGURES

Figure 1. Dutch cone penetrometer and three associated operation steps. 2

Figure 2. Schematics of different types of cones: electric cone penetrometer (measure q_c and f_s), Type 1 piezocone (measure q_c, f_s, and u_1), and Type 2 piezocones with a cross-sectional area of 10 and 15 cm^2 (measure q_c, f_s, and u_2), respectively 3

Figure 3. Example data from a CPTu sounding in southwestern Illinois. 4

Figure 4. Photos for onshore equipment for piezocone testing: (A) truck-mounted system, (B) track-mounted system, and (C) anchored cone penetrometer rig. 6

Figure 5. Bedrock geology map for the State of Illinois. 8

Figure 6. A map showing that glacial drift mantles cover the bedrock in the state of Illinois. 9

Figure 7. Map of quaternary deposits for the state of Illinois 10

Figure 8. Map of generalized drift thickness in Illinois. 11

Figure 9. Map of Illinois showing the nine IDOT state districts and sites of collected CPTu data. 12

Figure 10. General schematic of the ConeTec seismic piezocone penetrometer 14

Figure 11. Photos of (A) several of the Georgia Tech cone penetrometers in varying sizes and sensor configurations and (B) manual seismic source used by Georgia Tech. 15

Figure 12. Photos of Georgia Tech CPT rig in the State of Illinois: (A) side view and (B) rear view. 16

Figure 13. Photos of GT field crew using the Vertek HT cone penetrometer system. 19

Figure 14. Histogram summaries on the numbers of cone penetration tests per district. 21

Figure 15. Summary histograms showing the exploration depths (ft) per district. 21

Figure 16. Equation. Hydrostatic porewater pressure. 22

Figure 17. Equation. Calculation of total overburden stress. 22

Figure 18. Equation. Effective vertical stress 22

Figure 19. Equation. Corrected total cone resistance. 23

Figure 20. Schematic of porewater pressure distribution on the piezocone element and measurement corrections for tip and sleeve readings. 23

Figure 21. Equation. Total sleeve friction. 24

Figure 22. Equations. Normalized piezocone parameters. 24

Figure 23. Equations. Normalized porewater pressure ($\boldsymbol{U}$) and friction ratio ($\boldsymbol{Rf}$). 24

Figure 24. Unit weight from CPT measurements. 26

Figure 25. Equation. CPT material index (Jefferies & Been, 2015). 27

Figure 26. Contours of constant material index $\boldsymbol{Ic - JB}$ and associated soil behavioral zones. 28

Figure 27. Equation. Modified CPT material index (Robertson & Wride, 1998). 29
Figure 28. Equation. Normalized tip resistance (iterative method by Robertson, 2009). 29
Figure 29. Equation. Alternate CPT soil behavior type index, I_B (Robertson, 2016). 29
Figure 30. Soil behavior classification charts for CPTu by Robertson. 31
Figure 31. Soil behavior classification chart for $\boldsymbol{Qt - U}$ presented by Schneider et al. (2008a). 32
Figure 32. Soil behavior classification chart for $\boldsymbol{Qt - Fr}$ presented by Schneider et al. (2012). 32
Figure 33. Updated soil behavior types presented by Robertson (2016) superimposed over $\boldsymbol{Qt - Fr}$ groupings given by Robertson (2009). 33
Figure 34. Equation. Normalized rigidity index parameter for assessing cemented soils. 33
Figure 35. Chart to estimate if soils have significant microstructure. 34
Figure 36. Equation. Relative density ($\boldsymbol{DR}$), reported as a percentage (%). 34
Figure 37. Relative density of NC to OC quartz-silica sands estimated using CPT. 35
Figure 38. Relative density for calcareous-carbonate sands from CPT. 36
Figure 39. Relative density of carbonate-calcareous sands from CPT. 37
Figure 40. Equations. Clean sand-equivalent cone tip resistance. 37
Figure 41. Equation. Relative density based on the clean sand-equivalent cone tip resistance. 38
Figure 42. Equation. Clean sand-equivalent cone tip resistance. 38
Figure 43. Drainage conditions during penetration in different soils. 39
Figure 44. Equation. Effective friction angle for CPT drained penetration in sand-like materials. 39
Figure 45. Equations. Bearing capacity and porewater bearing factors from NTH solution. 40
Figure 46. Bearing capacity factor and failure surface of the NTH solution. 40
Figure 47. Equation. Cone resistance number for NTH solution. 41
Figure 48. Equation. Friction angle approximation for CPTu in NC to LOC clays. 41
Figure 49. Equation. Friction angle approximation for CPT in fissured over-consolidated clays. 41
Figure 50. Equation. Undrained shear strength from CPTu based on $\boldsymbol{qnet}$ and $\boldsymbol{Nkt}$. 42
Figure 51. Cone factors for evaluating undrained shear strength of clays. 43
Figure 52. Equation. Remolded undrained shear strength. 43
Figure 53. Equation. Clay sensitivity definition. 44
Figure 54. Equation. Simplified equation to evaluate sensitivity in low–medium sensitive clays. 44
Figure 55. Equation. Yield stress ratio (also known as over-consolidation ratio). 45
Figure 56. Equations. SCE-CSSM expressions for YSR of clays from CPTu. 45

Figure 57. Equation. SCE-CSSM simplified expression for YSR of clays using CPTu. 45
Figure 58. Equations. Pre-consolidation stress screening procedure for clays. 46
Figure 59. Equation. Generalized methodology for obtaining YSR in soils from CPT. 46
Figure 60. Equation: Value of m' exponent as a function of $\boldsymbol{Ic - RW}$. 47
Figure 61. Yield stress exponent ($\boldsymbol{m}$') as a function of $\boldsymbol{Ic - RW}$. 47
Figure 62. Equation. YSR from CPT for clean sands. 47
Figure 63. Equation. At-rest coefficient definition. 48
Figure 64. Equation. At-rest coefficient ($\boldsymbol{K0}$) formulation for virgin loading-unloading. 48
Figure 65. Soil compressibility relationship with the CPT material index. 49
Figure 66. Equation. Definition of state parameter ($\boldsymbol{\psi}$). 49
Figure 67. Equation. Shear modulus estimated from shear wave velocity. 52
Figure 68. Equation. Drained Young's modulus. 53
Figure 69. Equations. Drained Young's modulus based on $\boldsymbol{Ic}$ and $\boldsymbol{qnet}$ in sands 53
Figure 70. Equation. SCE-CSSM expression for rigidity index—insensitive clays. 54
Figure 71. Equation. SCE-CSSM expression for rigidity index—sensitive clays. 54
Figure 72. Equation. Relationship between the friction angles at maximum obliquity ($\boldsymbol{\phi 2'}$) and maximum deviator stress ($\boldsymbol{\phi 1'}$) and parameter $\boldsymbol{aq}$. 54
Figure 73. Equation. Rigidity index associated with $\boldsymbol{G50}$ 54
Figure 74. Equation. Coefficient of consolidation definition 56
Figure 75. Definitions of u_{50} and t_{50} for monotonic pore pressure decay 56
Figure 76. Three definitions of t_{50} from dilatory pore pressure response. 57
Figure 77. Evaluation of dissipation test in Taranto clay with dilatory response. 58
Figure 78. Equation. Coefficient of consolidation formulation developed by Teh and Houlsby (1991). 58
Figure 79. Equation. Coefficient of consolidation proposed by Mayne (2001). 59
Figure 80. Equation. Hydraulic conductivity estimation from PPD tests. 59
Figure 81. Equation. Simplified approximation for hydraulic conductivity proposed by Robertson (2010a). 59
Figure 82. Equations. Simplified approximation for hydraulic conductivity proposed by Ansari et al. (2014). 60
Figure 83. Equations. Simplified approximation for hydraulic conductivity estimation from CPT material index, $\boldsymbol{Ic - RW}$, as proposed by Robertson & Cabal (2015). 60

Figure 84. Equation. Shear wave velocity calculation from path length and travel distance. 61
Figure 85. Scheme of the wavelets recorded during an SCPTu sounding and the estimation of time interval using manual picking methods (first arrival, first peak, and first crossover). 61
Figure 86. Illustration of cross-correlation method to determine the time shift between two independent signals. 62
Figure 87. Equation. Equation to calculate the coefficient of determination (r^2). 62
Figure 88. Equation. Resultant cross-spectrum form. 63
Figure 89. Equation. Phase shift angle at the predominant frequency. 63
Figure 90. Equation. Phase delay time. $\boldsymbol{f}$ indicates frequency. 63
Figure 91. Automated wave source for continuous profiling of shear wave velocity and shear wave signals recorded using the auto-source. 64
Figure 92. Equation. Shear modulus estimated from shear wave velocity. 65
Figure 93. Equation. Young's modulus. 65
Figure 94. Equation. Liquefaction factor of safety. 66
Figure 95. Equation. Calculation of cyclic stress ratio. 67
Figure 96. Equation. Calculation of liquefaction factor of safety. 67
Figure 97. Bearing capacity factor for shallow foundations over sand-like materials. 70
Figure 98. Bearing factor for shallow foundations in clay according to Tand et al. (1986). 72
Figure 99. Equation. A nonlinear load-displacement-capacity response. 72
Figure 100. Equations. Unified direct CPT method for shallow foundations. 73
Figure 101. Equation. Trend between soil formation factor ($\boldsymbol{hs}$) and CPT material index ($\boldsymbol{Ic}$). 73
Figure 102. CPT direct method to evaluate load-displacement-capacity curves of shallow foundations for all soil types. 73
Figure 103. Equation. Static axial capacity of a single pile. 74
Figure 104. Scheme of the axial capacity of a single pile. 75
Figure 105. Pile side resistance $\boldsymbol{Cse}$ factor from Unicone method from Eslami and Fellenius (1997). 82
Figure 106. Definition of influence zone for base capacity. 82
Figure 107. Factors of the Enhanced Unicone method for axial pile capacity. 83
Figure 108. Equations. Elastic solution for load-displacement response of a rigid pile. 83
Figure 109. Elastic solution for load-displacement response of a rigid pile. 84
Figure 110. Equation. Elastic solution for load-displacement response of a compressible pile. 84

Figure 111. Equations. Displacement influence factor for load-displacement response of a compressible pile. 85
Figure 112. Elastic solution for axial load-displacement and load-transfer response of a compressible pile. 85
Figure 113. Map of the site locations and CPT data collected in District 1. 86
Figure 114. Characteristics of CPT data collected in District 1. 87
Figure 115. A photo of location of sites with SCPT/CPTu data—District 1. 88
Figure 116. Summary of CPT data at site 1 in District 1. 88
Figure 117. CPT soil stratigraphy based on Robertson (2009) SBT chart for District 1—site 1. 89
Figure 118. Map of location of sites with SCPT/CPTu data—District 2. 89
Figure 119. Characteristics of CPT data in District 2. 90
Figure 120. Photo of CPTs locations at site 2 in District 2. 91
Figure 121. Summary of CPT data at site 2 in District 2. 91
Figure 122. Representative soil stratigraphy based on Robertson (2009) SBT chart for District 2—site 2. . 92
Figure 123. Map of location of sites with SCPT/CPTu data—District 3. 92
Figure 124. Characteristics of CPT data in District 3. 93
Figure 125. Photo of CPTs locations at site 4 in District 3. 94
Figure 126. Summary of CPT data at site 4 in District 3. 94
Figure 127. Soil stratigraphy based on Robertson (2009) SBT chart of District 3—site 4. 95
Figure 128. Map of location of sites with SCPT/CPTu data—District 4. 95
Figure 129. Characteristics of CPT data in District 4. 96
Figure 130. Photo of CPTs locations and summary of CPT data at site 1 in District 4. 97
Figure 131. Soil stratigraphy is based on Robertson (2009) SBT chart of District 4—site 1. Other estimated geoparameters are also shown—see Appendix A for details. 97
Figure 132. Map of location of sites with SCPT/CPTu data—District 5. 98
Figure 133. Characteristics of CPT data in District 5. 98
Figure 134. Photo of CPTs locations at site 4 in District 5. 99
Figure 135. Summary of CPT data at site 4 in District 5. 100
Figure 136. Soil stratigraphy based on Robertson (2009) SBT chart of District 5—site 4. 100
Figure 137. Location of sites with SCPT/CPTu data—District 6. 101
Figure 138. Characteristics of CPT data in District 6. 101
Figure 139. Photo of CPTs locations at site 1 in District 6. 103

Figure 140. Summary of CPT data at site 1 in District 6. 103
Figure 141. Soil stratigraphy based on SBT charts of District 6—site 1. 104
Figure 142. Map of location of sites with SCPT/CPTu data—District 7. 104
Figure 143. Characteristics of CPT data in District 7. 105
Figure 144. Photo of CPTs locations in and summary of CPT data at site 1 in District 7. 106
Figure 145. Soil stratigraphy based on SBT charts of District 7—site 1. 106
Figure 146. Map of location of sites with SCPT/CPTu data—District 8. 107
Figure 147. Characteristics of CPT data in District 8. 107
Figure 148. Photo of CPTs locations in and summary of CPT data at site 1 in District 8. 108
Figure 149. Soil stratigraphy based on SBT charts of District 8—site 1. 108
Figure 150. Map of site location in District 9. 109
Figure 151. Characteristics of CPT data in District 9. 109
Figure 152. Photo of CPTs locations in and summary of CPT data at site 1 in District 9. 110
Figure 153. Soil stratigraphy based on SBT charts of District 9—site 1. 111
Figure 154. The variation of $(q_c/P_a)/N$ with respect to mean grain size D_{50}. 114
Figure 155. An example of fitting data for a SPT-CTP correlation in carbonate soils. 115
Figure 156. An example of SPT-CPT correlation based on fines content. 116
Figure 157. Example of SPT-CPT correlation based on soil behavior type index. “Proposed Update” refers to the correlation proposed by Robertson (2012). 117
Figure 158. Example of SPT-CPT correlation based on soil behavior type index. 118
Figure 159. Example of SPT-CPT correlation based on soil behavior type index. 118
Figure 160. Pairing data points through q_c screening. 121
Figure 161. Screening example (CPT: D6-Site1-14 and borehole: SPT-9) for Illinois data. 122
Figure 162. Pairs of CPT-SPT data from Illinois after screening and removal of outliers. 122
Figure 163. Proposed SPT-CPT correlations considering a functional form similar to that of Robertson (2012). The coefficients of the correlation have been updated using the compiled data. The Robertson (2012) correlation is also shown for reference. 124
Figure 164. $\boldsymbol{N60}$ estimation versus measured values from CPT using models for Illinois. 125
Figure 165. Photo of locations of Florence CPT soundings and borings for Shelby tube samples. 126
Figure 166. Shelby tubes distribution for laboratory testing by both IDOT and GT. 127
Figure 167. Plasticity chart. 129

Figure 168. Comparison of piezocone tests at the Florence site performed by Georgia Tech and ConeTec. 130

Figure 169. Example of dissipation tests conducted in Florence. 131

Figure 170. Florence data on CPT soil behavior type (SBTn): Qtn-Fr chart of Robertson (2009). 132

Figure 171. Florence data on CPT soil behavior type (SBTn): $\boldsymbol{Qt(1-Bq)}$ +1 vs $\boldsymbol{Fr}$ (%) chart of Jefferies and Been (2015). 132

Figure 172. Florence data on CPT soil behavior type (SBTn): Qtn vs Fr chart of Robertson (2016). ... 133

Figure 173. Interpretations unit weight from GT SCPTu at Florence, Illinois. 134

Figure 174. Interpretations of yield stress ratio (YSR) and pre-consolidation stress (σ_p') from GT SCPTu at Florence, Illinois. 135

Figure 175. Interpretations of effective friction angle and undrained shear strength from GT SCPTu at Florence, Illinois. 136

Figure 176. Florence site: (a) seismic wavelets throughout depth in clay layer, (b) interpreted in situ V_s of soil profile with lab data from Georgia Tech SCPTu D6-Site1-19. 137

Figure 177. Comparison of measured N_{60} values and equivalent N_{60} estimated values from Georgia Tech SCPTu D6-Site1-19. 138

Figure 178. Typical CPT sounding at the Northwestern University site. 139

Figure 179. Experimentation site at Northwestern University: soil behavior type profiles based on Robertson (2009, 2016). 140

Figure 180. National geotechnical experimentation site at Northwestern University: CPT interpretations and laboratory test comparison. 141

Figure 181. Schematics of the laboratory shear wave measurement setup. 157

Figure 182. Laboratory shear wave measurement Photos: consolidation cell with wave measurement settling on an oedometer (left); inside view of the top cap showing bender element for shear wave velocity measurement. This setup can also measure compressive wave through piezoelectric pads (right). 157

LIST OF TABLES

Table 1. Available Reports on CPT Practice. Soil Characterization, Geotechnical-Based Design, SPT-CPT Correlations (SPT), Processing Software, Data-Driven Approach 6

Table 2. List of CPT Soundings Reviewed or Completed, or Both, in Illinois During This Project 20

Table 3. Relationships for Estimating Total Unit Weight from CPT for All Soil Types 25

Table 4. Soil Unit Weight Estimated from CPTu for Clay-Type Soils 27

Table 5. Soil Behavior Type Using Ic According to Jefferies & Been (2015) 28

Table 6. Relative Density of Quartz and Silica Sands from CPT 36

Table 7. Undrained Shear Strength of Clays from CPTu Readings 42

Table 8. CPTu Screening Procedure for Clay-Type Identification 46

Table 9. Estimation of At-Rest Coefficient ($K0$) from CPT Measurements 48

Table 10. Estimation of Compressibility from CPT Measurements 49

Table 11. Estimation of State Parameter (ψ) from CPT Measurements 50

Table 12. Shear Wave Velocity from CPT Measurements for All Soil Types 51

Table 13. Shear Wave Velocity Estimates from CPT Measurements in Sands 51

Table 14. Shear Wave Velocity Estimates from CPT Measurements in Clays 52

Table 15. Small-Strain Shear Modulus from CPT Measurements 52

Table 16. Constrained Modulus from CPT Measurements 53

Table 17. Fines Content (FC%) Evaluation from Ic 55

Table 18. Unit Weight Calculated from Shear Wave Velocity 65

Table 19. Friction Angle and Yield Stress of Sands from Shear Wave Velocity 65

Table 20. Undrained Strength and Yield Stress of Clays from Shear Wave Velocity 66

Table 21. Direct Evaluation of Bearing Capacity from CPTu Test in Sands 69

Table 22. Correlation Factor to Evaluate Bearing Capacity on Sand-Like Materials 70

Table 23. Direct Evaluation of Bearing Capacity from CPTu Test in Clays 71

Table 24. Direct CPT Methods for the Evaluation of Axial Pile Capacity 76

Table 25. Available SPT-CPT Correlations Based on Median Grain Size (D_{50}) in mm 114

Table 26. Available SPT-CPT Correlations Based on Fines Content 116

Table 27. SPT-CPT Correlations in Literature Based on Soil Behavior Type Index 117

Table 28. SPT-CPT Other SPT-CPT Correlations in the Literature 119
Table 29. SPT-CPT Correlations for a Range of Soil Types 119
Table 30. SPT-CPT Correlations for the State of Illinois 123
Table 31. Laboratory Testing Performed in Shelby Tubes Next to Borehole EMB-1-1 127
Table 32. Summary of Soil Classification Testing and Consolidation Test at Florence Site (EMB-1-1) 128

LIST OF SYMBOLS

γ_w	Unit weight of water
γ_T	Total unit weight of soil
σ_{atm}	Atmospheric pressure (101.3 kPa ≈ 100 kPa)
σ_{vo}	Total vertical stress
σ'_{v0}	Effective vertical stress
σ_p'	Effective yield stress or pre-consolidation
ψ	State parameter
ϕ'	Effective stress friction angle
a_{net}	Cone net area ratio
B_q	Pore pressure ratio = $\Delta u_2/q_{net}$
C_c	Virgin compression index
C_N	Overburden correction factor
C_r	Recompression index
D_R	Relative density
f_s	Sleeve friction
FC	Fines content
F_r	Normalized friction ratio
I_c	Material index
I_{c-RW}	Material index from Robertson & Wride (1998)
I_{c-JB}	Material index from Jefferies & Davies (1993)
m_q	Resistance-depth ratio
N_{kt}	Cone factor for undrained strength using q_{net}
$N_{\Delta u}$	Cone factor for undrained strength using Δu_2
N_{ke}	Cone factor for undrained strength using q_{eff}
q_c	Measured cone resistance tip
q_{eff}	Effective cone resistance tip
q_{net}	Net cone resistance tip
q_t	Corrected cone resistance tip
q_{t1}	Stress normalized tip resistance
Δq_{c1N}	Equivalent clean sand correction factor based on fines content
q_{c1N}	Tip resistance that would be obtained at an overburden stress of 1 atm
q_{c1Ncs}	Clean sand-equivalent cone tip resistance
Q_E	Normalized effective cone resistance
Q_t	Normalized tip resistance
Q_{tn}	Normalized tip resistance (iterative method)
OCR	Over-consolidation ratio
s_u	Undrained shear strength
u_3	Pore pressure measurements taken behind the sleeve
u_2	Pore pressure measurements taken on the shoulder of the penetrometer tip
u_1	Pore pressure measurements taken on the face of the penetrometer tip
u_0	Hydrostatic porewater pressure
U	Normalized porewater pressure parameter
YSR	Yield stress ratio = σ'_p/σ'_{vo} (or apparent over-consolidation ratio, OCR)
z	Depth

LIST OF ABBREVIATIONS

AASHTO	American Association of State Highway and Transportation Officials
ASTM	American Society for Testing and Materials
CPT	Cone penetration test
CPTu	Piezocone penetration test
GT	Georgia Tech, or more fully: Georgia Institute of Technology
ICT	Illinois Center of Transportation
IDOT	Illinois Department of Transportation
ISO	International Organization for Standardization
LOC	Lightly over-consolidated
NC	Normally consolidated
NTH	Norwegian Institute of Technology
OC	Over-consolidated
SBT	Soil behavior type
SBTn	Normalized soil behavior type
SCPTu	Seismic piezocone penetration test
SPT	Standard penetration test
USCS	Unified Soil Classification System
USDA	United States Department of Agriculture

CHAPTER 1: INTRODUCTION

HISTORY OF CONE PENETROMETER FOR IN SITU TESTING

Penetration tests in geotechnical practice were developed later than boring and augering methods for soil investigations. Nevertheless, penetrometer tests have become widely used to characterize in situ soil response due to their valuable, expedient, and relatively cost-effective information (Massarsch, 2014). The early documentation of penetrometers was in the 14th century by Konard Kyeser (1366–1405), who described probes with a screw form (Cambefort, 1963). Afterward, different penetration probes and methods were developed in Europe (mainly Germany, France, and England) and North America. The main challenge at the early stages was the lack of standardization of probe geometries, procedures, and interpretation methods used in different countries. In this context, the first European Symposium on Penetration Testing (ESOPT I) held in Sweden in 1974 aimed to discuss different penetration tests and probes, especially to promote the standardization of procedures (Massarsch, 2014).

The cone penetration test (CPT) has become one of the preferred techniques for soil investigations because it is relatively easy to standardize, gives repeatable measurements, and cost-effectively provides continuous soil profiles (Robertson, 2016). In 1930, Pieter Barentsen developed the Dutch cone penetrometer in the Netherlands, which obtained the measurement of the tip resistance (Barentsen, 1936). This probe had a conical tip and was pushed manually into the subsurface to measure the soil resistance using a hydraulic pressure gauge, as shown in Figure 1. The next significant advance was in 1965 when Begemann introduced a friction sleeve above the cone to measure skin friction (Begemann, 1953, 1965). Before this time, only the total soil resistance was measured.

A. Dutch cone penetrometer field operation

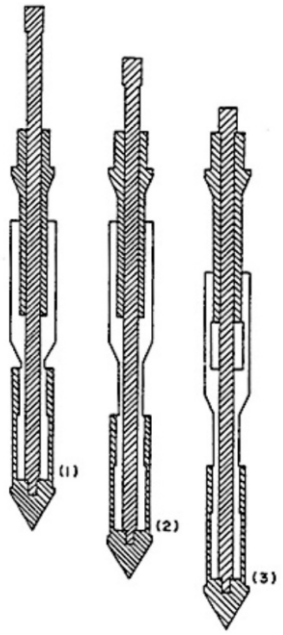

B. Dutch cone penetrometer

Figure 1. Dutch cone penetrometer and three associated operation steps.

Source: Adapted from Massarsch (2014)

The electric cone penetrometer was introduced in Germany after World War II, with subsequent prototypes developed at Delft in 1948 (Broms & Flodin, 1988; Massarsch, 2014). The first electric cone with measurement of both tip resistance and friction was commercially available in 1965 by Fugro. Subsequently, in 1975, in Norway, the USA, and Sweden, the pore pressure measurement was incorporated into the probe to measure pore pressures during penetration and perform pore pressure dissipation tests (Torstensson, 1975; Wissa et al., 1975). Then, in addition to measuring the tip resistance and sleeve friction, pore pressure measurements were also possible in what is known as a CPTu or piezocone penetration test. Soon after, an accelerometer was incorporated within the probe to permit downhole seismic testing to measure the shear wave velocity of the soil (Campanella & Robertson, 1984); this test is typically known as a seismic piezocone test (SCPTu). Generally, an SCPTu test is performed at discrete measurements at 1 m (3.28 ft) intervals. However, recent researchers have proposed equipment and processing methods to continuously measure the shear wave profiles (Ku et al., 2013a; Ku et al., 2013b). The CPT probe can include additional instrumentation to measure its inclination during the sounding and other sensors, including electrical resistivity, dielectric, pH, gamma, videocam, acoustic sounds, and more.

PIEZOCONE TESTING

The CPTu test is standardized by ASTM D 5778 (2020) and ISO 22476-1 (2022). It consists of an electronic steel probe with a conical tip advanced vertically into the soil at a constant rate. According to the standard, the apex angle of the cone tip is 60°, the cone base area is 10 or 15 cm^2 (1.55 or 2.32 sq. in), and the pushing rate = 20 mm/s (0.79 in/s). During the penetration of the piezocone into the

soil, three independent readings are recorded with depth, generally taken every 10 to 50 mm (0.39 to 1.97 in) of penetration: cone tip resistance, q_c; sleeve friction, f_s; and porewater pressure, u_2. The porewater pressure can be measured at different parts of the probe. If the measurement is made on the face of the penetrometer tip, it is named the u_1 position, and if it is taken at the shoulder, it is called u_2. Readings can also be taken behind the sleeve, designated u_3. Both ASTM and its equivalent ISO standard require that the pore pressure filter element be positioned at the shoulder of the probe (i.e., the u_2 position), because the measured tip resistance q_c must be converted to a total cone tip resistance, designated q_t. Figure 2 shows a schematic of several penetrometers, including the placement of the sensors to measure the tip resistance, sleeve friction, and pore pressure. Figure 2 shows a standard electric cone penetrometer (q_c and f_s), type 1 piezocone (q_c, u_1, and f_s), and type 2 piezocones (q_c, u_2, and f_s) in two sizes. As noted earlier, a type 2 CPTu is necessary since q_c is upgraded to the total cone tip resistance (q_t), which requires the u_2 readings.

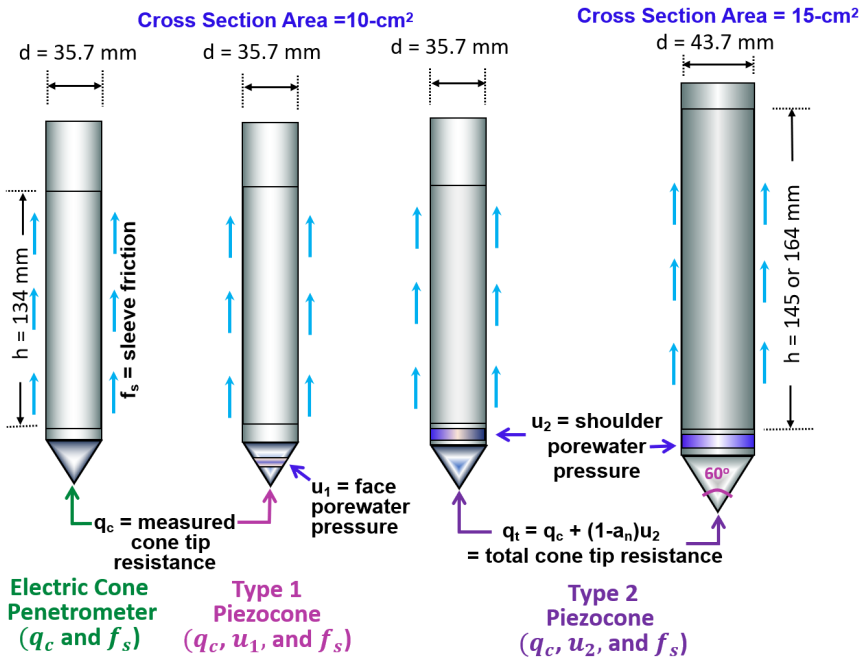

Figure 2. Schematics of different types of cones: electric cone penetrometer (measure q_c and f_s), Type 1 piezocone (measure q_c, f_s, and u_1), and Type 2 piezocones with a cross-sectional area of 10 and 15 cm² (measure q_c, f_s, and u_2), respectively.

Source: Mayne et al. (2023a)

A representative example of the results of a piezocone sounding performed in southwestern Illinois is shown in Figure 3. Overall, the 31 m (102 ft) CPTu sounding indicates 16 m (52.5 ft) of clay overlying a dense sandy layer. The q_t and f_s readings in the clay are quite low. Therefore, their plots are presented on two scales (high and low), and both are shown on these portions of the sounding, corresponding to Figure 3-A and 3-B, respectively. In Figure 3-C, the light-blue dashed line indicates the equilibrium porewater pressure (u_0) calculated from a known groundwater elevation. In intact clays and clayey silts, the u_2 reading will be above u_0 values due to undrained penetration, while in clean sands, the $u_2 \approx u_0$. This is clear at 16 m depth, where the clay layer meets the sand stratum.

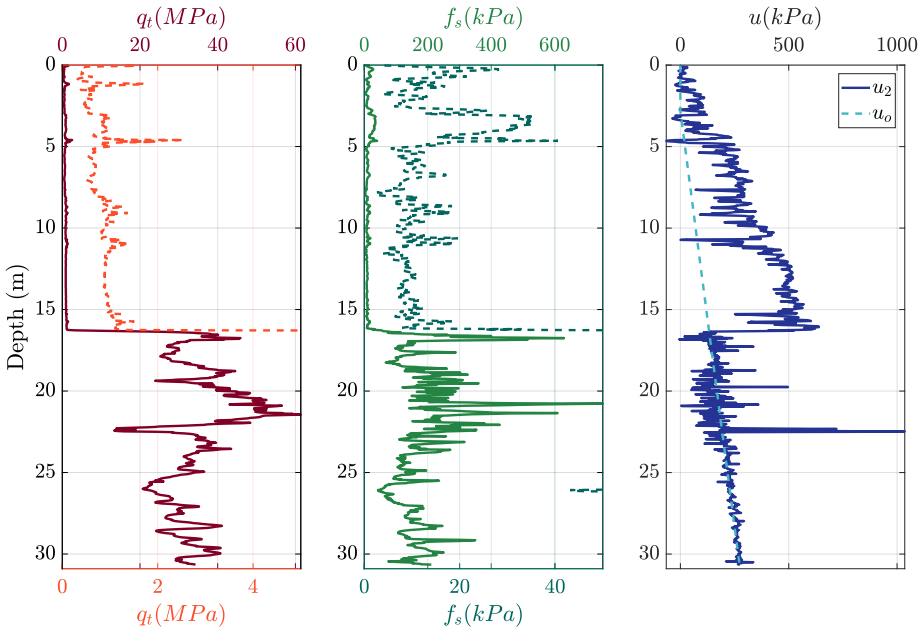

A. B. C.

(A) Corrected tip resistance, (B) sleeve friction, (C) u_2: Dynamic porewater pressure at u_2 position (behind the shoulder) and u_0: equilibrium porewater pressure (at rest porewater pressure).

Figure 3. Example data from a CPTu sounding in southwestern Illinois.

Source: Georgia Tech

FIELD EQUIPMENT

The field equipment required to perform piezocone testing includes the following (Robertson & Cabal, 2015):

1. Electronic piezocone penetrometer.
2. An electrical cable for transmitting data from the penetrometer to a computer.
3. Depth sensor, such as a depth wheel or electrical potentiometer, or infrared device.
4. Pushing equipment that includes the thrust mechanism, reaction frame, and pushing rods.
5. Data acquisition system. It is typically tied to a field laptop computer located at the ground surface.

The first component, the electronic penetrometer, includes the 60° apex conical tip and the load cells and transducers to measure tip resistance, sleeve friction, and porewater pressure at the shoulder of the cone. Of note, this probe can include additional sensors, such as geophones or accelerometers, to perform seismic piezocone testing (SCPTu) or other specific sensors like temperature, pH, and electrical resistivity or combined. The second component is an electrical cable that connects the

electronic penetrometer to the data acquisition system (fifth component) to obtain the readings in a digital format. The electrical cable is advanced into the soil by a series of hollow extension rods, each with a standard length of 1 m (3.28 ft). These rods are connected to the equipment that pushes the probe into the ground (Niazi, 2021).

The third component, the depth sensor, measures the distance the cone has advanced into the ground. The depth sensor should be in a separate platform than the pushing equipment to avoid its displacement during the cone advance. Moreover, the resolution of the depth sensor should agree with the resolution and data acquisition date of the penetrometer to properly match the readings with the corresponding depth. The depth recorder is connected to the data acquisition system used to connect the electrical cable.

The fourth component includes the equipment that pushes the penetrometer vertically into the ground at a constant rate of 20 mm/s (0.79 in/s). The thrust mechanism usually comprises a hydraulic actuator and pump systems mounted on a vehicle or platform that serves as a reaction frame (Mayne, 2007a). The platform used depends on whether the sounding is performed onshore (on land) or offshore (on water). The equipment is mobilized using trucks or track-mounted equipment for onshore testing. Figure 4 shows some examples of onshore equipment.

A. Truck-mounted system from ConeTec

B. Track-mounted system from ConeTec

C. Anchored rig from Pagani

Figure 4. Photos for onshore equipment for piezocone testing: (A) truck-mounted system, (B) track-mounted system, and (C) anchored cone penetrometer rig.

Sources: ConeTec Group and Pagani Geotechnical

PRACTICES OF OTHER STATE TRANSPORTATION AGENCIES USING CPT-BASED TESTING AND DESIGN

Several U.S. state DOTs and national reports provide guidelines for cone penetration, piezocone, and seismic cone testing. Table 1 summarizes the information available from these references considering three categories: (1) soil characterization and parameters estimation, (2) geotechnical design, and (3) correlations between the cone penetration test and standard penetration test (SPT), the latter was included as a specific topic of interest by IDOT. This information was reviewed and served as a partial basis for providing the guidelines and interpretation procedures recommended for IDOT in Chapter 5 of this report.

Table 1. Available Reports on CPT Practice. Soil Characterization, Geotechnical-Based Design, SPT-CPT Correlations (SPT), Processing Software, Data-Driven Approach

State/Agency	Soil Characterization	Geotechnical Design	SPT-CPT Correlations	Comments
Louisiana Transportation Research Center, LTRC (Titi & Abu-Farsakh, 1999; Alshibli et al., 2008; Abu-Farsakh et al., 2008; Abu-Farsakh et al., 2011; Chen & Liu, 2018).	✓	✓	✓	
National Cooperative Highway Research Program, Synthesis 368 (Mayne, 2007b)	✓	✓		

State/Agency	Soil Characterization	Geotechnical Design	SPT-CPT Correlations	Comments
Ohio Department of Transportation Office of Research and Development (Stern & Fox, 2011)	✓	✓	✓	Excluding liquefaction assessment
Wisconsin Highway Research Program (Schneider & Hotstream, 2011)	✓	✓	✓	Excluding liquefaction assessment
Guide to Cone Penetration Testing, 7th Edition (Robertson & Cabal, 2022)	✓	✓	✓	
Minnesota Department of Transportation (Dagger et al., 2018)	✓	✓		Excluding liquefaction assessment
Indiana Department of Transportation and Purdue University. Volume 1: CPT interpretation-Estimation of soil properties (Niazi, 2021) Volume 2: CPT-Based Design of Foundations (Sakleshpur et al., 2021)	✓	✓	✓	Excluding liquefaction assessment Includes Excel format files for CPTu processing

ILLINOIS GEOLOGY

In this section, we discuss the geology of Illinois, as it is relevant in interpreting any subsurface exploration, including SCPTu tests. As illustrated by Figure 5, sedimentary rocks ranging in age from about 510 million (Cambrian) to 290 million (Pennsylvanian) years are found in Illinois and were deposited in and near ancient fluctuating seas. Cretaceous sands and gravels deposited in extreme southern and western Illinois are about 100 to 66 million years old. Tertiary rocks were deposited as coastal plain and deltaic sediments between 66 and 2 million years ago. As discussed in the *Guide to the Geologic Map of Illinois* (ISGS, 1961), the uppermost geomaterials of Illinois are young—a mere 15,000 years old. During the Ice Age, most of Illinois was repeatedly invaded by huge glaciers, sometimes towering a mile or higher, that carried ground-up rock materials within them as they gouged out the bedrock in the north and ponderously pushed south. When the last of the glaciers melted from Illinois about 15,000 years ago, the terrain that emerged looked far different than that from the preglacial land. Old hills and valleys had vanished, new ones had formed, and a mantle of unconsolidated rock material formed the overburden carried by the ice and dropped as the ice melted, lay over most of the region. Most of this material, called glacial drift, was brought in by the ice during the last two of the four major periods of glaciation—the Illinoian period from 150,000 to 100,000 years ago and the Wisconsin event from about 75,000 to 15,000 years ago. The older drift introduced during the Kansan and Nebraskan glacial periods is almost entirely buried beneath the later drifts. The glaciers covered all of Illinois except the northwestern corner, the southwestern edge along the Mississippi River, and extreme southern Illinois, as shown in Figure 6. In those areas, the land is much as before the glaciers came. In the glaciated portion of the state, however, the bedrock

generally is covered by the rock debris the ice carried from as far away as Canada. As the fringes of the ice melted, these loads of rock material were, in some places, dumped as ridges (moraines), which are the hills and mounds on the flat prairies of the present landscape. Such material also filled ancient river valleys, but new valleys were cut by torrents of water released by the melting ice. The geological processes in Illinois caused the surface geology shown in Figure 7. Figure 8 illustrates the thickness of glacial drift (depth to bedrock). The surface geology of Illinois will be used when interpreting the collected SCPTu data.

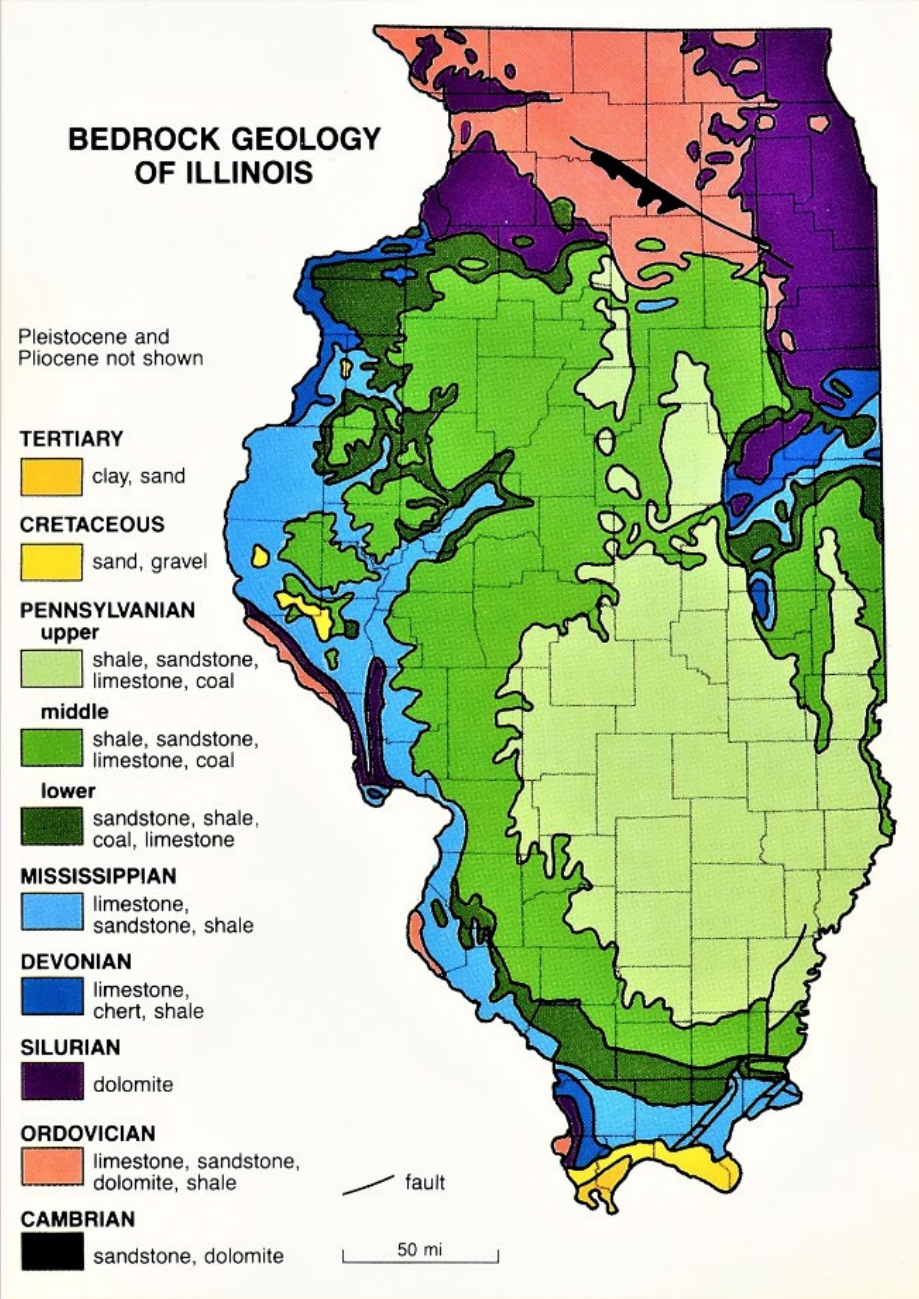

Figure 5. Bedrock geology map for the State of Illinois.

Source: Illinois State Geological Survey (1961)

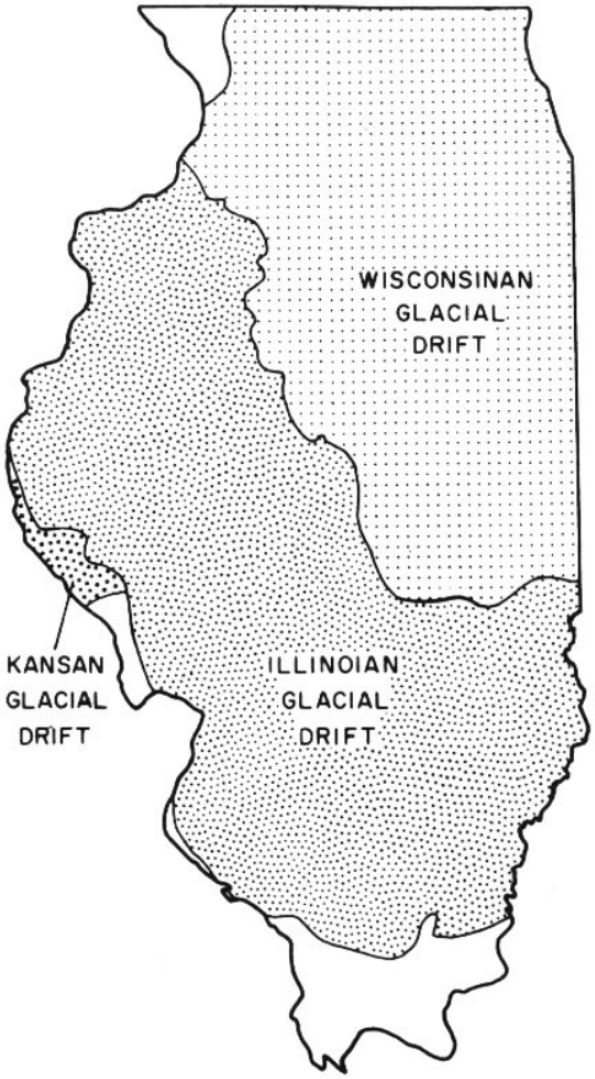

Figure 6. A map showing that glacial drift mantles cover the bedrock in the state of Illinois.

Source: Illinois State Geological Survey (1961)

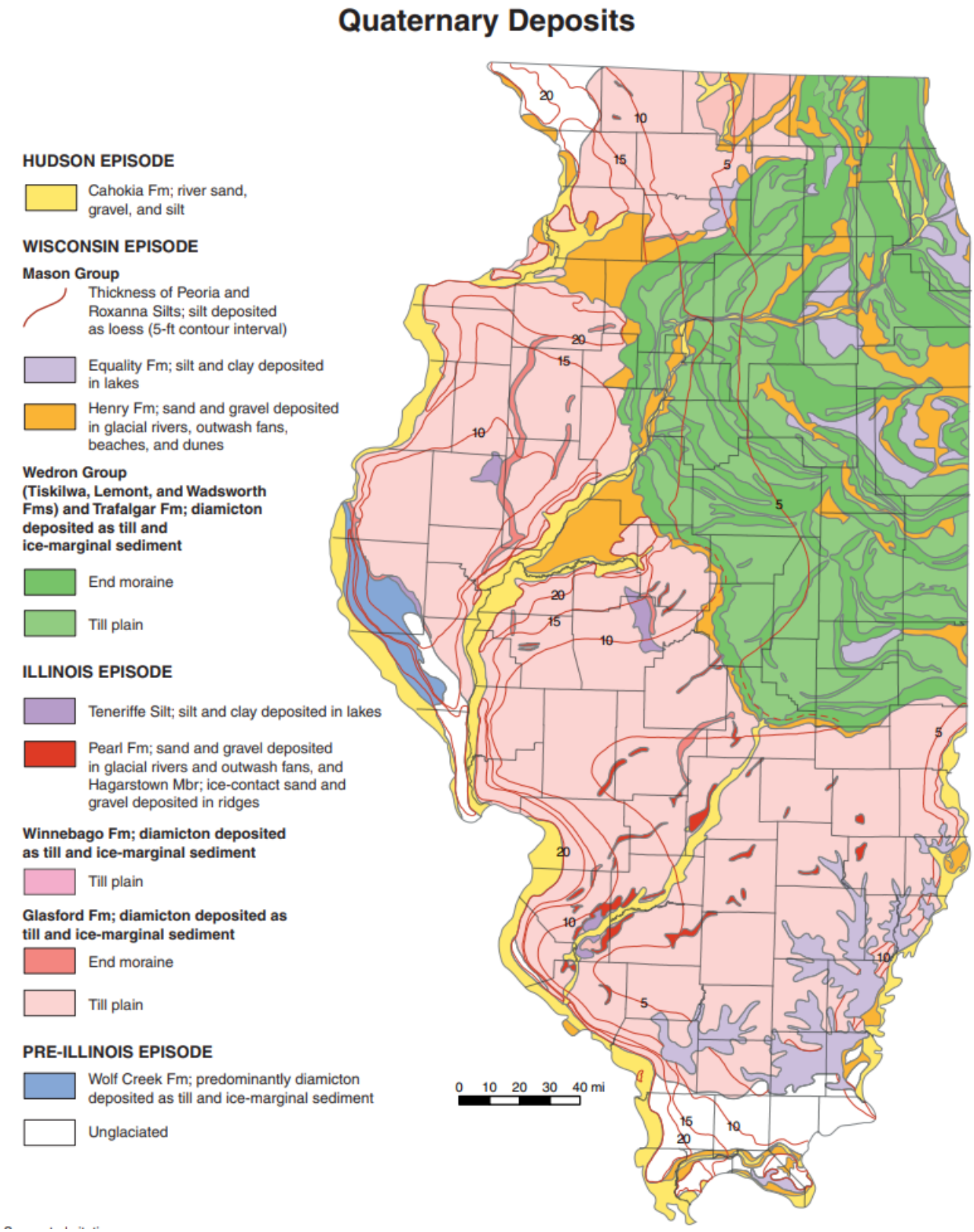

Figure 7. Map of quaternary deposits for the state of Illinois.

Source: Illinois State Geological Survey (2005)

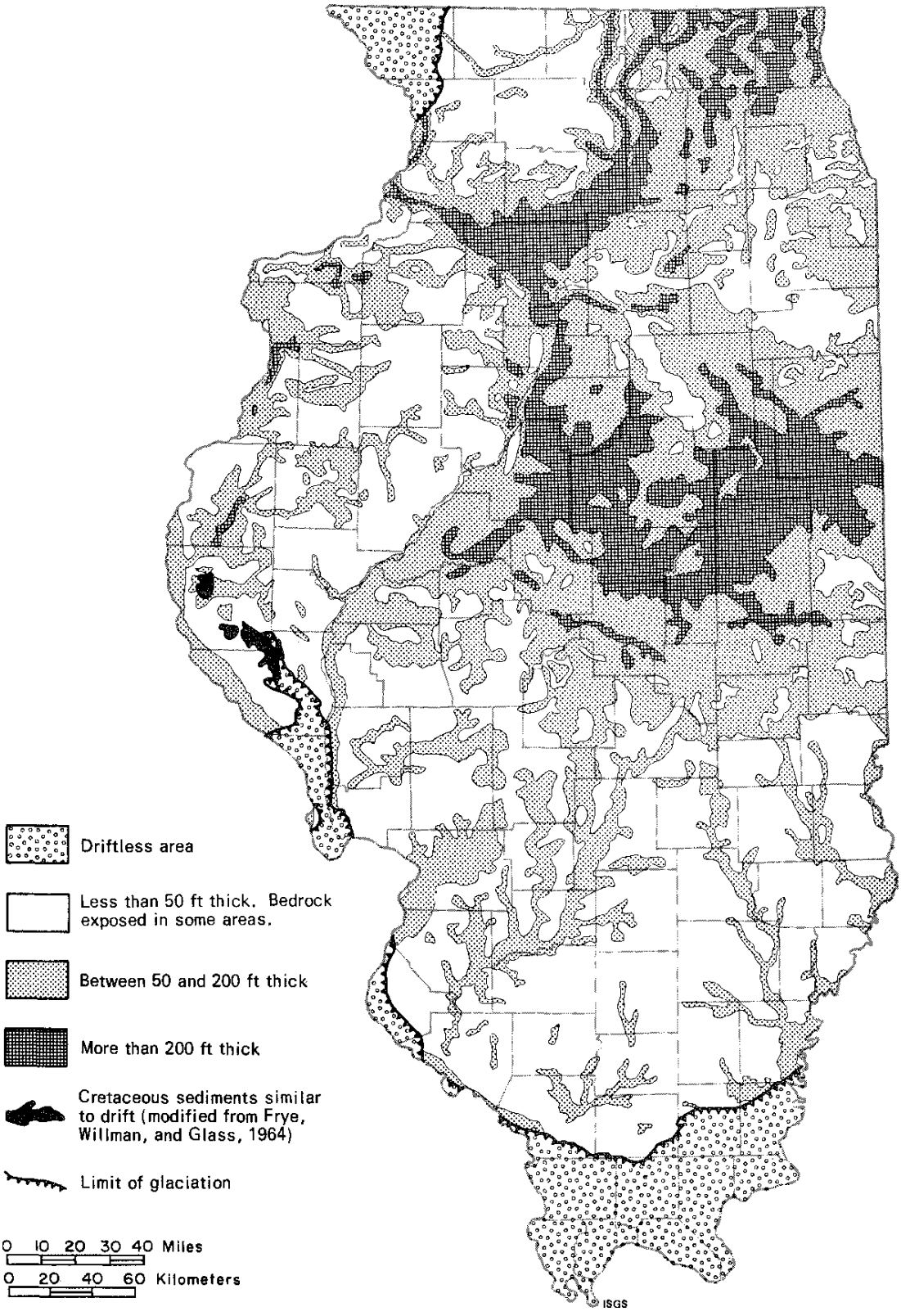

Figure 8. Map of generalized drift thickness in Illinois.

Source: Piskin & Bergstrom (1975)

CHAPTER 2: FIELD TESTING AND GENERATED SCPTU/CPT DATA

This chapter describes the SCPTu fieldwork conducted as part of this study. Additional data have been collected by accessing SCPTu information through Georgia Tech and IDOT. Georgia Tech and IDOT conducted several meetings and exchanged information to define the selected testing locations, which are presented in Figure 9. The chosen test locations for SCPTu considered all nine districts to gather a wide breadth of data across the state of Illinois. A small group of Georgia Tech graduate students from the School of Civil & Environmental Engineering were trained to conduct the required field testing. In addition, ConeTec Group, working with Georgia Tech, collaborated to conduct SCPTu soundings at selected locations.

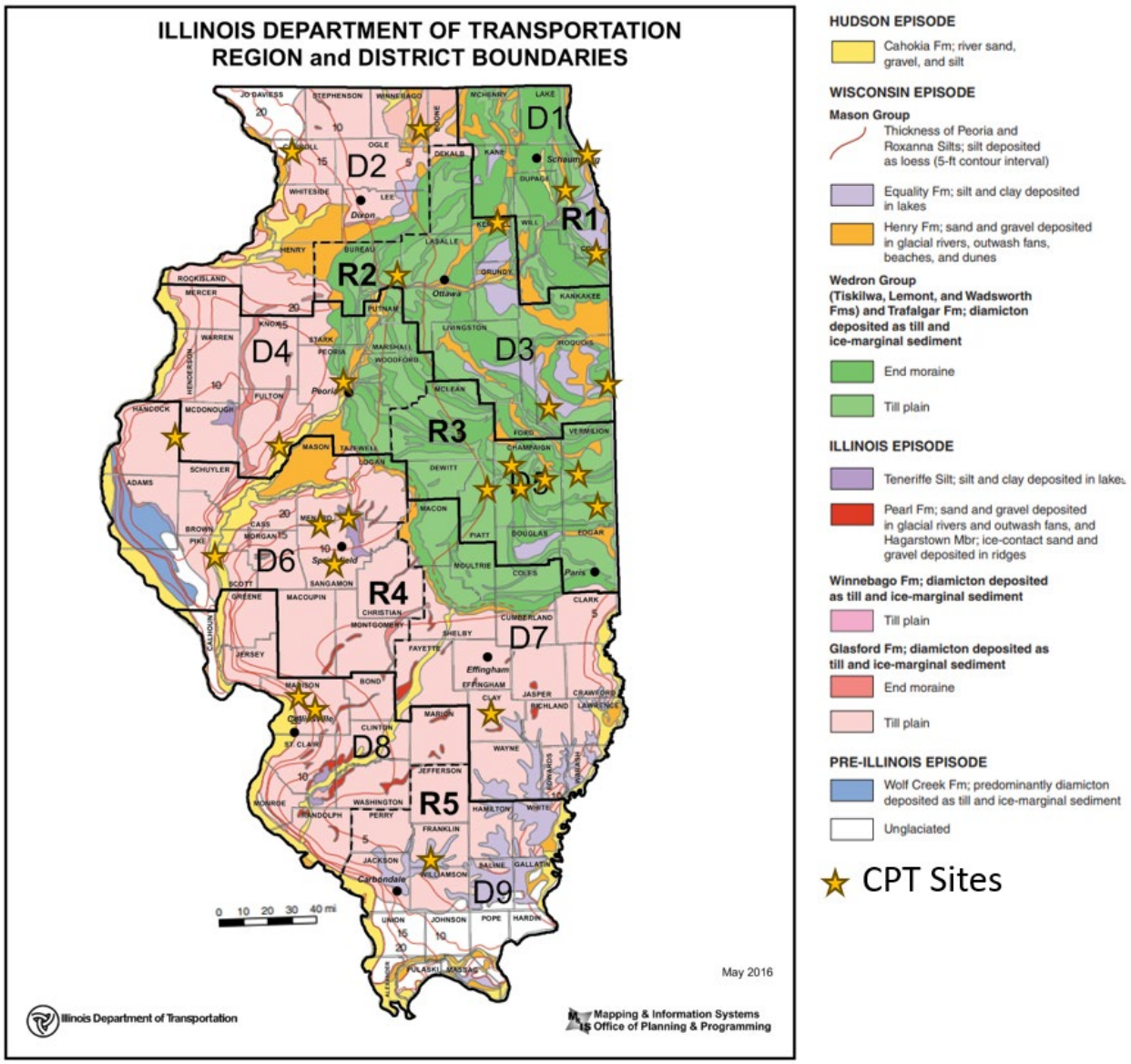

Figure 9. Map of Illinois showing the nine IDOT state districts and sites of collected CPTu data.

Source: Georgia Tech

This chapter is organized as follows: First, we describe the SCPTu systems used in this project (i.e., Georgia Tech and ConeTec SCPTu systems). We then discuss the SCPTu field testing procedures and shared details on the training of Georgia Tech students, which would be potentially useful for IDOT in their training program. Finally, we close this chapter by providing details on the SCPTu information generated as part of the project. A total of 157 CPT, CPTu, and SCPTu soundings were collected at 25 locations across the nine IDOT districts. This includes the conducted tests and additional SCPTu information provided by IDOT and collected by Georgia Tech. IDOT also provided historical information on boreholes and Shelby tubes, which is also discussed. The generated information in this project is used in Chapters 4, 5, and 6 of this report in the interpretation of geotechnical conditions and soil engineering parameters within the State of Illinois.

CONE PENETROMETER EQUIPMENT

Two CPT systems were used during this study: (a) Georgia Tech (GT) system and (b) ConeTec equipment, as described subsequently.

The SCPTu GT system includes a truck-mounted hydraulic thrust mechanism with adequate reaction capacity, a data acquisition system, electric cables, push rods, and a penetrometer with desired sensors. Figure 10 shows a general schematic of a seismic piezocone penetrometer. Figure 11-A shows a selection of several of the GT-acquired penetrometers with varying sensor configurations, including resistivity module, u_1 and u_2 pore pressure sensors, seismic, and full-size and mini-cone systems. For the IDOT soundings, new equipment was acquired by GT and used in this project consisting of a Vertek HT series (the former Hogentogler CPT product line) seismic piezocone system, which offers penetration readings (q_t, f_s, u_2), downhole shear wave velocity (V_s), as well as bi-axial inclination with depth. Figure 11-B shows a simple manual source, one of several seismic generating sources used by GT. The data acquisition system comprises a signal processing unit, transmission cable, depth recorder, and a laptop computer. The specific components vary, but recently developed electronic systems contain the signal conditioning, amplification, and digital output directly within the penetrometer instead of a processing unit on the surface.

Modern penetrometers will, at a minimum, provide three data channels with depth: tip resistance (q_c), sleeve friction (f_s), and pore pressure (u_2). The CPT group at Georgia Tech utilizes a Hogentogler SCPTu system (aka Vertek H-T) with a 10 cm^2 (1.55 sq. in.) cross-sectional area and 150 cm^2 (23.25 sq. in.) sleeve. The penetrometer contains a dual-axis geophone (both horizontal) for pseudo-interval V_s measurements. The specific depth gauge used is an encoder-type depth wheel from Vertek/Hogentogler. The encoder-type depth wheel has several advantages over the proximity type. First, it is capable of higher depth resolutions for each depth interval (5 mm [0.20 in.]), as compared to the proximity type (2 cm [0.79 in.]). In addition, it can read the push direction (i.e., up or down), which allows for more accurate measurements as it will automatically account for any uplift in the penetrometer during the release of the ram pressure to install new rod sections. The pore pressure filter is 5 mm (0.20 in.) thick and pre-saturated, using either glycerine or silicone fluid to take the u_2 readings.

Figure 12 shows pictures of the Georgia Tech CPT truck. The rig consists of a Ford F-350 model truck with a modified flatbed. The hydraulic pushing mechanism with two ram sets is mounted at the rear

of the bed along with anchors and leveling pistons, as shown in Figure 12-B. For a more in-depth description and discussion of the various configurations of sensors of the SCPTu GT CPT equipment, see Mayne (2007b) and Niazi (2021).

The ConeTec system used in this study included a 25-ton CPT truck. The soundings were conducted using an integrated electronic piezocone penetrometer and data acquisition system manufactured by Adara Systems Ltd., a subsidiary of ConeTec. The cone specifications include a cross-sectional area of 15 cm^2 (2.32 sq. in.), sleeve area of 225 cm^2 (34.88 sq. in.), tip capacity of 1500 bar, sleeve capacity of 10 bar, and pore pressure capacity of 35 bar. The penetrometers are designed with equal end area friction sleeves, a net end area ratio of 0.8, and cone tips with a 60-degree apex angle. The pore pressure filter is 6 mm (0.24 in.) thick and made of porous plastic (polyethylene), having an average pore size of 125 µm (90–160 µm). ConeTec's piezocone penetrometers are compression-type designs in which the tip and friction sleeve load cells are independent and have separate load capacities. The piezocones use strain-gauged load cells for tip and sleeve friction and a strain-gauged diaphragm-type transducer for recording pore pressure. The piezocones also have a platinum resistive temperature device (RTD) for monitoring the temperature of the sensors, an accelerometer-type dual-axis inclinometer, and two geophone sensors for recording seismic signals.

An illustration of a piezocone penetrometer is presented in Figure 10. Moreover, ConeTec's piezocone penetrometers are manufactured with one horizontally active geophone (28 hertz) and one vertically active geophone (28 hertz). Both geophones are rigidly mounted in the body of the cone penetrometer.

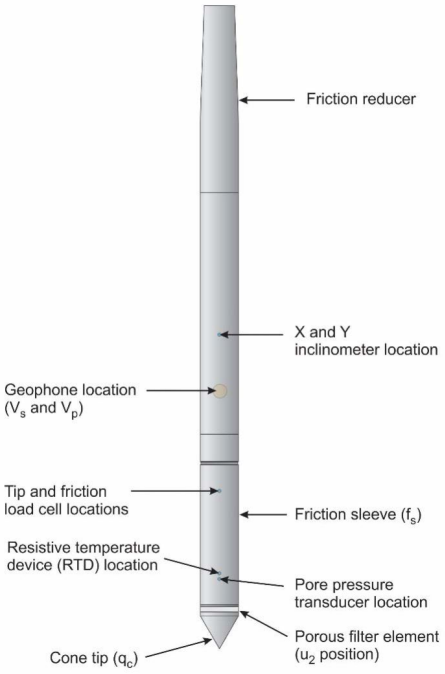

Figure 10. General schematic of the ConeTec seismic piezocone penetrometer.

Source: ConeTec Group

A. Several of the GT-acquired cone penetrometers in varying sizes and sensor configurations from Mayne (2007b)

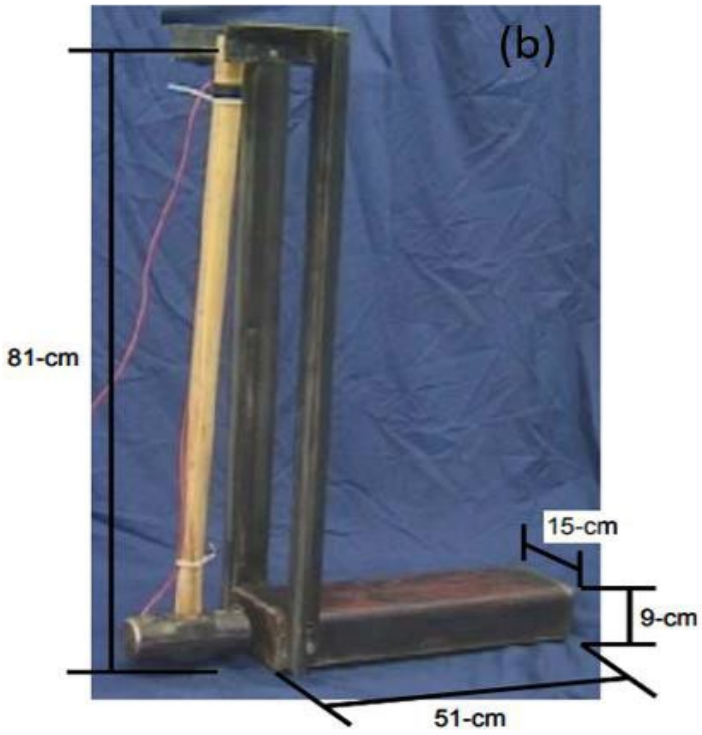

B. A manual seismic source used by Georgia Tech, as detailed by McGillivray (2007)

Figure 11. Photos of (A) several of the Georgia Tech cone penetrometers in varying sizes and sensor configurations and (B) manual seismic source used by Georgia Tech.

Source: Mayne (2007b)

A. Georgia Tech CPT rig in operation in the State of Illinois

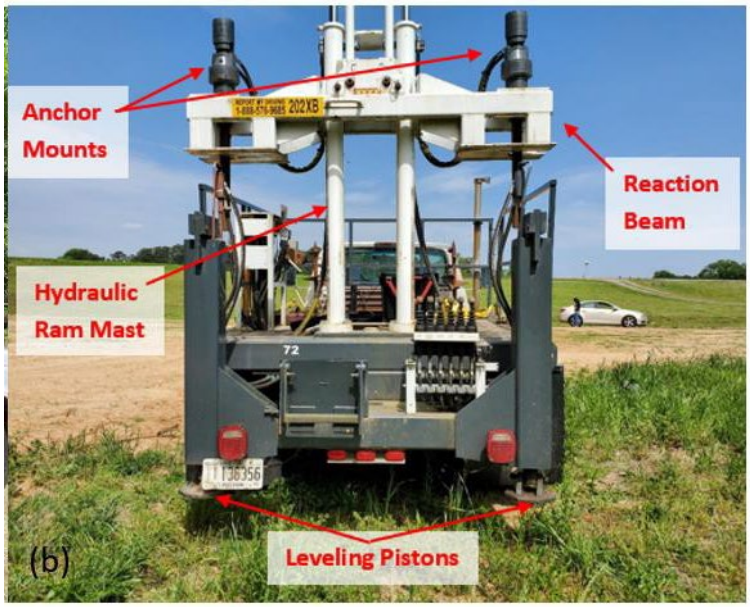

B. Rear operating end of Georgia Tech's CPT system

Figure 12. Photos of Georgia Tech CPT rig in the State of Illinois: (A) side view and (B) rear view.

Source: Arnold et al. (2023)

SCPTU TESTING PROCEDURES

Procedures for conducting the piezocone penetration test (CPTu) are standardized by ASTM D 5778 (2020) and ISO 22476-1 (2022). For SCPTu, the seismic portion to collect shear wave data is governed by ASTM D 7400 (2019).

The CPT rig operated by Georgia Tech is shown in Figure 12. The truck weighs only 6 tons in order to meet state requirements regarding normal vehicle licensing, taxes, and mobility. Therefore, to achieve the full 20-ton desired capacity, it relies on twin earth anchors to provide adequate reaction forces when performing the test. The reaction beam, as labeled, is lifted using the hydraulic ram and contains the anchor mounts. Because both anchors are attached to the same lifting mechanism, they must be inserted into the ground simultaneously. This can make anchoring difficult as both anchors will not always penetrate at the same speed or consistency. As such, it takes a skillful operator with care to ensure good anchor connections to the ground without inducing tilting in the mast of the ram. Other CPT systems will either use dead weight or individual anchors for efficiency and ease of use. As important as good anchoring, leveling is also key to accurate data collection. This CPT system also has two leveling pistons or outriggers on the rear of the truck.

The general procedure for testing with the Georgia Tech CPT truck used in the State of Illinois begins with a site reconnaissance to determine feasible locations to perform testing. Once the locations are determined, the vehicle is driven to the location and parked in a manner that the front is slightly higher in elevation than the rear. The rear tires are blocked as well, with the emergency brake engaged for safety but also to ensure no movement of the vehicle during the test. From there, the rig is leveled using the pistons prior to anchoring. This is to ensure the anchors are penetrated vertically and not at an angle. Note that for SCPTu testing, the source block is placed under one of the leveling piston feet at this point. The anchor extensions and flights are then attached to the reaction beam and anchored into the ground. Depending on the ground conditions, there are larger or smaller anchor flights. Larger flight anchors are more difficult to anchor but provide much more reaction force. For example, it may be easier and sufficient to use the smaller flight anchors in stiff ground conditions. Additionally, multiple extensions can be added to the anchors, allowing for deeper anchoring and, thus, more reaction force. Typically, extending the anchor depth is only necessary for very soft soil or for deeper pushes. Once sufficient anchoring is achieved, the reaction beam is detached from the ram and sits directly on the truck body. This allows for the ram to be raised to advance the penetrometer while maintaining reaction force. The level of the rig is then checked again and adjusted as needed.

After anchoring and leveling, the electronics connections and penetrometer are then assembled. Since the rig is not enclosed, the electronics must be stored between uses and re-assembled for each push. For shear wave velocity measurements, the horizontal alignment of the seismic source (shown in Figure 11-B) is positioned so that the axis is parallel with one of the two horizontal geophone directions. The bottom plate is placed under one of the leveling pistons in order to provide good ground surface contact. Additional details on the source mechanism and source-to-receiver placement are discussed in McGillivray (2007).

Once all the components are wired and connected, the penetrometer is prepared. This involves installing a new saturated pore pressure filter element to the penetrometer and saturating the openings by filling the cavity with silicon fluid. The conical tip is then installed over the filter, and the penetrometer is connected to the transmission cable. After all components are ready, the software is opened to check that the depth gauge, source, and penetrometer channels are all reading correctly.

The penetrometer is then ready to be attached to the friction reducer and first rod. The friction reducer is a small rod attachment that is slightly larger in diameter than the standard cone rods. This is to aid in reducing the overall friction along the rods as the cavity formed is slightly larger than the rods themselves. The penetrometer with connections and rod is then carefully maneuvered into the hydraulic ram, and the test can begin. Additional rods can be coupled as needed by simply connecting them with the ones attached to the penetrometer. Per ASTM D 5778 (2020), the penetrometer is advanced at 2 cm/s ± 0.5 (0.79 in/s ± 0.2) until sounding termination. The test can be terminated for a variety of reasons: (a) desired depth was reached, (b) excessive inclination, or (c) very high tip resistance or other reading reaching limit capacity. Once the test has been completed, the software readings are stopped, and data are saved to a hard drive. The depth wheel is removed, and the rods are pulled upward and removed until the penetrometer is retrieved, usually at a faster rate than penetration (e.g., 20 cm/s (7.87 in/s)). Final baseline readings from the penetrometer channels are then reviewed and recorded to ensure the penetrometer load cell measurements are consistent with those at the beginning of the test.

ConeTec procedures are also conducted in general accordance with the current ASTM D 5778 (2020) standards. Prior to the start of a CPTu sounding, a suitable penetrometer is selected, the cone and data acquisition system are powered on, the pore pressure system is saturated with either glycerin or silicone oil, and the baseline readings are recorded with the cone hanging freely in a vertical position. The data are recorded at fixed depth increments using a depth wheel attached to the push cylinders or a spring-loaded rubber depth wheel held against the cone rods. The typical recording interval is 2.5 cm (0.98 in). The data acquisition systems consist of a Windows-based computer, a signal interface box, and a power supply. The signal interface combines depth increment signals, seismic trigger signals, and downhole digital data. The combined data are then sent to the Windows-based computer for collection and presentation. More detailed information regarding ConeTec procedures for seismic cone penetration testing and pore pressure dissipation testing can be found in Mayne et al. (2023b).

The Georgia Tech testing procedure described previously for this project has been implemented based on periodic training (except during the required COVID-19-related lockdowns) of graduate Georgia Tech students at three main locations: (a) the W21 parking lot testing site near the Mason Building (Civil Engineering at GT); (b) a testing site situated at the Cobb County Water Authority in Marietta, Georgia; and (c) the national testing site “Spring Villa Geotechnical Test Site” at Opelika, Alabama that is managed by Auburn University on behalf of Alabama DOT. Georgia Tech graduate students have been instructed to drive the GT rig in compliance with state standards for safety and operation. Various training phases were required to drive and operate the vehicle. Students have also been trained in the operation of the hydraulic systems on the GT truck. These systems include the leveling feet, anchor system, and main ram for pushing (and pulling) the rods and penetrometer. While performing these operations, the GT students were reminded of the importance of maintaining a safe work environment for themselves and others.

The GT crew, led by PhD researcher Cody Arnold and the project principal investigators, initially pushed several “dummy” tests at the W21 Georgia Tech testing site to ensure they were knowledgeable in prudent operations. The GT crew has also been exposed on numerous occasions to professional CPT soundings performed by local firms, including EGCsi Geophysics and Ahlberg

Engineering, both of whom own and operate Pagani-type CPT rigs in the Atlanta area. This allowed them to learn how SCPTu soundings are conducted at professional standards for accuracy, safety, and efficiency. Figure 13 shows the GT crew practicing their skills prior to transitioning to using an actual penetrometer during the multiple trainings using the Vertek HT system.

Figure 13. Photos of GT field crew using the Vertek HT cone penetrometer system.

Source: Georgia Tech

INFORMATION GENERATED ON THIS PROJECT

A listing of the cone penetration test soundings per district conducted by Georgia Tech and ConeTec Group is given in Table 2. Also, the table includes information on the number of tests with shear wave velocity (SWV) measurements or dissipation tests, or both. In addition, Table 2 shows the listing of CPTs facilitated by IDOT and made available to Georgia Tech as part of previous efforts. The total

information collected as part of this project includes 156 cone penetration test soundings, shear wave velocity measurements taken at 28 locations, and pore pressure dissipations (PPD), which were available at 45 locations. Of note, the number of tested sites exceeded the 21 sites specified in the project scope. Figure 14 shows a histogram of the number of penetration tests per district (the number of tests with shear wave velocity measurements and dissipation tests is also presented in the histogram), highlighting that most data have been generated for District 6. Figure 15 shows a histogram of exploration depths per district. These data generated in this study are further processed and interpreted in Chapters 5 and 6.

Table 2. List of CPT Soundings Reviewed or Completed, or Both, in Illinois During This Project

ICT District	CPT Work	# of CPTs	CPTs with PPD Tests	CPTs with SWV tests	Source*
D1	ConeTec	3	2	0	ConeTec
	Georgia Tech	1	0	1	This project
D2	Georgia Tech	3	3	1	This project
D3	Georgia Tech	1	1	1	This project
	ConeTec and Georgia Tech	6	4	2	This project
	Rubino Engineers	8	0	0	IDOT
D4	ConeTec and Georgia Tech	2	2	2	This project
D5	ConeTec	17	10	3	This project
	Georgia Tech	2	1	0	This project
D6	Georgia Tech	1	1	1	This project
	ConeTec	21	14	11	IDOT
	Rubino Engineers	79	2	0	IDOT
D7	Georgia Tech	1	1	1	This project
D8	ConeTec and Georgia Tech	2	2	0	This project
D9	Georgia Tech	1	1	1	This project

*Notes:

This project: CPTs generated by Georgia Tech as part of this project.

IDOT: CPTs provided by IDOT and processed as part of this project.

ConeTec: CPT provided for ConeTec and processed as part of this project.

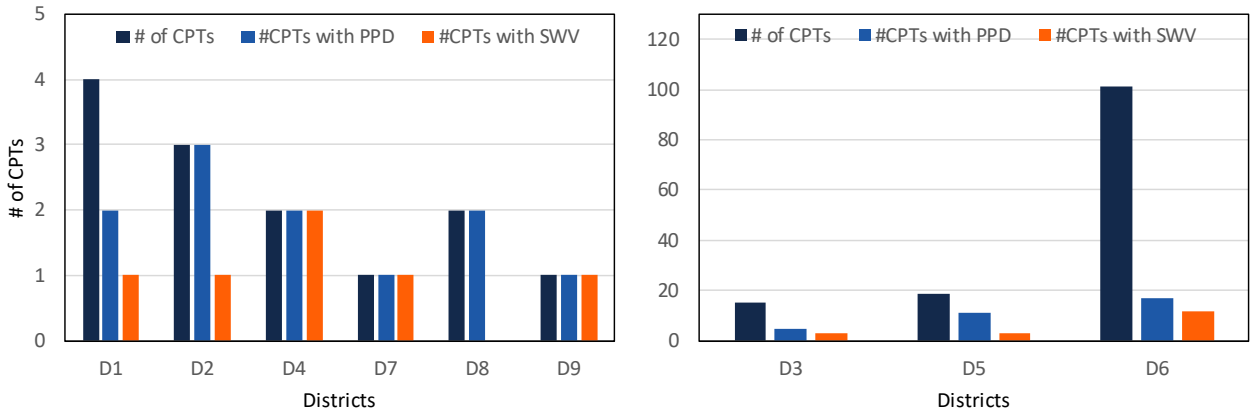

Figure 14. Histogram summaries on the numbers of cone penetration tests per district.

Source: Georgia Tech

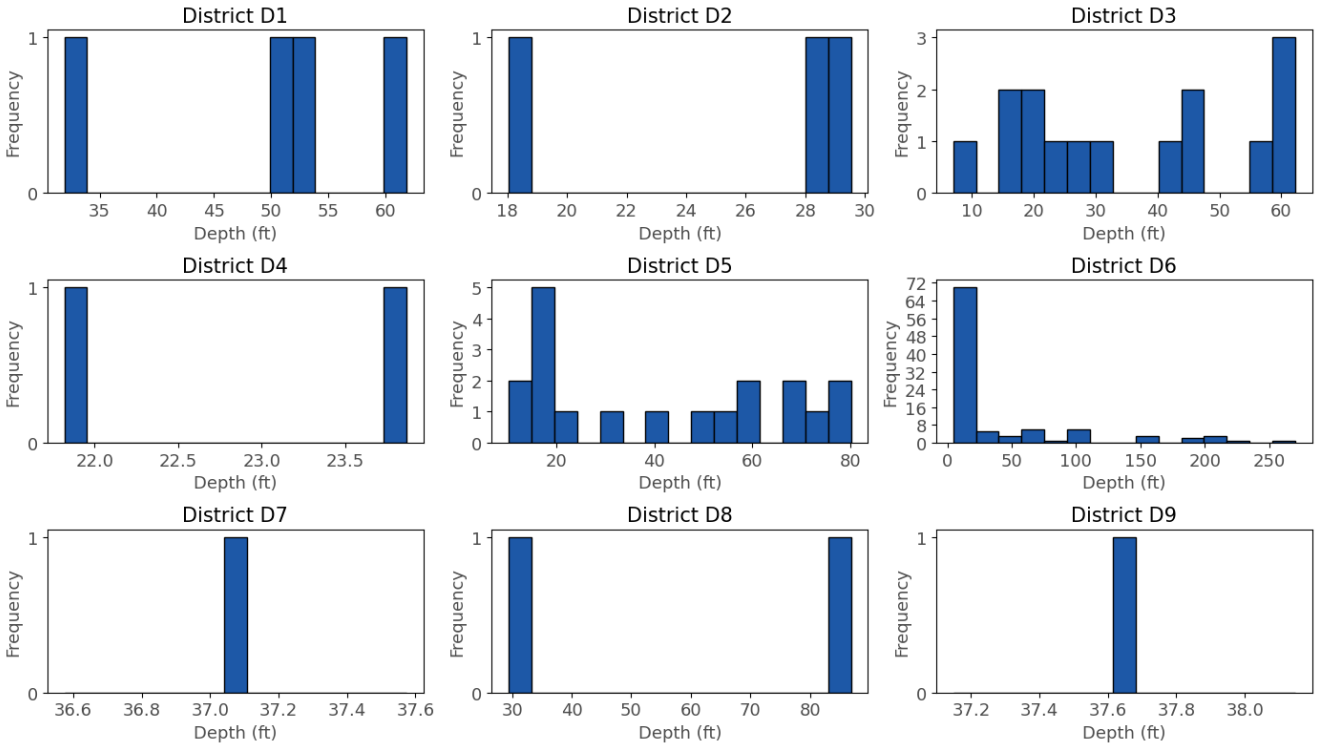

Figure 15. Summary histograms showing the exploration depths (ft) per district.

Source: Georgia Tech

CHAPTER 3: RECOMMENDED PROCEDURES FOR INTERPRETING CPT/SCPTU DATA AND CPT/SCPTU-BASED DESIGN PROCEDURES

This chapter presents recommended procedures and guidelines for interpreting CPT/SCPTu data in the State of Illinois, including soil behavior type, stratigraphic profiling, and the assessment of geoparameters that are key for engineering projects (i.e., soil strength, stiffness, compressibility, stress history, hydraulic properties). In addition, CPT/SCPTu-based design procedures that IDOT can potentially adopt are also described.

BASIC DEFINITIONS OF IN SITU STRESSES

Hydrostatic Pore Water Pressure

The equilibrium or hydrostatic porewater pressure (u_0) is required for calculating the excess porewater pressure: $\Delta u_2 = u_2 - u_0$. The porewater pressure (u_o) at depth z below the ground surface is computed using the following expression in Figure 16:

$$u_o = \gamma_w(z - z_{wt})$$

Figure 16. Equation. Hydrostatic porewater pressure.

where γ_w is the unit weight of water (9.8 kN/m^3 = 62.4 pcf), and z_{wt} is the depth of the groundwater table. For shallow soils that are above the groundwater table ($z < z_{wt}$) and saturated due to capillarity, the same equation applies. For $z < z_{wt}$ in the case of dry soils and no capillarity, then the usual assumption is $u_0 = 0$.

Total and Effective Stress

The total (σ_{vo}) and effective (σ'_{vo}) vertical overburden stresses are fundamental to processing piezocone data since the measured soil properties depend on the stress state. The total stress profile can be calculated using the continuous profile of unit weight and depth. The total overburden stress at a depth (z) is defined by the equation in Figure 17:

$$\sigma_{v0_z} = \sum(\gamma_{T_z} * h_z)$$

Figure 17. Equation. Calculation of total overburden stress.

where γ_{T_z} is the total soil unit weight, and h_z is the thickness of each layer (given by the difference in depth between consecutive data points). The next step is to calculate the effective vertical stress as follows in Figure 18:

$$\sigma'_{vo} = \sigma_{vo} - u_o$$

Figure 18. Equation. Effective vertical stress.

PIEZOCONE PARAMETERS

Corrected Tip Resistance and Sleeve Friction

A modern electronic cone penetrometer collects three readings with depth: (a) cone tip resistance, q_c, (b) sleeve friction, f_s, and (c) penetration porewater pressure, u_2. The specific mechanical geometry of the penetrometer components is influenced by water pressure that acts on the cone tip and the ends of the friction sleeve (Lunne et al., 2002). Consequently, it is necessary to correct the q_c value and calculate the total cone resistance (q_t) using the following equation in Figure 19 (ASTM D 5778, 2020):

$$q_t = q_c + u_2(1 - a_{net})$$

Figure 19. Equation. Corrected total cone resistance.

where q_c and u_2 were defined previously as the measured tip resistance and the porewater pressure during penetration measured at the shoulder of the cone, and a_{net} is the net area ratio. The net area ratio factor is determined from laboratory calibration of the penetrometer in a pressurized triaxial cell and ranges experimentally between 0.35 and 0.85 (Robertson & Cabal, 2015). A scheme of the geometry of the piezocone components and the conceptual porewater pressure distribution is shown in Figure 20. For both the Vertek H-T and ConeTec penetrometers used on this project, the a_{net} values were 0.80.

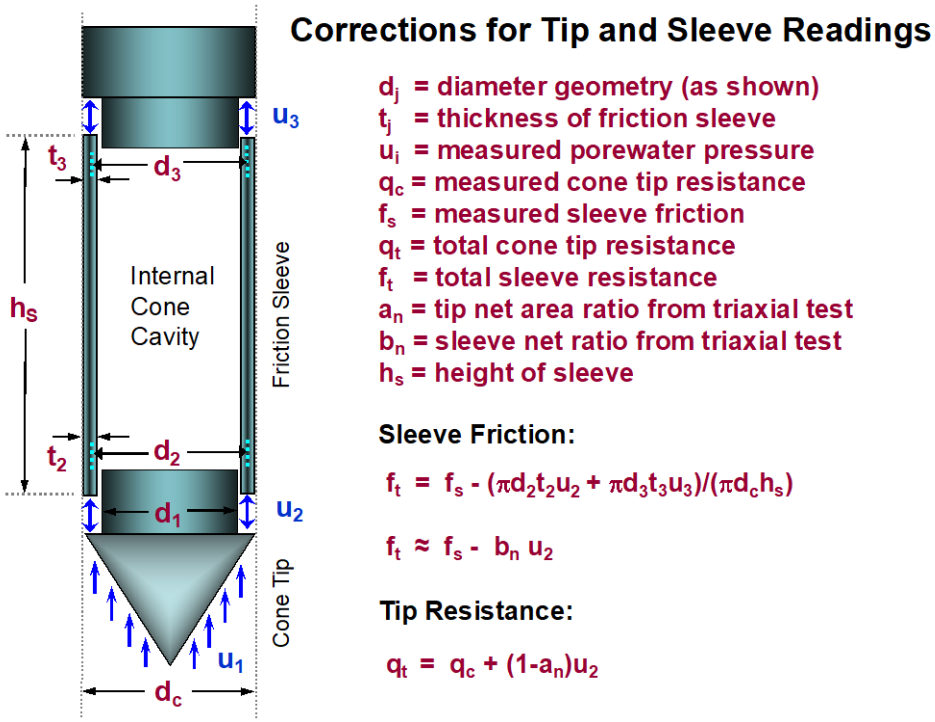

Figure 20. Schematic of porewater pressure distribution on the piezocone element and measurement corrections for tip and sleeve readings.

Source: Jamiolkowski et al. (1985)

The sleeve friction reading is also affected by porewater pressures (u_2 and u_3, as depicted in Figure 21), but for a practical matter, it is not usually corrected because most commercial penetrometers only take one pressure reading. An approximate correction to total sleeve friction (f_{st}) can be made using:

$$f_{st} \approx f_s - u_2 \cdot b_{net}$$

Figure 21. Equation. Total sleeve friction.

where b_{net} is determined similarly to a_{net}using a pressurized triaxial cell (Mayne, 2007a). Typical values of b_{net}range from 0.00 (ideal) to 0.02. For both the Vertek H-T and ConeTec penetrometers used on this project, the b_{net} values were 0.00.

The total cone resistance is particularly important on soils where high excess porewater pressures are generated during penetration, such as saturated clays and silts, as well as silty to clayey sands. On the contrary, the correction is less significant for soils with high permeability, such as clean sands.

Normalized Piezocone Parameters

The measured CPT parameters (q_t, f_s and u_2) generally increase with vertical stress. Consequently, it is necessary to normalize the measured parameters to account for the dependency on overburden stress. The most widely used normalized parameters are the normalized cone resistance (Q_t), normalized friction ratio (F_r), and pore pressure ratio (B_q), defined as follows in Figure 22 (Robertson, 1990; Wroth, 1984):

$$Q_t = \frac{q_t - \sigma_{vo}}{\sigma'_{vo}}$$

$$F_r = \frac{f_s}{q_{net}}\ 100\% = \frac{f_s}{q_t - \sigma_{vo}}\ 100\%$$

$$B_q = \frac{u_2 - u_o}{q_t - \sigma_{vo}} = \frac{\Delta u}{q_t - \sigma_{vo}}$$

Figure 22. Equations. Normalized piezocone parameters.

Some alternative parameters include: (a) the normalized porewater pressure (U) and (b) friction ratio (R_f)

$$U = B_q \cdot Q_t$$

$$R_f = (f_s/q_t)\ 100\%$$

Figure 23. Equations. Normalized porewater pressure (U) and friction ratio (R_f).

CORRELATIONS FOR UNIT WEIGHT

The unit weight of soil is a critical parameter needed to post-process piezocone data. The continuous profile of unit weight is used to estimate total and effective stress, which are required for calculating normalized piezocone parameters and strength properties. (Further details on the calculation of these parameters will be given in subsequent sections.) Given the dependency of the estimated parameters on the unit weight, the reliability of the estimations will be affected by the accuracy of the unit weight estimation. There are multiple relations available in the literature to estimate the unit weight of soil using CPT data for a general case (all soil types); a selection of these correlations is summarized in Table 3. The principal difference among the approaches to estimate the unit weight is the size and characteristics of the dataset used in the study to perform the correlation and the geologic setting and local geomaterials used to populate the empirical trends.

Table 3. Relationships for Estimating Total Unit Weight from CPT for All Soil Types

Equation	Reference
$\gamma_T = \gamma_w \left(1.236 + 0.27 * \log(R_f) + 0.36 \log\left(\frac{q_t}{\sigma_{atm}}\right)\right)$ The equation can be deconvoluted in terms of f_s and q_t: $\gamma_T = \gamma_w \left(1.776 + 0.27 * \log\left(\frac{f_s}{\sigma_{atm}}\right) + 0.09 \log\left(\frac{q_t}{\sigma_{atm}}\right)\right)$ Where σ_{atm} is the atmospheric pressure (taken as 101.3 kPa).	Robertson & Cabal (2010)
$\gamma_T = \gamma_w \left(1.22 + 0.345 \log\left(100 \frac{f_s}{\sigma_{atm}} + 0.01\right)\right)$	Mayne (2014)
$\gamma_T = 26 - \frac{14}{1 + [0.5 \cdot \log(f_s + 1)]^2}$ A simplified expression is also provided: $\gamma_T \approx 12 + 1.5 \ln(f_s + 1)$ The differences between the fitting expressions are shown in Figure 24-A.	Mayne (2014)
$\gamma_T = \gamma_w \left(0.254 \cdot \log\left(\frac{q_t - u_2}{\sigma_{atm}}\right) + 1.54\right)$ The dataset and fitting equation from this study is shown in Figure 24-B.	Mayne et al. (2023b)

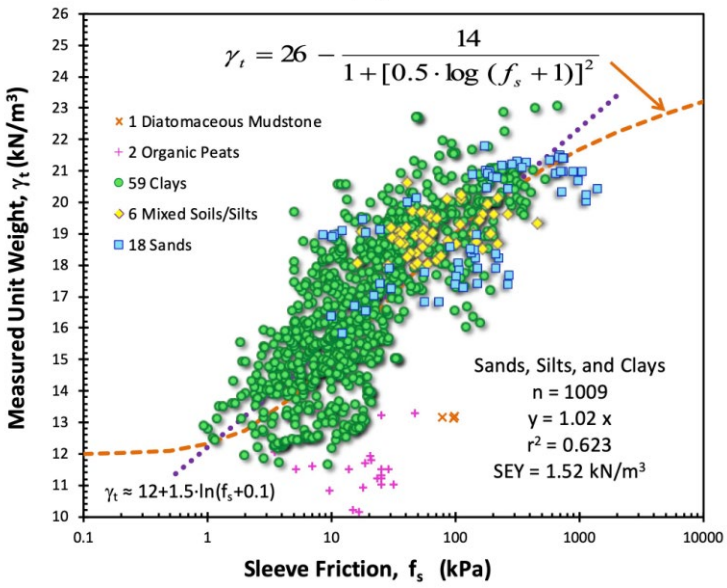

A. Unit weight from sleeve friction

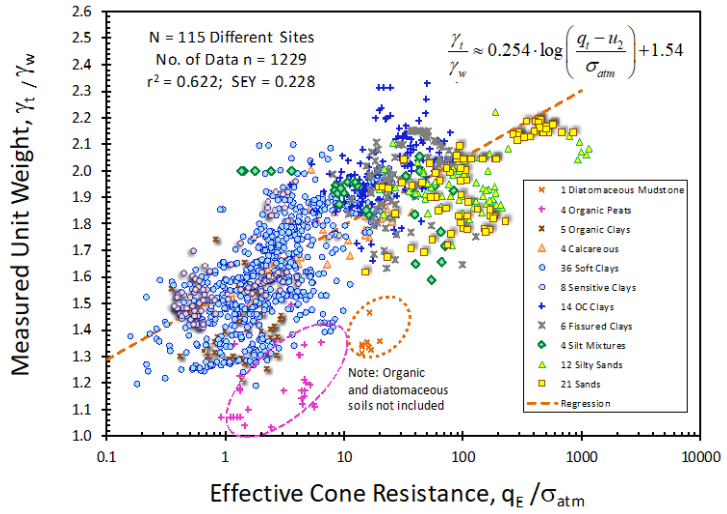

B. Unit weight from effective cone resistance

Figure 24. Unit weight from CPT measurements.

Source: Mayne (2014) and Mayne et al. (2023)

Most of the correlations to estimate the unit weight depend on the sleeve friction (f_s), which in soft clay deposits shows a small magnitude and high variability (Mayne & Peuchen, 2013). Therefore, some studies have proposed correlations applicable only to clay deposits, which use the depth resistance ratio ($m_q \approx q_t/z$) instead of the sleeve friction, as shown in Table 4.

Table 4. Soil Unit Weight Estimated from CPTu for Clay-Type Soils

Equation	Reference	Note
$\gamma_T = \gamma_w + 0.125 \cdot m_q$ This equation applies for $m_q < 80\ kN/m^3$, where m_q is the resistance-depth ratio, calculated as: $m_q = \frac{\Delta q_t}{\Delta z} \approx \frac{q_t}{z}$	Mayne & Peuchen (2013)	This equation applies to soft to firm normally-consolidated (NC) and lightly-over consolidated (LOC) clays.
$\gamma_T = 0.636 \cdot (q_t)^{0.072} \cdot (10 + m_q/8)$ This equation applies for $m_q < 80\ kN/m^3$.	Mayne & Peuchen (2013)	This equation applies to soft to firm NC and LOC clays. The correlation has unit-dependent values requiring q_t (kPa) and m_q, γ_T in (kN/m3).
When $m_q > 80 \frac{kN}{m^3}$, typical of stiff to hard clays, the fitting that applies to NC and LOC is no longer representative. Depending on the type of material, the authors propose a range for the unit weight: Stiff to hard intact clays: $\gamma_T = 19 - 21.8\ \mathrm{kN/m^3}$ Fissured clays: $\gamma_T = 18 - 20.7\ \mathrm{kN/m^3}$ Carbonate fine-grained soils: $\gamma_T = 16.9 - 17.1\ \mathrm{kN/m^3}$	Mayne (2014)	These values apply to stiff to hard OC clays.

CORRELATIONS AND INTERPRETATION FOR SOIL BEHAVIOR

Soil Behavior Type Index

The CPT material index, I_c, is a parameter used as a proxy for soil behavior type (SBT). The index I_c was initially defined by Jefferies and Davies (1993), who proposed that the boundaries in the soil behavior type could be approximated as concentric circles, with I_c as the radius of those circles. The material index was later modified by Jefferies and Been (2015) to accommodate soils with high B_q values (Figure 25):

$$I_{c-JB} = \sqrt{\left(3 - log\left(Q_t \times \left(1 - B_q\right) + 1\right)\right)^2 + (1.5 + 1.3\, log(F_r))^2}$$

Figure 25. Equation. CPT material index (Jefferies & Been, 2015).

The relation between material index, I_c, and soil classification system with six different soil zones, as proposed by Jefferies and Been (2015), is shown in Table 5.

Table 5. Soil Behavior Type Using I_c According to Jefferies & Been (2015)

Index, I_c	Soil Classification
I_c < 1.25	Gravelly sands
1.25 < I_c< 1.90	Sands—clean sand to silty sand
1.90 <I_c< 2.54	Sand mixture—silty sand to sandy silt
2.54 < I_c< 2.82	Silt mixture—clayey silt to silty clay
2.82 < I_c < 3.22	Clays
I_c> 3.22	Organic soils

The subindex *JB* refers to the definition given by those authors, thus I_{c-JB}. Figure 26 shows the soil classification chart on the plane of dimensionless penetration resistance $Q_t \times (1 - B_q) + 1$ as a function of friction ratio (F_r), where I_{c-JB} can be considered as a proxy of soil behavior.

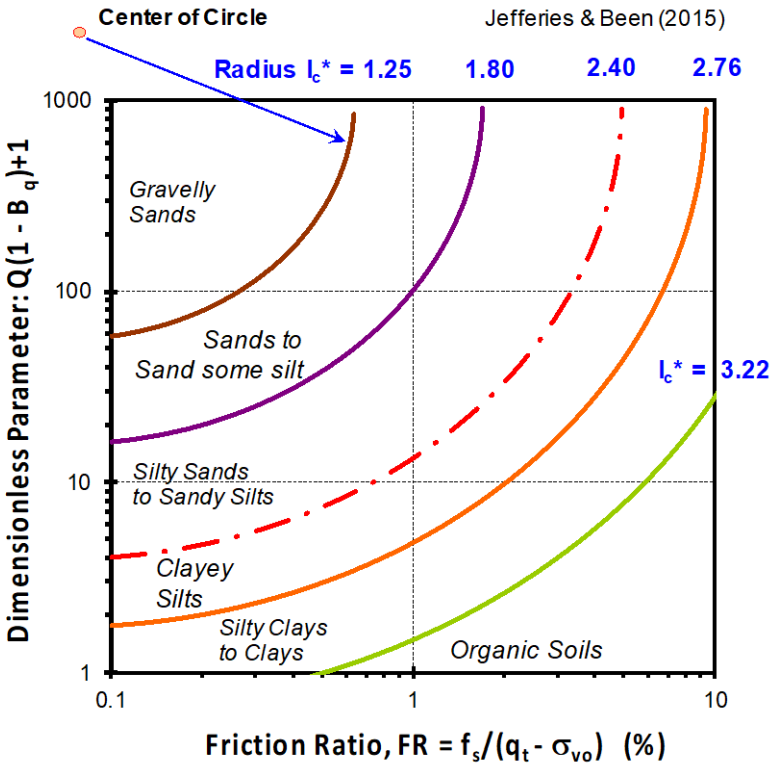

Figure 26. Contours of constant material index I_{c-JB} and associated soil behavioral zones.

Source: Jefferies & Been (2015)

The I_{c-RW} expression was simplified by Robertson and Wride (1998), removing the contribution of the pore pressure ratio (B_q) from the equation, mainly because they were investigating soil

liquefaction of sands and granular soils where $B_q \approx 0$. This definition of I_c is the most used in the literature and is often designated I_{c-RW} (Figure 27):

$$I_{c-RW} = \sqrt{(3.47 - log(Q_t))^2 + (1.22 + log(F_r))^2}$$

Figure 27. Equation. Modified CPT material index (Robertson & Wride, 1998).

Further studies defined the parameter Q_{tn} as an upgraded normalized cone resistance with a variable stress exponent (n) that depends on soil type or I_{c-RW} (Robertson, 2009; Robertson & Wride, 1998; Zhang et al., 2002), as shown in Figure 28:

$$Q_{tn} = \left[\frac{q_t - \sigma_{vo}}{\sigma_{atm}}\right]\left(\frac{\sigma_{atm}}{\sigma'_{vo}}\right)^n \text{ where } n = 0.381(I_c) + 0.05(\sigma'_{vo}/\sigma_{atm}) - 0.15 \leq 1.0$$

Figure 28. Equation. Normalized tip resistance (iterative method by Robertson, 2009).

Initially, Q_t is used to calculate the soil behavior type index and the value of I_{c-RW} determines the exponent n for upgrading Q_t to Q_{tn}. The value of I_{c-RW} is updated accordingly, thus requiring an iteration process. About three iterations are usually sufficient to provide the final values of Q_{tn}, n, and I_{c-RW}.

Further research showed that the boundaries to differentiate soil behavior based on the concentric circles defined by I_{c-RW} show a good performance for young-uncemented soils. However, for soil types such as sand-like dilative, transitional-like dilative, and clay-like dilative, for example, the soil behavior type boundaries on the log (Q_t) - log F_r plane are better represented by a hyperbolic shape boundary, to accurately differentiate between SBT zones (Schneider et al., 2012). Robertson (2016) proposed an alternate soil behavior type index (I_B) based on this observation (Figure 29):

$$I_B = 100 \cdot \frac{(Q_{tn} + 10)}{Q_{tn} \cdot F_r + 70}$$

Figure 29. Equation. Alternate CPT soil behavior type index, I_B (Robertson, 2016).

A value of I_B of 32 is the boundary between sand-like and transitional behavior, and a value of 22 represents the boundary between transitional and clay-like behavior.

CPT Charts for Soil Behavior Classification

In practice, one of the predominant uses of CPT is soil behavior classification for stratigraphical delineation. The soil behavior type (SBT) classification differs from the commonly used classification systems such as the Unified Soil Classification System (USCS: ASTM D 2487, 2006), AASHTO, or USDA methods, which rely on laboratory testing or visual-manual examination of soil samples. The SBT charts classify soil according to its in situ mechanical response, contrary to the USCS system, which is based on the classification of grain-size distribution and plasticity. The fundamental differences

between the systems can generate disagreement on the soil classification of the two systems, especially for sand and silt mixtures (Robertson, 2009).

One of the widely used charts is that by Robertson (1990, 1991), who presented two charts, the first one using the normalized cone resistance (Q_t) and the normalized friction ratio (F_r), and the second one using Q_t and the pore pressure ratio (B_q). In these charts, nine distinct zones of soil classification are presented. The original $Q_t - B_q$ chart was discussed by Jefferies and Davies (1991), who showed that the chart did not show an acceptable performance on zones with negative pore pressure values generated due to the occurrence of cavitation (Jefferies & Davies, 1991). This led to a corrected $Q_t - B_q$ chart by Robertson (1991). These charts are sometimes referred to as SBTn charts because they use normalized piezocone parameters.

Robertson (2009) updated the Q-F chart to use Q_{tn} instead of Q_t to include the stress variant exponent into the normalization. Moreover, Mayne (2014) proposed additional algorithms to identify soils in zones 1, 8, and 9, as follows:

- Step 1: Find sensitive soils of zone 1 when: $Q_{tn} < 12 \exp(-1.4\, F_r)$
- Step 2: Identify zone 8 when $1.5 < F_r < 4.5\%$, and zone 9 when $F_r > 4.5\%$.
- Step 3: Identification of the remaining zones (2 through 7) relies on the material index as shown in Figure 26.

The resultant modified chart after Robertson (2009) is shown in Figure 30.

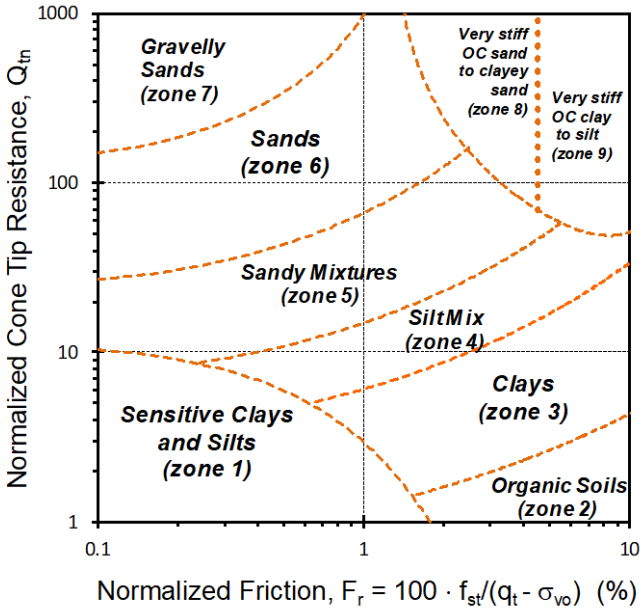

A. Chart $Q_{tn} - F_r$ (Updated by Robertson, 2009)

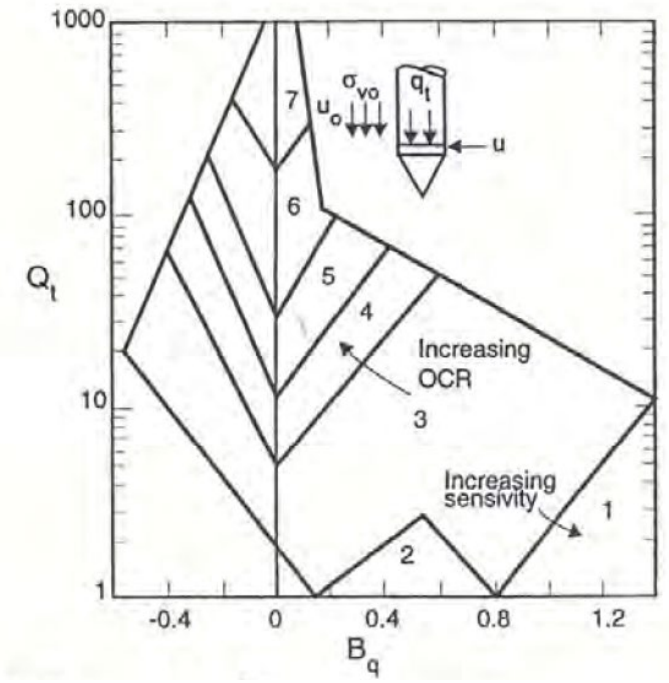

B. Chart $Q_t - B_q$ (Robertson, 1991)

Figure 30. Soil behavior classification charts for CPTu by Robertson.

Schneider et al. (2008a) presented a chart that uses the normalized ratio $U = \Delta u_2/\sigma'_o$ instead of B_q, because it shows a better performance for evaluating SBT from piezocone data. Further work (Schneider et al., 2012) extended the classification system and proposed a chart using the normalized tip resistance and friction ratio. Figure 31 and Figure 32 show the charts developed by Schneider et al. (2008, 2012), which group soil types into five distinct zones.

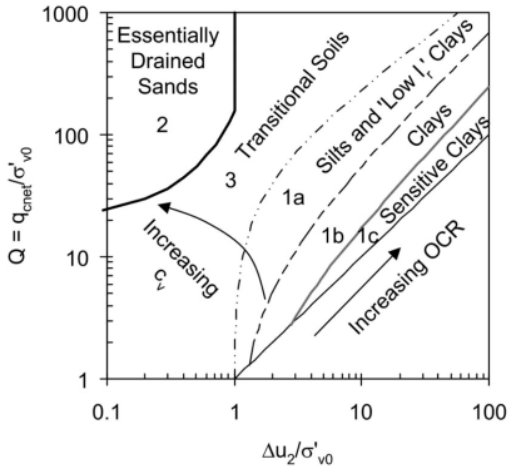

Zone	Soil Type
1a	SILTS and 'Low I_r' CLAYS
1b	CLAYS
1c	Sensitive CLAYS
2	Essentially drained SANDS
3	Transitional soils

A. Chart $\log Q_t - \log U$

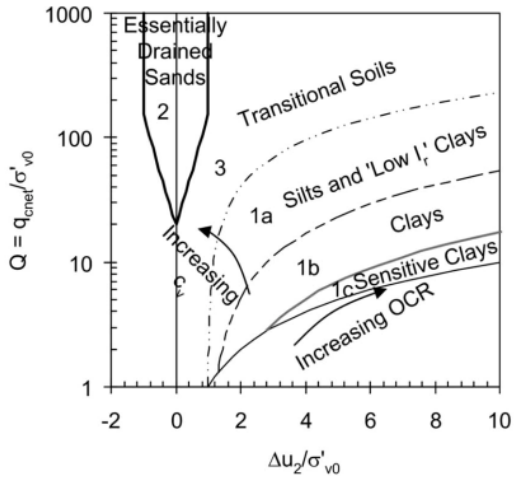

Zone	Soil Type
1a	SILTS and 'Low I_r' CLAYS
1b	CLAYS
1c	Sensitive CLAYS
2	Essentially drained SANDS
3	Transitional soils

B. Chart $Q_t - U$

Figure 31. Soil behavior classification chart for $Q_t - U$ presented by Schneider et al. (2008a).

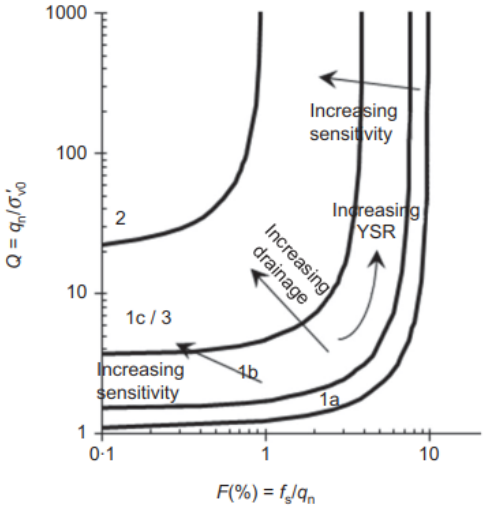

Classification zone	Simplified description of soil type
1a	Low-I_R clays ($I_R = G/s_u$)
1b	Clays
1c	Sensitive clays
3	Silts and transitional soils
2	Essentially drained sands and sand mixtures

Figure 32. Soil behavior classification chart for $Q_t - F_r$ presented by Schneider et al. (2012).

Robertson (2016) presented updated charts that use modified soil behavior type definitions for the zones (e.g., clay-like behavior, sand-like behavior, and transitional behavior). In contrast, the previous charts use physical descriptions that were sometimes confused with the terminology used in textural classification systems. This chart also includes the hyperbolic shape of the boundaries of SBT zones observed by Schneider et al. (2012) and represented by the modified soil behavior type index (I_B) (Robertson, 2016).

Another important feature of the updated chart is the differentiation between dilative and contractive behavior, which describes how the volume changes during shearing. The chart includes a boundary that separates the contractive from the dilative behavior, and this boundary is defined using the normalized cone resistance equivalent value of a clean sand ($Q_{tn,cs}$) parameter equal to 70.

The boundary was defined based on the contours of the state parameter (Jefferies & Been, 2015; Plewes et al., 1992), using a state parameter value of −0.05 as a proxy to differentiate between contractive and dilative behavior, in consideration of the similarity between state parameter contours and $Q_{tn,cs}$ contours, noted by Robertson (2010b). Figure 33 shows the updated chart, where the continuous orange lines represent the boundaries of the updated Robertson (2016) charts, and the gray markers show the SBT zones from the older Robertson (2009) charts.

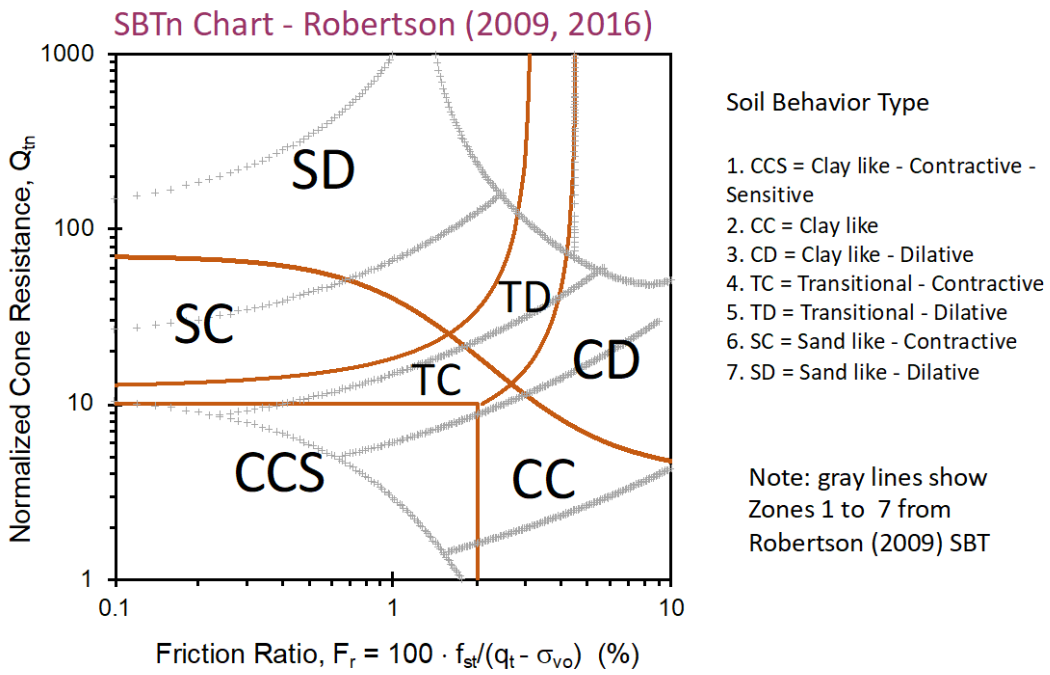

Figure 33. Updated soil behavior types presented by Robertson (2016) superimposed over $Q_t - F_r$ groupings given by Robertson (2009).

Another important part of the classification system is using a means to identify soils with significant microstructure or cementation. This approach is based on the seismic piezocone (SCPTu) measurements since it requires the small-strain properties of soil (i.e., shear wave velocity, V_s, and shear modulus $G_o = \rho_t V_s^2$: where is ρ_t total density). The chart uses in the vertical axis Q_{tn} and for the horizontal axis, the small strain rigidity index $I_G = G_o/q_n$, with $q_n = q_{net} = q_t - \sigma_{vo}$. In this chart, the young and uncemented soils, which are labeled by Robertson (2016) as ideal soils or unstructured soils, will fall within a relatively narrow zone in the plot. This zone can be bounded by the normalized rigidity index parameter (K_G^*), which is defined as:

$$K_G^* = \frac{G_0}{q_{net}} (Q_{tn})^{0.75}$$

Figure 34. Equation. Normalized rigidity index parameter for assessing cemented soils.

The soil is considered ideal (e.g., young and uncemented) if it is in the zone bounded by a K_G^*, between 100 and 300, as shown in Figure 35. Outside of this zone are the soils with significant

microstructure, which have aging and bonding that causes significant microstructure or cementation, or both.

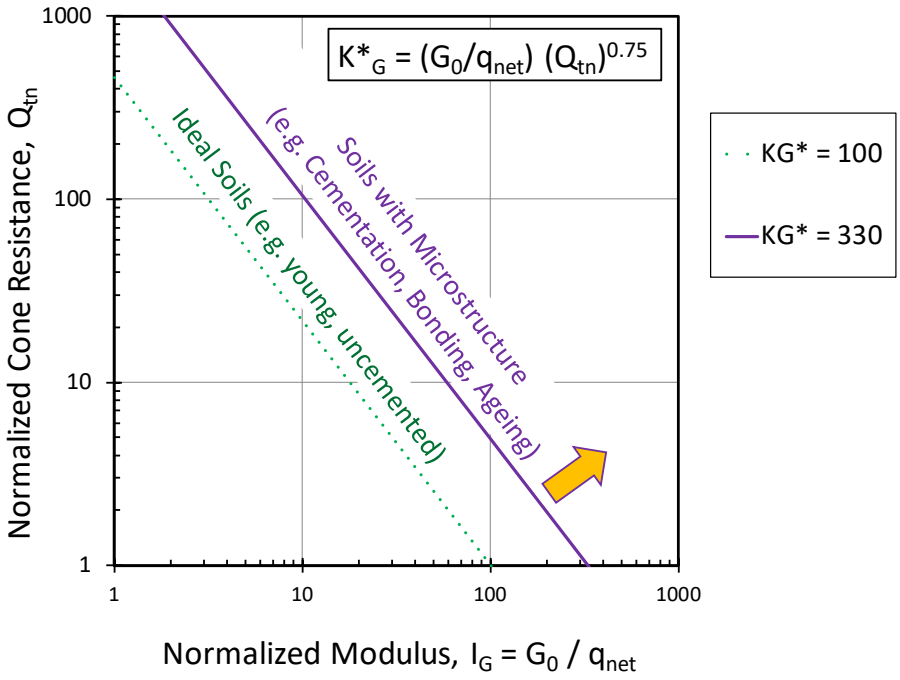

Figure 35. Chart to estimate if soils have significant microstructure.

Source: Modified from Robertson (2016)

CORRELATIONS FOR RELATIVE DENSITY OF SANDS

The relative density (D_R) is a state variable used as a proxy for the degree of compactness of a sand. Commonly, the relative density is calculated as follows:

$$D_R = \left(\frac{e_{max} - e_o}{e_{max} - e_{min}}\right) \cdot 100$$

Figure 36. Equation. Relative density (D_R), reported as a percentage (%).

where e_{max} is the maximum void ratio, e_{min} the minimum void ratio, and e_o the void ratio at the current state. The CPT can be used to estimate the relative density of sands with different mineralogy. Equations to calculate D_R are divided into two main groups: (1) quartz and silica sands and (2) calcareous–carbonate sands.

For quartz and silica sands, Jamiolkowski et al. (2001) performed several series of CPT calibration chamber tests (n = 456), corrected for boundary effects, and developed an expression for relative density of sands with medium compressibility level. As shown in Figure 37-A, there is some scatter on the data due to different compressibility levels of the sand. Moreover, Kulhawy and Mayne (1990) presented an equation for evaluating D_R from CPT that accounts for the stress history of the sand

(i.e., over-consolidation ratio, OCR), as shown in Figure 37-B. The latter graph shows that both methods provide similar values for most ranges of D_R, especially when the normalized cone resistance $q_{c1} < 300$. Table 6 summarizes the equations to calculate the relative density for quartz and silica sands.

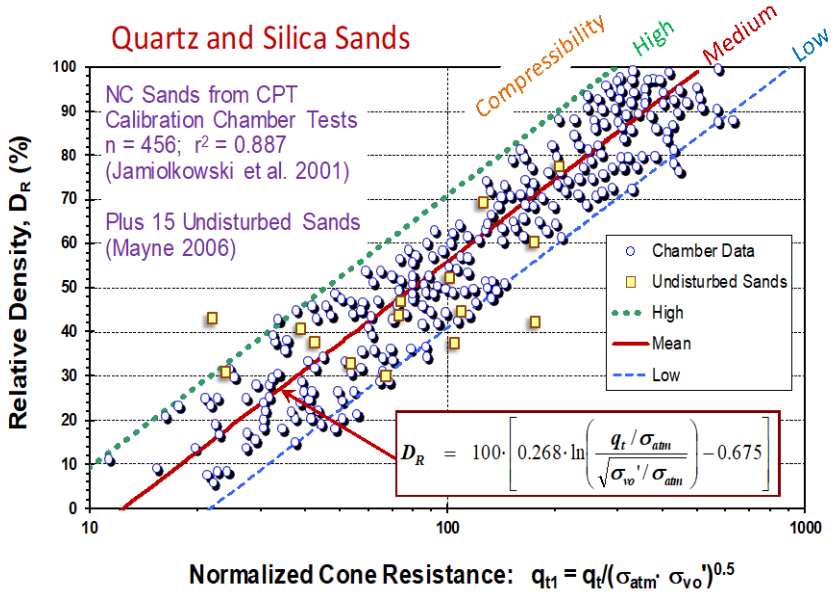

A. NC sands

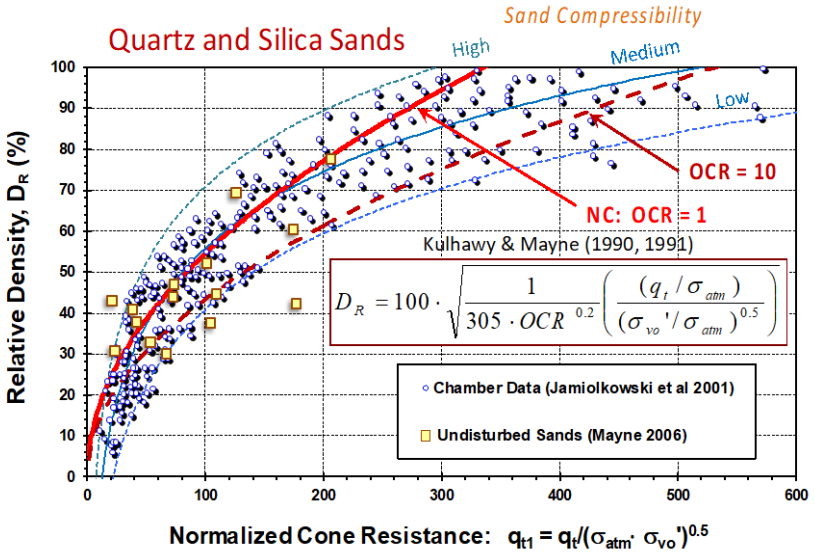

B. NC and OC sands

Figure 37. Relative density of NC to OC quartz-silica sands estimated using CPT.

Source: Adapted from Mayne (2014)

Table 6. Relative Density of Quartz and Silica Sands from CPT

Equation	Reference	Note
$D_R = 100 \cdot [0.268 \cdot \ln(q_{t1}) - 0.675]$ $where\ q_{t1}$ is the stress normalized tip resistance and calculated as: $q_{t1} = \frac{\frac{q_t}{\sigma_{atm}}}{\sqrt{\sigma'_{vo}/\sigma_{atm}}}$	Jamiolkowski et al. (2001)	The equation applies to NC quartz to silica sands of medium/normal compressibility.
$D_R = 100 \cdot \sqrt{\frac{q_{t1}}{305 \cdot OCR^{0.2}}}$	Kulhawy & Mayne (1990)	The method applies to NC-OC quartz-silica sands. Note: The calculation of OCR will be included in further sections.
$D_R = 100 \cdot \sqrt{\frac{Q_{tn}}{c}}$	Robertson & Cabal (2015)	Parameter c is a constant that increases with age and ranges between 300 and 400. A value of 350 can be used for clean, uncemented quartz sand. Q_{tn} is the normalized tip resistance defined in the previous section (iterative method by Robertson, 2009).

For calcareous-carbonate sands, the relative density exhibits an approximately linear trend with respect to q_{t1}, suggesting grain breaking, fracturing, and particle crushing for relative densities higher than 30% (Mayne, 2014), as shown in Figure 39. In this case, the relative density equation is simplified as shown in Figure 38:

$$D_R(\%) = 0.87 \cdot q_{t1}$$

Figure 38. Relative density for calcareous-carbonate sands from CPT.

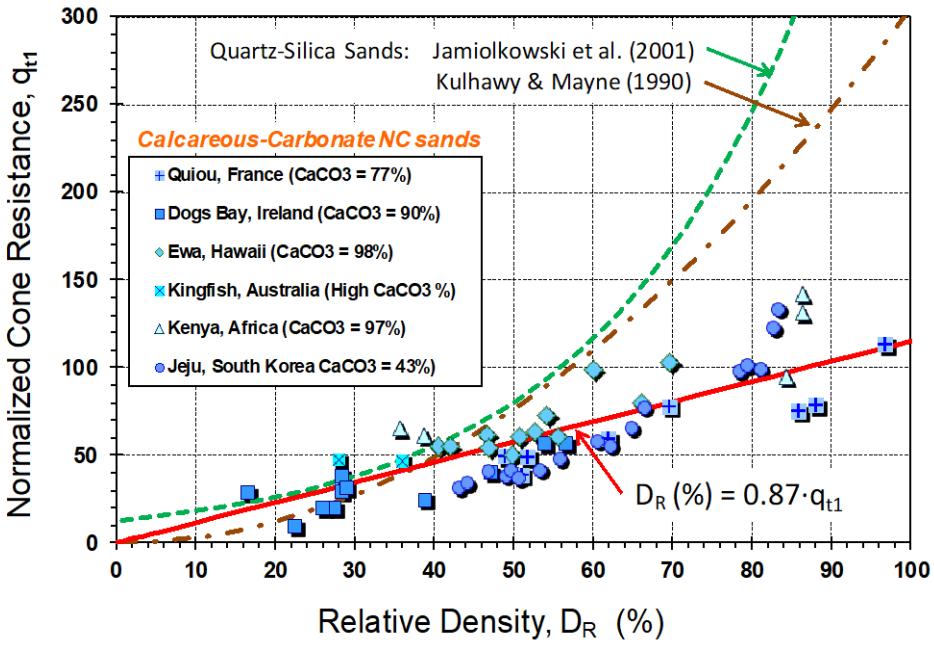

Figure 39. Relative density of carbonate-calcareous sands from CPT.

Source: Mayne (2014)

Strictly speaking, ASTM D 4254 (2002) for relative density only permits evaluating DR in sands with fine content (FC) less than 15%. Consequently, there are CPT correlations that use a clean sand-equivalent cone tip resistance (q_{c1Ncs}), which is calculated as follows in Figure 40:

$$q_{c1Ncs} = q_{c1N} + \Delta q_{c1N}$$

$$q_{c1N} = q_{cN} \cdot C_N = \frac{q_c}{\sigma_{atm}} \cdot C_N$$

$$C_N = \left(\frac{\sigma_{atm}}{\sigma'_{vo}}\right)^m = \left(\frac{\sigma_{atm}}{\sigma'_{vo}}\right)^{(1.338-0.249 \cdot q_{c1Ncs})^{0.264}} \leq 1.7$$

$$\Delta q_{c1N} = \frac{11.9 + q_{c1N}}{14.6} \cdot exp\left(1.63 - \frac{9.7}{FC + 2}\right) - \left(\frac{15.7}{2 + FC}\right)^2$$

Figure 40. Equations. Clean sand-equivalent cone tip resistance.

Source: Boulanger & Idriss (2014)

where q_{c1N} is equivalent clean sand adjustment factor, C_N is the overburden correction factor, and FC is the fines content (percentage by weight of soil particles passing a No. 200 sieve).

The equivalent clean sand adjustment factor, (Δq_{c1N}), is derived from liquefaction case histories, showing that the liquefaction triggering correlation shift with an increase in fines contents (Boulanger

& Idriss, 2014). Once the clean sand equivalent cone resistance is calculated, the relative density can be evaluated using the following empirical correlations (Figure 41).

$$D_R = 100 \cdot \left[0.465 \left(\frac{q_{c1Ncs}}{C_{dq}} \right)^{0.264} - 1.063 \right]$$

Figure 41. Equation. Relative density based on the clean sand-equivalent cone tip resistance.

Source: Idriss & Boulanger (2008)

C_{dq} is a constant ranging between 0.64 and 1.55. The common value used is 0.9. Using $C_{dq} = 0.9$, the equation simplifies as follows (Figure 42):

$$D_R = 100 \cdot (0.478(q_{c1Ncs})^{0.264} - 1.063\ )$$

Figure 42. Equation. Clean sand-equivalent cone tip resistance.

Source: Idriss & Boulanger (2008)

CORRELATIONS FOR SOIL STRENGTH

Quantifying the strength of soils subject to shear loading is fundamental to designing and analyzing geotechnical infrastructure. The CPT can directly evaluate strength parameters such as effective friction angle (ϕ') and undrained shear strength (s_u), as well as state parameter (ψ) and yield stress ratio (YSR), also termed over-consolidation ratio (OCR). The in situ measurement of soil strength is important for geotechnical practice because these parameters are essential for designing shallow and deep foundations, slope stability, retaining walls, excavations, and constitutive and numerical modeling. The following subsections provide some guidelines for using CPTu measurements to evaluate soil strength parameters.

Effective Friction Angle

The effective friction angle is one of the most critical soil mechanical properties because it controls soil strength. Consequently, the effective friction angle is a fundamental parameter for geotechnical analysis and design. At the standard and constant pushing rate of 20 mm/s (0.79 in/s), the mechanical response of various soil types could be either drained, undrained, or partially drained during the probe penetration (DeJong et al., 2012). The drainage behavior during penetration depends on the flow characteristic of the soil (coefficient of consolidation and permeability) and the penetration rate of the probe, as illustrated by Figure 43.

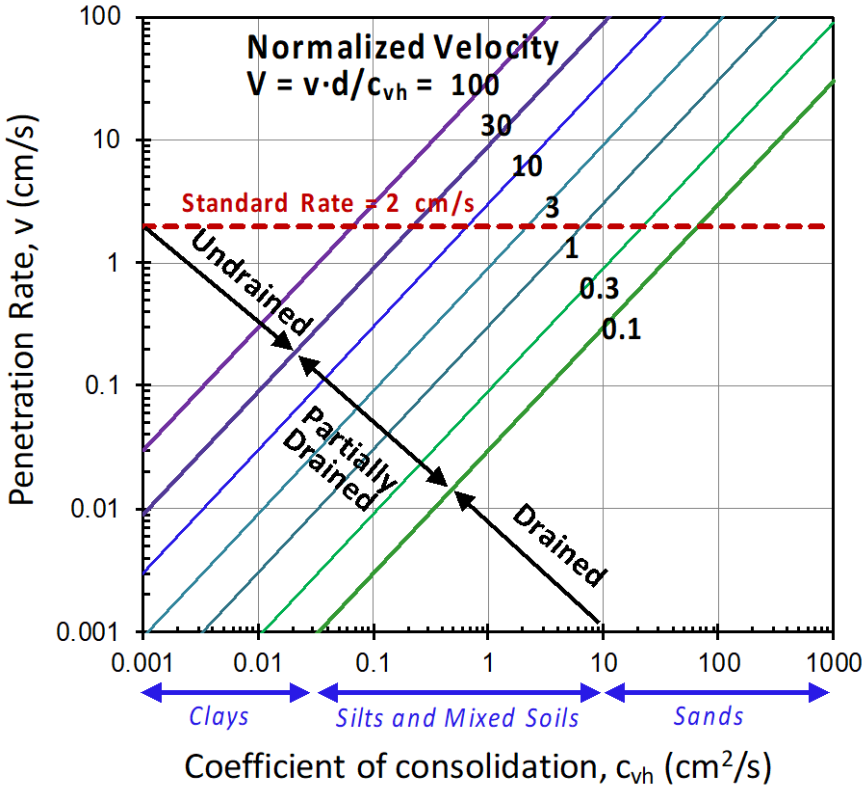

Figure 43. Drainage conditions during penetration in different soils.

Source: DeJong et al. (2012)

There are methods available to estimate the friction angle depending on the drainage conditions, specifically the soil behaves drained when the CPT is advanced at a standard rate of 20 mm/s (0.79 in./s) into high permeability soils (typically for clean sands and granular materials) or considered as fully undrained penetration in low permeability soils (typically on clay materials) during penetration.

Friction Angles for Soils with Drained Behavior

An I_{c-RW} value lower than 2.6 represents drained behavior, typically observed in sands and silty sands (Robertson, 2009).

Using data from triaxial compression tests on undisturbed samples of clean to silty sands, the effective friction angle in sand-like materials can be calculated using the normalized cone resistance (Q_{tn}) using the following expression in Figure 44 (Uzielli & Mayne, 2019):

$$\phi' = 17.6° + 11.0 \cdot log(Q_{tn})$$

Figure 44. Equation. Effective friction angle for CPT drained penetration in sand-like materials.

The original formulation was proposed by Kulhawy and Mayne (1990), and it used $q_{t1} = (q_t/\sigma_{atm}) \cdot (\sigma_{atm}/\sigma'_{v0})^{0.5}$ instead of Q_{tn}. Robertson and Cabal (2022) substituted Q_{tn}, which has been shown to provide similar, if not identical, results (Uzielli & Mayne 2019).

Friction Angles for Soils with Undrained Behavior

On the contrary, when the I_{c-RW} value is higher than 2.6, cone penetration is considered undrained, typically occurring in fine-grained soils such as clays and clayey silts. The evaluation of the effective friction angle for these cases was developed by the Norwegian Institute of Technology (NTH) using an effective stress limit plasticity solution (Senneset et al., 1989; Senneset & Janbu, 1985). The NTH approach uses the bearing capacity approach and a Mohr-Coulomb constitutive model to represent effective stress behavior. The solution considers the tip bearing factor N_q and the porewater bearing factor N_u, which accounts for the excess pore pressure generated at the cone tip and reduces the ultimate bearing capacity (Senneset et al., 1989), as shown in Figure 45:

$$N_q = tan^2\left(45 + \frac{1}{2}\phi^{'}\right) exp\left((\pi - 2\beta)\, tan\, \phi^{'}\right)$$

$$N_u = 6\, tan\, \phi' \,(1 + tan\, \phi')$$

Figure 45. Equations. Bearing capacity and porewater bearing factors from NTH solution.

Where β is the angle of plastification that determines the size of the failure zone, Figure 46 shows a scheme of the failure surface and how the N_q parameter varies with the friction angle.

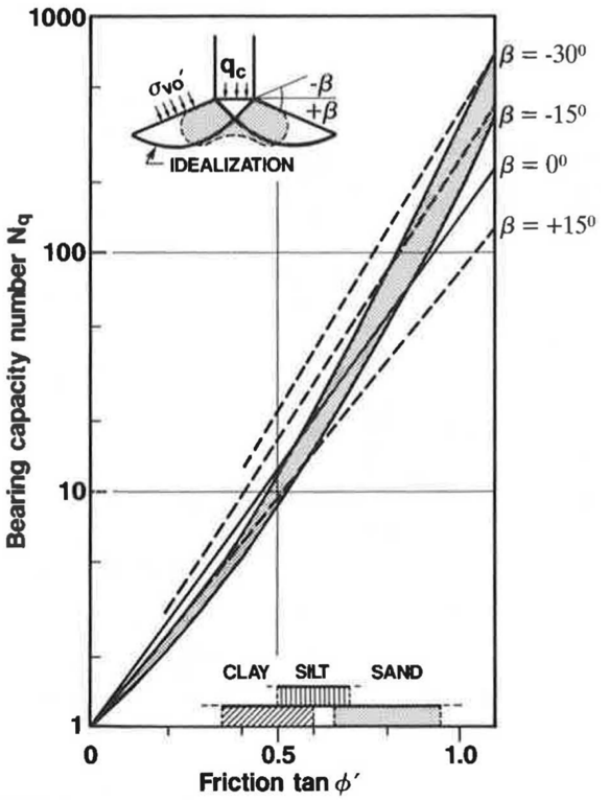

Figure 46. Bearing capacity factor and failure surface of the NTH solution.

Source: Senneset et al. (1989)

Finally, the approach defines the cone resistance number (N_m), which relates the bearing capacity factors and the total cone tip resistance (Janbu & Senneset, 1974), as shown in Figure 47:

$$N_m = \frac{N_q - 1}{1 + N_u B_q} = \frac{q_t - \sigma_{vo}}{\sigma'_{vo} + a'}$$

Figure 47. Equation. Cone resistance number for NTH solution.

The parameter a' is the effective attraction ($a' = c' \cot \phi'$). Setting $a' = c' = 0$, the right side of the equation would equal the normalized tip resistance (Q_t). Since the full inversion of the equation to obtain the friction angle directly is not possible, a set of approximate solutions was found, as shown in Figure 48 (Mayne 2005, 2007a, 2016):

$$B_q > 0.05: \phi' \approx 29.5 \cdot B_q^{0.121}\left[0.256 + 0.336 B_q + log(Q_t)\right]$$

Figure 48. Equation. Friction angle approximation for CPTu in NC to LOC clays.

The approximations are valid for NC to LOC clays (OCRs < 2.5) over the following ranges: $20° \leq \phi' \leq 45°$, and $B_q \leq 1.0$. For OCRs > 2.5, the Q_t should be replaced with $Q' = Q_t \cdot OCR^{\Lambda}$, where $\Lambda \approx 0.7$ to 0.8 for clays of low to medium sensitivity and $\Lambda \approx 1.0$ for highly sensitive to quick clays. This is a modified version of the NTH solution. A quick approximation of OCR in clays can be calculated as $OCR \approx Q_t/3$.

Fissured over-consolidated (OC) clays exhibit values of u_2 close to zero and thus have low values of B_q < 0.05. Therefore, in this case, the approximation for the NTH solution is given by Ouyang and Mayne (2019) in Figure 49:

$$B_q \leq 0.05: \phi' \approx 8.18\, ln(2.13\, Q')$$

Figure 49. Equation. Friction angle approximation for CPT in fissured over-consolidated clays.

If sensitive clays are identified because of the stress-strain-strength behavior and significant strain softening post-peak, which is observed in these types of clays, the modified version of the NTH solution can be used to calculate ϕ'_1 (i.e., friction angle defined at the maximum deviator stress), while the original NTH version will provide a value for ϕ'_2 (i.e., friction angle defined at maximum obliquity). Moreover, a screening procedure and criterion are presented later in Table 8 and Figure 71 to identify sensitive clays. More details can be found in Mayne et al. (2023a).

Undrained Shear Strength

The undrained shear strength (s_u) is an important parameter in evaluating the strength of clay-type materials. The value of s_u is often taken as the maximum shear stress at constant volume for a given stress path. Additionally, s_u does not have a unique value but actually has a family of values depending on the loading mode and test type (e.g., triaxial compression, extension, direct shear, plane strain, etc.) (Mayne, 2008). Three different expressions can be used to estimate s_u, based on

q_{net}, Δu, and q_{eff}, where each expression has an associated cone factor (N_{kt}, $N_{\Delta u2}$, and N_{ke}, respectively). The s_u evaluation using q_{net}, shown in Figure 50, is the most common and reliable (Mayne & Peuchen, 2018):

$$s_u = \frac{q_{net}}{N_{kt}} = \frac{q_t - \sigma_{vo}}{N_{kt}}$$

Figure 50. Equation. Undrained shear strength from CPTu based on q_{net} and N_{kt}.

The factor N_{kt} can be estimated using empirical methods (Low et al., 2010; Lunne et al., 2005; Mayne et al., 2015) or theoretical approaches (Konrad & Law, 1987; Mayne, 2016). The factor N_{kt}, developed by Mayne and Peuchen (2018), used a database with 407 paired datasets from high-quality laboratory consolidated anisotropic undrained compression (CAUC) triaxial tests and associated field CPTu readings on 62 various clays and will be used herein (Mayne & Peuchen 2018). The approach gives a direct way to calculate N_{kt}, the value of which depends on the value of B_q. The s_u can also be estimated using the measured excess porewater pressure Δu and the effective cone resistance q_e, as shown in Table 7.

Table 7. Undrained Shear Strength of Clays from CPTu Readings

Undrained Shear Strength	Cone Factor	Comment
$s_u = \frac{q_{net}}{N_{kt}} = \frac{q_t - \sigma_{vo}}{N_{kt}}$	$N_{kt} = 10.5 - 4.6\,ln(B_q + 0.1)$	The expression is valid only for B_q > -0.1 (Mayne & Peuchen, 2018).
$s_u = \frac{\Delta u}{N_{\Delta u}} = \frac{u_2 - u_o}{N_{\Delta u}}$	$N_{\Delta u} = 7.9 + 6.5\,ln(B_q + 0.3)$	The factor $N_{\Delta u}$ increases as B_q increases and can be calculated using the given expression (Agaiby, 2018).
$s_u = \frac{q_e}{N_{ke}} = \frac{q_t - u_2}{N_{ke}}$	$N_{ke} = 4.5 - 10.66\,ln(B_q + 0.2)$	The cone factor N_{ke} is inversely proportional to B_q (Agaiby, 2018).

Figure 51 shows the cone factors, including the datasets used for the fitting process presented by (Mayne & Peuchen, 2018).

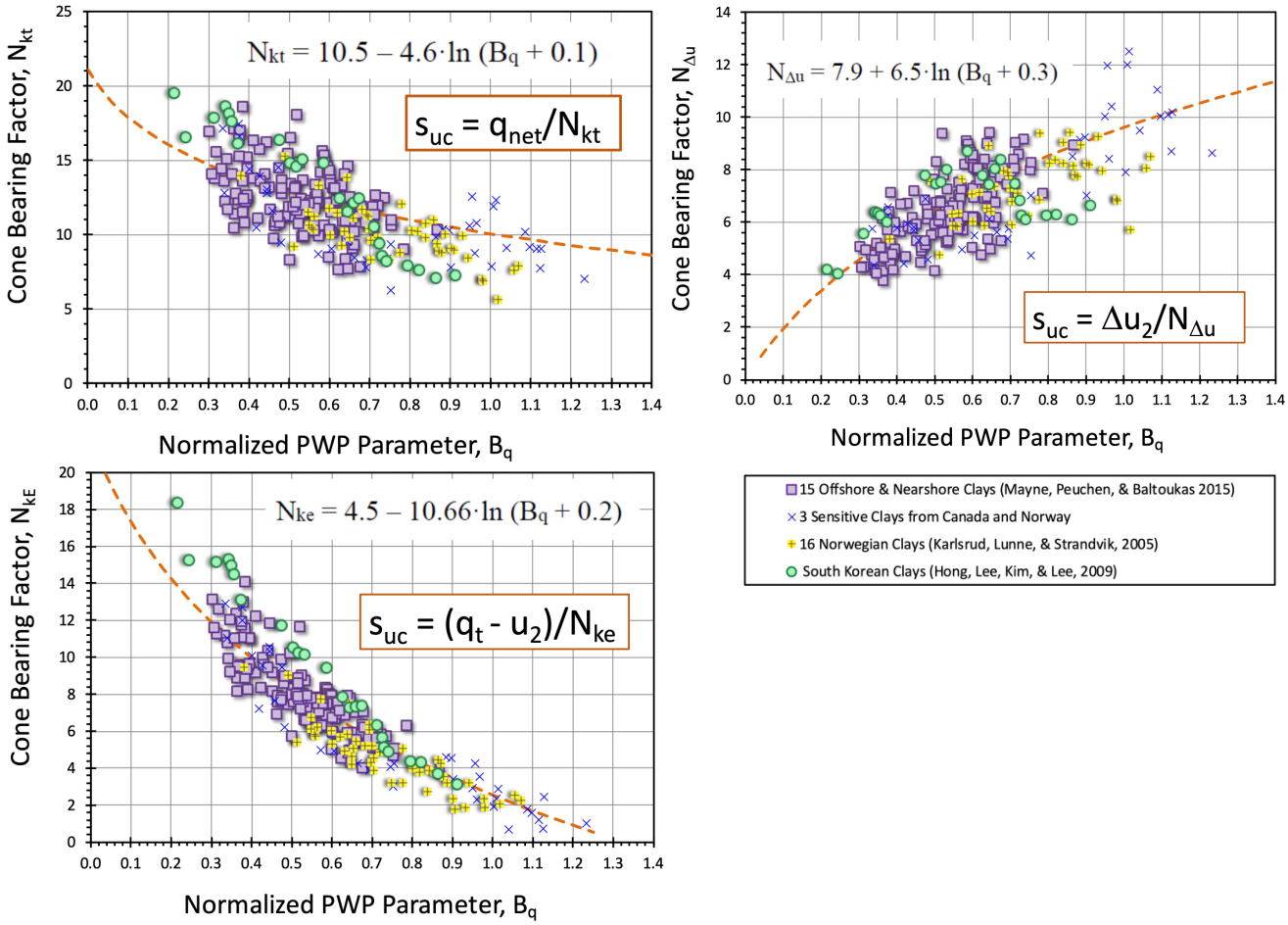

Figure 51. Cone factors for evaluating undrained shear strength of clays.

Source: After Mayne & Peuchen (2018)

Also of note, the sleeve friction can be taken as a direct measure of the remolded shear strength, as shown in Figure 52 (Robertson & Cabal, 2015):

$$s_{u\,(remolded)} \approx f_s$$

Figure 52. Equation. Remolded undrained shear strength.

However, the above only works for low to medium sensitivity clays where $S_t < 15$ (Mayne et al., 2023a). In highly sensitive to quick clays, the sleeve friction significantly overestimates the remolded strength, and therefore, alternative methods such as vane shear tests or full-flow penetrometers, including the T-bar and ball, should be explored.

Clay Sensitivity

Clay sensitivity is defined as the ratio between the undrained shear strength at peak and the remolded shear strength at the same water content (Figure 53):

$$S_t = \frac{s_{u\ (peak)}}{s_{u\ (remolded)}}$$

Figure 53. Equation. Clay sensitivity definition.

Both the undrained strength at peak and the remolded shear strength can be evaluated from CPTu measurements. There are three independent equations to calculate $s_{u\ (peak)}$; these equations use different cone factors (N_{kt}, $N_{\Delta u}$, and N_{ke}) and cone measurements (q_{net}, Δu_2 , and q_{eff}) (Agaiby, 2018). Typically, f_s is taken as a measurement of $s_{u\ (remolded)}$. This approximation shows a good performance for insensitive soils. However, the approximation is less reliable for sensitive and quick clays because the f_s in these materials is considerably low, which causes the measurements to be outside the accuracy range of the f_s load cell (Mayne et al., 2023a). Moreover, for low f_s values, the porewater pressure effects can impact the reading, making it necessary to correct f_s, accounting for the pore pressure measurements at the shoulder (u_2), and behind the sleeve (u_3).

A common simplified equation to evaluate sensitivity was proposed by Robertson (2009), who used q_{net} and a cone factor N_{kt} constant and equal to 14 to calculate $s_{u\ (peak)}$, and f_s to calculate $s_{u\ (remolded)}$. For this case, the equation to calculate sensitivity reduces to the equation shown in Figure 54 (Robertson, 2009):

$$S_t = \frac{7.1}{F_r}$$

Figure 54. Equation. Simplified equation to evaluate sensitivity in low–medium sensitive clays.

Note that this equation uses the approximation of $s_{u\ (remolded)} \approx f_s$, which is less reliable for highly sensitive soils and quick clays.

CORRELATIONS FOR IN SITU STATE AND STRESS HISTORY PARAMETERS

Pre-consolidation Stress (σ_p) and Yield Stress Ratio (YSR)

The yield stress ratio ($YSR = \sigma'_p/\sigma'_{v0}$), also referred to as the over-consolidation ratio (OCR), is an important geotechnical parameter because it governs soil strength, stiffness, lateral stress, and compressibility. The YSR differentiates the regime between normally consolidated (NC) and over-consolidated (OC) clays. Moreover, YSR is a fundamental parameter for settlement evaluations and constitutive modeling, especially for elastoplastic models with a yield surface.

It is important to note that it is common to use the term OCR in geotechnical literature. The term YSR has been adopted more recently to account for different processes that generate a pre-consolidation besides mechanical loading-unloading (removal of overburden stress, such as erosion, excavation, and glaciation), such as desiccation, bonding, groundwater changes, diagenesis, and aging, among others (Agaiby & Mayne, 2019; Low et al., 2011; Pineda et al., 2016).

YSR is defined as the ratio between the yield stress (σ'_{vy}), or pre-consolidation stress (σ'_p), and the current effective vertical stress (σ'_{vo}), as shown in Figure 55:

$$YSR = \frac{\sigma'_{vy}}{\sigma'_{vo}}$$

Figure 55. Equation. Yield stress ratio (also known as over-consolidation ratio).

Yield Stress Ratio

For clay-type materials, YSR can be evaluated from CPTu measurements using a hybrid solution based on spherical cavity expansion (SCE) and critical state soil mechanics (CSSM), and the following expressions in Figure 56 (Mayne, 1991, 2005):

$$YSR = 2 \cdot \left[\frac{q_{net}/\sigma'_{v0}}{\left(\frac{2}{3}\right) M \cdot (ln(I_r) + 1) + \frac{\pi}{2} + 1}\right]^{1/\Lambda} = 2 \cdot \left[\frac{(q_t - \sigma_{v0})/\sigma'_{v0}}{\left(\frac{2}{3}\right) M \cdot (ln(I_r) + 1) + \frac{\pi}{2} + 1}\right]^{1/\Lambda}$$

$$YSR = 2 \cdot \left[\frac{\Delta u/\sigma'_{v0} - 1}{\left(\frac{2}{3}\right) M \cdot ln\,(I_r) + \frac{\pi}{2} + 1}\right]^{1/\Lambda} = 2 \cdot \left[\frac{(u_2 - u_0)/\sigma'_{v0} - 1}{\left(\frac{2}{3}\right) M \cdot ln(I_r) + 1}\right]^{1/\Lambda}$$

Figure 56. Equations. SCE-CSSM expressions for YSR of clays from CPTu.

where I_r is rigidity index ($= G/S_u$) and M is the slope of the critical state line (CSL) in the Cambridge University p'-q space, which can be calculated as $M = 6sin\phi'/3 - sin\phi'$ for triaxial compression, and $\Lambda = 1 - \mathrm{C_s}/C_c$ is the plastic volumetric strain potential, calculated from the ratio between the compression and swelling indices, and can be adopted as 0.8 for many insensitive clays, and increases to 1 for sensitive clays. The rigidity index will be covered in the next section. However, by combining the expressions above, a third expression can be formulated, removing the dependence on the rigidity index, as shown in Figure 57:

$$YSR = 2 \cdot \left[\frac{q_e/\sigma'_{vo}}{1.95M + 1}\right]^{1/\Lambda} = 2 \cdot \left[\frac{1}{1.95M + 1}\left(\frac{q_t - u_2}{\sigma'_{vo}}\right)\right]^{1/\Lambda}$$

Figure 57. Equation. SCE-CSSM simplified expression for YSR of clays using CPTu.

Yield Stress Screening Procedure for Clay-Type Identification

A first-order value for the yield stress (σ'_y) or pre-consolidation stress (σ'_p) of clays can be estimated using different variables measured by the CPT in clays, leading to three independent expressions, as shown in Figure 58 (Mayne, 2007a):

$$\sigma_y' = 0.33\ q_{net} = 0.33\ (q_t - \sigma_{vo})$$

$$\sigma_y' = 0.54\ \Delta u = 0.54(u_2 - u_o)$$

$$\sigma_y' = 0.60\ q_e = 0.6(q_t - u_2)$$

Figure 58. Equations. Pre-consolidation stress screening procedure for clays.

Note that these first-order expressions are obtained merely by inputting characteristic values of ϕ' = 30°, I_R = 100, and Λ = 1 into the aforementioned equations of Figures 56 and 57.

The three alternative expressions for assessing σ_y' are useful to differentiate between well-behaved or "normal" clays from organic clays and sensitive clays. In standard practice, clay is referred to as normal when it does not present special characteristics in its overall behavior, in contrast to sensitive, organic, cemented, or calcareous clays. Thus, these expressions provide a screening procedure to identify types of clays. When the clays are normal to well-behaved clays, the three expressions are approximately equal; thus, the three equations are redundant, while for organic or sensitive clays, there will be a hierarchy between these expressions as follows:

Table 8. CPTu Screening Procedure for Clay-Type Identification

Clay Type	Hierarchy
Normal or well-behaved clays	$0.33\ q_{net} \approx 0.54\ \Delta u \approx 0.60\ q_e$
Organic clays	$0.54\ \Delta u < 0.33\ q_{net} < 0.60\ q_e$
Sensitive or structured clays	$0.60\ q_E < 0.33\ q_{net} < 0.54\ \Delta u$

Examples of the screening process for a variety of clays can be found in Agaiby and Mayne (2021a).

Generalized Methodology for YSR in All Soils

Recently, a generalized methodology was developed to evaluate the yield stress of soils using the net cone resistance q_{net} and the material index I_{c-RW} (Agaiby & Mayne, 2019). The authors proposed the following expression in Figure 59 for the yield stress:

$$\sigma_y^{'} = 0.33 \cdot (q_t - \sigma_{vo})^{m^{'}} \cdot \left(\frac{\sigma_{atm}}{100}\right)^{1-m^{'}}$$

Figure 59. Equation. Generalized methodology for obtaining YSR in soils from CPT.

The exponent m' varies depending on the soil type and can be estimated using mean grain size (D_{50}), fines content (FC), or CPT material index I_{c-RW}, or both (Agaiby, 2018). An updated expression to calculate m' exponent as a function of I_{c-RW} was recommended by Robertson & Cabal (2022), shown in Figure 60:

$$m' = 1 - \frac{0.28}{1 + (I_{c-RW}/2.6)^{15}}$$

Figure 60. Equation: Value of m' exponent as a function of I_{c-RW}.

where $m' = 1$ for undrained and intact clays and $m' = 0.9$ for organic soils.

Figure 61 shows the variation of exponent m' as a function of I_{c-RW}:

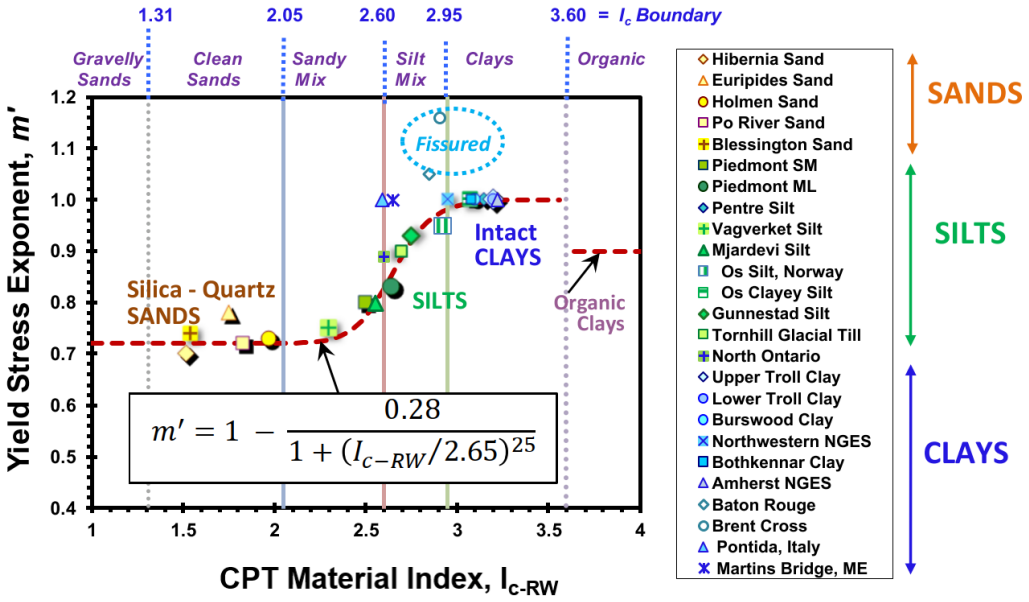

Figure 61. Yield stress exponent (m') as a function of I_{c-RW}.

Source: Agaiby & Mayne (2019)

YSR for Clean Sands

For clean sands, the YSR has been evaluated from CPT data obtained in calibration chambers (Figure 62). The use of calibration chambers was utilized for this application due to the difficulties of extracting intact sand samples for measurement of the yield stress in the laboratory and correlating the cone tip resistance (Mayne, 2005, 2007a; Mayne et al., 2009):

$$YSR = \left[\frac{0.192 \left(\frac{q_{net}}{\sigma_{atm}} \right)^{0.22}}{(1 - \sin \phi') \left(\frac{\sigma'_{vo}}{\sigma_{atm}} \right)^{0.31}} \right]^{\frac{1}{\sin \phi' - 0.27}}$$

Figure 62. Equation. YSR from CPT for clean sands.

The YSR for sands depends on CPT net cone resistance ($q_{net} = q_t - \sigma_{vo}$) and soil friction angle, which can be evaluated from the CPTu measurements, as discussed in previous chapters.

At-Rest Coefficient (K_0)

The geostatic effective vertical stress can be evaluated from piezocone measurements, as the previous sections show. In contrast, the in situ horizontal stress depends on the geological history of the soil. Therefore, it is common to estimate the at-rest earth pressure coefficient (K_0), which represents the ratio between the horizontal and vertical effective stresses for the condition of no lateral strains ($\varepsilon_h = 0$), as shown in Figure 63:

$$K_o = \frac{\sigma_h'}{\sigma_v'}$$

Figure 63. Equation. At-rest coefficient definition.

For the case of virgin loading and unloading, K_0 is related to soil friction angle and yield stress ratio (YSR) (Mayne & Kulhawy, 1982), as shown in Figure 64. Both parameters (ϕ' and YSR) can be assessed from piezocone readings, as explained in previous sections:

$$K_o = (1 - sin\,\phi')\,YSR^{sin\,\phi'}$$

Figure 64. Equation. At-rest coefficient (K_0) formulation for virgin loading-unloading.

Alternative expressions are available depending on the soil type:

Table 9. Estimation of At-Rest Coefficient (K_0) from CPT Measurements

At-Rest Coefficient	Reference
$K_o = 0.1 \cdot \left(\frac{q_t - \sigma_{vo}}{\sigma_{vo}'}\right)$	For fine-grained soils, an approximate correlation was proposed using a dataset of 12 intact and 5 fissured clays (Kulhawy & Mayne, 1990).
$K_o = 0.192 \cdot \left(\frac{q_t}{\sigma_{atm}}\right)^{0.22} \cdot \left(\frac{\sigma_{vo}'}{\sigma_{atm}}\right)^{-0.31} \cdot YSR^{0.27}$	For sands, the correlation was developed using 26 calibration chamber test programs on quartz and feldspar sands (Mayne, 2005).

Soil Compressibility (λ_{10})

The soil compressibility (λ_{10}), approximated as the slope of the critical state line in e-log(p') space, can be estimated using CPT measurements. Two approaches are available: (a) the approach by Plewes et al. (1992), who uses the normalized friction ratio to estimate compressibility (λ_{10}), and (b) the approach proposed by Jefferies and Ken (2015) that relies on soil behavior index. Table 10 shows both expressions.

Table 10. Estimation of Compressibility from CPT Measurements

Compressibility	Reference
$\lambda_{10} = \frac{F_r}{10}$	Plewes et al. (1992)
$\lambda_{10} = \frac{1}{34 - 10\ I_{c-JB}}$ where I_{c-JB} is the index soil behavior proposed by Jefferies & Been (2015)	Been & Jefferies (1992), Jefferies & Been (2015)

This correlation was analyzed by Reid (2015), who extended the database used to evaluate the correlation and show that the general trend observed was consistent with the previous reports. However, the author highlights a considerable scattering of the correlations, as shown in Figure 65.

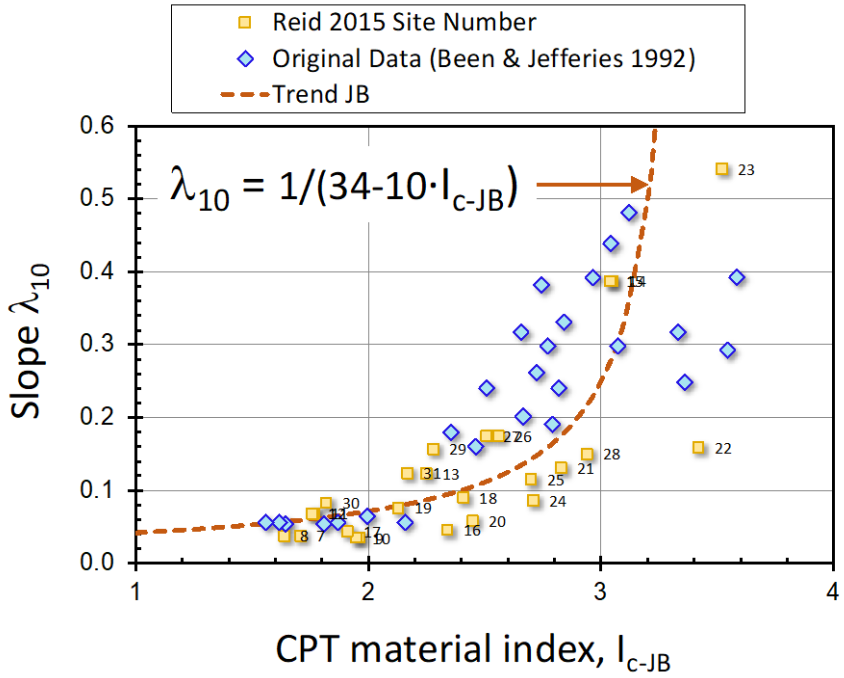

Figure 65. Soil compressibility relationship with the CPT material index.

Source: Reid (2015)

State Parameter (ψ)

The state parameter (ψ) is used to characterize the current state of the soil relative to the critical state. The state parameter is defined as the difference between the void ratio at its initial state (e_0) and void ratio at the critical state (e_{CSL}) for a constant confinement stress (Jefferies & Been, 2015), as shown in Figure 66:

$$\psi = e_0 - e_{CSL}$$

Figure 66. Equation. Definition of state parameter (ψ).

Table 11. Estimation of State Parameter (ψ) from CPT Measurements

State Parameter (ψ)	Reference
$$\psi = -\frac{1}{m'} \cdot ln\left[\frac{Q_p(1-B_q)+1}{k'}\right]$$ Where Q_p is the normalized cone resistance using the mean stress (p_0): $$Q_p = \frac{q_t - p_0}{p_0'}$$ $$p_0 = \frac{1}{3}\sigma_{vo}(1+2\cdot K_0)$$ $$p_0' = \frac{1}{3}\sigma_{vo}'(1+2\cdot K_0)$$ The terms k' and m' are empirical fitting parameters which depend on the soil's compressibility (λ_{10}) and the critical state stress ratio (M_c): $$m' = 11.9 - 13.3\cdot\lambda_{10}$$ $$k' = M_c\cdot(3+0.85/\lambda_{10})$$	Been et al. (1986, 1987) proposed a method in sands, using laboratory tests correlated with CPT measurements made on chamber tests (Been et al., 1986, 1987). Later, this framework was further extended to include silts and clay (Been, 2016; Jefferies & Been, 2015).
$$\psi = \frac{ln\left[\frac{Q_t(1-B_q)}{\left(3.6+\frac{10.2}{F_R}\right)}\right]}{(1.33\,F_R - 11.9)}$$	Plewes et al. (1992) proposed an equation that uses the normalized parameters Q_t, B_q, and F_R. The approach delineates the contours of the state parameter using the soil behavior type chart from Jefferies & Davies (1993). This method applies to sand and silty sands.
$$\psi = 0.56 - 0.33\,log\,Q_{tn,cs}$$ Where $Q_{tn,cs}$ is calculated as follows: $$Q_{tn,cs} = K_c\cdot Q_{tn}$$ K_c is and adjustment factor calculated based on I_{c-RW}: $K_c = 15 - \frac{14}{1+(I_c/2.95)^{11}}$ for $I_c < 3.0$	Robertson (2010b) proposed an approximate means to estimate the state parameter of sands using the normalized cone resistance equivalent to a clean sand value ($Q_{tn,cs}$).

$\boldsymbol{\psi}$ can be used in practice to assess is a soil unit is loose or dense, for example $\boldsymbol{\psi < -0.05}$ corresponds to dense soils. $\boldsymbol{\psi}$ can be estimated from CPTu data as illustrated by Table 11 where $\boldsymbol{\psi}$ is estimated from CPTu data considering three different methodologies proposed by Been et al. (1986, 1987), Plewes et al. (1992), and Robertson (2010b). The parameters needed for estimating $\boldsymbol{\psi}$ have been previously defined.

CORRELATIONS FOR SOIL STIFFNESS AND SOIL MODULI

The soil stiffness encompasses different parameters (shear wave velocity, shear modulus, Young's modulus, and constrained modulus) depending on the loading, confinement, and draining conditions. Determining soil stiffness is important for calculations to evaluate settlements and strain profiles. Moreover, research has shown that small-strain properties can be used to help assess the existence of microstructure in soils since aging and bonding increase and stiffen the small-strain response of soil (Robertson, 2016).

Shear Wave Velocity Estimation with CPT

The shear wave velocity is a small-strain parameter that is fundamental to performing dynamic analysis and liquefaction assessment (Niazi, 2021). The shear wave velocity can be directly measured using seismic piezocone tests (SCPTu). Even though the direct measure is preferred, there are correlations to estimate shear wave velocity using the CPT, and these can be used for low-risk projects (Robertson, 2009). Some correlations were developed using a dataset including all soil types (Table 12), while other correlations apply only to sands (Table 13) or clays (Table 14).

Table 12. Shear Wave Velocity from CPT Measurements for All Soil Types

Equation	Reference	Note
$V_s = (10.1\,log(q_t) - 11.4)^{1.67} \cdot {R_f}^{0.3}$ where V_s is in (m/s), q_t , f_s in (kPa), and R_f in (%).	Hegazy & Mayne (1995)	The study was performed on data from 61 sites, including clays, sands, intermediate soils, and mine tailings.
$V_s = 2.62 \cdot {q_t}^{0.395} \cdot {I_{c-RW}}^{0.912} \cdot z^{0.124} \cdot ASF$ where V_s is in (m/s), q_t in (kPa), and z in (m).	Andrus et al. (2007)	ASF is an age scaling factor, 0.92 for Holocene deposits and 1.12 for Pleistocene soils.
$V_s = \left[\alpha_{vs}\,\frac{(q_t - \sigma_{vo})}{\sigma_{atm}}\right]^{0.5}$ $\alpha_{vs} = 10^{(0.55 I_{c-RW} + 1.68)}$ where V_s is in (m/s), q_c , f_s and σ'_{vo} (kPa).	Robertson (2009)	The study was performed on Holocene to Pleistocene, mostly uncemented deposits.

Table 13. Shear Wave Velocity Estimates from CPT Measurements in Sands

Equation	Reference	Note
$V_s = 277 \cdot {q_t}^{0.13} \cdot {\sigma'_{vo}}^{0.27}$ where V_s is in (m/s), q_t and σ'_v (Mpa).	Baldi (1989)	The study was performed on quartzitic sand.
$V_s = 135 \cdot {q_t}^{0.23} \cdot \left(\frac{\sigma'_{vo}}{\sigma_{atm}}\right)^{0.135}$ where V_s is in (m/s), q_t and σ'_v (kPa).	Fear & Robertson (1995)	The study was performed on tailing sand, with 30% of fines content and carbonate content.
$V_s = 13.18 \cdot {q_t}^{0.192} \cdot {\sigma'_{vo}}^{0.179}$ $V_s = 12.02 \cdot {q_t}^{0.319} \cdot {f_s}^{-0.0466}$ where V_s is in (m/s), q_t, f_s, and σ'_v (kPa).	Hegazy & Mayne (1995)	The study was performed on 24 sand sites.
$V_s = 124.7\left(\frac{q_t}{\sigma_{atm}}\right)^{0.135}\left(\frac{f_s}{\sigma_{atm}}\right)^{0.014}\left(\frac{\sigma'_{vo}}{\sigma_{atm}}\right)^{0.169}$ where V_s is in (m/s), q_t, f_s, σ'_v , and σ_{atm} in same units.	Perret et al. (2016)	For sandy soil $I_{c-RW} < 26$ and $B_q < 0.1$.

Table 14. Shear Wave Velocity Estimates from CPT Measurements in Clays

Equation	Reference	Note
$V_s = 1.75 \cdot {q_t}^{0.627}$ where V_s is in (m/s), and q_t in (kPa).	Mayne & Rix (1995)	The study was performed on 31 clay sites. The clays range from intact to fissured.
$V_s = 3.18 \cdot {q_t}^{0.549} {f_s}^{0.025}$ where V_s is in (m/s), and q_t and f_S in (kPa).	Hegazy & Mayne (1995)	The study was performed on 36 clay sites.

Maximum Shear Modulus

The maximum shear modulus (G_o) is a small-strain parameter applicable for shear-strain levels lower than 10^{-4}%. The shear modulus can be determined from shear wave velocity as follows in Figure 67:

$$G_o = \rho \, V_s^2$$

Figure 67. Equation. Shear modulus estimated from shear wave velocity.

Where ρ is the mass density (calculated as the unit weight divided by the acceleration of gravity $\rho = \gamma / g$). Table 15 shows some available correlations to evaluate the small-strain shear modulus from CPT measurements.

Table 15. Small-Strain Shear Modulus from CPT Measurements

Equation	Reference	Note
$G_o = 50 \, \sigma_{atm} \left[\frac{(q_t - \sigma_{vo})}{\sigma_{atm}} \right]^{m^*}$	Mayne (2007a)	$m^* = 0.6$ for quartzite to silica sands, and $m^* = 1.0$ for intact clays of low to medium sensitivity.
$G_0 = \alpha_G \, (q_t - \sigma_{vo})$ for an average unit weight of 18kN/m3. $\alpha_G = 0.0188 \left[10^{(0.55 I_c + 1.68)} \right]$ G_0, q_t and σ_{v0} in same units.	Robertson (2009)	Formulation for uncemented coarse-grained soils, it is less reliable for fine-grained soils when $I_c > 2.6$.

Drained Young's Modulus

The drained Young's modulus applies to drained soils where $I_{c\text{-}RW} < 2.60$. For uncemented soils that are not structured, Robertson (2009) suggested a simplified elastic solution that can be appropriate for many design applications. This simplified formulation approximates Young's modulus as 80% of the small-strain shear modulus (Figure 68):

$$E' \approx 0.8\, G_o$$

Figure 68. Equation. Drained Young's modulus.

Robertson (2009) also proposed a direct equation to determine the drained Young's modulus from CPT parameters, which applies mainly to uncemented silica sands, as shown in Figure 69:

$$E' = \alpha_E (q_t - \sigma_{vo})$$

$$\alpha_E = 0.015\left[10^{(0.55 I_c + 1.68)}\right]$$

Figure 69. Equations. Drained Young's modulus based on I_c and q_{net} in sands.

Constrained Modulus

The constrained modulus (D') is a drained parameter measured from a one-dimensional consolidation test (oedometer test), where D' depends on the stress history of the soil:

For OC soils: $\mathrm{D}' = \frac{1+e_0}{C_s} \ln(10) \sigma'_{vo}$

For NC soils: $\mathrm{D}' = \frac{1+e_0}{C_c} \ln(10) \sigma'_{vo}$

Table 16 summarizes the most used equations to evaluate the constrained modulus directly from CPT measurements.

Table 16. Constrained Modulus from CPT Measurements

Equation	Reference	Note
$\mathrm{D}' = \alpha_{\mathrm{D}} (q_t - \sigma_{vo})$	Kulhawy & Mayne (1990), Mayne (2001, 2007a)	α_{D} is an empirical factor that ranges from 2–8. The recommended value is 5.
$\mathrm{D}' = \alpha_{\mathrm{D}} (q_t - \sigma_{vo})$ If $I_c > 2.2$ (fine-grained soils): $\alpha_{\mathrm{D}} = Q_{tn}$, when $Q_{tn} < 14$ $\alpha_{\mathrm{D}} = 14$, when $Q_{tn} > 14$ If $I_c < 2.2$ (coarse-grained soils): $\alpha_{\mathrm{D}} = 0.018\left[10^{(0.55 I_c + 1.68)}\right]$	Robertson (2009), Robertson & Cabal (2022)	The study was performed on 36 clay sites. Robertson & Cabal (2022) updated the factor of 0.03 to 0.018, and it is consistent with the observation that $D' \sim G_0$ (Mayne, 2001) in sands.

Rigidity Index

The rigidity index is defined as the ratio of shear modulus to shear strength ($I_R = G/\tau_{max}$). For undrained behavior $\tau_{max} = s_u$, the complexity relies on the value of the shear modulus (G), because it varies greatly from a high value at the nondestructive range (G_{max}) to a low value at failure (G_f).

The SCE-CSSM solution gives the following expression in Figure 70 for insensitive clays ($a_q \leq 0.5$) to calculate I_R from CPTu measurements (Mayne, 2001):

$$I_R = exp\left(\frac{1.5 + 2.925 \cdot M \cdot a_q}{M(1 - a_q)}\right)$$

Figure 70. Equation. SCE-CSSM expression for rigidity index—insensitive clays.

where $M = 6 \cdot sin\phi'/3 - sin\phi'$ is the slope of the CSL, and a_q is the slope of $(u_2 - \sigma_{vo})$ versus $q_{net} = q_t - \sigma_{vo}$. An equivalent form is $a_q = B_q - 1/Q_t$. This method requires a definition of the clay layer boundaries to estimate the a_q slope for the appropriate layer.

For sensitive clays ($a_q > 0.5$), the following equation in Figure 71 is provided (Agaiby & Mayne, 2018):

$$I_R = \exp\left[\frac{1.5 + 2.925 \cdot M_1 \cdot a_q}{M_2 - M_1 \cdot a_q}\right]$$

Figure 71. Equation. SCE-CSSM expression for rigidity index—sensitive clays.

M_1 corresponds to the effective friction angle at peak strength (ϕ_1' at q_{max}), while M_2 relates to the friction angle at large strains (ϕ_2' at $(\sigma_1'/\sigma_3')_{max}$ i.e., maximum obliquity). Maximum obliquity and maximum deviator stress (q_{max}) are two different criteria to determine the friction angle from a shear triaxial test. ϕ_2' can be calculated with the original NTH formulation, and ϕ'_1 can be calculated with the following expression in Figure 72:

$$\frac{\phi_1'}{\phi_2'} = 1 - \frac{0.30}{1 + (0.60/a_q)^{12}}$$

Figure 72. Equation. Relationship between the friction angles at maximum obliquity (ϕ_2') and maximum deviator stress (ϕ_1') and parameter a_q.

Krage et al. (2014) recommend G_{50} as the best method to provide reasonable values of I_R because it represents the stress and strains levels that are half way to peak strength (Schnaid et al., 1997). G_{50} is the secant shear modulus associated with 50% of the mobilized strength. In this case, I_{R50} is calculated from the following expression in Figure 73 (Krage et al., 2014):

$$I_{R50} = \frac{1.81 \cdot G_{max}}{(q_{net})^{0.75}(\sigma'_{v0})^{0.25}}$$

Figure 73. Equation. Rigidity index associated with G_{50}.

CORRELATIONS FOR FINES CONTENT

The fines content (FC) is defined as the percentage of soil particles smaller than 0.075 mm passing sieve #200. FC is an important parameter for evaluating liquefaction susceptibility. Typically, the correlations available to evaluate FC with the CPT test are based on the CPT material index (I_c), as shown in Table 17.

Table 17. Fines Content (FC%) Evaluation from I_c

Equation	Reference
If I_c < 1.26: $FC = 0$ If 1.26< I_c < 3.5: $FC = 1.75\ I_c^{3.25} - 3.7$ If I_c >3.5: $FC = 100$	Robertson & Wride (1998)
If 1.26 < I_c < 2.05: $FC = 1.75\ I_c^{3.25} - 3.7$ If 2.05< I_c < 2.82: $FC = 0.75\ I_c^{6.14}$	Baez et al. (2000)
$FC = 80(I_c + C_{FC}) - 137$ $C_{FC} \in [-0.29, 0.29]$ can be adjusted to site-specific data. If there are no data available, $C_{FC} = 0$.	Boulanger & Idriss (2014)
$FC = 1.3\ I_c^{3.77}$ $FC = \left(\frac{293}{I_B}\right)^{1.65}$	Agaiby & Mayne (2020)

Research and geotechnical practice have shown that most correlations are often site-dependent, which introduces high uncertainty in the estimation for a general dataset. In the study performed by Agaiby and Mayne (2020), a database developed from 53 sites covering a wide range of soil types was used; however, the general format and algorithm would be best utilized if calibrated using site-specific data for a given geologic setting and local soils.

POREWATER PRESSURE DISSIPATION TESTING

The insertion of the penetrometer into soils with low permeability (e.g., fine-grained soils) generates significant excess pore pressure relative to the hydrostatic (Burns & Mayne, 2002). If the penetration process is stopped, the pore pressures will dissipate with time, eventually reaching the hydrostatic conditions. Using the curve of pore pressure dissipation as a function of time, the in situ coefficient of consolidation can be calculated via the theory of cavity expansion and critical state soil mechanics approach or strain path method, as well as other solutions. The subsequent subsections will detail how to apply these methods to estimate the coefficient of consolidation (c_{vh}). The subindex vh denotes that the dissipation process occurs in the vertical and horizontal directions. The c_{vh} of the soil is related to its permeability and compressibility (specifically the constrained modulus) through the following equation in Figure 74:

$$c_{vh} = \frac{k_{vh} \cdot D'}{\gamma_w}$$

Figure 74. Equation. Coefficient of consolidation definition.

where k_{vh} is the hydraulic conductivity or soil permeability, D' is the constrained modulus of the soil, and γ_w is the unit weight of water.

The dissipation test is used to evaluate the coefficient of consolidation. The CPT provides a continuous profile of the estimated constrained modulus. With these two variables, the soil permeability, also termed hydraulic conductivity, can also be evaluated.

On the Assessment of t_{50}

During a dissipation test on fine-grained soils, it is common to observe two different types of behavior: monotonic and dilatory. In soft clays, a monotonic response occurs when the magnitude of pore pressure decays continuously with time after stopping the sounding. In stiff to hard or fissured over-consolidated clays, a dilatory response is observed whereby the pore pressure temporarily increases with time up to a maximum value, followed by a subsequent monotonic decrease (Burns & Mayne, 1998).

The dissipation results are often represented by a single measured value of time, often taken at 50% degree of consolidation, designated t_{50}. The value of t_{50} corresponds to the value of u_2 measured at the half-way point during dissipation. For monotonic responses, the evaluation of u_{50} and t_{50} is straightforward. Specifically, the u_{50} value would be the middle point between the maximum measured pore pressure (u_{2max}) and the hydrostatic pore pressure (u_0). The value t_{50} corresponds to the measured time when the u_{50} occurs, as illustrated in Figure 75.

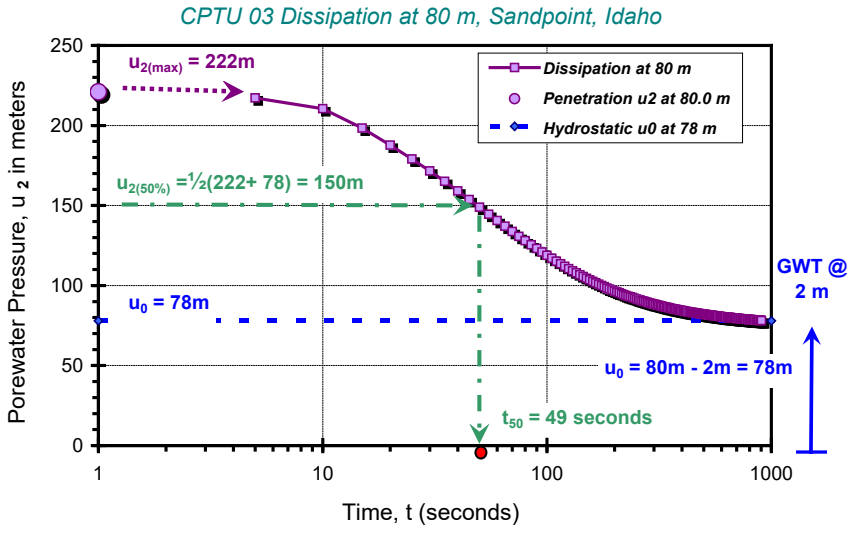

Figure 75. Definitions of u_{50} and t_{50} for monotonic pore pressure decay.

Source: Mayne et al. (2023a)

In contrast, for a dilatory response, the estimation of t_{50} is not as straightforward and requires adjusting and fitting the curve before the assessment of u_{50} and t_{50} (Sully et al., 1999; Burns & Mayne 2002; Chai et al., 2012; Mahmoodzadeh & Randolph, 2014).

According to Sully et al. (1999), there are three methods to evaluate the t_{50} for dilatory responses. These methods differ in the point where the maximum pore pressure is considered and the corresponding time, as depicted in Figure 76. The first method uses the initial value from the u_2 reading from the dissipation curve as measured without fitting or shifting the curve. The second method uses a linear fit of the dissipation curve after the peak and extrapolates the fitted curve to estimate the pore pressure at the initial time. The third method shifts the dissipation curve in time, using the point corresponding to the maximum measured pore pressure as zero time.

Finally, it is recommended to use the square root of time on the x-axis (i.e., method 2) because work by Danziger et al. (1997), DeJong and Randolph (2012), Mayne et al. (2023a), and others have shown this approach to be the more reliable means of assessing a representative and realistic value of t_{50} from dilatory curves.

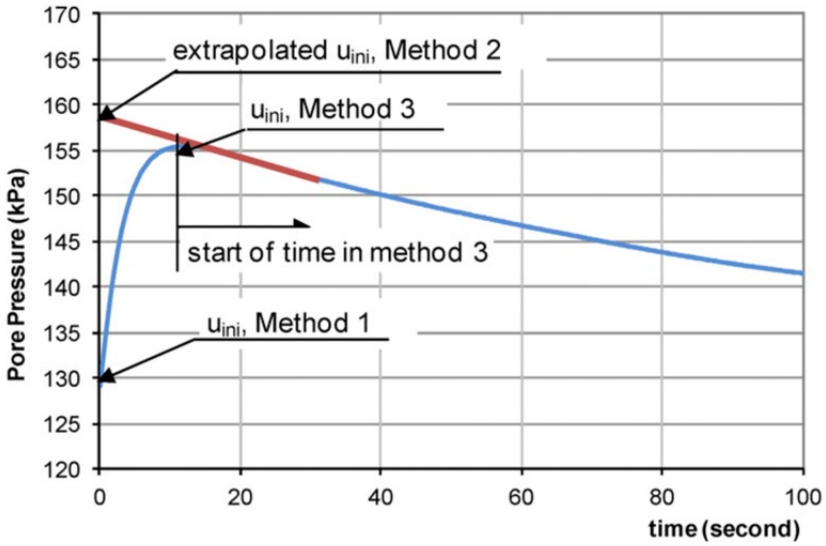

Figure 76. Three definitions of t_{50} from dilatory pore pressure response.

Source: Mahmoodzadeh & Randolph (2014)

For simplicity, method 2 is recommended to determine the maximum u_2 value by extrapolating the linear portion of the dissipation curve after the peak, as shown by the example presented in Figure 77 for hard Taranto clay in Italy (data from Pane et al., 1995).

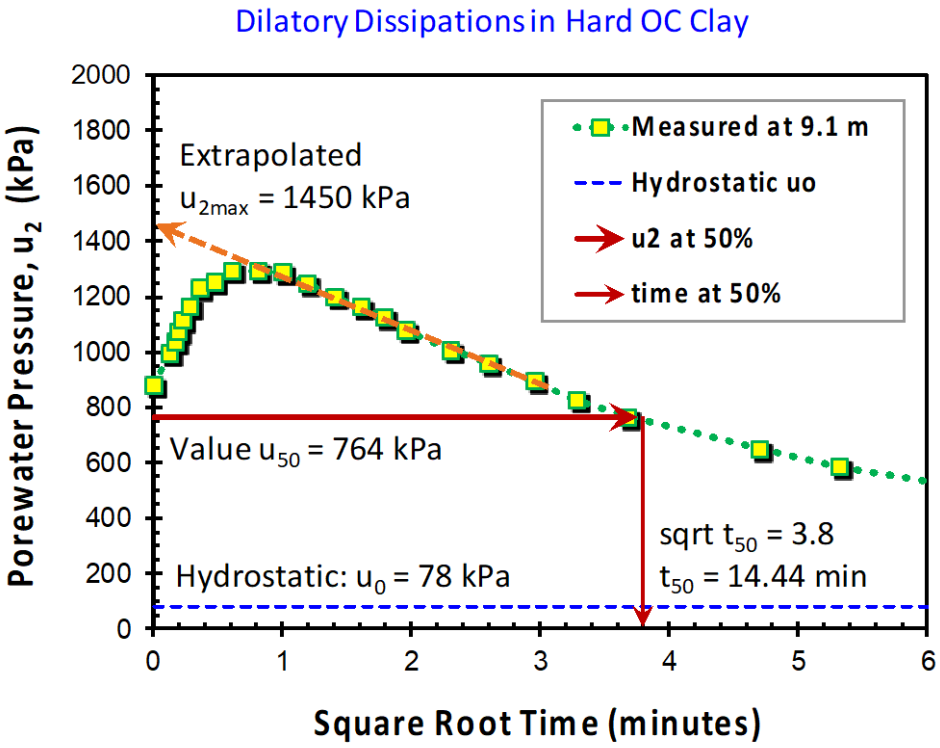

Figure 77. Evaluation of dissipation test in Taranto clay with dilatory response.

Source: Mayne et al. (2023a)

Coefficient of Consolidation

The coefficient of consolidation from the dissipation test can be evaluated by the strain path method or the cavity expansion–critical state soil mechanics (CE-CSSM) approach. The strain path method developed by Teh and Houlsby (1991) aims to represent the complex deformation patterns of soil during cone penetration. The authors proposed the following equation in Figure 78 for the coefficient of consolidation in the horizontal direction (c_h):

$$c_h = \frac{T^* \cdot (a_c)^2 \cdot \sqrt{I_r}}{t}$$

Figure 78. Equation. Coefficient of consolidation formulation developed by Teh and Houlsby (1991).

where T^* is the time factor, a_c the radius of the cone, t the time, and I_r the rigidity index, which represents the ratio between the shear modulus (G) and the undrained strength (S_u): $I_r = G/S_u$. The authors provide values for the time factor for different degrees of consolidation and penetrometer positions where the pore pressure is measured. The time factor corresponding to 50% of consolidation T^*_{50} is 0.245 for the pore pressure measured at the shoulder position (u_2), consistently, the time for 50% of consolidation (t_{50}) should be used in the calculation to compute the coefficient of consolidation (Teh & Houlsby, 1991). Often a default value of $I_R = 100$ is assumed, as the authors provide no guidance on the assessment of this parameter.

The second method to evaluate the coefficient of consolidation includes the CE-CSSM approach, which have provided analytical solutions to the piezocone dissipation tests by solving the second-order partial differential equation that describes the consolidation process (Burns & Mayne, 1998, 2002). Approximate solutions have been obtained by fitting the theoretical and measured dissipation tests curves (Mayne, 2001), where the coefficient of consolidation is determined as follows in Figure 79:

$$c_{vh} = \frac{T'_{50}(a_c)^2(I_R)^{0.75}}{t_{50}}$$

Figure 79. Equation. Coefficient of consolidation proposed by Mayne (2001).

where T'_{50} is the time factor for 50% of consolidation and has a value of 0.028, a_c is the cone radius, I_R is the undrained rigidity index of the clay, and t_{50} is the time where 50% of the excess of pore pressure is dissipated, measured with the piezocone. The rigidity index is evaluated using the expressions given in Figures 70 and 71. The CPTu provides all the needed geoparameters.

Correlations for Hydraulic Conductivity

The permeability or hydraulic conductivity (k_{vh}) can be evaluated from CPTu measurements using either dissipation test results or based on the soil behavior type. The first approach is to use the coefficient of consolidation (c_{vh}) measured during the dissipation test, and the constrained modulus (D') to calculate the permeability as follows in Figure 80:

$$k_{vh} = \frac{c_{vh} \cdot \gamma_w}{D'}$$

Figure 80. Equation. Hydraulic conductivity estimation from PPD tests.

Additionally, some authors propose a simplified approximation that uses the value of t_{50} measured during the dissipation test, as shown in Figure 81 (Robertson, 2010a):

$$k_h = (1.67 \cdot 10^{-6}) \cdot 10^{[1-log(t_{50})]} \cdot \left(\frac{\gamma_w}{D'}\right)$$

Figure 81. Equation. Simplified approximation for hydraulic conductivity proposed by Robertson (2010a).

The equation is unit dependent and gives k_h in (m/s). Furthermore, Ansari et al. (2014) proposed an approach based on numerical simulations of the dissipation test, where the penetration and dissipation process were explicitly modeled. The method uses the measured t_{50} during dissipation test and strength properties of the soil as input parameters (Figure 82):

$$k_{vh}(m/s) = \frac{6 \cdot 10^{-6}}{t_{50}^{*}(s)}$$

$$t_{50}^{*} = t_{50}\left[\frac{\sigma_{vo}^{'}(kPa)}{27kPa}\right]\left(\frac{1+2\cdot K_o}{1.6}\right)^{-0.75}\left(\frac{I_R}{108}\right)^{0.48}\left[\frac{1.784(cm)}{a_c(cm)}\right]$$

Figure 82. Equations. Simplified approximation for hydraulic conductivity proposed by Ansari et al. (2014).

where σ'_{vo} is the effective vertical stress, K_o the at-rest earth pressure coefficient, $I_R = G_o/s_u$ the rigidity index, and a_c the radius of the cone. This approach applies only to soft clays with $YSR \leq 1.2$ (Ansari et al., 2014).

Finally, Robertson and Cabal (2015) proposed an approach based on the soil behavior type and $I_{c\text{-}RW}$ parameters (Figure 83):

$$k_{vh}(m/s) = 10^{(0.952-3.04\, I_{c-RW})} \text{ for } 1.0 < I_{c-RW} \leq 3.27$$

$$k_{vh}(m/s) = 10^{(-4.52-1.37\, I_{c-RW})} \text{ for } 3.27 < I_{c-RW} \leq 4.0$$

Figure 83. Equations. Simplified approximation for hydraulic conductivity estimation from CPT material index, I_{c-RW}, as proposed by Robertson & Cabal (2015).

This approach gives an estimate of the permeability for all soil types, which is useful for soils with high permeability, where the dissipation process occurs rapidly, making the measurement of the flow characteristics difficult (Robertson & Cabal, 2015).

SEISMIC CONE PENETRATION TESTING

The shear wave velocity gives essential information about the mechanical behavior of soils, specifically related to the small-strain stiffness. It is a fundamental parameter in seismic hazard and site response evaluations because it is an input for site amplification studies and can be used to estimate the liquefaction resistance of soils (Schneider et al., 2001; Youd & Idriss, 2001).

The process of pushing a piezocone into the ground generates large strains during the probe advance. On the contrary, the shear wave velocity measures the small strain soil behavior in the nondestructive range, and therefore, relates to the initial tangent shear modulus ($G_0 = G_{max}$). In addition, the small-strain information is helpful to identify soils with potentially challenging microstructures like cementation, bonding, or aging, in addition to the applications involving seismic site response as previously mentioned (Robertson, 2016).

The shear wave velocity is calculated as the path length difference (ΔR) of the wave divided by the time interval that the wave took to travel this distance (Δt), as shown in Figure 84:

$$V_s = \frac{\Delta R}{\Delta t}$$

Figure 84. Equation. Shear wave velocity calculation from path length and travel distance.

Non-Continuous Profile Methods

The most common methods to assess the time interval include: (1) first arrival, (2) first peak, and (3) first crossover. These methods rely on the manual picking of data points and were predominantly used when the signals were recorded in an analog format. The disadvantages of these methods are that they require judgment from the user and only use one point in the entire wavelet to estimate the time interval.

Concerning the first arrival method, the time interval could be challenging to identify due to the presence of faster compression waves and reflections on the interface (Liao & Mayne, 2006). The crossover methods use the polarization of shear waves to estimate the time interval, requiring generating two waves with opposite directions (left and right strike). The disadvantages of this method are the increase in the testing time and signal disturbance, which can cause an offset of one signal (Ku et al., 2013a). Figure 85 shows a schematic of the manual picking methods to estimate the time interval.

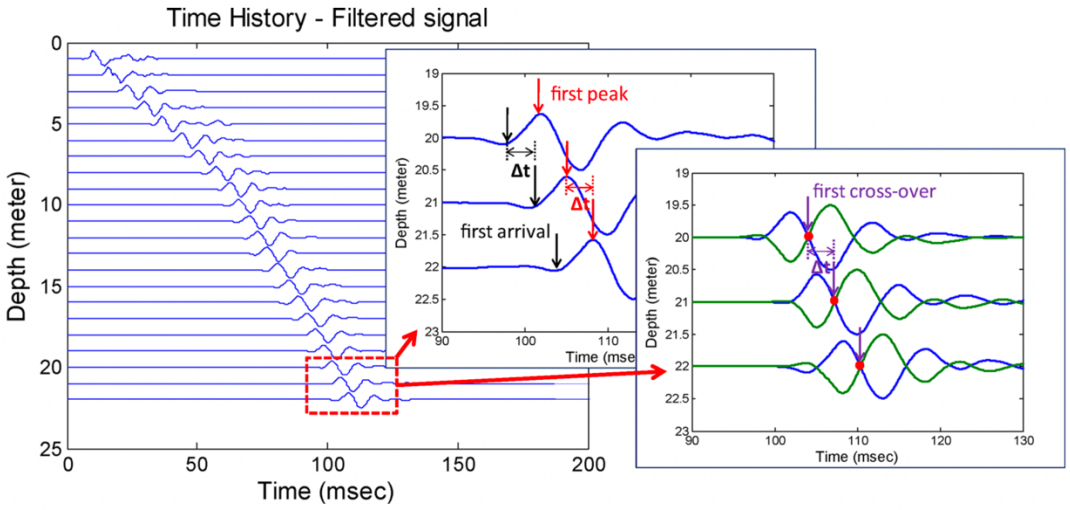

Figure 85. Scheme of the wavelets recorded during an SCPTu sounding and the estimation of time interval using manual picking methods (first arrival, first peak, and first crossover).

Source: Ku et al. (2013b)

Cross-Correlation Method

The cross-correlation method determines the time interval by finding the time shift of two independent shear wave signals. A cross-correlation measures the similarity between two signals taken at different depths by shifting one of the signals in time and calculating the coefficient of determination (r^2) for each time shift evaluated. The chosen time interval will correspond to the time

shift associated with the maximum r^2. The time interval is thus defined by a statistical evaluation that uses much of the entire wavelet (e.g., n = 4000) instead of just relying on a single point, as in the manual picking methods.

The cross-correlation methods assume that the signals at different depths (usually 1 m intervals) will have a similar shape, and the main difference would be a time shift. The time shift is calculated by shifting one signal at a constant time and estimating r^2, as illustrated in Figure 86.

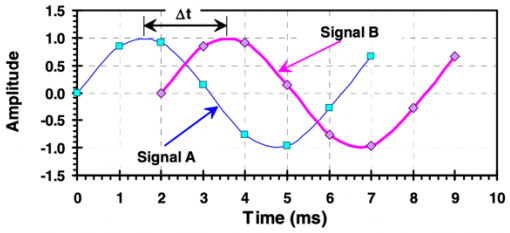

A. Time shift between two independent shear wave signals

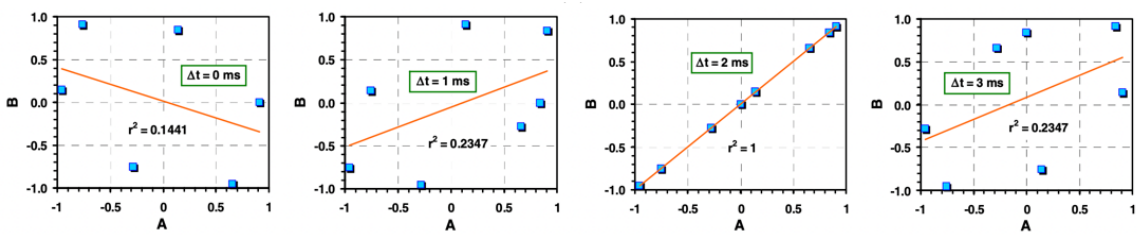

B. Coefficient of determination (r^2) for different time shift values

Figure 86. Illustration of cross-correlation method to determine the time shift between two independent signals.

Source: Liao & Mayne (2006)

To calculate the coefficient of determination (r^2), two independent signals x_i and y_i (with i = 1, 2, …, N, where *N* is the signal length) will be correlated as a function of time shift, *k*. Assuming that the depth *y* is greater than the depth of *x*, the signal *y* will be shifted forward in time by a factor of *k* times the sampling interval; therefore, the shifted signal will be *yi+k*. Subsequently, the first N-k points on the signal *x* will be compared to the last N-k points on the signal *y*. The value of r^2 is defined in Figure 87:

$$r^2 = \frac{(\sum(x_i - \bar{x})(y_{i+k} - \bar{y}))^2}{\sum(x_i - \bar{x})^2 \sum(y_{i+k} - \bar{y})^2}$$

Figure 87. Equation. Equation to calculate the coefficient of determination (r^2).

where $\bar{x}$ is the average of the first N-k points on *x*, and $\bar{y}$ is the average of the last N-k points on *y*. The calculation is repeated for different k values, which evaluates different time shifts between the signals. The time interval used to calculate the shear wave velocity will be defined as the time shift (*k*) corresponding to the maximum r^2 since it is the time shift where the signals have a higher correlation.

For further details on the method, refer to the following studies: Ku et al. (2013a, 2013b) and Liao and Mayne (2006).

Phase Shift

The phase-shift method compares independent signals taken at different depths in the frequency domain. The analysis in the frequency domain for a single signal consists of determining the power spectral density (PSD), which gives the relative power contribution of each frequency level to the signal. This can be extended to two signals by determining the cross-spectral analysis of two signals, *x* and *y*, to determine the correlations of the signals at different frequencies. The resultant cross-spectrum is a complex number with the following form (Figure 88):

$$\Phi_{xy} = C_o(k) + iQ(k)$$

Figure 88. Equation. Resultant cross-spectrum form.

Where *k* represents the frequency, C_o is the real part or co-spectrum, and Q is the imaginary part or quadrature spectrum. The time shift is then calculated using the predominant frequency of the cross-spectrum. First, the phase shift angle at the predominant frequency is calculated as follows in Figure 89:

$$\theta = tan^{-1}\left(\frac{Q(k)}{C_o(k)}\right)$$

Figure 89. Equation. Phase shift angle at the predominant frequency.

Then, the phase delay time is calculated as follow in Figure 90:

$$\Delta t_f = \frac{\theta}{(360 * f)}$$

Figure 90. Equation. Phase delay time. f indicates frequency.

For further details on the phase-shift method, refer to Ku et al. (2013a, 2013b) and Liao and Mayne (2006).

Continuous Profile Methods

In lieu of these older approaches, robust data acquisition systems and enhanced signal processing algorithms allow for post-processing that uses most of the wavelet data for the time interval estimation instead of a single point (Liao & Mayne, 2006). There are mainly two methods: cross-correlation, which uses the time domain of the signal, and phase shift, which uses the frequency domain of the signal. It is important to note that it is necessary to use these methods to generate a continuous shear wave velocity profile when an automated wave source or auto-source is used in the field (refer to Figure 91) (Ku et al., 2013a, 2013b). However, the cross-correlation and the phase-shift methods can also be applied to non-continuous measurements (usually taken every meter when a rod is added).

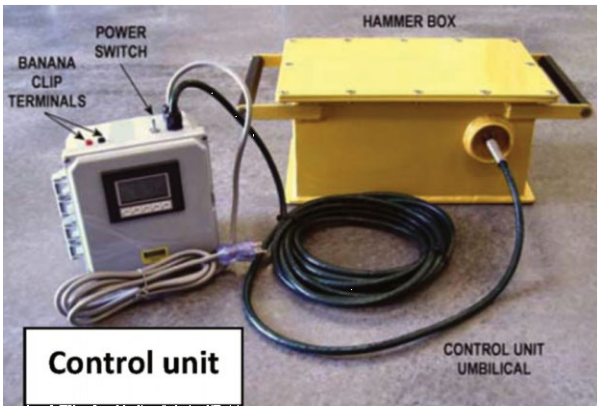

A. A photo of automated wave source for continuous profiling of shear wave velocity

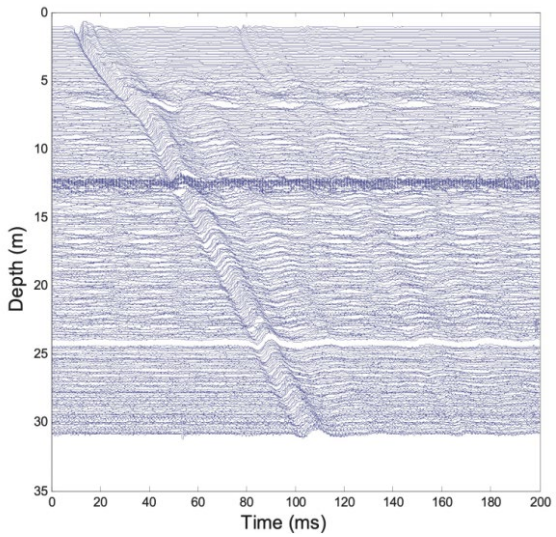

B. Shear wave signals recorded using the auto-source

Figure 91. Automated wave source for continuous profiling of shear wave velocity and shear wave signals recorded using the auto-source.

Source: Adapted from Ku et al. (2013a)

Soil Parameters from Shear Wave Velocity

Soil Stiffness Based on V_s

The stiffness of soils at small-strain levels corresponds to shear strains lower than 10^{-4}% (Robertson & Cabal, 2010) and can be determined from seismic piezocone tests (SCPTu). The small-strain shear modulus G_o is a fundamental parameter that applies to drained and undrained behavior because, at this low strain level, porewater pressures have not yet been generated (Mayne, 2001). The seismic piezocone provides a direct in situ measurement of the small-strain shear modulus because the shear wave velocity and the small-strain shear modulus are related by the equation in Figure 92:

$$G_o = \rho_T V_s^2$$

Figure 92. Equation. Shear modulus estimated from shear wave velocity.

where ρ_T is the total mass density. Note that mass density can also be estimated using the CPT from unit weight since $\rho_T = \gamma_T / g_a$, where g_a is the gravitational constant (= 9.8 m/s^2 = 32 ft/s^2). Furthermore, the equivalent Young's modulus can be calculated from the measured G_o and the Poisson ratio (υ) (Figure 93):

$$E_o = 2(1 + \upsilon)G_o$$

Figure 93. Equation. Young's modulus.

Unit Weight Based on V_s

The total unit weight can be evaluated using the shear wave velocity measured by SCPTu tests. Some of the available correlations are shown in Table 18.

Table 18. Unit Weight Calculated from Shear Wave Velocity

Equation	Reference	Note
$\gamma_t = 4.17 \cdot \ln(V_{s1}) - 4.03$ $V_{s1} = V_s / (\sigma_{atm}/\sigma'_{vo})^{0.25}$ γ_t (k/m3), V_s (m/s), and z (m).	Mayne (2007a)	The regression was performed with a total of 731 points and included a variety of soils such as peat, intact clays, fissured clays, silts, sands, gravels, and undisturbed sands.
$\gamma_t = 8.31 \cdot \log(V_s) - 1.61 \cdot \log(z)$ γ_t (k/m3), V_s (m/s), and z (m).	Mayne (2001, 2007b)	Equation for particulate geomaterials that are not cemented or bonded. The regression was performed using a database of 1,018 points, including various soil types.

Soil Parameters for Sands Based on V_s

The following correlations can be used to estimate soil parameters for sand-like materials.

Table 19. Friction Angle and Yield Stress of Sands from Shear Wave Velocity

Equation	Reference	Note
Effective friction angle: $\phi'(°) = 3.9 \cdot {V_{s1}}^{0.44}$	Uzielli et al. (2013)	Valid for $125\ m/s \leq V_{s1} \leq 225\ m/s$.
Preconsolidation stress (σ'_p) or yield stress (σ'_y): $\sigma'_p\ (kPa) = 101.3 \cdot \left(\frac{V_s}{158}\right)^{3.43}$	Mayne et al. (2023a)	V_s in m/s.

Soil Parameters for Clays Based on V_s

The following correlations can be used to estimate soil parameters for clay-like materials.

Table 20. Undrained Strength and Yield Stress of Clays from Shear Wave Velocity

Equation	Reference	Note
Undrained shear strength: $s_u\ (kPa) = 0.021 \cdot V_s^{1.52}$	L'Heureux & Long (2017)	Undrained shear strength for triaxial compression mode. V_s in m/s.
Preconsolidation stress (σ_p') or yield stress (σ_y'): $\sigma_p'(kPa) = 101.3 \cdot \left(\frac{V_s}{100}\right)^{1.50}$	Mayne et al. (1998), updated in Mayne et al. (2023a)	Applies only to intact clays. V_s in m/s.
$\sigma_p'(kPa) = 0.00769 \cdot V_s^{2.009}$	L'Heureux & Long (2017)	V_s in m/s.
$\sigma_p' = \left(\frac{G_o}{158 \cdot \sigma_{atm}}\right)^{0.8} \cdot \sigma_{atm}$	Mayne (2005)	$G_0 = G_{max}$ is the small-strain shear modulus, and is it calculated as a function of the shear wave velocity and unit weight. G_o, σ_{atm} in the same units.

CPT-BASED LIQUEFACTION TRIGGERING PROCEDURES

The CPT-based liquefaction triggering procedures involve evaluating the cyclic resistance ratio (CRR) at a given depth using CPTu data. The CRR profile is estimated based on the site-specific penetration resistance for a given CPTu. Most available methodologies linked cone penetration values to the performance of previous case histories. On the other hand, the cyclic stress ratio (CSR) represents the cyclic loading imposed on the soil during an earthquake, and it is estimated based on the design earthquake of the site. If the calculated CSR exceeds CRR, the soil may be susceptible to liquefaction under seismic conditions. In other words, the liquefaction factor of safety is defined as follows in Figure 94:

$$FS = \frac{CRR}{CSR}$$

Figure 94. Equation. Liquefaction factor of safety.

Two of the main CPT-based liquefaction triggering procedures are:

- Robertson and Wride (1988) procedure: Please refer to the most recent version of the *Guide to Cone Penetration Testing for Geotechnical Engineering* (Robertson & Cabal, 2022).
- Idriss and Boulanger procedure: Please refer to the most recent version of the report *CPT and SPT-based Liquefaction Triggering Procedures* (Boulanger & Idriss, 2014).

The main steps of a liquefaction-triggering procedure are the following:

1. Data Collection: Obtain CPTu data (q_c and f_s) by conducting cone penetration tests at the site of interest.

2. Calculation of Effective Stress Parameters: Including the total vertical overburden stress (σ_{v0}) and effective vertical stress (σ'_{v0}).

3. Calculation of Cyclic Stress Ratio (CSR): The CSR is typically defined as the ratio of cyclic shear stress to effective vertical stress ($CSR = \frac{\tau_{av}}{\sigma'_{v0}}$), where τ_{av} is the average cyclic shear stress. The CSR profile with depth can be calculated with a specific seismicity analysis. A simplified approach to estimate CSR was also developed by Seed and Idriss (1971), as shown in Figure 95:

$$CSR = \frac{\tau_{av}}{\sigma'_{vo}} = 0.65\left[\frac{a_{max}}{g}\right]\left(\frac{\sigma_{v0}}{\sigma'_{v0}}\right)r_d$$

Figure 95. Equation. Calculation of cyclic stress ratio.

Where a_{max} is the peak ground surface acceleration at the site; g is the acceleration due to gravity and r_d is a stress reduction factor, which is dependent on depth. Authors have proposed different formulations for the r_d factor; the formulation will depend on the selected procedure.

4. Compute the CRR using the calculated parameters from CPT: The formulation to calculate CRR depends on the selected methodology. The value of CRR calculated corresponds to a magnitude 7.5 earthquake, level ground conditions, and atmospheric pressure of 1 atm. If site conditions are different, corrections factors are included in the factor of safety calculations, as follows in Figure 96.

$$FS = \frac{CRR_{7.5,\sigma'_{v0}=1atm,level\ ground}}{CSR} \cdot MSF \cdot K_\sigma \cdot K_\alpha$$

Figure 96. Equation. Calculation of liquefaction factor of safety.

where MSF is the magnitude scaling factor which corrects for other different earthquakes, K_σ is the overburden stress correction factor, and K_α is the driving shear stress correction factor.

CPT-BASED GEOTECHNICAL DESIGNS

For foundation design, the CPT data can be used either (1) to assess individual values of soil engineering parameters for input into classical solutions for bearing capacity and settlements or (2) in direct CPT methods that can address shallow footings or piling foundations.

Shallow Foundations

Foundation systems aim to transmit structural loads into the ground, using safety and performance-based criteria for their design. Shallow foundations are placed at a depth less than the width of the foundation (Briaud, 2013). Shallow foundations are subdivided into spread footings (rectangular, circular, or strip footings if the length is considerably larger than the width) and mat foundations or rafts. The design process of a shallow foundation involves a two-step process: (1) safety considerations, where the foundation is designed to withstand the external loads without exceeding the bearing capacity of the soil that is reduced with an adequate factor of safety (FS), (2) performance considerations, which refers to the tolerable displacements of the structure during its operation over the life of the structure.

SCPTu soundings can be used in practice to support the design of shallow foundations in two primary ways (Saftner et al., 2018): (1) provide continuous profiles of relevant geotechnical parameters such as unit weight, friction angle, undrained strength, yield stress, and constrained modulus, using the procedures previously covered in the previous subsection; (2) direct methods, where the measurements taken with the piezocone are scaled up to provide design evaluation of shallow foundations directly. The subsequent subsections will cover the direct approaches to evaluating bearing capacity and shallow foundation settlements using the piezocone.

Bearing Capacity

The bearing capacity is the maximum stress that the foundation can resist (q_{ult}). There are multiple approaches to evaluating the bearing capacity of soils, including limit equilibrium, limit plasticity, cavity expansion theory, numerical modeling, and empirical-based estimations. The most widely used solution in practice is limit plasticity theory, which is based on calculating upper and lower limits for the bearing capacity (Azizi, 1999). The upper limit considers the balance of internal and external failure mechanics. In contrast, the lower limit is based on equilibrium and yield conditions. The limit plasticity solution uses total stress analysis; therefore, consider either fully drained or fully undrained conditions (Saftner et al., 2018). Based on this differentiation, the direct methods to calculate bearing capacity from SCPTu are divided into solutions for sand-like materials, which are assumed to be fully drained, and clay-like, which assume undrained conditions with no volume change.

Bearing Capacity of Sand-Like Materials

The bearing capacity for sand-like materials that behave fully drained and do not generate excess porewater pressures can be directly calculated from CPTu measurements, as shown in Table 21. As evident from the table information, a standard criterium to define the bearing capacity (q_{ult}) used in Europe is the loading associated with a ratio (s/B) of settlement (s) to the width of the footing (B) of 10% or 0.1. Of note, the methods summarized in Table 21 have been formulated considering axial or vertical loading.

Table 1. Direct Evaluation of Bearing Capacity from CPTu Test in Sands

Reference	Method*
(Eslaamizaad & Robertson, 1996; Robertson & Cabal, 2015)	The studies are based on tests on shallow foundations of different shapes (i.e., circular and square) on dense and loose to medium sands where CPT data were available. The authors proposed the following equation: $$q_{ult} = K_{\Phi} \cdot q_{c-AVE}$$ where q_{c-AVE} is the average tip resistance from the base of the distance to a depth of B. Robertson and Cabal (2015) recommend a $K_{\Phi} = 0.16$. Eslaamizaad and Robertson (1996) originally suggested that K_{Φ} ranges between 0.16 to 0.3, as shown in Figure 97.
(Lee & Salgado, 2005)	The study combines nonlinear finite element analysis and CPTu data to provide the q_{ult} for circular footings and various relative density and K_o conditions: $$q_{ult} = \beta \cdot q_{c-AVE}$$ where q_{c-AVE} from the depth of the footing until a distance equal to the diameter of the footing, B, and β is a correlation factor that depends on the characteristics of the sands in terms of D_R, and K_0. The study considers a D_R ranging from 30% to 90% and K_o values of 0.45, 0.7, and 1, with these considerations β ranges between 0.19 to 0.36. Table 22 summarizes the β values from the study.
(Mayne & Illingworth, 2010)	The study is based on 30 footing load tests on 12 different clean quartz to silica sand deposits and footings with different shapes (square, rectangular, and circular), with an equivalent B in the range of 0.5 to 6 m. The bearing capacity for an s/B ratio of 0.1 is: $$q_{ult} = 0.18 \cdot q_{c-mean}$$ where q_{c-mean} is the tip resistance averaged on a range of 1.5 B. The coefficient of determination of the regression is $r^2 = 0.976$.
(Lehane., 2012)	The study is based on 47 loading tests of footings with a typical width of 1 m and embedment (D) of 0.5 m. The ultimate capacity is associated with the load for a settlement (s) with a ratio (s/B) of 0.1: $$q_{ult} = 0.16 \cdot q_{c-AVE}$$ where q_{c-AVE} is the average tip resistance up to a depth of $[B(m)]^{0.7}$.

Note: * *B* is the footing width or diameter, *B(m)* indicates meter units, and *D* is the embedment.

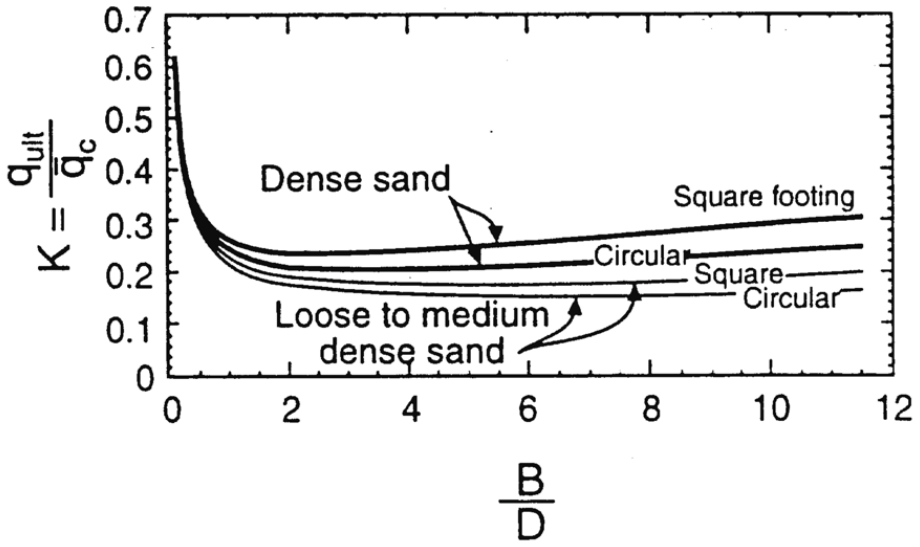

Figure 97. Bearing capacity factor for shallow foundations over sand-like materials.

Source: Robertson & Cabal (2015)

Table 22. Correlation Factor to Evaluate Bearing Capacity on Sand-Like Materials

Sand Relative Density	**Correlation Factor, $\beta = q_{ult}/q_c$(AVE)**		
Dr (%)	**K_0 = 0.45**	**K_0 = 0.7**	**K_0 = 1.00**
30	0.36	0.29	0.25
50	0.30	0.27	0.24
70; B = B_r	0.26	0.25	0.23
70; B > B_r	0.26(0.9+0.10B/ B_r)	0.25(0.92+0.08 B/ B_r)	0.23(0.94+0.07 B/ B_r)
90; B = B_r	0.22	0.21	0.19
90; B > B_r	0.22(0.85+0.15B/ B_r)	0.21(0.85+0.15 B/ B_r)	0.19(0.85+0.15 B/ B_r)

Note: * B_r is the reference footing diameter of the study equal to 1 m.

Adapted from Lee & Salgado (2005)

Bearing Capacity of Clay-Like Materials

Due to the low permeability of clay-like materials relative to the advancing standard rate of the CPT (20 mm/s), the behavior of these materials is generally considered to be fully undrained during penetration. Therefore, most direct methods using CPT focus on undrained responses. Table 23 summarizes the main methods to evaluate the bearing capacity of clay-like materials.

Table 23. Direct Evaluation of Bearing Capacity from CPTu Test in Clays

Reference	Method
(Schmertmann, 1978)	This study used the average q_c over a depth of 1.5B below the footing. The study used data from the mechanical cone and divided the equations into square and strip footings as follows: Square footing: $$q_{ult} = 2.75\ \sigma_{atm}\ \left(\frac{q_c}{\sigma_{atm}}\right)^{0.52}$$ Strip footing: $$q_{ult} = 1.05\ \sigma_{atm}\ \left(\frac{q_c}{\sigma_{atm}}\right)^{0.7}$$
(Tand et al., 1986)	The bearing capacity is calculated using the following equations, which were developed based on data acquired from mechanical and electric CPT: $$q_{ult} = R_k\ (q_c^* - \sigma_{vo}) + \sigma_{vo}$$ $$q_c^* = (q_{c1}\ q_{c2})^{0.5}$$ where q_{c1} is the geometric mean from the footing base up to a depth of 0.5B, and q_{c2} is the geometric mean on a depth range from 0.5B to 1B measured from the footing base, R_k is an empirical base-factor shown in Figure 98.
LCPC Method (Frank & Magnan, 1995)	The proposed equation to calculate the bearing capacity on clays is the following: $$q_{ult} = k_c\ q_c + \sigma_{vo}$$ $$k_c = 0.32\ \left[1 + 0.35\left(0.6 + 0.4\frac{B}{L}\right)\frac{D}{L}\right]$$
(Robertson & Cabal, 2015)	The ultimate bearing capacity for cohesive, fine-grained soils is: $$q_{ult} = K_{su}\ q_c + \gamma D$$ where q_c is the tip resistance average on a depth of B measured from the base of the footing and K_{su} depends on the ratio B/D and ranges from 0.3 to 0.6, with a value of 0.3 generally assumed on clay materials.
(Saftner et al., 2018)	The study combines limit bearing capacity solutions for undrained case ($q_{ult} = N_c\ s_u$), with piezocone-based solutions for the undrained strength to provide direct expressions for the bearing capacity on strip or square/circular footings: $$Strip\ footings: \quad q_{ult} = 0.373(q_t - \sigma_{vo})$$ $$Square/circular: \quad q_{ult} = 0.445(q_t - \sigma_{vo})$$

Note* *B* is the footing width or diameter, *D* is the embedment, and *L* is the footing length.

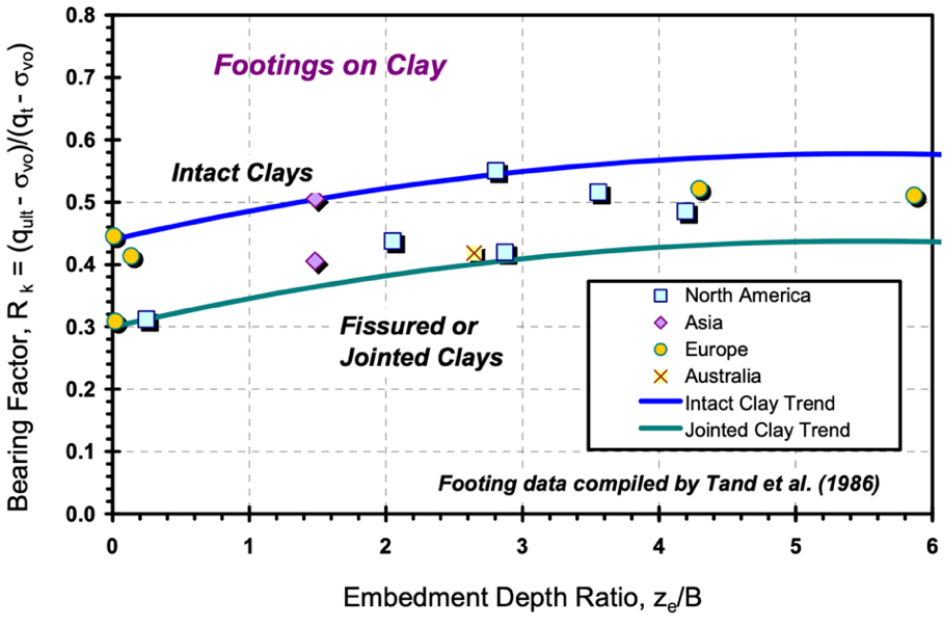

Figure 98. Bearing factor for shallow foundations in clay according to Tand et al. (1986).

Source: Saftner et al. (2018)

Direct Methods for Stress-Displacement Curves

Loading tests of shallow foundations have shown that the load-displacement curve is not linear, showing different responses depending on the soil type. Nonlinear solutions based on approximate elastic solutions have been proposed to evaluate the stress-displacement response of shallow footings, shown in Figure 99 (Fowler et al., 2001; Mayne, 2020; Mayne & Poulos, 1999):

$$s = \frac{q\ d_e\ I_{GH}\ I_F\ I_E(1-\nu^2)}{E_0\ [1-(p_{footing}/\ p_{ult})^{0.3}]}$$

Figure 99. Equation. A nonlinear load-displacement-capacity response.

Where q is the applied stress, s is the center point displacement, d_e the equivalent foundation diameter, ν the Poisson's ratio—which can be assumed as 0.2 for drained conditions and 0.5 for undrained conditions, E_0 the small strain elastic modulus, $p_{footing}$ the applied footing stress, p_{ult} the bearing capacity, and I_{GH}, I_F, I_E are the foundation elasticity factors that depend on the footing characteristics (i.e., I_{GH} displacement influence factor, I_F rigidity correction factor, and I_E embedment correction factor) (Mayne, 2007b, 2019). The foundation influence factors I_{GH}, I_F, and I_E are obtained from elasticity solutions (Mayne 2007b, 2019). For the simple case of a flexible footing on homogeneous ground with no embedment: $I_{GH} = I_F = I_E = 1$.

An additional approach to evaluate the stress displacement has been based on an extensive database of full-scale load tests performed on footings of different characteristics (Dagger et al., 2018; Mayne, 2020; Mayne & Woeller, 2014). Figure 102 shows the variety of soil types included and the stress-

normalized displacement behavior of the foundations. This method is a generalized and direct approach because it uses a single equation for all soil types and only requires piezocone data as an input. In this method, the footing pressure is normalized by the net cone resistance ($p_{footing}/q_{net}$) and is directly proportional to the square root of the ratio of displacement to the footing width (s/B), as shown in Figure 100:

$$\frac{p_{footing}}{q_{net}} = h_s \left(\frac{s}{B}\right)^{0.5}$$

$$p_{footing} = h_s \, q_{net} \left(\frac{s}{B}\right)^{0.5} \leq p_{ult}$$

Figure 100. Equations. Unified direct CPT method for shallow foundations.

The proportionality constant that relates the normalized stress-displacement quantities is an empirical soil formation factor, h_s, which can be computed from the CPT material index (I_c), presented in Figure 101.

$$h_s = 2.8 - \frac{2.3}{1 + (I_c/2.4)^{15}}$$

Figure 101. Equation. Trend between soil formation factor (h_s) and CPT material index (I_c).

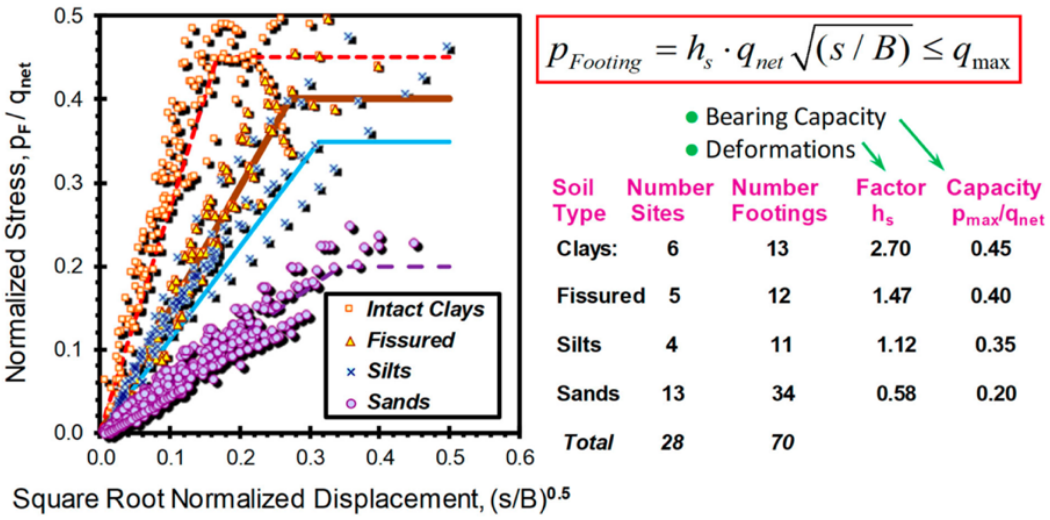

Soil Type	Number Sites	Number Footings	Factor h_s	Capacity p_{max}/q_{net}
Clays:	6	13	2.70	0.45
Fissured	5	12	1.47	0.40
Silts	4	11	1.12	0.35
Sands	13	34	0.58	0.20
Total	*28*	*70*		

Figure 102. CPT direct method to evaluate load-displacement-capacity curves of shallow foundations for all soil types.

Source: Mayne (2020)

As discussed previously, some design guidelines define the ultimate capacity of the shallow foundation as the load associated with an (s/B) ratio of 10% (e.g., Lehane, 2019). This criterion can

be used in the equation of the direct method to evaluate the bearing capacity depending on the soil type.

Of important note, for footings on clays that exhibit undrained behavior (generally found when $I_{c\text{-}RW} > 2.6$), this method provides only the magnitude of displacement due to the undrained distortion (often called "immediate settlement"), and the additional displacements generated by drained primary consolidation and creep settlements must be considered separately (Mayne, 2020). Drained settlements due to primary consolidation can be handled using a value of constrained modulus (D'), as detailed by Schmertmann (1986).

Deep Foundations

For vertical loading, the design of deep foundations (i.e., driven, vibrated, auger, bored piles, among others) involves the evaluation of (1) the foundation capacity and (2) the displacement. The design of deep foundations is significantly impacted by the construction method (i.e., prefabricated or cast-in-place) since the soil-structure interaction during construction will influence the capacity of the foundation system.

Several efforts have highlighted the usefulness of the SCPTu in deep foundation design (e.g., Niazi & Mayne, 2013). Similarly to the use of the piezocone on shallow foundations, for deep foundations, the use of SCPTu in practice is also divided into two main approaches: (1) the evaluation of geotechnical parameters (i.e., variables covered in previous sections, such as drained friction angle, undrained strength, and K_0) used as input in common analytical frameworks implemented in practice such as limit equilibrium and plasticity solutions; (2) direct methods to evaluate pile capacity from piezocone measurements. The subsequent subsection will focus on direct methods that use piezocone readings directly to design deep foundations. With the SCPTu, the fundamental shear modulus (G_0) and its Young's modulus companion (E_0) are obtained from the V_s profile, thus providing a direct measure of the ground stiffness along the sides and beneath the base of the pile foundation.

Axial Pile Capacity

The static axial capacity of a single pile (Q_t) is the sum of the shaft capacity or side component (Q_s) and the base capacity or end-bearing component (Q_b), as shown in Figure 103. Refer to Figure 104:

$$Q_t = Q_s + Q_b = \sum (f_{p_i} \cdot A_{s_i}) + q_b \cdot A_b$$

Figure 103. Equation. Static axial capacity of a single pile.

where f_{p_i} and A_{s_i} are the unit shaft resistance and shaft area of the soil element *i*, respectively, q_b and A_b are the unit end-bearing resistance and the area of the pile base.

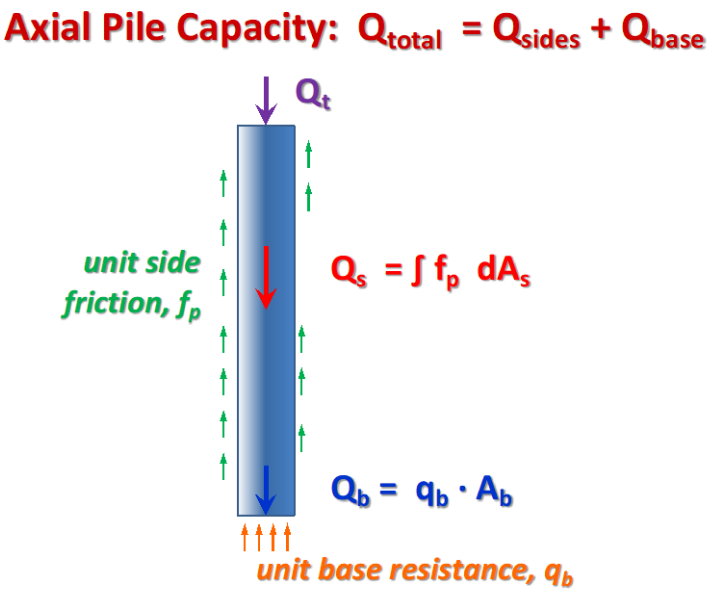

Figure 104. Scheme of the axial capacity of a single pile.

Source: Dagger et al. (2018)

Previous research has pointed out that the penetrometer can be viewed as a reduced-scale pile and that the soil properties and mechanisms that act on a pile foundation apply similarly to a piezocone (Ardalan et al., 2009; Eslami & Fellenius, 1997; Mayne, 2007b). This observation has led to multiple direct methods to evaluate axial capacity from piezocone measurements by scaling up the CPTu measurements to evaluate pile capacity. The early methods were developed using the mechanical cone and, therefore, used mainly the tip resistance (q_c), with the subsequent development of the electronic piezocone and the incorporation of sensors to measure the sleeve friction (f_s) and pore water pressure (u_2), the corrected tip resistance (q_t) was used, leading to a more reliable estimate for axial pile capacity predictions. Previous work has summarized and evaluated the performance of different direct methods to evaluate axial capacity (e.g., Mayne, 2020; Saftner et al., 2018; Niazi & Mayne, 2013; Lehane 2019; Sakleshpur et al., 2021; Schneider et al., 2008b). Some selected primary methods are summarized in Table 24.

Table 24. Direct CPT Methods for the Evaluation of Axial Pile Capacity

Reference	Method
Unicone Method (Eslami & Fellenius, 1997; Fellenius, 2009)	The method applies to all soil and pile types. Moreover, it uses the three continuous readings from the electronic piezocone. The unit side friction is calculated as follows: $$f_p = C_{se} \cdot q_E$$ $$q_E = q_t - u_2$$ where C_{se} is a correlation coefficient that depends on soil types, as shown in Figure 105. The base capacity is calculated using the following equation: $$q_b = C_{te} \cdot q_{Eg}$$ where C_{te} is the toe correlation coefficient, and it takes a value of 1, except for pile diameters (d) larger than 0.4 m, in this case $C_{te} = 1/(3d)$. q_{Eg} is the geometric mean of q_E on the influence zone for the pile base. The influence zone of the Unicone method goes from $4 \cdot d$ below the pile tip to $8 \cdot d$ above if the pile is installed from the weak soil into a dense soil, and from $4 \cdot d$ below the pile tip to $2 \cdot d$ above if the pile is installed from a dense soil into a weak soil.
University of Western Australia UWA-05 (Lehane et al., 2005)	This method applies to driven piles on sand-like materials. The unit side friction is calculated as follows: $$f_p = (f_t/f_c)\left[0.03 \cdot q_c \cdot A_{rs,eff}^{0.3} \cdot \left(\max\left(\frac{h}{d}, 2\right)^{-0.5}\right) + \Delta\sigma_{rd}^{'}\right] \cdot \tan\delta_{cv}$$ $$(f_t/f_c) = 1 \; for \; compression, and \; 0.75 \; for \; tension$$ $$A_{rs,eff} = 1 - IFR\left(\frac{d_i}{d}\right)^2$$ where δ_{cv} is the interface friction angle, *IFR* is the incremental filling ratio, which is related to soil displacement on the pile tip and can be calculated as $IFR = \frac{\Delta L_p}{\Delta z}$ if it is not measured. The average $IFR = \min\left[1, \left(\frac{d_i(m)}{1.5}\right)^{0.2}\right]$, $d_i(m)$ is the inner pile diameter in meters, and $\Delta\sigma_{rd}'$ is the change in radial stress during pile loading, calculated as follows: $$\Delta\sigma_{rd}' = \frac{2 \cdot G \cdot \Delta y}{r^*}$$ $\Delta y \approx 2R_a \approx 0.02 \; mm$ is the radial displacement during pile loading. G is the operational shear modulus, which is calculated as follows: $$G \approx 185 \; q_c \; q_{c1N}^{-0.7}$$ $$q_{c1N} = \frac{(q_c \backslash \sigma_{atm})}{(\sigma_{vo}' \backslash \sigma_{atm})^{0.5}}$$ r^* is the modified radius of open-ended (OE) piles calculated as follows: $$r^* = (r^2 - r_i^2)^{0.5}$$

Reference	Method
	where r and r_i are the external and internal pile radii, respectively. The base capacity is calculated as follows: $$q_{b0.1} = q_{c,average} \cdot (0.15 + 0.45 \cdot A_{rb,eff})$$ $$A_{rb,eff} = 1 - FFR\left(\frac{d_i}{d}\right)^2$$ where $q_{c,average} = (q_{c1} + q_{c2})/2$, q_{c1} is the minimum average calculated from the pile base to a distance on the range of 0.7d to 3.75d below the pile, and q_{c2} is the average over the pile base up to a distance of 8d (Begemann, 1963). FFR is the final filling ratio, calculated as the average of IFR over the last 3d of the pile penetration. The factors IRF and FFR are measures of the effective shaft and base area, respectively. These factors are especially relevant to the behavior of OE-driven piles.
Imperial College Procedure (ICP-05) (Jardine et al., 2005)	This method applies to driven piles and uses different equations to evaluate the axial capacity of sands and clays. Only a direct approach for the base capacity is provided. The equations to evaluate unit side friction on sand-like materials depend on additional parameters such as the interface friction angle (δ_f'), which can be correlated with mean grain size (D_{50}): $$f_p = a(\sigma_{rc}' + \Delta\sigma_{rd}')\tan(\delta_f')$$ $$\sigma_{rc}' = 0.029b\, q_c \left(\frac{\sigma_{vo}'}{\sigma_{atm}}\right)^{0.13}\left[\max\left(\frac{h}{r^*}, 8\right)\right]^{-0.38}$$ $$\Delta\sigma_{rd}' = \frac{2 \cdot G \cdot \Delta y}{r^*}$$ $\Delta y \approx 2R_a \approx 0.02\ mm$ is the radial displacement during pile loading. $$a = 0.9\ for\ open-end\ piles\ in\ tension, 1\ for\ other\ cases$$ $$b = 0.8\ for\ tension, 1.0\ compression$$ G is the operational level of shear modulus, which is calculated as follows: $$G = 185\, q_c\, q_{c1N}^{-0.7}$$ $$q_{c1N} = \frac{(q_c \backslash \sigma_{atm})}{(\sigma_{vo}' \backslash \sigma_{atm})^{0.5}}$$ The base capacity on sand-like materials is calculated as follows: **Sand-like materials** For close-ended piles (d/d_{CPT} is the relative pile to CPT cone diameter): $$q_b = q_{c,average} \cdot \max\left[1 - 0.5 \cdot \log\left(\frac{d}{d_{CPT}}\right), 0.3\right]$$

Reference	Method
	where $q_{c,average}$ is the average of q_c on the influence zone of $\pm 1.5 \cdot d$ measured from the pile tip. For open-ended piles: The pile is unplugged if $d_i \geq 2.0\ (D_r - 0.3)$, $(D_r = 0.4 \ln\left(\frac{q_{c1N}}{22}\right)$, is the nominal relative density) or $d_i \geq 0.083 \cdot \frac{q_{c,average}}{\sigma_{atm}} \cdot d_{CPT}$: $$q_b = q_{c,average} \cdot A_r$$ Otherwise, the pile is plugged, and the base capacity is calculated as follows: $$q_b = q_{c,average} \cdot \max[0.5 - 0.25 \log(d/d_{CPT})\,; 0.15 \cdot A_r]$$ $$A_r = 1 - \left(\frac{d_i}{d}\right)^2$$ d_i, d: inner and outer pile diameters. **Clay like materials** For close-ended piles: $$q_b = 0.8 \cdot q_{c,average}; for\ undrained\ loading$$ $$q_b = 1.3 \cdot q_{c,average}; for\ drained\ loading$$ For open-ended, plugged piles: $$q_b = 0.4 \cdot q_{c,average}; for\ undrained\ loading$$ $$q_b = 0.65 \cdot q_{c,average}; for\ drained\ loading$$
Fugro-05 (Kolk et al., 2005)	The method applies to driven piles on silica sands; it gives both the base capacity and the side friction. For the unit side friction, the method differentiates between compression and tension loading as follows: **Compression loading** The applicable equation depends on the ratio of the height above the pile (h) and the equivalent pile radius $R^* = (R^2 - R_i^2)^{0.5}$; where R_i is the internal pile radius, and R the external radius. For non-circular piles R^* is assessed using the equivalent circular area. For $h/R^* \geq 4$: $$f_p = 0.08 \cdot q_c \cdot \left(\frac{\sigma_{vo}^{'}}{\sigma_{atm}}\right)^{0.05} \cdot \left(\frac{h}{R^*}\right)^{-0.9}$$ For $h/R^* \leq 4$: $$f_p = 0.08 \cdot q_c \cdot \left(\frac{\sigma_{vo}^{'}}{\sigma_{atm}}\right)^{0.05} \cdot (4)^{-0.9} \cdot \left(\frac{h}{4R^*}\right)$$

Reference	Method
	Tension loading $$f_p = 0.045 \cdot q_c \cdot \left(\frac{\sigma_{vo}^{'}}{\sigma_{atm}}\right)^{0.15} \cdot \left(\max\left(\frac{h}{R^*}\,;4\right)^{-0.85}\right)$$ The base capacity at a tip displacement of 10% of the pile diameter is calculated as follows: $$q_{b0.1} = 8.5 \cdot q_{c,average} \cdot \left(\frac{\sigma_{atm}}{q_{c,average}}\right)^{0.5} \cdot A_r^{0.25}$$ $$A_r = 1 - \left(\frac{R_i}{R}\right)^2$$ $q_{c,average}$ is the average of q_c on the interval of $\pm 1.5\ d$ over the tip level.
Norwegian Geotechnical Institute NGI-05 (Clausen et al., 2005)	This method applies to driven piles on sand-like materials. The unit side friction is calculated using the following equation: $$f_p = (z/L) \cdot \sigma_{atm} \cdot F_{D_r} \cdot F_{sig} \cdot F_{tip} \cdot F_{load} \cdot F_{mat} \geq f_{min} = 0.1 \cdot \sigma_{vo}'$$ where *z* is the depth on the profile, *L* is the length of the pile, and the additional factors depend on the soil and pile characteristics and are defined as follows: $$F_{D_r} = 2.1(D_r - 0.1)^{1.7}$$ where $D_r = 0.4 \ln\left(\frac{q_{c1N}}{22}\right)$ is the nominal relative density, which may have values greater than 1.0, and $q_{c1N} = \frac{(q_c \backslash \sigma_{atm})}{(\sigma_{vo}' \backslash \sigma_{atm})^{0.5}}$ $$F_{sig} = \left(\frac{\sigma_{vo}^{'}}{\sigma_{atm}}\right)^{0.25}$$ $$F_{tip} = 1\ for\ open-ended\ piles\ and\ 1.6\ for\ close-ended\ piles$$ $$F_{load} = 1.0\ for\ tension, and\ 1.3\ for\ compression$$ $$F_{mat} = 1.0\ for\ steel\ and\ 1.2\ for\ concrete\ piles$$ The equation to calculate the base capacity depends on whether the pile is close-ended or open-ended. For close-ended piles: $$q_b = q_{c,tip} \cdot \left[\frac{0.8}{(1 + D_r^2)}\right]$$ For open-ended piles (d_i is inner pile diameter): $$q_b = \min\left[q_{b01(plugged)};\ q_{b01(unplugged)}\right]$$ $$q_{b01(plugged)} = q_{c,tip} \cdot \left[\frac{0.7}{(1 + 3D_r^2)}\right]$$ $$q_{b01(unplugged)} = q_{c,tip} \cdot A_r + 12 \cdot f_{p,average} \cdot L/d_i$$

Reference	Method
	where $f_{p,average}$ is the unit friction averaged over the pile embedment depth (*L*).
HKU Method (Yu & Yang, 2012)	This method applies only to sand-like materials and provides only an estimate of the base capacity of open-ended steel pipe piles: $$Q_b = (\pi/4)\left[d^2 \cdot q_{plug} + \left(d^2 - d_i^2\right) \cdot q_{ann}\right]$$ $$q_{plug} = 1.063 \exp(-1.933PLR) \cdot q_{ca}$$ $$PLR = H/L$$ where *L* is the length of the pile, *H* is the height of the plug, *d* is the outer diameter of the pile, and d_i is the inner diameter. $$q_{ann} = 1.063 - 0.045(L/d)$$ $$q_{ca} = 0.5\ (M_A + M_B)\ ; if\ M_a \leq M_B, otherwise\ , q_{ca} = M_B$$ $$q_{ann} \geq 0.46 \cdot q_{ca}$$ where M_A and M_B are the geometric average of q_c on the depth range defined by zones A and B, which are shown in Figure 106.
Enhanced Unicone (Niazi & Mayne, 2015, 2016)	This method uses the three continuous SCPTu readings and is based on a database of 330 load tests performed on all soil types. This method uses the CPT material index (I_c), and the soil classification chart from Robertson (2009) to obtain the pile unit side friction as follows: $$f_p = q_E \cdot \theta_{PT} \cdot \theta_{TC} \cdot \theta_{RATE} \cdot 10^{(0.732 \cdot I_c - 3.605)}$$ where $q_E = q_t - u_2$ is the effective cone resistance, θ_{PT} is a coefficient that depends on the pile type, θ_{TC} is the coefficient for loading direction, θ_{RATE} is a rate coefficient. The coefficient values are shown in Figure 107. $$q_b = q_E \cdot 10^{(0.325 \cdot I_c - 1.218)}$$
Unified CPT-Based axial pile capacity design method (Lehane et al., 2022a; Lehane et al., 2020; Lehane et al., 2022b)	This method aims to unify the most common direct CPT methods, which are an alternative to the API (American Petroleum Institute) design methods (API, 2011). The methods provide solutions for sand and clay-like materials. **Sand-like materials** The formulation applies to siliceous sands and circular-driven piles. Moreover, the method considers essential features that affect axial pile capacity, such as the level of soil displacement, soil-pile interphase angle, and method to average q_c to evaluate base capacity, among others. The pile unit side friction is calculated as follows: $$f_p = (f_t/f_c) \cdot (\sigma'_{rc} + \Delta\sigma'_{rd}) \cdot \tan 29°$$ $$(f_t/f_c) = 1\ in\ compression\ and\ 0.75\ in\ tension$$ $$\sigma'_{rc} = \left(\frac{q_c}{44}\right) \cdot A_{re}^{0.3} \cdot \left[\max\left(1; \left(\frac{h}{d}\right)\right)\right]^{-0.4}$$

Reference	Method
	$$\Delta\sigma_{rd}^{'} = \left(\frac{q_c}{10}\right)\left(\frac{q_c}{\sigma_v^{'}}\right)^{-0.33}\left(\frac{d_{CPT}}{d}\right)$$ $$A_{re} = 1 - PRL\left(\frac{d_i}{d}\right)^2$$ where A_{re} is the effective area ratio $A_{re} = 1$ for close-ended pile, *h* is the distance from the pile tip to the surface , d is the outer pile diameter, d_i is the internal pile diameter, d_{CPT} is the diameter of the CPT probe, PRL is the plug length ratio, which quantifies the degree of soil displacement during pile installation $PRL \approx \tanh\left[0.3 \cdot \left(\frac{d_i}{d_{cpt}}\right)^{0.5}\right]$. Finally, the shaft capacity of the pile would be: $$Q_s = \pi \cdot d \cdot \int_0^L f_p \cdot dz$$ The unit base capacity at a base displacement of 10% of the pile diameter is calculated as follows: $$q_{b0.1} = [0.12 + 0.38 \cdot A_{re}] \cdot q_p$$ where q_p can be calculated as the average q_c at a zone of $\pm 1.5 \cdot d$ centered on the pile tip. The base capacity would be: $$Q_b = q_{b0.1} \cdot \left(\frac{\pi \cdot d^2}{4}\right)$$ **Clay-like materials** The unit side friction for soils in zones 1, 2, 4 and 4 of the SBT chart (see Figure 30 for the SBT chart) is calculated as follows: $$f_p = 0.07 \cdot F_{st} \cdot q_t \cdot \left(\max\left[1, \frac{h}{D^*}\right]\right)^{-0.25}$$ $$D^* = (d^2 - d_i^2)^{0.5}$$ where F_{st} is 1 for calys with $I_{z1} = Q_{tn} - 12 \cdot \exp(-1.4 \cdot F_r) > 0$, and $F_{st} = 0.5 \pm 0.2$ for $I_{z1} < 0$. I_{z1} is the material index in zone 1 on the SBT chart. The unit base capacity is calculated as follows: $$q_{b0.1} = [0.2 + 0.6 \cdot A_{re}] \cdot q_p$$ $$A_{re} = 1 - PRL\left(\frac{d_i}{d}\right)^2$$ where q_p is the average q_t in the influence zone of $1d$ below the pile tip.

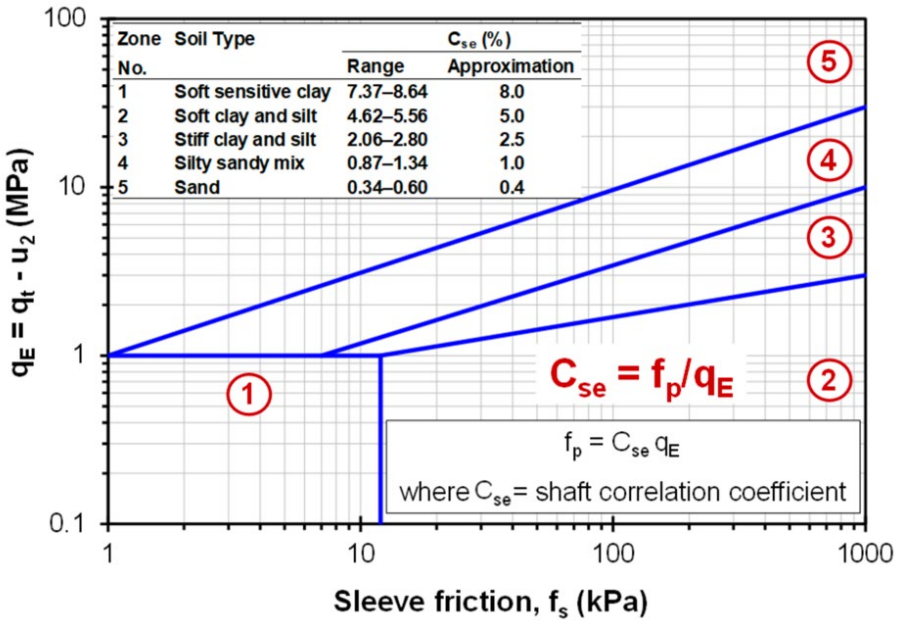

Figure 105. Pile side resistance C_{se} factor from Unicone method from Eslami and Fellenius (1997).

Source: Saftner et al. (2018)

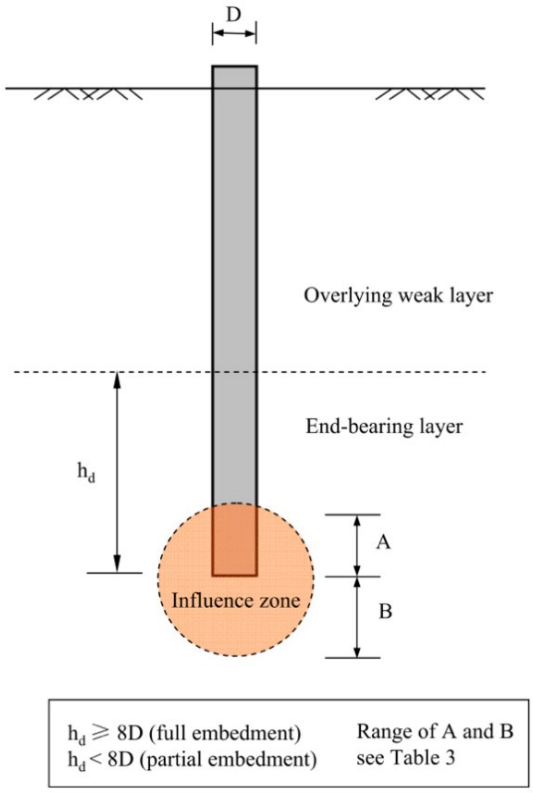

Figure 106. Definition of influence zone for base capacity.

Source: Yu & Yang (2012)

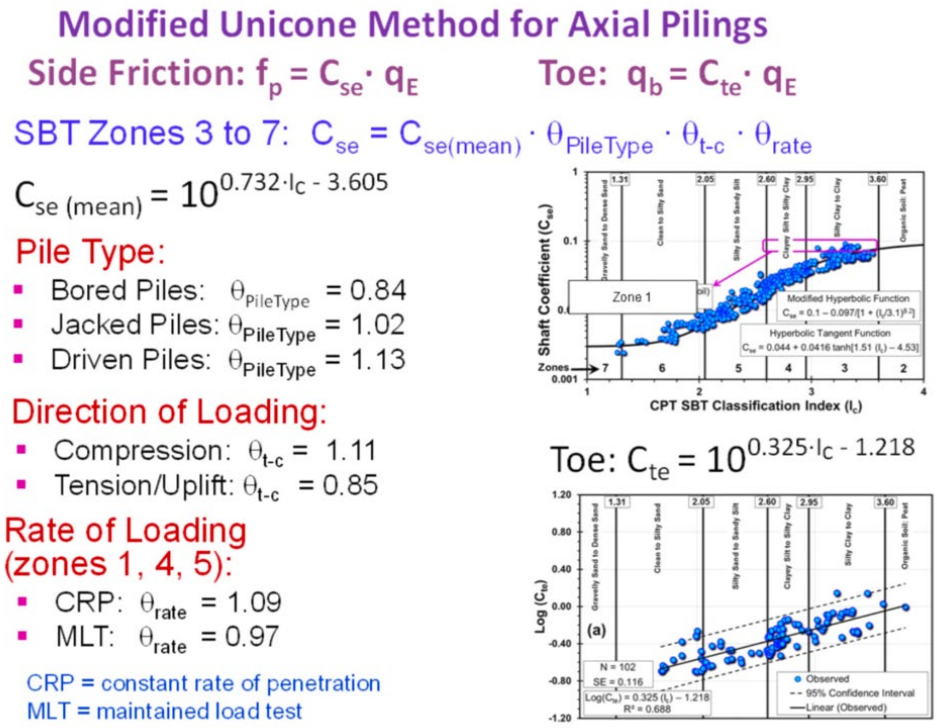

Figure 107. Factors of the Enhanced Unicone method for axial pile capacity.

Source: Saftner et al. (2018)

Displacement

The pile displacement (w_t) due to the axial loading is evaluated using elastic continuum theory (Poulos & Davis, 1980; Randolph, 2003). For a rigid pile the displacements are calculated using the following equation in Figure 108:

$$w_t = \frac{P_t \cdot I_\rho}{d \cdot E_{sL}}$$

$$I_\rho = \frac{1}{\frac{F_{CT}}{1-\nu^2} + \frac{\pi}{1+\nu} \cdot \frac{\rho_E \cdot \left(\frac{L}{d}\right)}{ln\left[5 \cdot \rho_E \cdot \left(\frac{L}{d}\right)(1-\nu)\right]}}$$

Figure 108. Equations. Elastic solution for load-displacement response of a rigid pile.

where P_t is the axial load, d the pile diameter, E_{sL} the elastic soil modulus at the base of the pile, I_ρ the displacement influence factor, F_{CT} a load direction factor that is equal to 1 for compression and 0 for tension, $\rho_E = E_{sM}/E_{sL}$ is the Gibson parameter, where E_{sM} is the elastic soil modulus at the mid-length of the pile. Figure 109 shows a scheme of the solution to calculate the load-displacement behavior of rigid piles.

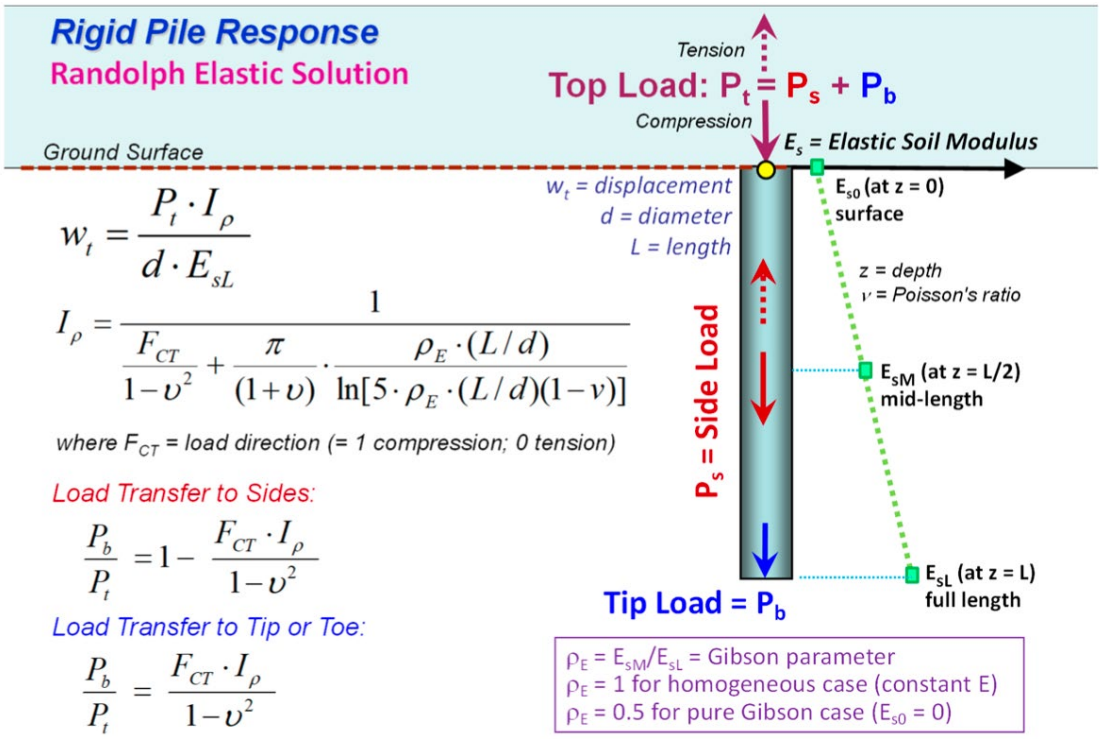

Figure 109. Elastic solution for load-displacement response of a rigid pile.

Source: Mayne, Dasenbrock, & Budge (2023)

Moreover, there are elastic solutions for a compressible pile subject to axial loading (Randolph & Wroth, 1978, 1979). The displacement at the top of a pile is given by the following equation in Figure 110:

$$w_t = \frac{P_t \cdot I_\rho}{d \cdot E_{sL}}$$

Figure 110. Equation. Elastic solution for load-displacement response of a compressible pile.

where P_t is the axial load, d the pile diameter, E_{sL} the elastic soil modulus at the base of the pile, and I_ρ the displacement influence factor, calculated as follows in Figure 111:

$$I_\rho = \frac{x_1}{x_3}$$

$$x_1 = 4 \cdot (1+\nu) \cdot \left[1 + \frac{1}{\pi\lambda} \cdot \frac{8}{1-\nu} \cdot \frac{\eta}{\xi} \cdot \frac{tanh(\mu L)}{\mu L} \cdot \frac{L}{d}\right]$$

$$x_3 = \frac{4}{(1-\nu)} \cdot \frac{\eta}{\xi} + \frac{1\pi\rho_E}{\zeta} \cdot \frac{tanh(\mu L)}{\mu L} \cdot \frac{L}{d}$$

$$\lambda = 2 \cdot (1 + \nu) \cdot \frac{E_p}{E_{sL}}$$

$$\zeta = ln\left\{[0.25 + (2.5 \cdot \rho_E \cdot (1 - \nu) - 0.25) \cdot \xi] \cdot \frac{(2 \cdot L)}{d}\right\}$$

$$\mu L = 2 \cdot \left(\frac{2}{\zeta \cdot \lambda}\right)^{0.5} \cdot \left(\frac{L}{d}\right)$$

Figure 111. Equations. Displacement influence factor for load-displacement response of a compressible pile.

where $\eta = d_{base}/d$ represents the ratio of the diameter of the pile at the base to that of the pile sides, $\xi = E_{sL}/E_b$ is the ratio of the modulus along the pile sides at a depth corresponding to the base of the pile (E_{sL} at depth z = L) and the modulus of the soil below the pile tip or toe (E_b). A schematic outline of the approach to calculate displacements for compressible piles is shown in Figure 112.

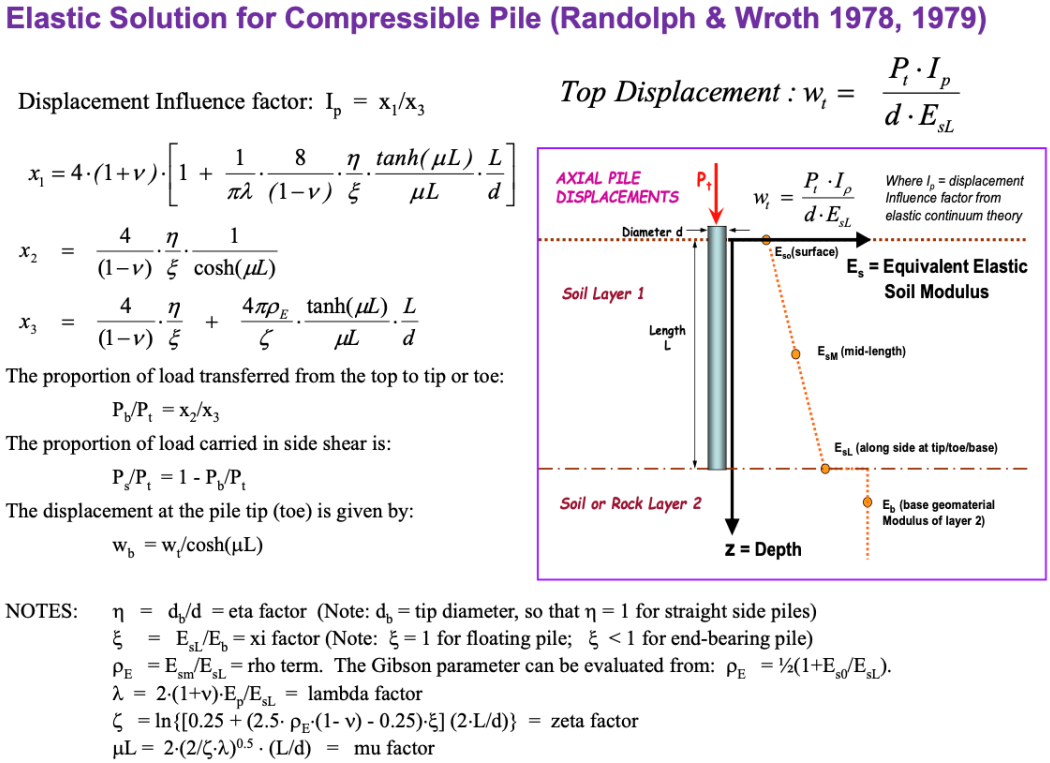

Figure 112. Elastic solution for axial load-displacement and load-transfer response of a compressible pile.

Source: Adapted from Mayne, Dasenbrock, & Budge (2023)

CHAPTER 4: PROCESSING OF GENERATED CPT DATA

The processing of the generated CPTu/SCPTu data is discussed in this chapter. First, the main characteristics of the CPTu/SCPTu data collected per district are presented. Then, one site is selected for each district to illustrate the variation of CPT/SCPTu variables, including the range of q_t, f_s, Q_{tn}, F_r, and I_c, the variation of q_t, f_s, u_2, B_q, and I_c versus depth, and the general stratigraphy at the selected sites relying on the CPT/SCPTu data. In general, the processing follows the procedures discussed in Chapter 3. The detailed processing of the data generated in this project is included in Appendix A. Chapter 6 provides in-depth discussions on the processing considering selected sites. The processing of CPT/SCPTu data is discussed next.

DISTRICT 1

Figure 113 shows District 1 and the three sites with available CPT/SCPTu data. Figure 114 shows the main characteristics of the collected data through q_t, f_s, Q_{tn}, F_r, and I_c histograms. In particular, the I_c plot shows the predominance of fine-grained soils with undrained behavior (I_c > 2.6). In addition, q_t and f_s are generally lower than 5 MPa and 100 kPa (725.2 and 14.5 psi). Site 1 in Figure 113 is selected for illustrating additional CPT/SCPTu details. Please refer to Appendix A for the processing of all CPTu/SCPTu data.

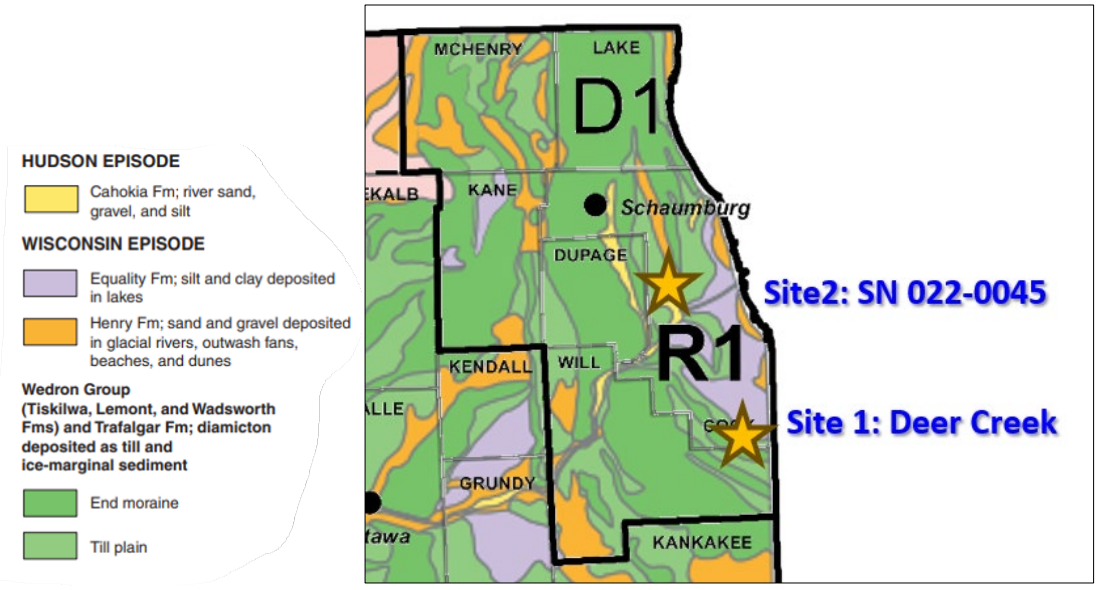

Figure 113. Map of the site locations and CPT data collected in District 1.

Source: Georgia Tech

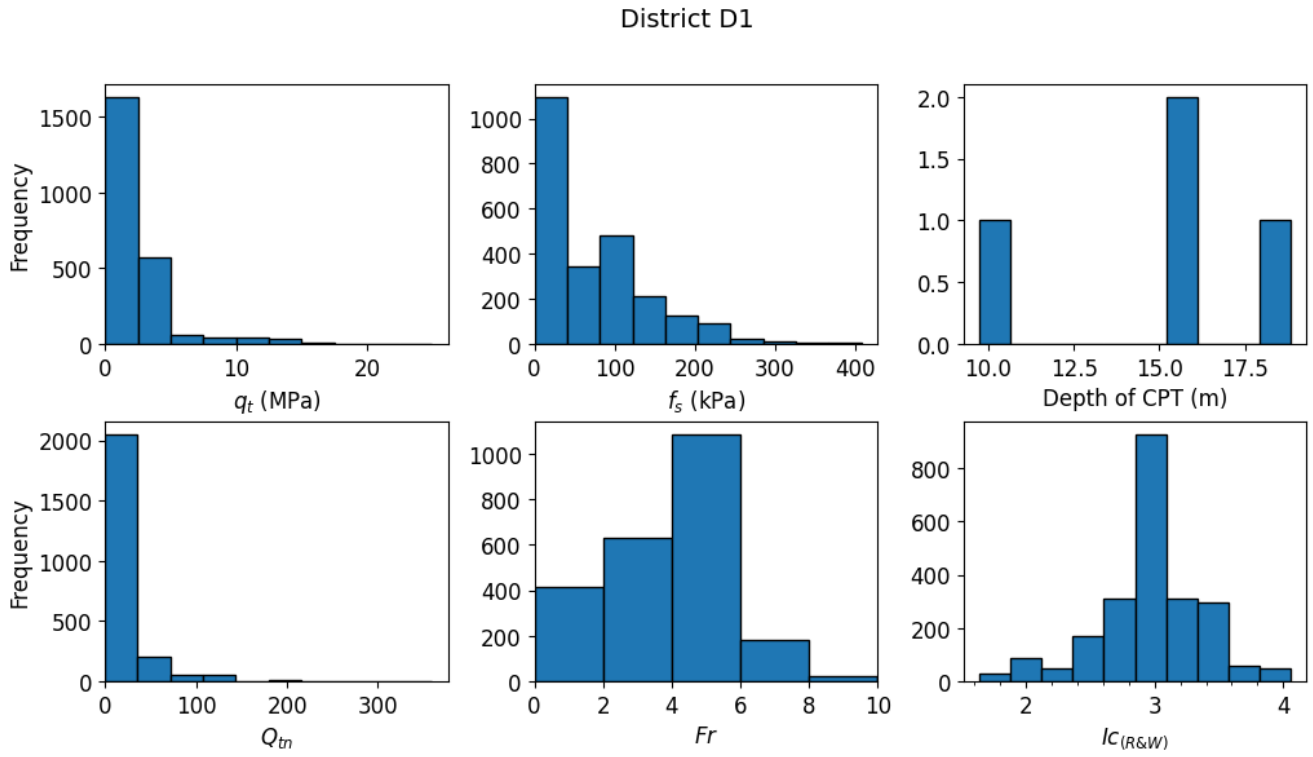

Figure 114. Characteristics of CPT data collected in District 1.

District 1: Site 1 (Deer Creek)

Site 1 is located at Deer Creek, where the quaternary soils are part of the Wisconsin glacial episode and are deposited as a till plain in the moraine region and silts and clays in lakes. Figure 115 shows the locations of the three available CPTs, while Figure 116 shows variations of q_t, f_s, u_2, B_q, and I_c versus depth. Figure 117 shows the soil stratigraphy based on the SBT charts of Robertson (2009). The predominantly clayey and silty layers through the profile show values of q_t, f_s, u_2, and B_q in the range of 0–5 MPa (0-725 psi), 50–400 kPa (7.2-58 psi), 0–400 kPa (0-58 psi), and 0–0.6, respectively. The fewer interbedded sand mixture layers show q_t, f_s, u_2, and B_q values in the range of 5–15 MPa (725–2175 psi), 100–200 kPa (14.4–29 psi), 0–50 kPa (0–7.2 psi), and 0–0.25. The I_{c-RW} profile shows the predominance of fine-grained soils with undrained behavior (I_c > 2.6). In general, the stratigraphy from the different CPTs is consistent, corresponding to clay/silt layers with interbedded sand mixture layers. Below 10 m (32.8 ft) (D1-Site1-1 and D1-Site1-3) and 6 m (19.7 ft) (D1-Site1-2), the clay units seem to be lightly over-consolidated (YSR of about 2), with a friction angle of about 28° and an undrained shear strength of 100 kPa (14.4 psi) (See Appendix A). On the other hand, for shallower depths, the YSR is about 1, the estimated friction angle is about 18°, and the undrained shear strength is 20 kPa (2.9 psi) (see Appendix A).

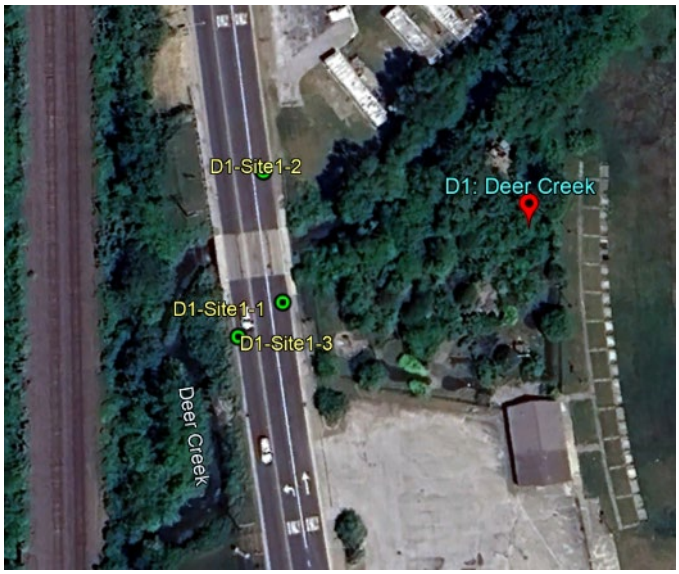

Figure 115. A photo of location of sites with SCPT/CPTu data—District 1.

Source: Georgia Tech

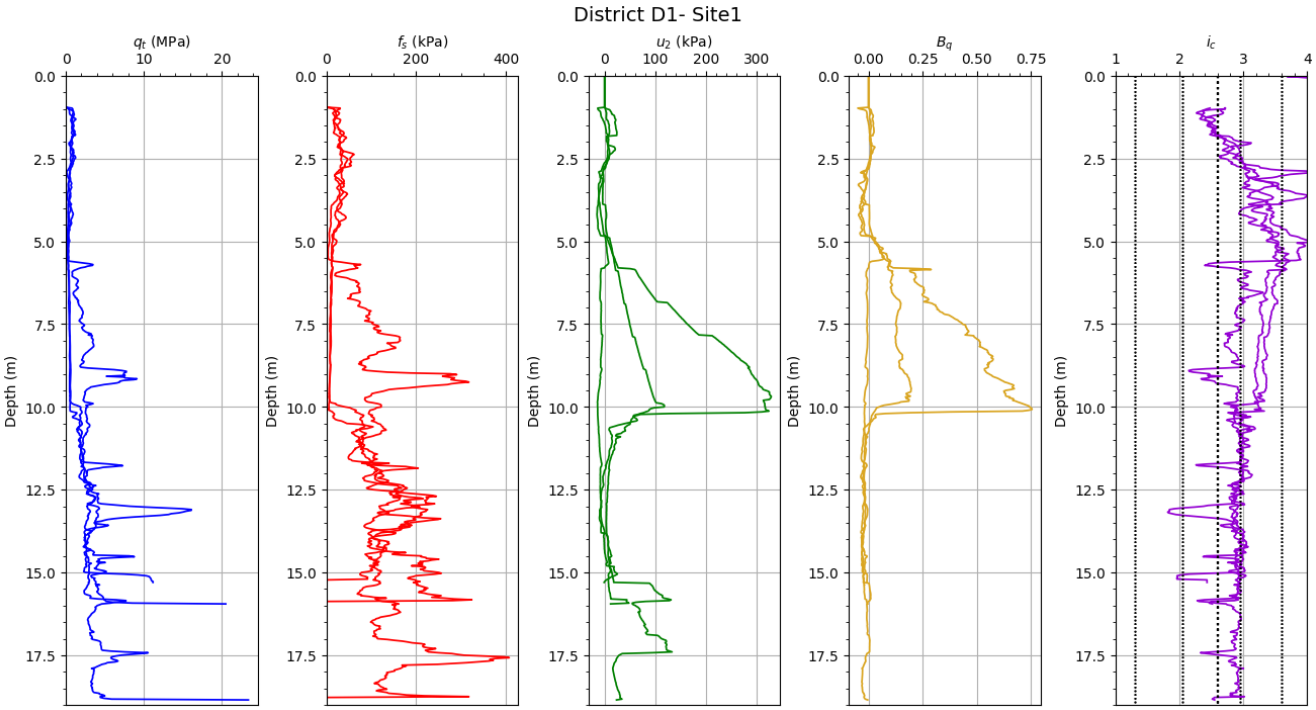

Figure 116. Summary of CPT data at site 1 in District 1.

Source: Georgia Tech

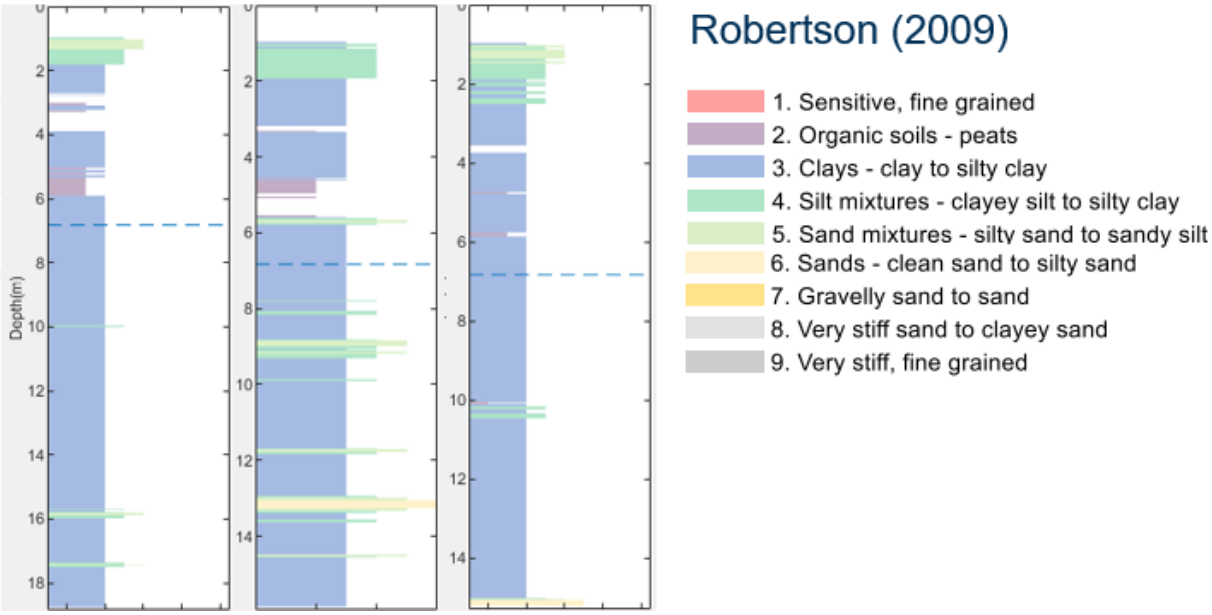

Figure 117. CPT soil stratigraphy based on Robertson (2009) SBT chart for District 1—site 1.

Source: Georgia Tech

DISTRICT 2

Figure 118 shows District 2 and the two sites with CPT/SCPTu data. Figure 119 shows the main characteristics of the collected data through q_t, f_s, Q_{tn}, F_r, and I_c histograms. The I_c plot shows the predominance of sandy mixtures ($2.05 < I_c < 2.80$) and fine-grained soils ($I_c > 2.6$) based on the collected data. In addition, q_t and f_s are generally lower than 5 MPa (725 psi) and 1,000 kPa (145 psi), respectively. Site 2 was selected to provide more discussion. Please refer to Appendix A for the processing of all CPTu/SCPTu.

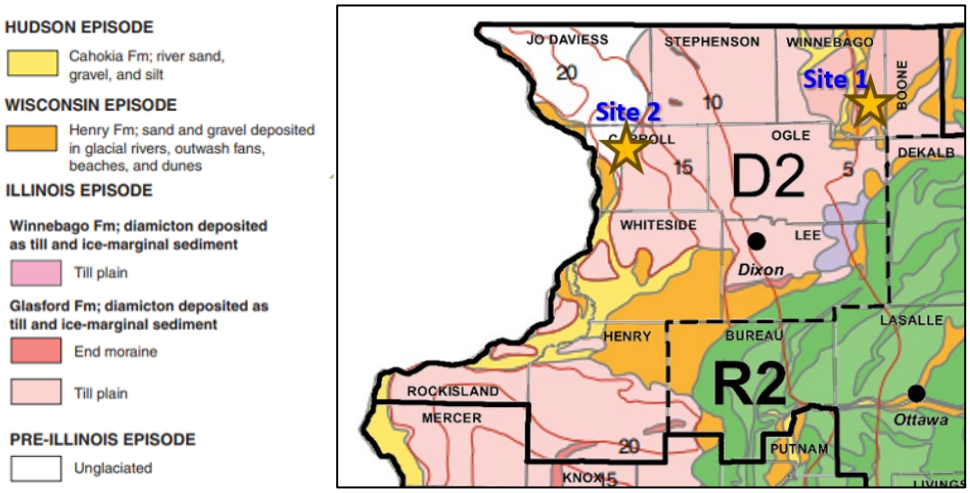

Figure 118. Map of location of sites with SCPT/CPTu data—District 2.

Source: Georgia Tech

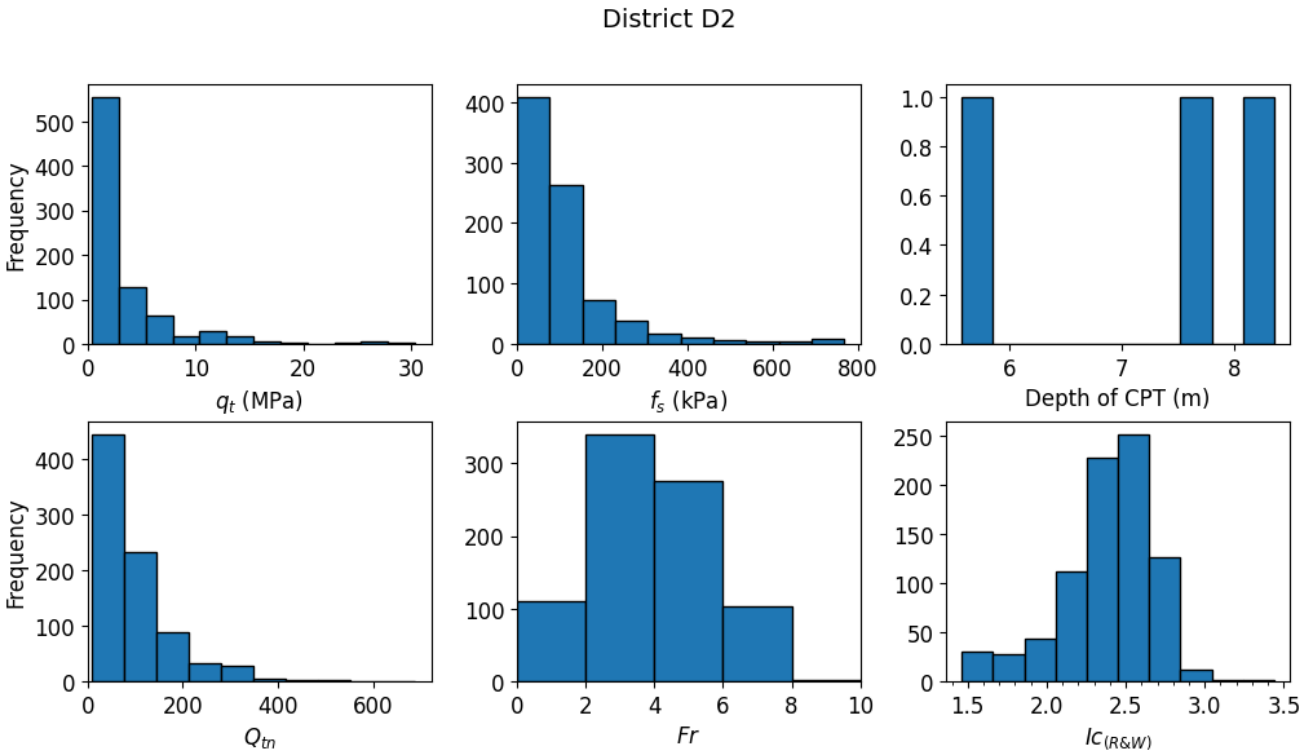

Figure 119. Characteristics of CPT data in District 2.

District 2: Site 2

Site 2 is in Mount Carroll, where the quaternary soils are part of the Wisconsin glacial episode, and soils are deposited as till plain. Figure 120 shows the locations of the CPTs collected for this site, while Figure 121 shows the variations of q_t, f_s, u_2, B_q, and I_c versus depth. Figure 122 shows the soil stratigraphy based on the SBT charts of Robertson (2009). Above 4.5 m (14.8 ft), sand and silt mixtures predominate and show values of q_t, f_s, u_2, and B_q in the range of 0.5–3 MPa (72.5–435 psi), 20–100 kPa (2.9–14.5 psi), 0–150 kPa (21.8 psi), and 0–0.04, respectively. Between 4.5 to 6.5 m (14.8 to 21.3 ft), the Robertson (2009) chart suggests a layer of stiff clayey sand and very fine-grained soil (Group 8 and 9), which shows values of q_t, f_s, u_2, and B_q in the range 7–20 MPa (1015–2900 psi), 100–400 kPa (14.5–58 psi), 100–2000 kPa (14.5–290 psi), and 0.05–0.25, respectively. Below 6.5 m (21.3 ft) depth, silty and clayey layers are found, which show values of q_t, f_s, u_2, and B_q in the range of 2–4 MPa (290–580 psi), 100–160 kPa (14.5–23.2 psi), 50–300 kPa (7.2–43.5 psi), and 0–0.07, respectively. The YSR values are generally between 2 and 7. Also, above a depth of 4.5 m (14.8 ft), the effective friction angle generally varies between 35° and 42°, and the undrained shear strength varies between 40 and 100 kPa (5.8 to 14.5 psi). The effective friction angles below 6 to 6.5 m (19.7 to 21.3 ft) vary between 20° and 35°, and the undrained shear strength varies between 100 and 200 kPa (14.5 and 29 psi). The observations on the stiff layer between 4.5–6.5 m (14.8 to 21.3 ft), particularly the pore pressure responses, are quite interesting, and it was interpreted as potentially being a Marl.

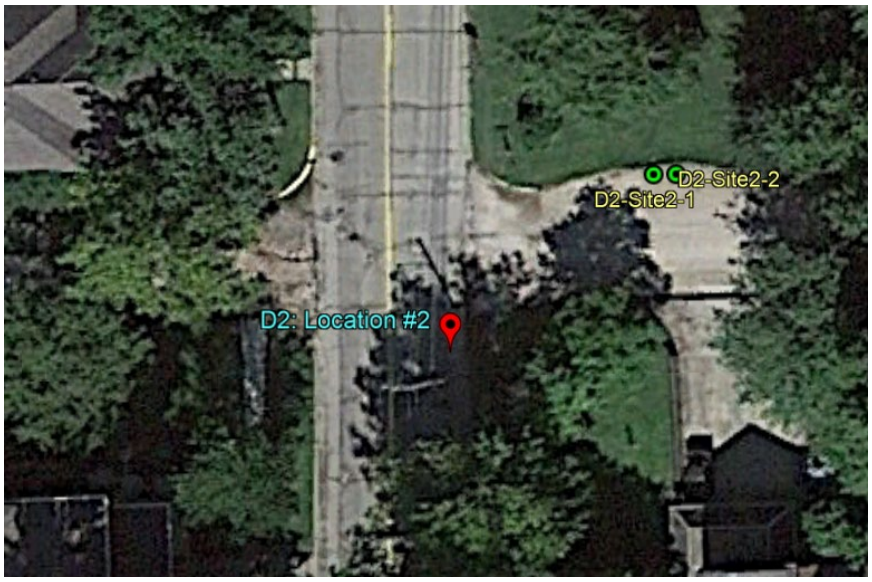

Figure 120. Photo of CPTs locations at site 2 in District 2.

Source: Georgia Tech

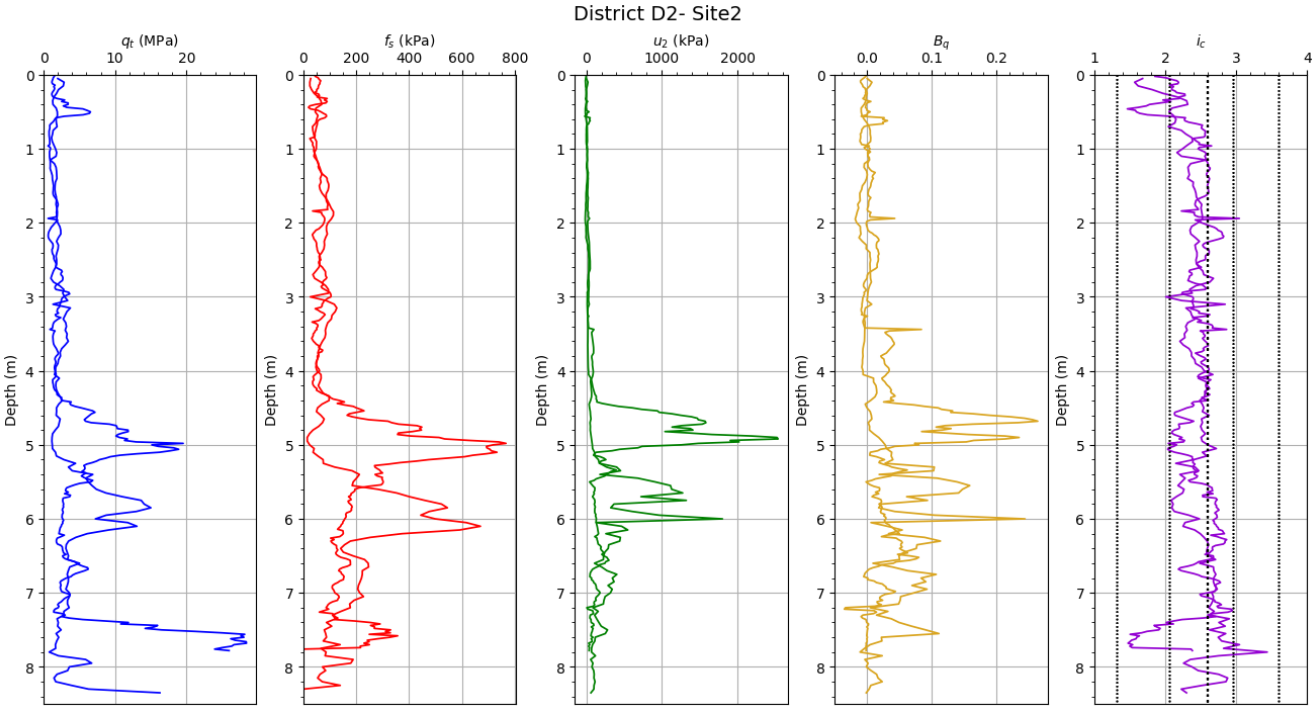

Figure 121. Summary of CPT data at site 2 in District 2.

Source: Georgia Tech

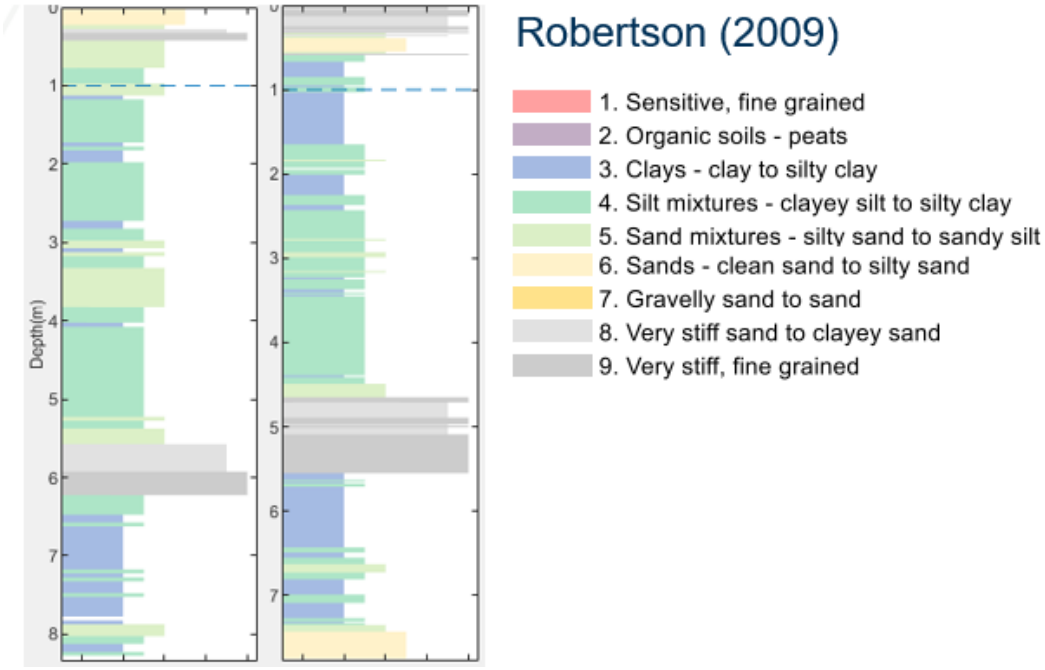

Figure 122. Representative soil stratigraphy based on Robertson (2009) SBT chart for District 2—site 2.

Source: Georgia Tech

DISTRICT 3

Figure 123 shows District 3 and the four sites with CPT/SCPTu data. Figure 124 shows the main characteristics of the collected data through q_t, f_s, Q_{tn}, F_r, and I_c histograms. The I_c plot shows the predominance of fine-grained soils with undrained behavior (I_c > 2.6). Site 4 in Figure 125 was selected to illustrate additional CPT/SCPTu details. Please refer to Appendix A for the processing of all CPTu/SCPTu data.

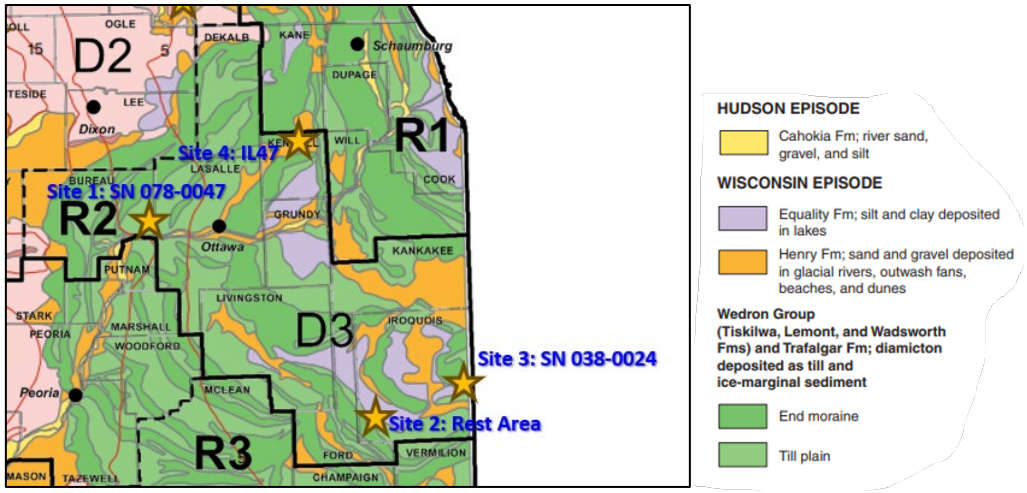

Figure 123. Map of location of sites with SCPT/CPTu data—District 3.

Source: Georgia Tech

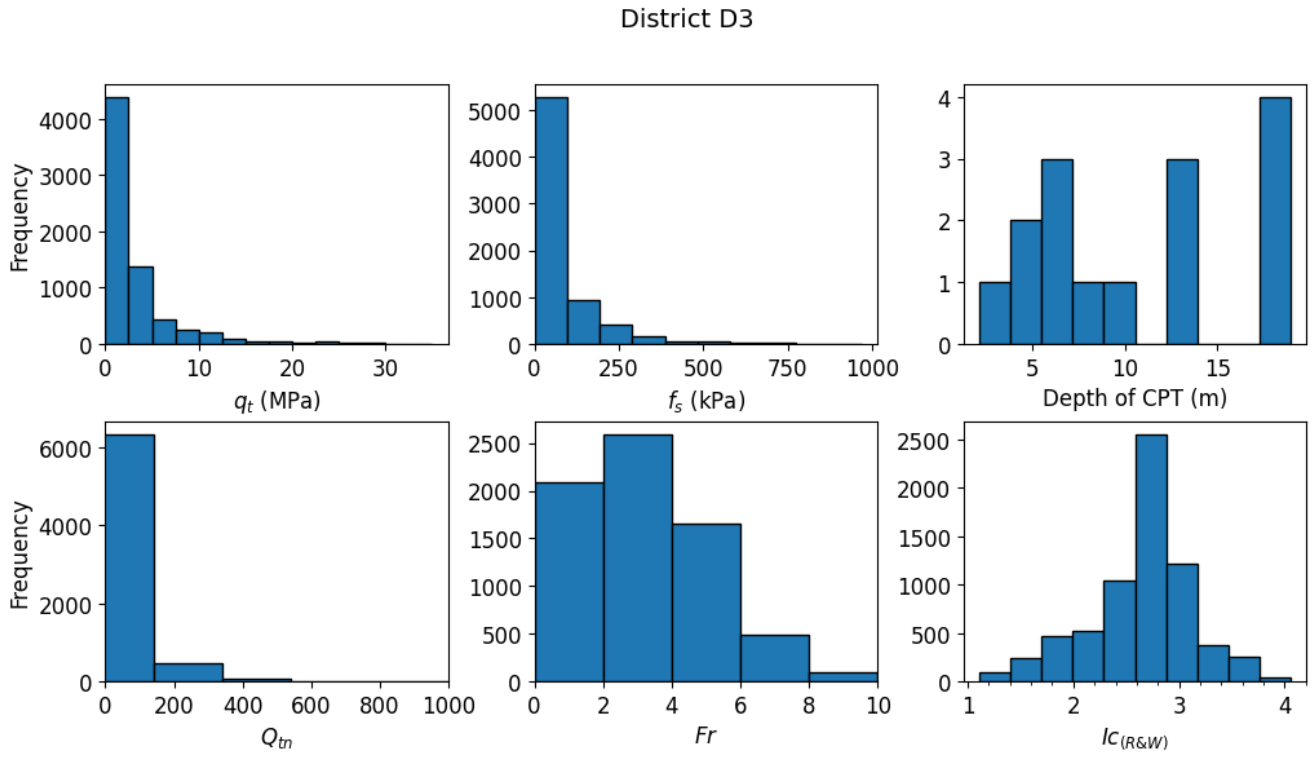

Figure 124. Characteristics of CPT data in District 3.

Source: Georgia Tech

District 3: Site 4 (IL 47)

Site 4 is in Bristol, where the quaternary soils are part of the Wisconsin glacial episode, and soils are deposited as end moraine sands and gravel from glacial rivers. Figure 125 shows the location of the CPTs, while Figure 126 shows the variations of q_t, f_s, u_2, B_q, and I_c versus depth. The information collected from this site shows a highly heterogeneous stratigraphy. Most CPTs show a superficial layer of sands and gravelly sands with less than 1 m (3.3 ft) depth, followed by fine-grained soils with variable thickness (3 to 7 m [9.8–23.0 ft]) until a sand layer is reached. The surficial sand layer show q_t, f_s, u_2, and B_q values in the range of 5–15 MPa (725–2176 psi), 50–100 kPa (7.25–14.5 psi), 0–50 kPa (0–7.25 psi), and close to 0, respectively. The fine-grained soil layer with variable thickness is composed of clays, silt mixtures, and sensitive fine-grained soils with interbedded sandy mixtures. This intermediate fine-grained layer shows q_t, f_s, u_2, and B_q values in the range of 0.5–1 MPa (72.5–145 psi), less than 50 kPa, 100–200 kPa (7.25, 14.5–29 psi), and 0.5–1. Finally, the deep sandy layer shows q_t, f_s, u_2, and B_q values in the range of 5–10 MPa (725–1450 psi), less than 50 kPa, 50–70 kPa (7.25, 7.25–10.15 psi), and close to 0, respectively. Figure 127 shows the soil stratigraphy based on the SBT charts of Robertson (2009) of six representative CPTs of this site. For the fine-grained soils below 2.5 m (8.2 ft) depth, YSR varies between 1.5 to 2, and the undrained shear strength varies between 20 to 40 kPa (2.9–5.8 psi). The deep sand layer has a friction angle that varies between 35 to 42º. Superficial layers of sand and fine-grained soils show higher strength parameters; this may be attributed to their over-consolidated condition with YSR between 2 and 5.

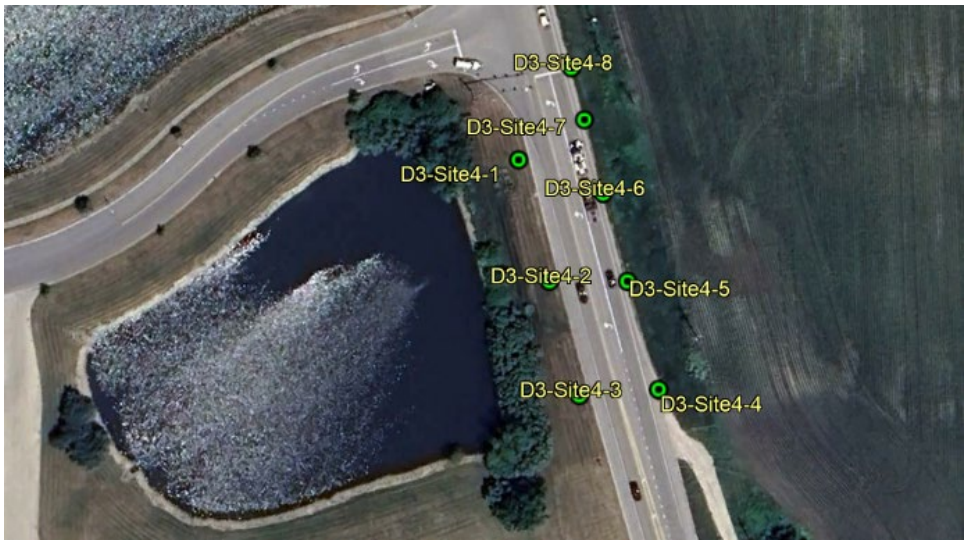

Figure 125. Photo of CPTs locations at site 4 in District 3.

Source: Georgia Tech

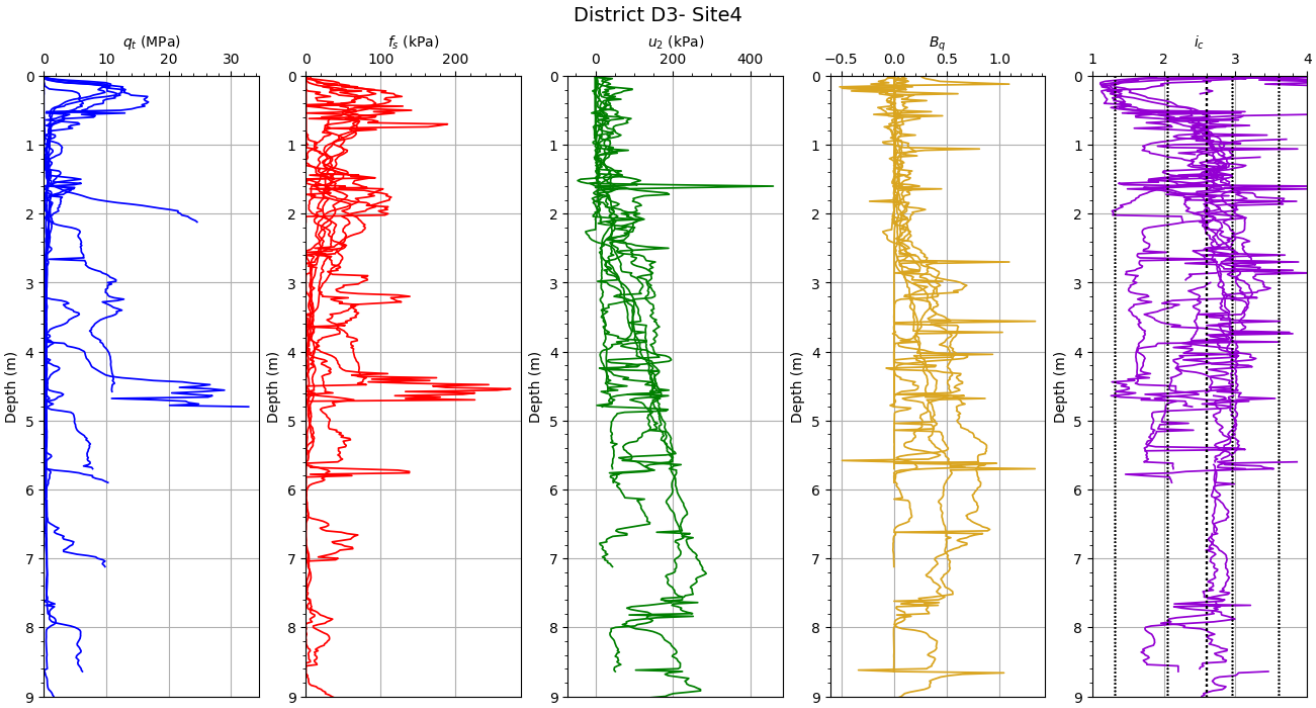

Figure 126. Summary of CPT data at site 4 in District 3.

Source: Georgia Tech

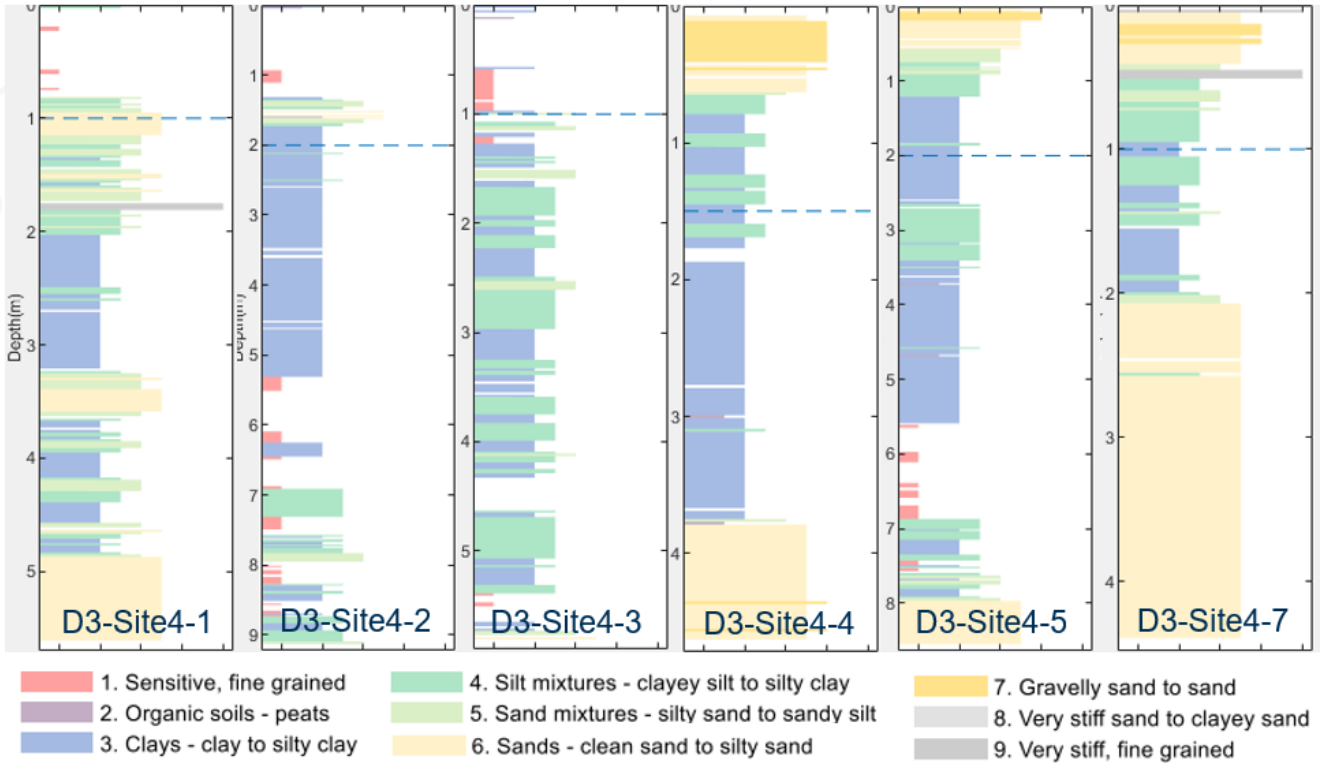

Figure 127. Soil stratigraphy based on Robertson (2009) SBT chart of District 3—site 4.

Source: Georgia Tech

DISTRICT 4

Figure 128 shows District 4 and the sites with CPT/SCPTu data. Figure 129 shows the main characteristics of the collected data through q_t, f_s, Q_{tn}, F_r, and I_c histograms. The I_c plot shows a predominance of sandy mixtures (2.10 < I_c < 3.10) and fine-grained soils (I_c > 2.6). Site 1 in Figure 130 was selected to illustrate additional CPT/SCPTu details. Please refer to Appendix A for the processing of all CPTu/SCPTu data.

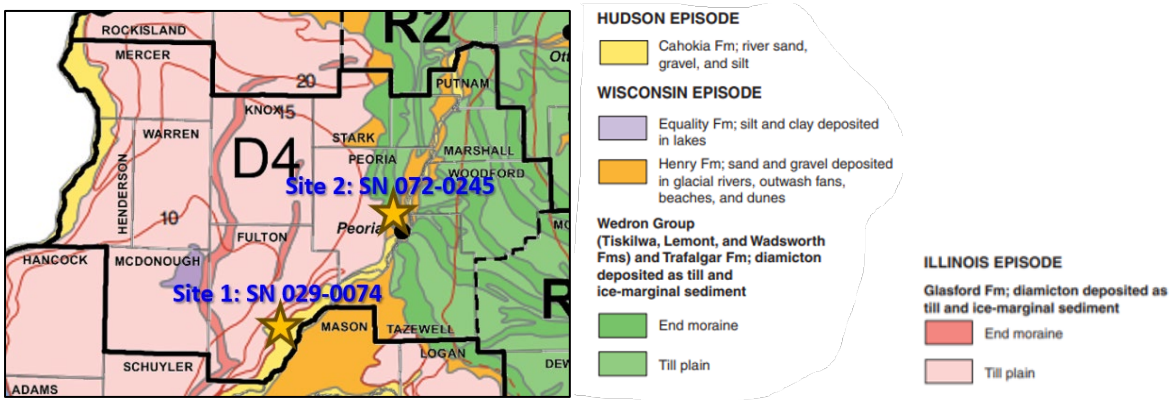

Figure 128. Map of location of sites with SCPT/CPTu data—District 4.

Source: Georgia Tech

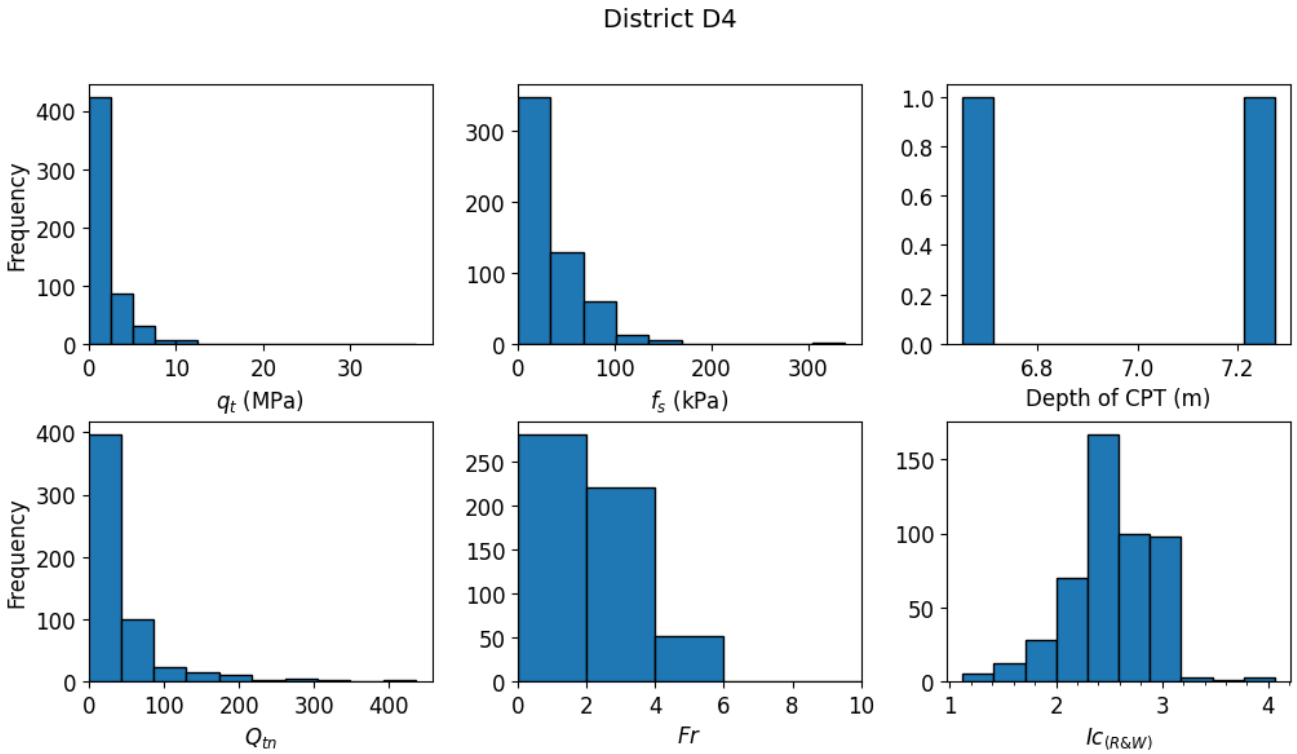

Figure 129. Characteristics of CPT data in District 4.

Source: Georgia Tech

District 4: Site 1 (SN 029-0074)

Site 1 is located 7 km (4.3 miles) from Lewistown, where the quaternary soils are part of the Illinois glacial episode, and soils are deposited as till plain, close to the postglacial Hudson episode, where soils are deposited as river sand, gravels, and silts. Figure 130 shows the location of the CPTs collected for this site, as well as the variations of q_t, f_s, u_2, B_q, and I_c versus depth. The CPT data show the presence of layer sand and sand mixtures above 2 m (6.56 ft) and below 6.2 m (20.34 ft) and an intermediate fine-grained soil with a thickness of about 4.2 m (13.78 ft). The sandy layers show q_t, f_s, u_2, and B_q values in the range of 5–10 MPa (725.2–1450.4 psi), 0–150 kPa (0–21.7 psi), 0–50 kPa (0–7.2 psi), and 0–0.15, respectively. The fine-grained soils are composed of clays and silt mixtures. The intermediate fine-grained layers show q_t, f_s, u_2, and B_q values in the range of 1–3 MPa (145–435 psi), 10–40 kPa (1.4–5.8 psi), 50–200 kPa (7.2–29.0 psi), and 0–0.25, respectively. Figure 131 shows the soil stratigraphy based on the SBT charts of Robertson (2009) of the CPT collected for this site. The friction angle for the sand and sandy mixtures is between 30° and 40°, while for the fine-grained soils, it is between 20° and 30°. Moreover, the undrained shear strength of the intermediate fine-grained layer varies between 20 and 50 kPa (2.9–7.2 psi).

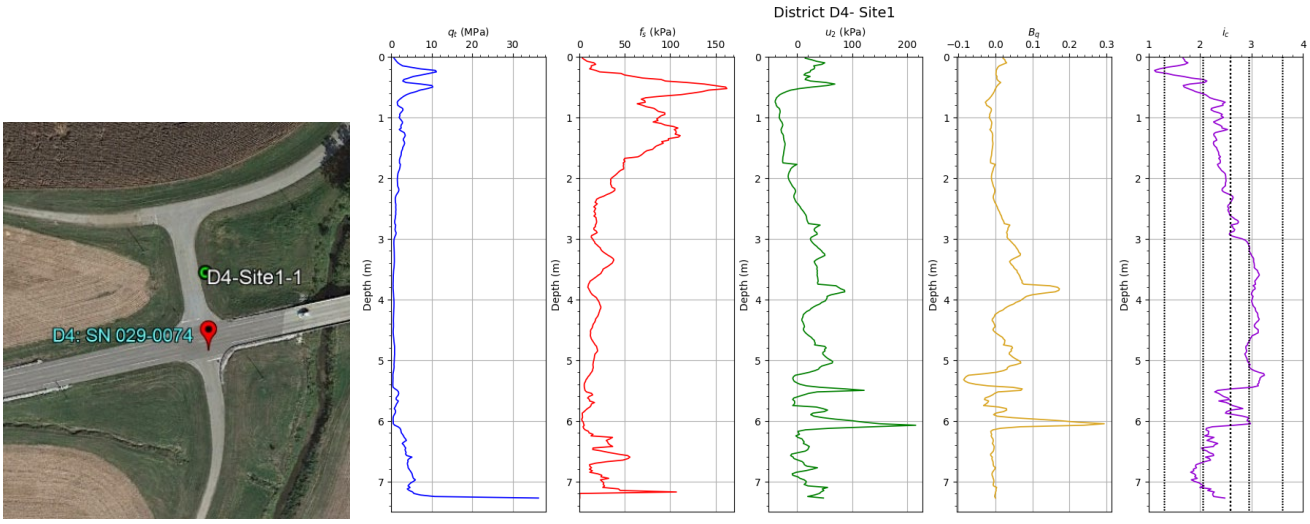

Figure 130. Photo of CPTs locations and summary of CPT data at site 1 in District 4.

Source: Georgia Tech

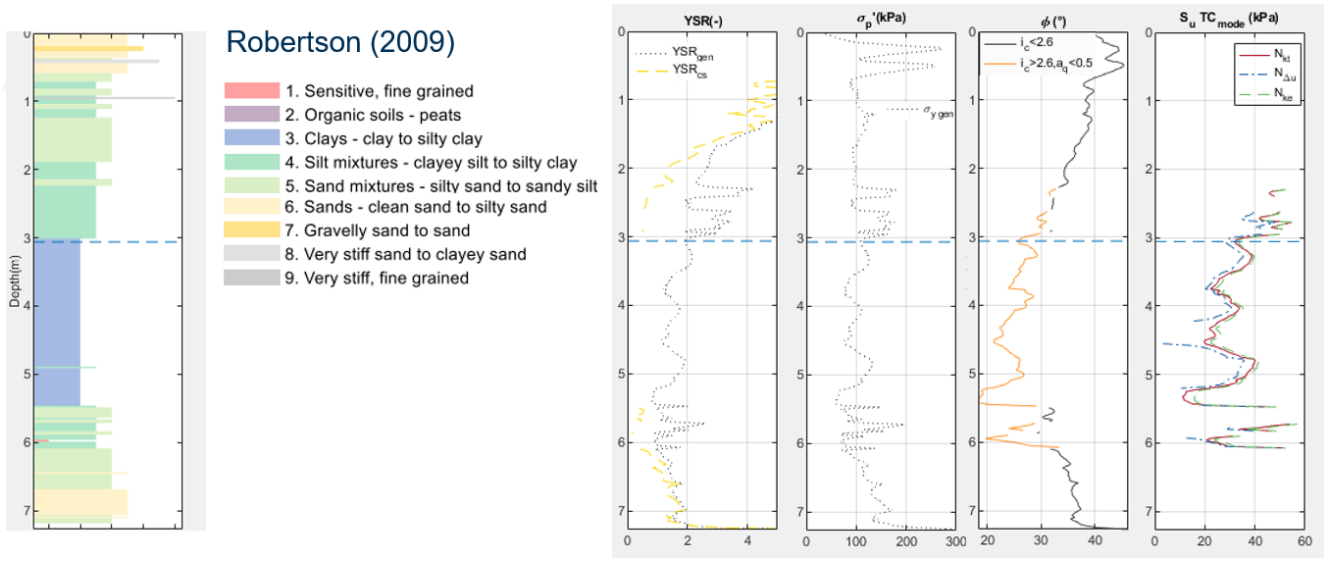

Figure 131. Soil stratigraphy is based on Robertson (2009) SBT chart of District 4—site 1. Other estimated geoparameters are also shown—see Appendix A for details.

Source: Georgia Tech

DISTRICT 5

Figure 132 shows District 5 and the sites with CPT/SCPTu data. Figure 133 shows the main characteristics of the collected data through q_t, f_s, Q_{tn}, F_r, and I_c histograms. The I_c plot shows the predominance of clays and silty mixtures (I_c > 2.6). Site 4 in Figure 134 was selected to illustrate additional CPT/SCPTu details. Please refer to Appendix A for the processing of all CPTu/SCPTu data.

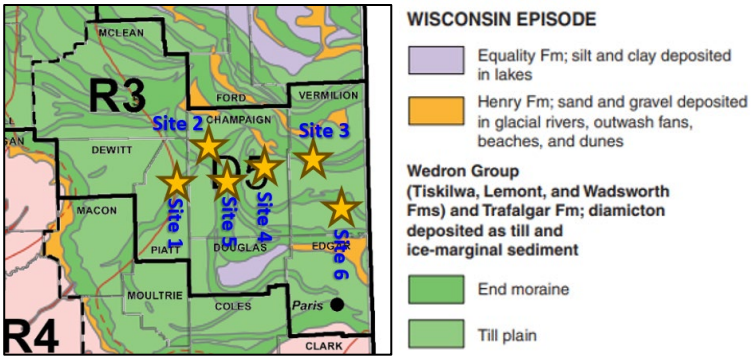

Figure 132. Map of location of sites with SCPT/CPTu data—District 5.

Source: Georgia Tech

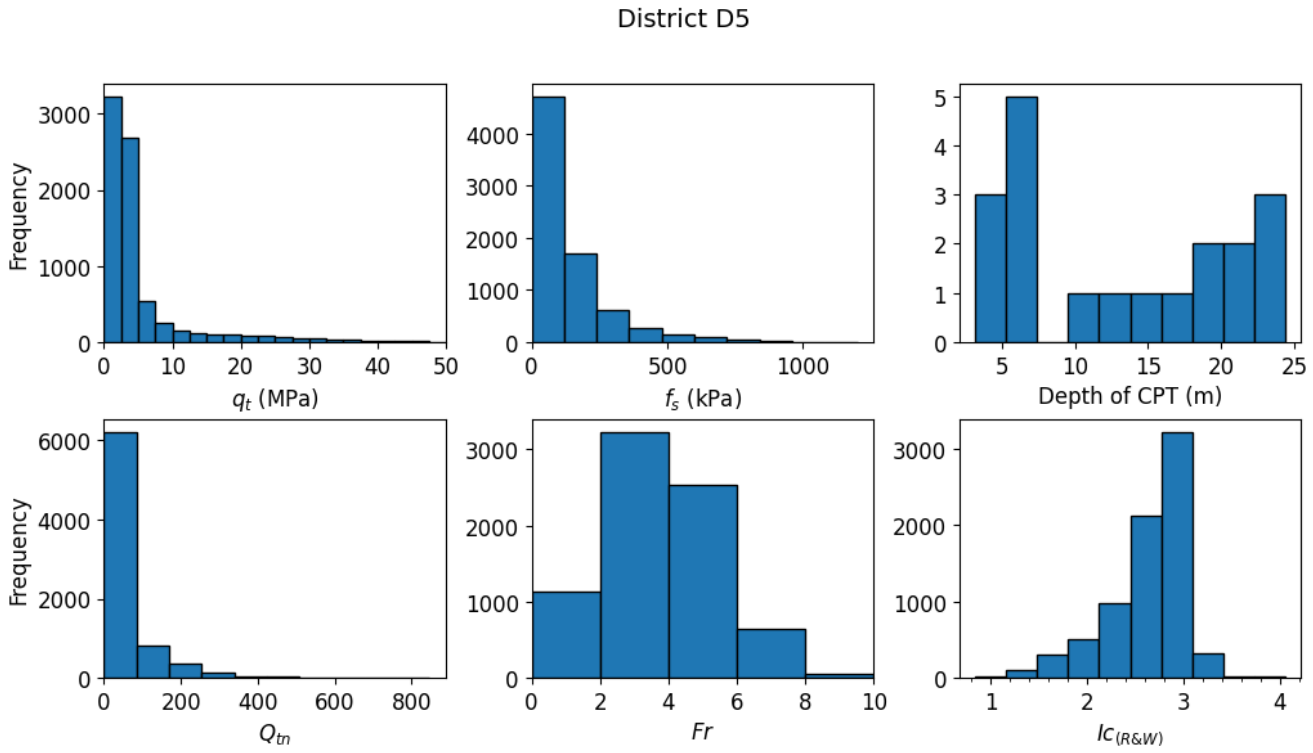

Figure 133. Characteristics of CPT data in District 5.

Source: Georgia Tech

District 5: Site 4 (SN 010-0180)

Site 4 is located 4 km (2.48 miles) from St. Joseph, where the quaternary soils are part of the Wisconsin glacial episode, and soils are deposited as till plain and end moraine. Figure 134 shows the location of the CPTs collected for this site, while Figure 135 shows the variations of q_t, f_s, u_2, B_q, and I_c versus depth. Soundings D5-Site4-1 and D5-Site4-2 are in the center pillar foundation, in the middle of an existing bridge, while soundings D5-Site4-3 and D5-Site4-4 are located at the opposite

sides of the bridge. The soil profiles from D5-Site4-1 and D5-Site4-2 CPTus show a surficial layer of sands and very stiff sands with less than 1 m (3.3 ft) thickness, followed by 5 m (16.4 ft) of silt mixtures. The silt mixtures show q_t, f_s, u_2, and B_q values in the range of 2–3 MPa (290–435 psi), 50–120 kPa (7.3–17.4 psi), 100–500 kPa (14.5–72.5 psi), and 0.1–0.25. The fine-grained soils at deeper locations are composed of clays and silt mixtures and show q_t, f_s, u_2, and B_q values in the range of 1–3 MPa (145–435 psi), 50–120 kPa (7.3–17.4 psi), 100–500 kPa (14.5–72.5 psi), and 0.1–0.25. Based on the procedures in Chapter 3, the friction angle is estimated to vary between 20 and 23, and the undrained shear strength between 80 and 100 kPa (11.6–14.5 psi). The soil profile from D5-Site4-3 and D5-Site4-4 is highly heterogeneous above 3 m (9.8 ft), composed of sandy mixtures, silty mixtures, and very stiff sand, followed by 8 m (26.2 ft) of clay. The clay layer shows q_t, f_s, u_2, and B_q values in the range of 1–3 MPa (145–435 psi), 50–120 kPa (7.3–17.4 psi), 100–500 kPa (14.5–72.5 psi), and 0.1–0.25. The friction angle varies between 20 and 30, and undrained shear strength is between 30 and 100 kPa (4.35–14.5 psi) above 9 m (29.5 ft) depth and between 100 and 200 kPa (14.5–29.0 psi) below. Figure 136 shows the soil stratigraphy based on the SBT charts from Robertson (2009) for the four available CPTs.

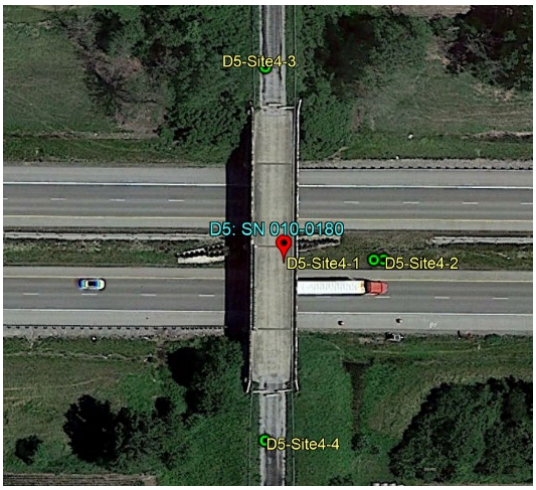

Figure 134. Photo of CPTs locations at site 4 in District 5.

Source: Georgia Tech

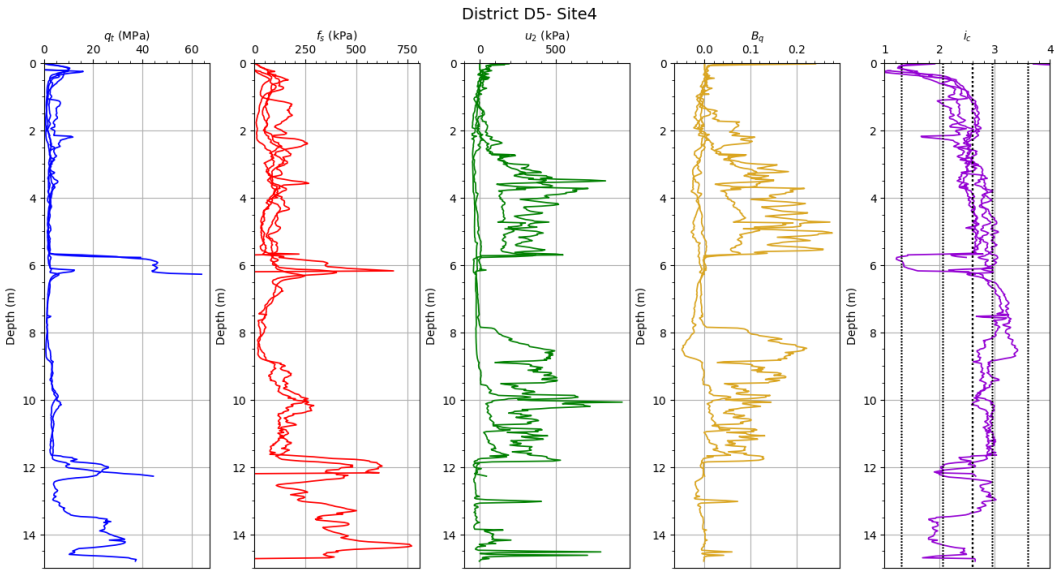

Figure 135. Summary of CPT data at site 4 in District 5.

Source: Georgia Tech

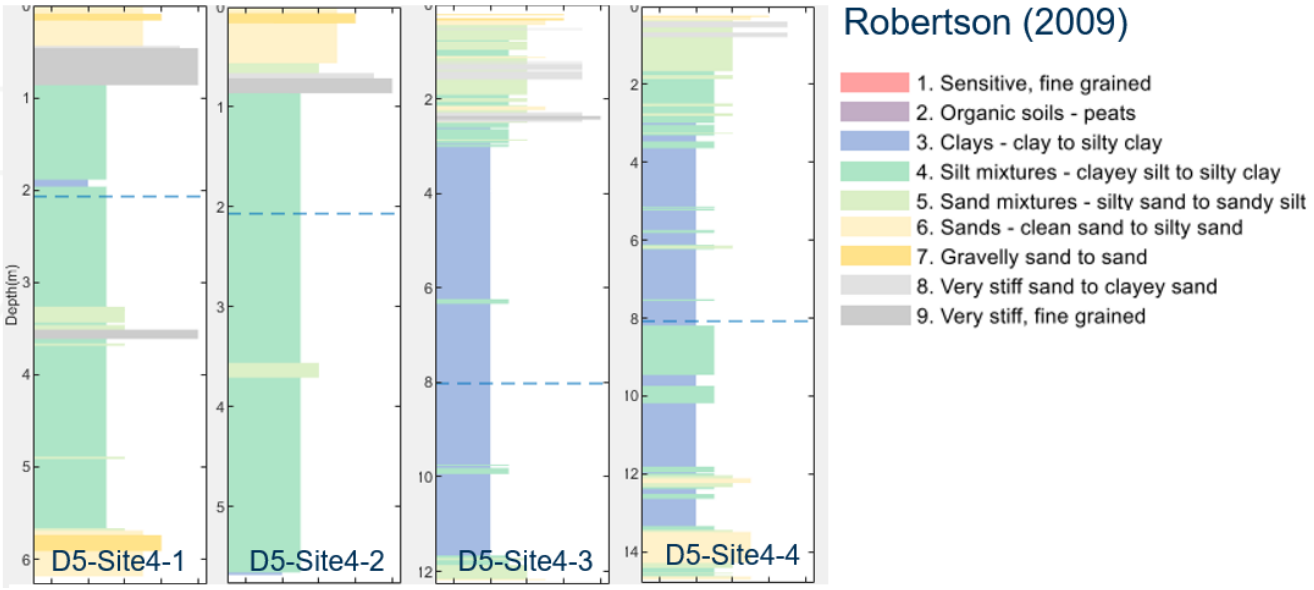

Figure 136. Soil stratigraphy based on Robertson (2009) SBT chart of District 5—site 4.

Source: Georgia Tech

DISTRICT 6

Figure 137 shows District 6 and the sites with CPT/SCPTu data. Figure 138 shows the main characteristics of the collected data through q_t, f_s, Q_{tn}, F_r, and I_c histograms. The I_c histogram shows a broad range of values, generally the first 15 m are associated with $I_c > 2.6$ and $I_c < 2.6$ for deeper

locations. Site 1 in Figure 139 was selected to illustrate additional CPT/SCPTu details. Please refer to Appendix A for the processing of all CPTu/SCPTu data.

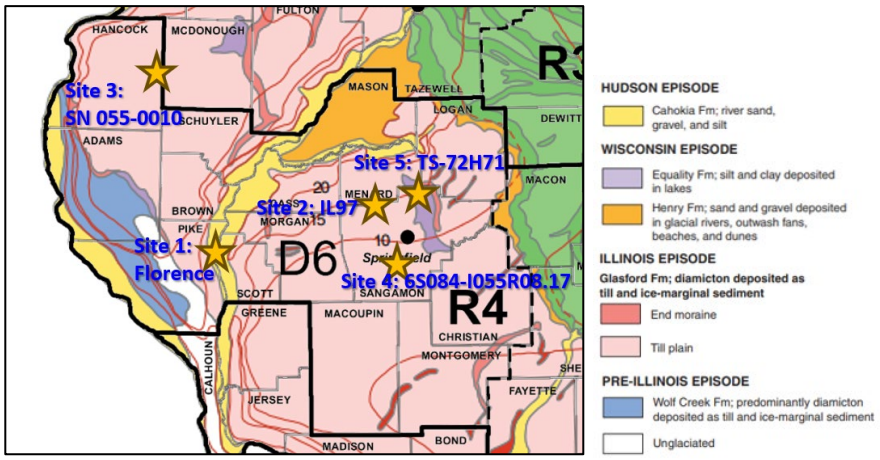

Figure 137. Location of sites with SCPT/CPTu data—District 6.

Source: Georgia Tech

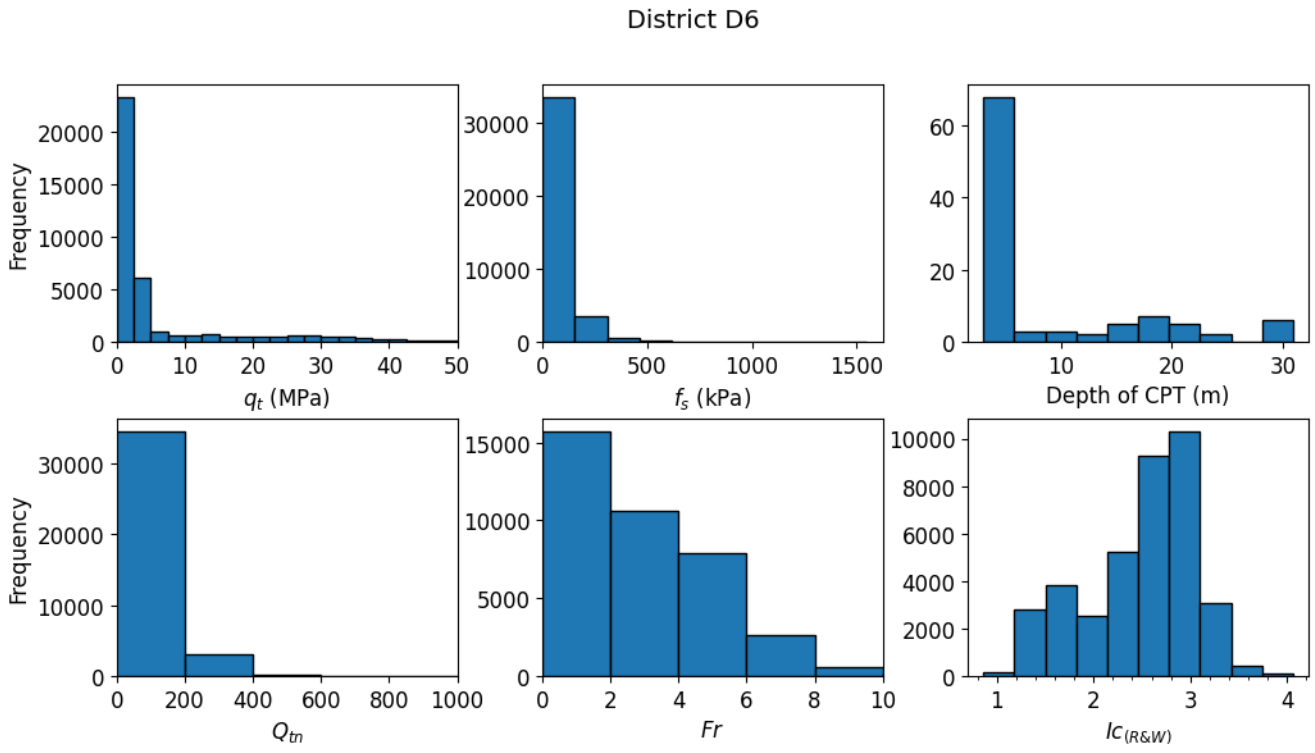

Figure 138. Characteristics of CPT data in District 6.

Source: Georgia Tech

District 6: Site 1 (IL River Bridge at Florence)

Site 1 is located at Florence, where the quaternary soils are part of the Illinois glacial episode, and soils are deposited as till plain, close to the postglacial Hudson episode where soils are deposited as river sand, gravels, and silt. Figure 139 shows the location of the CPTs at this site, while Figure 140 shows the variations of q_t, f_s, u_2, B_q, and I_c versus depth. The data processing shows three typical stratigraphies, which are illustrated in Figure 141, using two representative CPTs for each type of stratigraphy.

- The first type of stratigraphy corresponds to the west side of the river. The three CPTs in this area show a highly heterogeneous stratigraphy composed of silty mixtures, sand mixtures, clays, and interbedded sand layers with a thickness varying from 0.3 to 2 m (0.98–6.56 psi). The fine-grained soils show q_t, f_s, u_2, and B_q values in the range of 1–2 MPa (145–290 psi), 20–100 kPa (2.9–14.5 psi), 50–400 kPa (7.2–58.0 psi), and 0.1–0.5. The sandy layers show q_t, f_s, u_2, and B_q values in the range of 1–2 MPa (145–290 psi), 20–100 kPa (2.9–14.5 psi), 50–100 kPa (7.2–14.5 psi), and 0. The estimated undrained shear strength of the fine-grained soils varies between 40 and 60 kPa (5.8–8.7 psi). The sandy layers show a friction angle in the range of 33° and 40°.

- The second type of stratigraphy corresponds to the bridge's east side, 500 m (0.31 miles) from the riverbank. The stratigraphy is also highly heterogeneous in this case, and it is generally composed of clays and silty mixtures and an interbedded layer of sand with a thickness varying from 2 to 8 m (6.6 to 26.2 ft). Finally, a continuous layer of sand and gravely sand unit is reached at 18 m (59 ft) depth. The fine-grained soils show q_t, f_s, u_2, and B_q values in the range of 0.5–1.5 MPa (72.5–217.6 psi), 5–20 kPa (0.7–2.9 psi), 200–600 kPa (29–87 psi), and 0.1–0.5. The interbedded sandy layer show q_t, f_s, u_2, and B_q values in the range of 8–20 MPa (1160–2900 psi), 30–130 kPa (4.4–18.8 psi), 100–150 kPa (14.5–21.8 psi), and close to 0, respectively. The continuous deep layer of sand show q_t, f_s, u_2, and B_q values varying between 20–50 MPa (2901–7252 psi), 100–300 kPa (14.5–43.5 psi), 180–200 kPa (26.1–29.9 psi), and close to 0, respectively. The interbedded layer of sand has a friction angle in the range of 35° to 40°, while for the deep sandy layer, the friction angle is higher than 40°. The estimated undrained shear strength of the fine-grained soils shows high variability but generally varies between 30 and 60 kPa (4.4–8.7 psi).

- The third type of stratigraphy corresponds to the bridge's east side, at a distance larger than 500 m (0.31 miles) from the riverbank. The stratigraphy profile comprises clays and silty mixtures until a continuous layer of sand and gravelly sand is reached. The sandy layer is reached at different depths, varying from 16 to 12 m (52.5–39.4 ft). The fine-grained soils show q_t, f_s, u_2, and B_q values in the range of 0.5–1 MPa (72.5–145 psi), 5–40 kPa (0.7–5.8 psi), 150–500 kPa (21.8–72.5 psi), and 0.2–0.6, respectively. The continuous deep layer of sand show q_t, f_s, u_2, and B_q values in the range of 20–40 MPa (2900–5801 psi), 100–300 kPa (14.5–43.5 psi), 180–220 kPa (26.1–31.9 psi), and close to 0, respectively. Similar to the other stratigraphies, in the deep sandy layer, the friction angle is higher than

40°. The friction angle of the fine-grained soils is in the range of 28° to 33°, while the undrained shear strength is in the range of 20 to 50 kPa (2.9 to 7.2 psi).

Figure 139. Photo of CPTs locations at site 1 in District 6.

Source: Georgia Tech

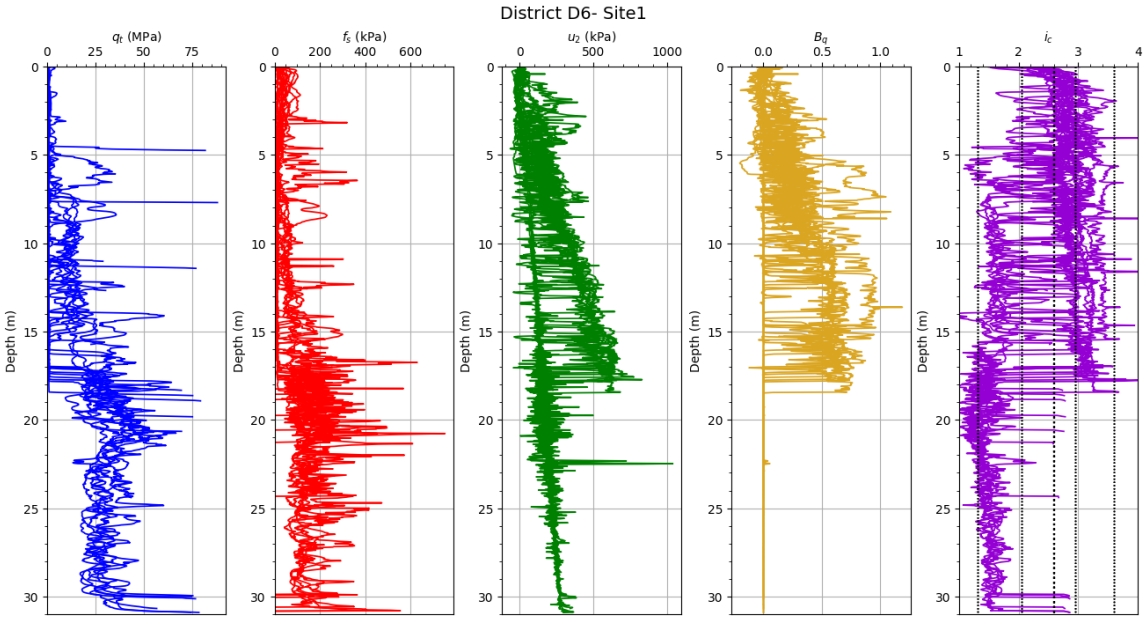

Figure 140. Summary of CPT data at site 1 in District 6.

Source: Georgia Tech

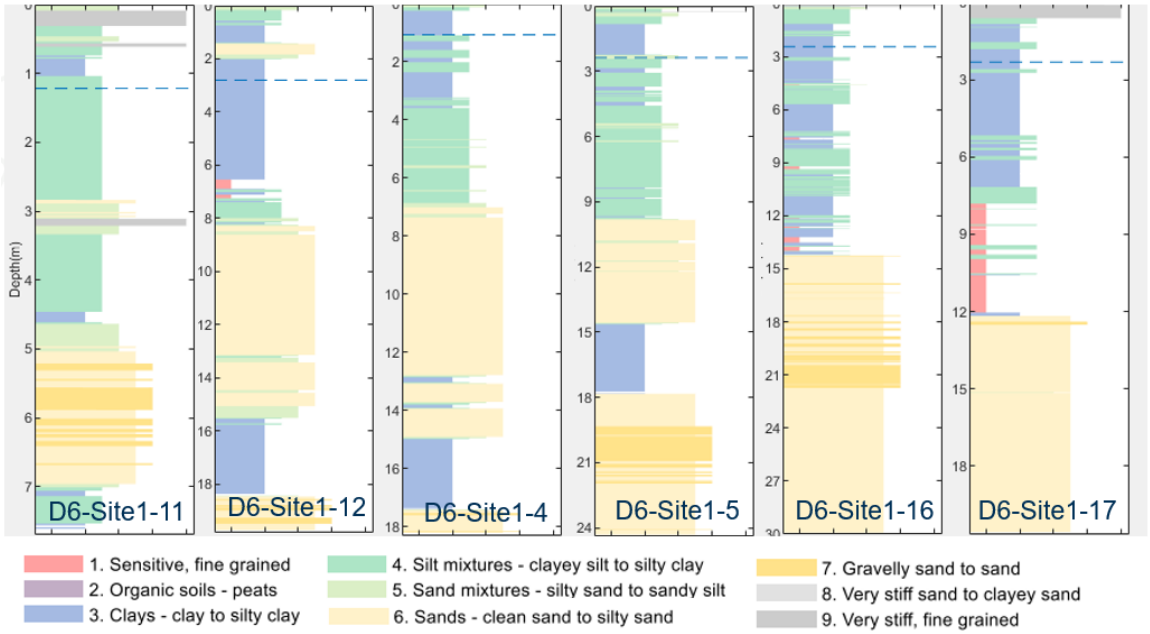

Figure 141. Soil stratigraphy based on SBT charts of District 6—site 1.

Source: Georgia Tech

DISTRICT 7

Figure 142 shows District 7 and the sites with CPT/SCPTu data. Figure 143 shows the main characteristics of the collected data through q_t, f_s, Q_{tn}, F_r, and I_c histograms. In particular, the I_c histogram indicates a predominance of silty mixtures and clay-type layers. Site 1 in Figure 144 was selected to illustrate additional CPT/SCPTu details. Please refer to Appendix A for the processing of all CPTu/SCPTu data.

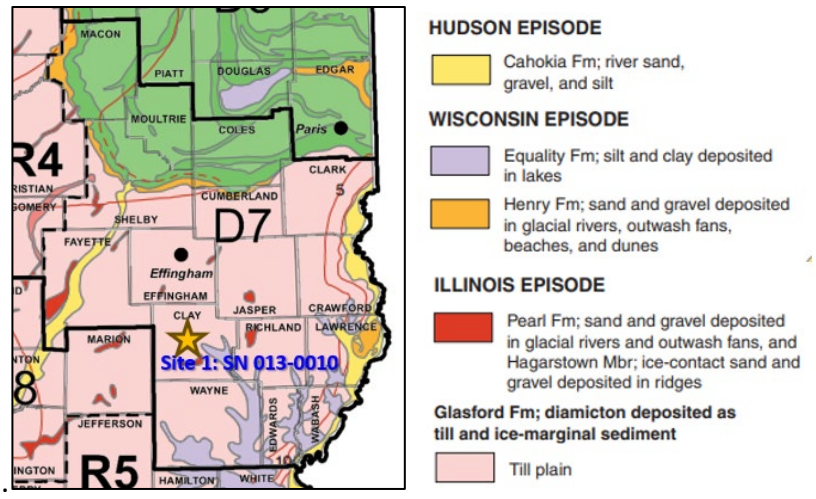

Figure 142. Map of location of sites with SCPT/CPTu data—District 7.

Source: Georgia Tech

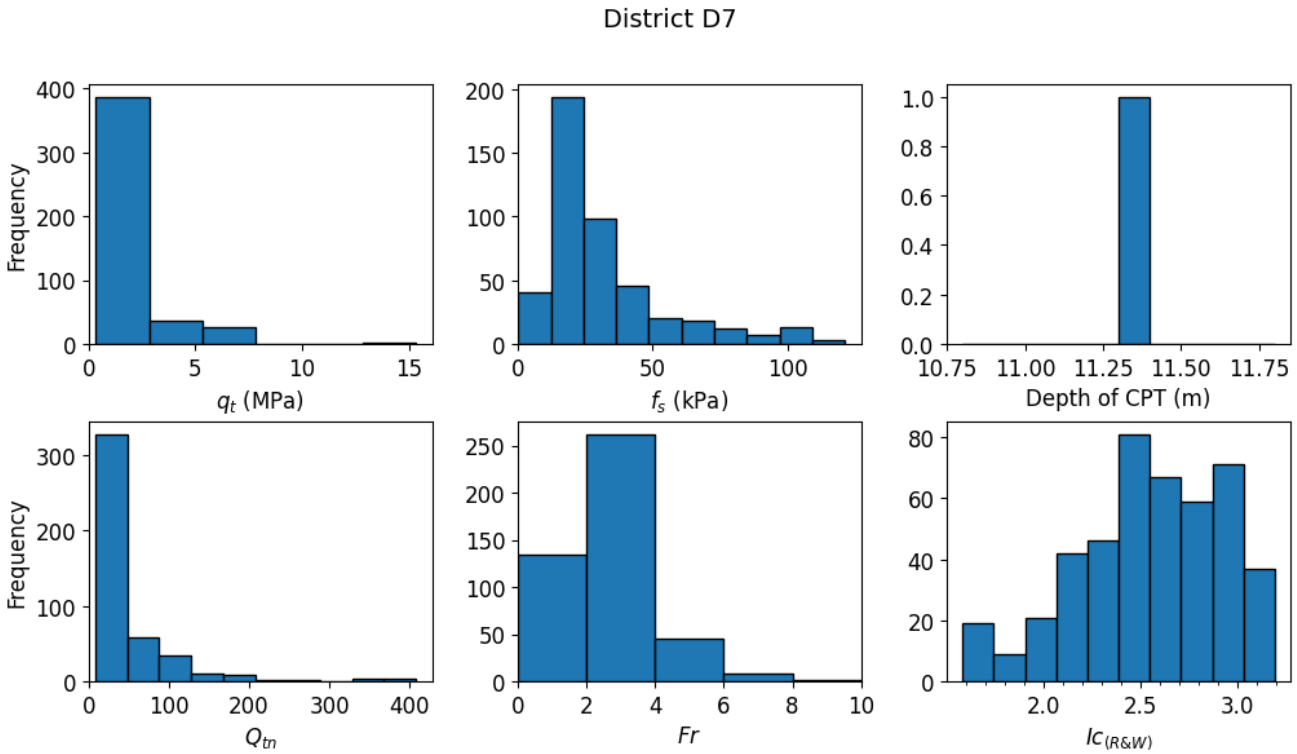

Figure 143. Characteristics of CPT data in District 7.

Source: Georgia Tech

District 7: Site 1 (SN 013-0010)

Site 1 is located 1 km (.062 miles) from Louisville, where the quaternary soils are part of the Illinois glacial episode, and soils have been deposited as till plains. Figure 144 shows the location of the CPT collected for this site, as well as the variations of q_t, f_s, u_2, B_q, and I_c versus depth. The CPT data show the presence of silty mixtures and clays through all the profiles, as well as an interbedded layer of sands and sandy mixtures with a thickness of about 2 m (6.6 ft). The sandy layers show q_t, f_s, u_2, and B_q values in the range of 2–7 MPa (290–1015 psi), 50–120 kPa (7.2–17.4 psi), 0–400 kPa (0–58 psi), and 0–0.2. The fine-grained soils show q_t, f_s, u_2, and B_q values in the range of 0.5–1.5 MPa (72.5–217.6 psi), 10–50 kPa (1.5–7.3 psi), 200–500 kPa (29–72.5 psi), and 0.2–0.8. Figure 145 shows the soil stratigraphy based on the Robertson (2009) SBT chart. Using the procedures discussed in Chapter 3, the friction angle for the sand and sandy mixtures is estimated to be between 32 and 38°, while for the fine-grained soils, the estimated friction angle can be as low as 22°. Finally, the undrained shear strength of the fine-grained soils is estimated to vary between 30 and 80 kPa (4.4 and 11.6 psi).

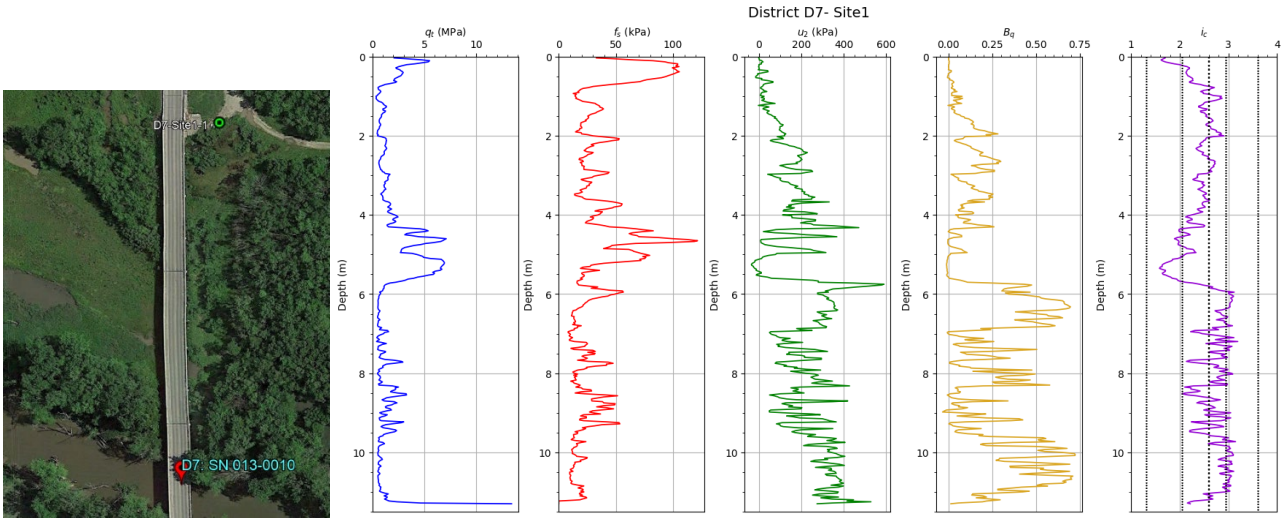

Figure 144. Photo of CPTs locations in and summary of CPT data at site 1 in District 7.

Source: Georgia Tech

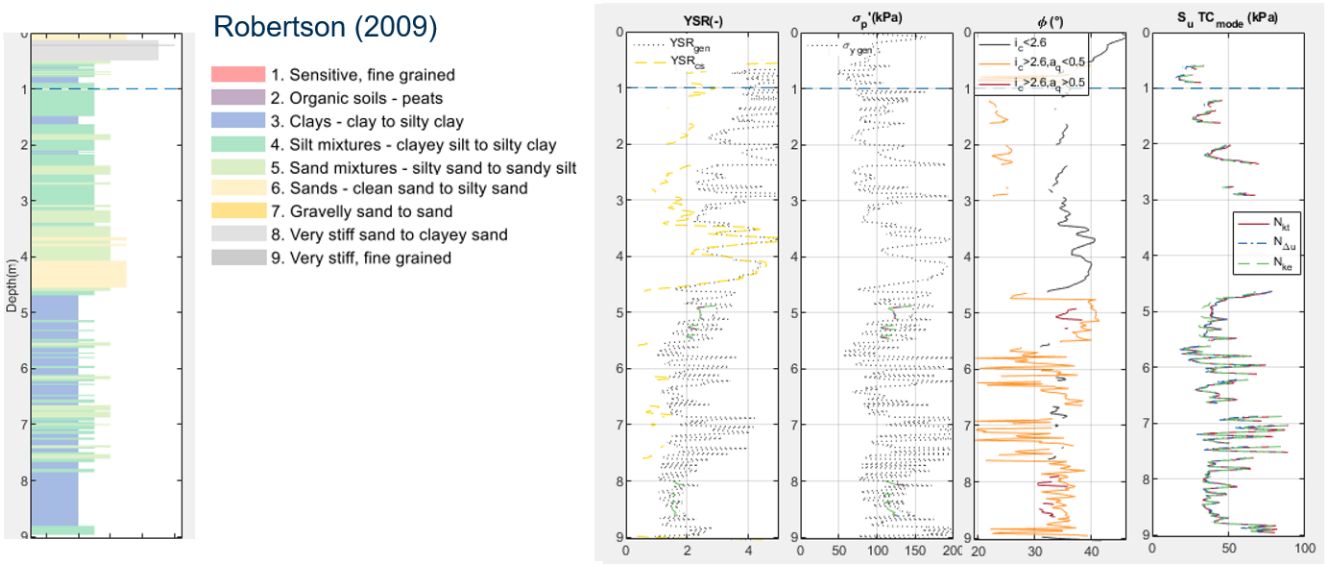

Figure 145. Soil stratigraphy based on SBT charts of District 7—site 1.

Source: Georgia Tech

DISTRICT 8

Figure 146 shows District 8 and the sites with CPT/SCPTu data. Figure 147 shows the main characteristics of the collected data through q_t, f_s, Q_{tn}, F_r, and I_c histograms. The I_c histogram indicates a broad range of materials from sandy layers to clayey soils. Site 1 in Figure 148 was selected to illustrate additional CPT/SCPTu details. Please refer to Appendix A for the processing of all CPTu/SCPTu data.

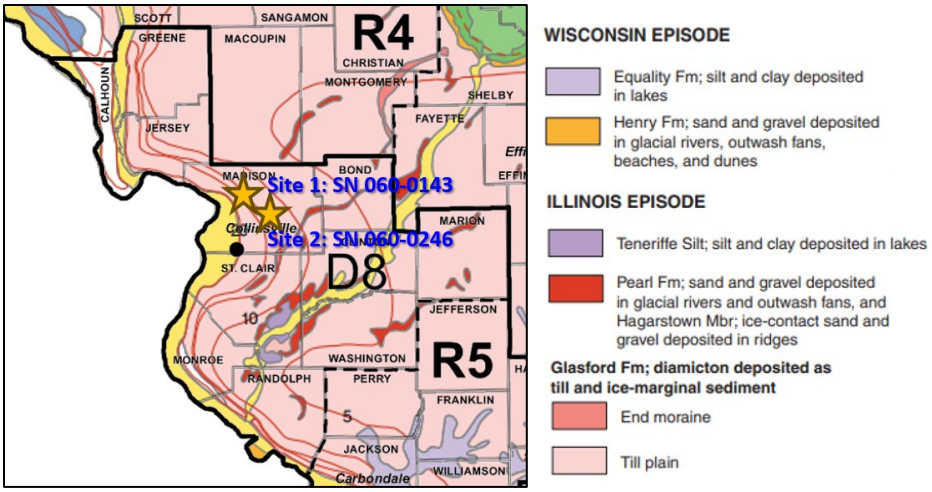

Figure 146. Map of location of sites with SCPT/CPTu data—District 8.

Source: Georgia Tech

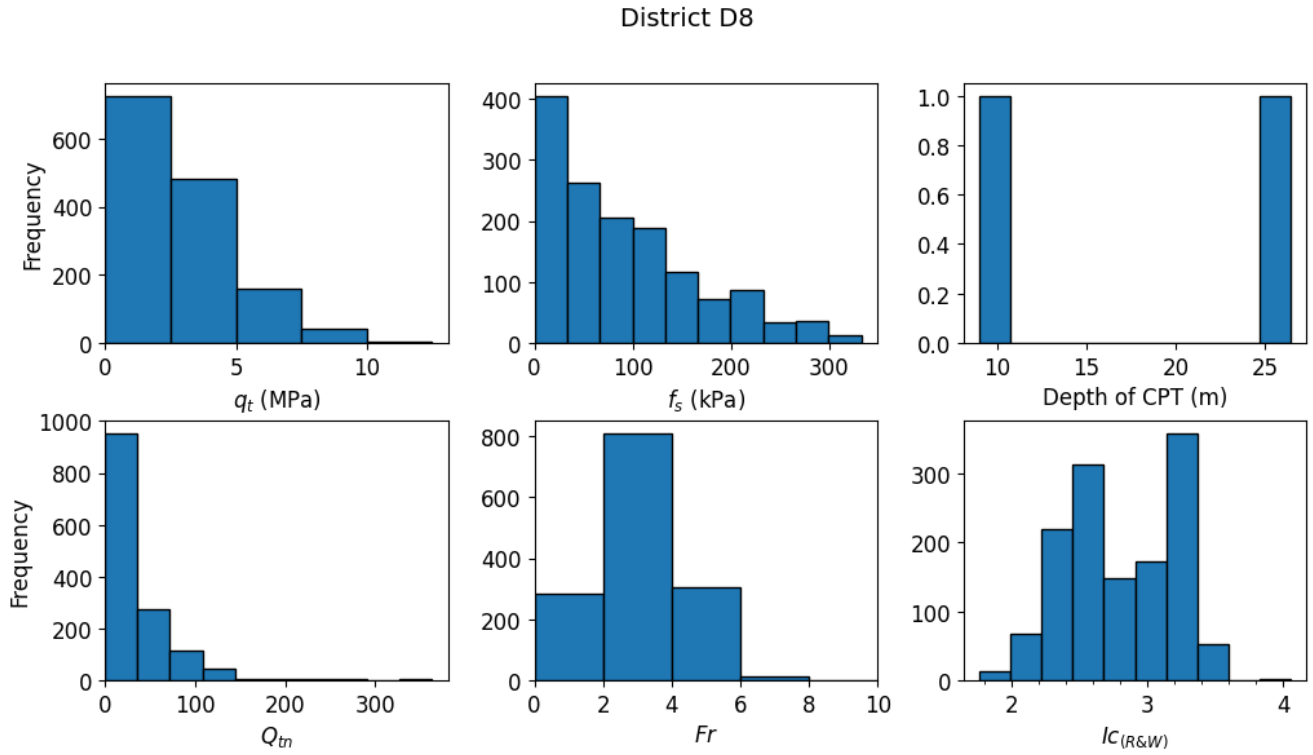

Figure 147. Characteristics of CPT data in District 8.

Source: Georgia Tech

District 8: Site 1 (SN 060-0143)

Figure 148 shows the location of the CPT conducted at this site, as well as the variations of q_t, f_s, u_2, B_q, and I_c versus depth. The CPT data show a heterogeneous top layer composed of silt and sand

mixtures with thin interlayers of clay until 12 m (39.4 ft) depth. The bottom layer is composed of clays and silt mixtures. The top layer shows q_t, f_s, u_2, and B_q values in the range of 2–10 MPa (290–1450 psi), 100–250 kPa (14.5–36.3 psi), 0–20 kPa (0–2.9 psi), and close to 0, respectively. The bottom layer shows q_t, f_s, u_2, and B_q values in the range of 1–3 MPa (145–435 psi), 20–120 kPa (2.9–17.4 psi), 100–600 kPa (14.5–87.0 psi), and 0–0.5. Figure 149 shows the CPT-based stratigraphy using the Robertson (2009) SBT chart. The friction angle for the top layer is between 30 and 35°, while for the bottom layer, it is between 18° and 28°. Moreover, the undrained shear strength of the top layer is between 150 and 220 kPa (21.8–31.9 psi), while for the bottom layer, it is between 60 and 120 kPa (8.7–17.4 psi).

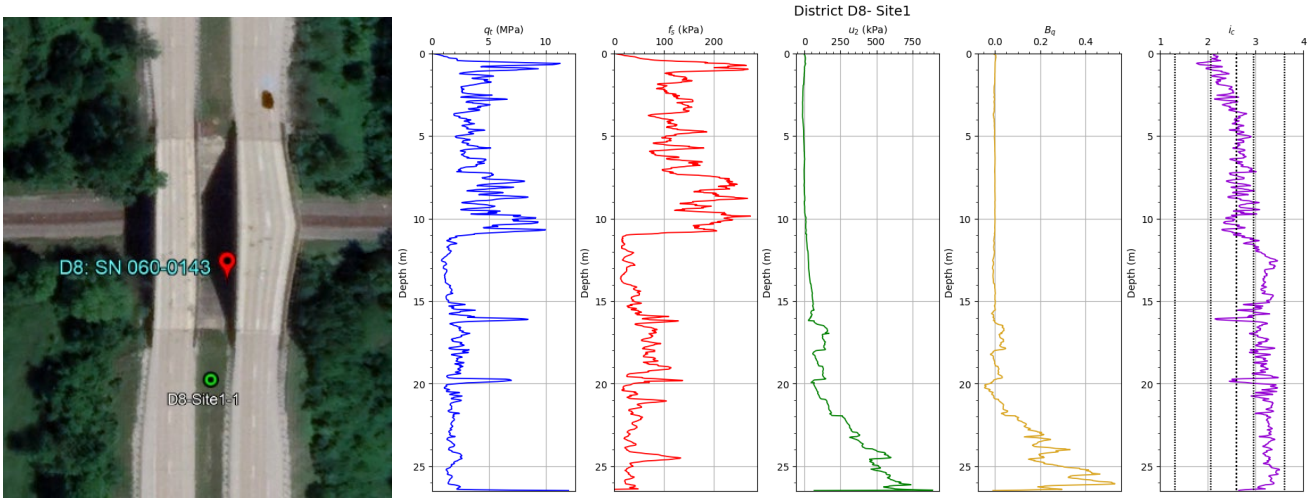

Figure 148. Photo of CPTs locations in and summary of CPT data at site 1 in District 8.

Source: Georgia Tech

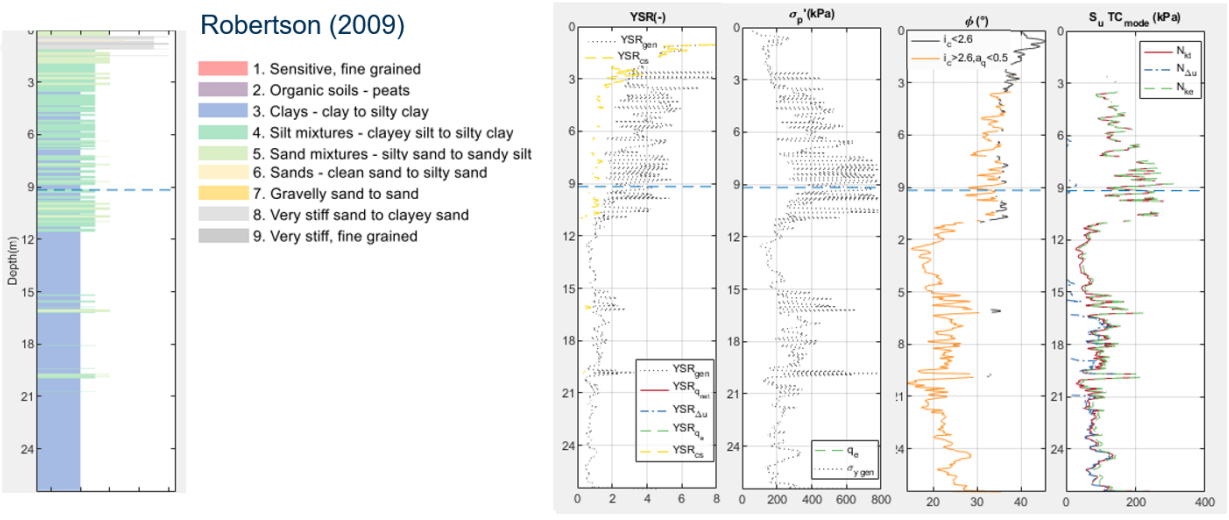

Figure 149. Soil stratigraphy based on SBT charts of District 8—site 1.

Source: Georgia Tech

DISTRICT 9

Figure 150 shows District 9 and the sites with CPT/SCPTu data. Figure 143 shows the main characteristics of the collected data through q_t, f_s, Q_{tn}, F_r, and I_c histograms. The I_c histogram shows a predominance of fine-grained soils. There is only one site (Site 1) where a CPT was conducted (Figure 152); additional details on the CPT response are discussed next. Please refer to Appendix A for the processing of all CPTu/SCPTu data.

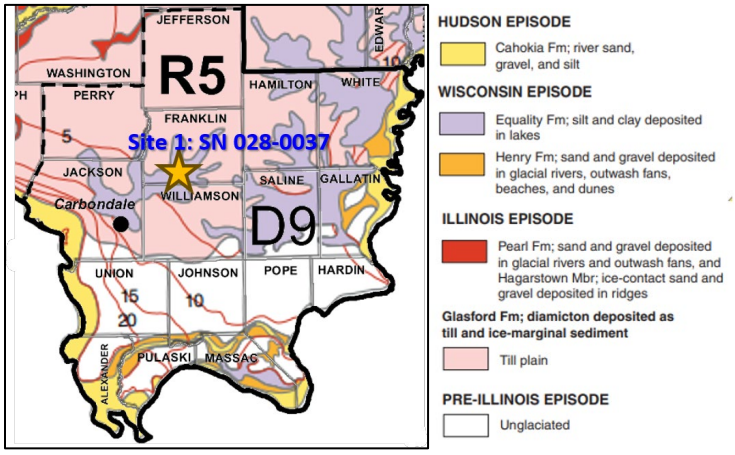

Figure 150. Map of site location in District 9.

Source: Georgia Tech

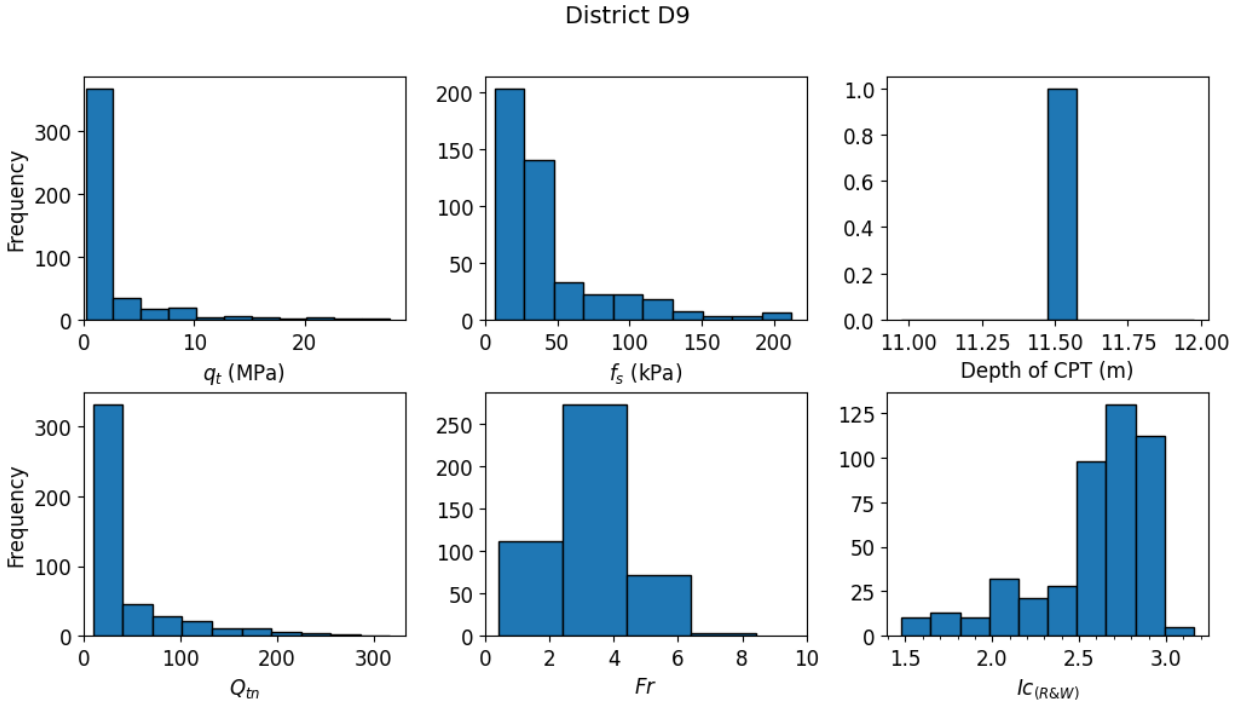

Figure 151. Characteristics of CPT data in District 9.

Source: Georgia Tech

District 9: Site 1 (SN 028-0037)

Site 1 is in Plumfield. Figure 152 shows the location of the CPT collected for this site, as well as the variations of q_t, f_s, u_2, B_q, and I_c versus depth. The CPT data show the presence of silty mixtures and clays through all the profile as well as thin layers of sands and sandy mixtures with a thickness lower than 0.5 m (1.64 ft) below 7 m (23.0 ft) depth. The interbedded sandy layers show q_t, f_s, u_2, and B_q values in the range of 4–15 MPa (580–2175 psi), 60–200 kPa (8.7–29.0 psi), 0–250 kPa (0–36.3 psi), and 0–0.1. The clays and silt mixtures show q_t, f_s, u_2, and B_q values in the range of 0.2–3 MPa (29–435 psi), 10–80 kPa (1.45–11.6 psi), 0–700 kPa (0–101 psi), and 0–0.6. Figure 153 shows the soil stratigraphy based on the Robertson (2009) SBT chart. Below 2 m (6.6 ft) depth, the YSR varies from 2 to 5. The estimated shear strength parameters show significant variability but indicate a superficial layer with lower undrained shear strength above 4 m (13.1 ft) depth, ranging between 10 and 20 kPa (1.45–2.9 psi). Meanwhile, the estimated undrained strength at deeper locations varies between 50 and 100 kPa (7.2–14.5 psi). For the interbedded sandy layers, the friction angle varies between 35° and 40°.

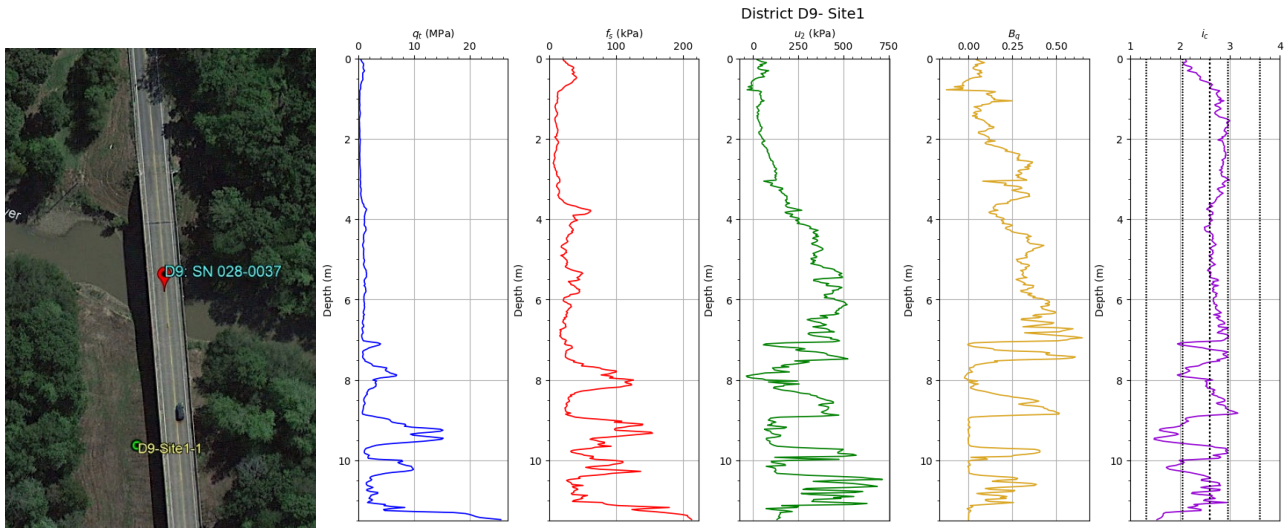

Figure 152. Photo of CPTs locations in and summary of CPT data at site 1 in District 9.

Source: Georgia Tech

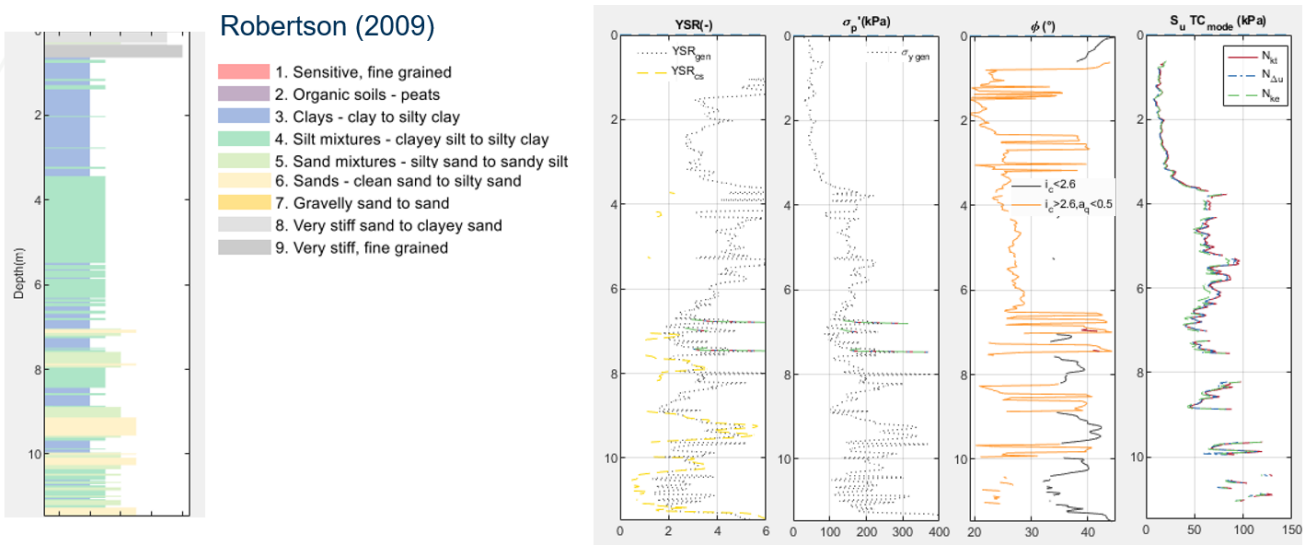

Figure 153. Soil stratigraphy based on SBT charts of District 9—site 1.

Source: Georgia Tech

CHAPTER 5: SPT-CPT CORRELATIONS

This chapter describes the SPT-CPT correlations developed for the State of Illinois based on the data generated in this study. First, we discuss existing and published SPT-CPT relationships, which are used to select the functional form of the developed SPT-CPT correlations for Illinois. Then, we discuss the criteria to select paired sets of SPT-CPT data for analysis. Finally, we present the developed relationships to estimate the number of blow counts in an SPT test from CPTu data.

It is also worth highlighting that the motivation of this chapter is to provide the IDOT correlations to take advantage of the historical SPT data collected over decades. As discussed in several references (e.g., Jefferies & Davies, 1993; Idriss & Boulanger, 2008) and this report, the advantages of CPT/SCPTu tests over SPT have been gradually recognized, especially during the last few years. However, providing procedures for relating future CPT/SCPTu data to SPT may be useful, as indicated by IDOT. In developing the correlations, we used information provided by IDOT as part of this project to extract SPT data, which does not necessarily reflect all available data at IDOT.

EXISTING SPT-CPT CORRELATIONS

The standard penetration test (SPT) has been used since 1902 (Kulhawy & Mayne, 1990) and involves the repeated blows of a drop hammer to drive a thick hollow tube (aka the “split spoon” or split-barrel sampler) a total of 18 inches into virgin ground during the drilling or augering operations of a soil boring. The number of blows to advance this sampler the last 12 inches is called the SPT resistance, or “N-value.” The test is repeated within the borehole at regular vertical depth intervals of 5 feet. Thus, a single number (N-value) is obtained at discrete points, possibly missing soil layers (less than 5 feet thick) and not capturing any lenses or strata within the non-sampled zone. Nevertheless, SPTs in borings have been typically utilized by DOTs in the US and Canada for quite some time and offer exploration capabilities in very hard ground and bedrock. Borings with SPT are labor-intensive, slow, and must be conducted with care, as heavy rods, hammers, augers, and casing are lifted above the working area of the drillers; thus, safety is a major concern. Soil borings with SPT advance at the rate of about 50 to 100 feet/day typically.

Moreover, the measured N-value has been shown to depend upon a number of factors that necessitate corrections, primarily related to the energy of the hammer system that has a highly variable range due to differences in equipment, operators, the conduct of the test, and other conditions. The corrected N-value is termed N_{60} and requires a calibration of the drill rig, hammer system, and field crew using a dynamic force measuring system that compares the kinetic energy with the potential energy (Idriss & Boulanger, 2008). Other factors that affect the measured N-value include the borehole diameter, rod type, length of rods, test depth, water table, and more (Rix et al., 2019). A serious consequence is this old test has shown difficulties in reliability, repeatability, and undue uncertainty in geoengineering applications, especially in the modern age of 2024.

The continuous nature and multiple measurements of CPT provide valuable information about soil variability that is difficult to match with typical borehole sampling and laboratory testing. The CPT collects at least three readings with depth: q_t, f_s, and u_2, which are all continuously recorded and

available in digital format during the sounding. As soon as the sounding reaches the intended depth, the results can be analyzed fully, plotted or shown graphically on computer monitors, and relayed wirelessly back to the chief engineer at the main office. A production CPT rig can conduct as many as 300 to 600 feet/day of vertical soundings. Moreover, CPT has much more repeatability compared to SPT tests. In round numbers, SPT, even with energy measurements and its subsequent correction, is four to five times less repeatable than CPT (Jefferies & Been, 2006).

The seismic piezocone test (SCPTu) can provide additional measurements of shear wave velocities and pore pressure dissipations at selected depths, thus offering five independent readings from the same sounding. Hence, several independent, reliable measurements can be made cost-effectively using CPT, compared to a single *N* value measured in a SPT (N is the number of blow counts) obtained typically every 0.5 to 1.5 m (1.64 to 4.92 ft). As a result, CPT is increasingly being preferred for in situ testing. Robertson (2012) highlights that Jefferies and Davies (1993) correctly suggested that the most reliable way to obtain SPT N values was to perform a CPT and convert the CPT to an equivalent SPT N_{60} blow count. The reliability of this SPT estimation may be higher than measuring the SPT value directly. More recently, Jarushi et al. (2015) have developed SPT-CPT correlations for the State of Florida using data from FDOT projects. Specifically, they developed correlations between q_c and N as well as f_s and N. In this type of correlation, N is usually replaced by N_{60}, the SPT value corresponding to hammer efficiency of 60%. Hammer efficiency refers to the ratio of delivered energy to theoretically applied energy.

Researchers have proposed several SPT-CPT correlations. According to Shahien and Ali Albatal (2014), they can be categorized generally into four groups:

1. Correlations based on median grain size, D_{50}.
2. Correlations based on fines content, $FC\%$
3. Correlations based on Soil Behavior Type Index, I_c
4. Correlations based on other variables/forms

Selected available correlations that are used in practice have been categorized using these groups in the following tables. The cone tip resistance is shown as q_t to indicate that the corrected tip resistance should be used in the correlations for fine-grained soils, while in sandy soils $q_t \approx q_c$. The N_{xx} subscripts refer to the "xx" energy ratio used in the correlation; if subscripts are omitted, no energy correction was performed.

Table 25 presents selected SPT-CPT correlations based on D_{50}. An example of correlating SPT-CPT data based on mean grain size is shown in Figure 154. The correlation proposed by Robertson et al. (1983) fits the hollow diamond data points. Kulhawy and Mayne (1990) added data and obtained a correlation for a broader range of particle sizes, from micrometer-sized clays to centimeter-sized gravelly sands.

Table 25. Available SPT-CPT Correlations Based on Median Grain Size (D_{50}) in mm

Correlations	Reference
$(q_t/P_a)/N = 5.48 + 1.36log_{10}D_{50}$	Muromachi & Kobayashi (1982)
$(q_t/P_a)/N_{55} = 7.5\ (D_{50})^{0.26}$ $(q_t/P_a)/N_{55} = 7.19\ (D_{50})^{0.27}$	Robertson et al. (1983) Bol (2023)
$(q_t/P_a)/N = 8.0\ (D_{50})^{0.3}$	Burland & Burbidge (1985)
$(q_t/P_a)/N_{60} = 6.0\ (D_{50})^{0.24}$	Seed & De Alba (1986)
$(q_t/P_a)/N_{60} = 4.95\ (D_{50})^{0.168}$	Andrus & Youd (1989)
$(q_t/P_a)/N = 5.44\ \ (D_{50})^{0.26}$	Kulhawy & Mayne (1990)
$(q_t/P_a)/N = 11.1\ (D_{50})^{0.261},\ 0 \leq N < 10$ $(q_t/P_a)/N = 8.4\ (D_{50})^{0.225}, 10 \leq N < 30$ $(q_t/P_a)/N = 6.0\ (D_{50})^{0.165}, 30 \leq N$	Suzuki et al. (1998)
$(q_t/P_a)/N_{60} = 3.86\ \ (D_{50})^{0.43}$	Anagnostopoulos et al. (2003)

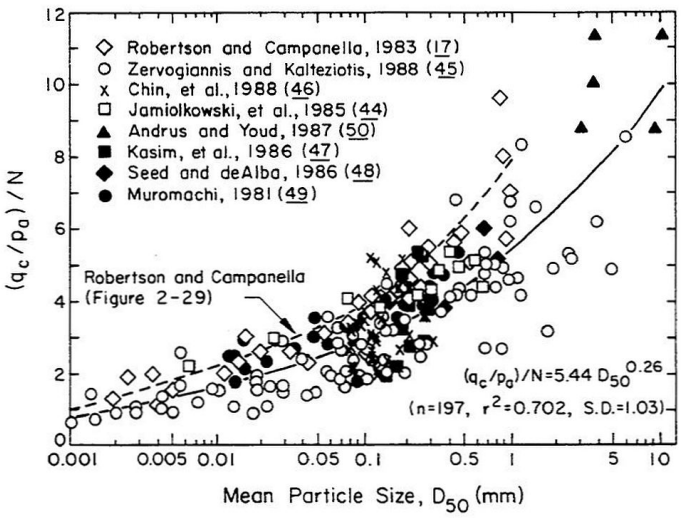

Figure 154. The variation of $(q_c/P_a)/N$ with respect to mean grain size D_{50}.

Source: Kulhawy & Mayne (1990)

When applying or producing SPT-CPT correlations, it is crucial to be aware of special soil conditions at the sites used to develop the correlations. For example, Lees et al. (2013) fitted SPT-CPT data for carbonate soil ranging from silt to sand, obtaining a relatively poor correlation with a r^2 of 0.56 (Figure 155-A). Further, he compared the Robertson et al. (1983) correlation with their dataset with mean particle size information, as shown in Figure 155-B. Carbonate soils are generally easy to crush, fracture, or compress, which could explain in part why the Robertson et al. (1983) correlation

developed for sands does not fit these data well. This example shows the importance of selecting a correlation according to the site-specific conditions and local geology.

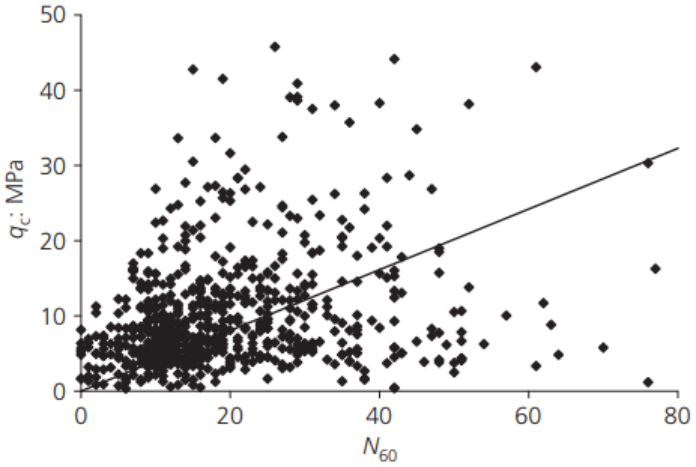

A. Correlation between CPT cone resistance q_c and SPT N value in carbonate soils (Lees et al., 2013)

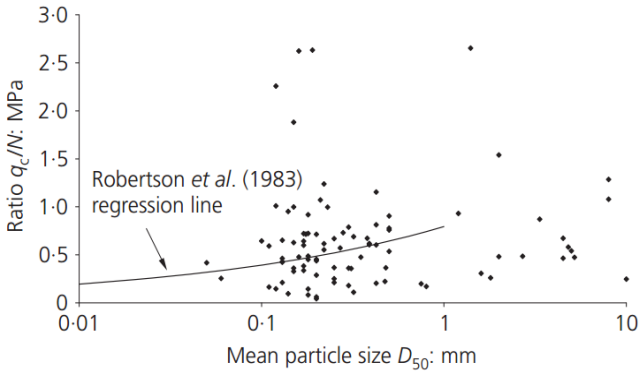

B. Variation of n = q_c/N with mean particle size D_{50} (Lees et al., 2013)

Figure 155. An example of fitting data for a SPT-CTP correlation in carbonate soils.

Source: Lees et al. (2013)

Fines content, $FC\%$, is also a commonly used index to relate SPT-CPT data. Shahien and Ali Albatal (2014) collected some correlations from the literature presented in Table 26. For example, Figure 147 shows the data and correlation. Kulhawy and Mayne (1990) proposed based on fines content. They collected data from four references and fitted a linear relationship between $(q_t/P_a)/N$ and fines content.

Table 26. Available SPT-CPT Correlations Based on Fines Content

Correlations	Reference
$(q_t/P_a)/N_{64} = 4.90 - 0.03\ (FC\%)$	Jamiolkowski et al. (1985)
$(q_t/P_a)/N_{55} = 4.70 - 0.05\ (FC\%)$	Chin et al. (1988)
$(q_t/P_a)/N = 4.25 - 0.024\ (FC\%)$	Kulhawy & Mayne (1990)
$(q_t/p_a)/N = 0.0026(FC)^2 - 0.263FC + 12.34$, for: $0 \leq N < 10$ $(q_t/p_a)/N = 0.00085(FC)^2 - 0.120FC + 8.733$, for: $10 \leq N < 30$ $(q_t/p_a)/N = 0.001(FC)^2 - 0.059FC + 5.59$, for: $30 \leq N\ and\ \ FC\% < 20$	Suzuki et al. (1998)

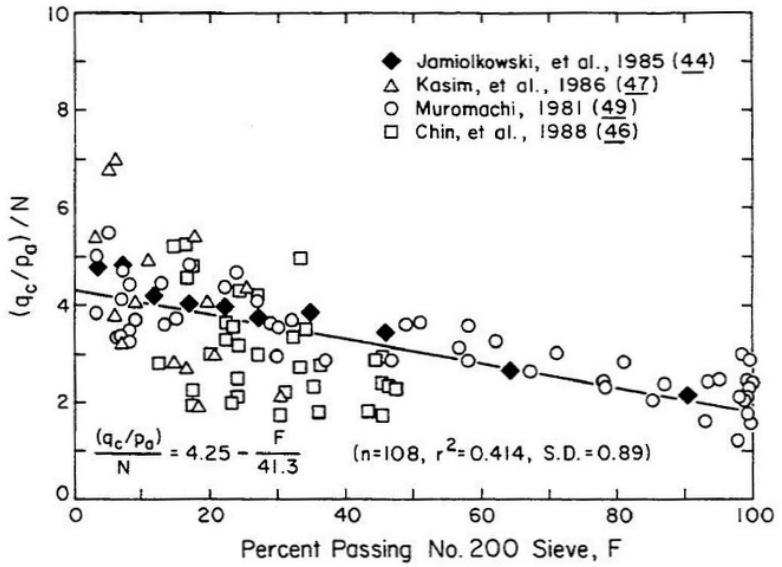

Figure 156. An example of SPT-CPT correlation based on fines content.

Source: Kulhawy & Mayne (1990)

A third group of relationships is based on soil behavior type index, I_c. Table 27 shows some selected SPT-CPT correlations based on I_c. Figure 157, Figure 158, and Figure 159 show examples of some of the correlations in Table 27, highlighting their adaptability to a wide range of soil types. Again, the specific geology and soil conditions are also critical for I_c-based correlations. For instance, Papamichael and Vrettos (2018) conducted a series of tests on marine and near-shore soils from the Mediterranean Region, finding that the correlation proposed by Robertson (2012) mainly for sands had limitations for their site, probably because of the differences in soil conditions.

Table 27. SPT-CPT Correlations in Literature Based on Soil Behavior Type Index

Correlations	Reference
$(q_t/P_a)/N_{60} = 8.5(1 - I_{c-JB}/4.75)$	Jefferies and Davies (1993)
$(q_t/P_a)/N_{60} = 8.5(1 - I_{c-RW}/4.6)$	Lunne et al. (1997)
$(q_t/P_a)/N_{60} = 10^{(1.1268-0.2817I_{c-RW})}$	Robertson (2012)
$(q_t/P_a)/N = 31.25\,exp(-0.68I_{c-RW})$, $0 \le q_t < 5$ $(q_t/P_a)/N = 18.60ex\,p(-0.54I_{c-RW})$, $5 \le q_t < 15$ $(q_t/P_a)/N = 10.21ex\,p(-0.35I_{c-RW})$, $15 \le q_t$	Suzuki et al. (1998)
$(q_t/P_a)/N_{60} = 43.44\ exp\ (-1.18I_c)$	Papamichael & Vrettos (2018)
$\frac{q_t/Pa}{N_{60}} = \frac{0.26\exp\,(8.22[1 - (I_{c-RW}/4.5)])}{(q_t/Pa)^{0.65}}$	Shahien & Ali Albatal (2014)

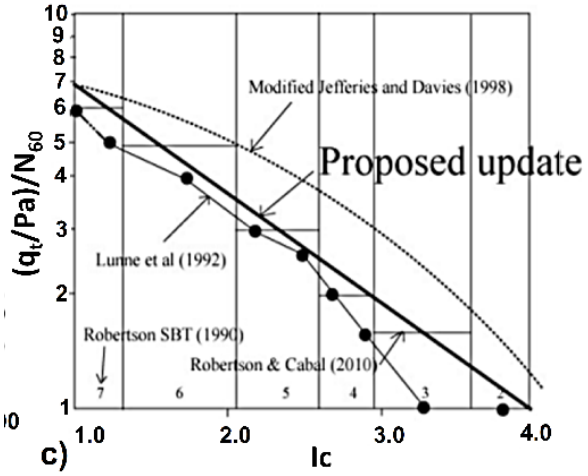

Figure 157. Example of SPT-CPT correlation based on soil behavior type index. "Proposed Update" refers to the correlation proposed by Robertson (2012).

Source: Robertson (2012)

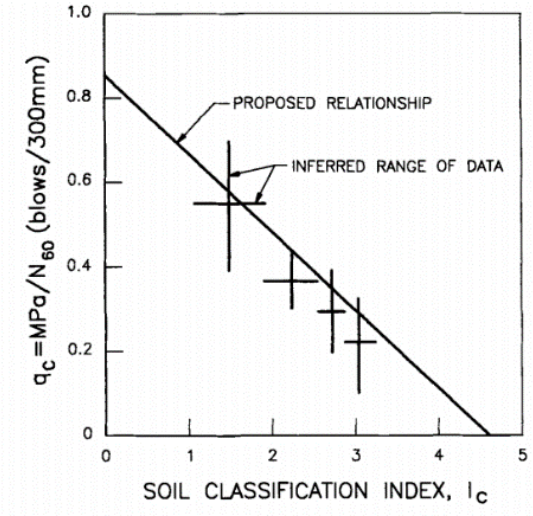

Figure 158. Example of SPT-CPT correlation based on soil behavior type index.

Source: Jefferies & Davies (1993)

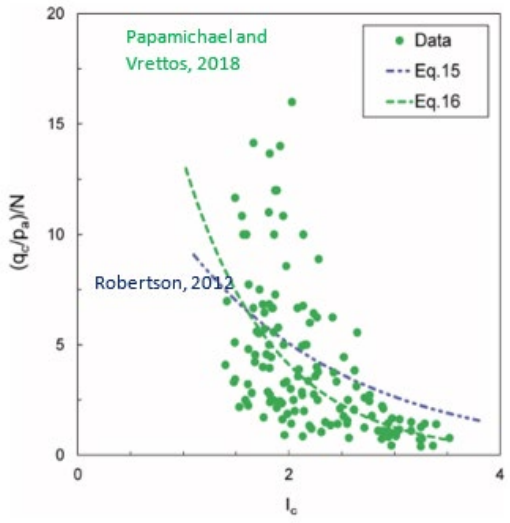

Figure 159. Example of SPT-CPT correlation based on soil behavior type index.

Source: Papamichael & Vrettos (2018)

In addition to the previously mentioned groups of SPT-CPT correlations, other relationships are functions of other variables. Table 28 shows some selected correlations in this category.

Table 28. SPT-CPT Other SPT-CPT Correlations in the Literature

Correlations	Reference
$\frac{q_{c1}/\sigma_{atm}}{(N_1)_{60}} = (2.092D_r + 2.224)^{3.788}/46(D_r)^2$	Idriss & Boulanger (2006)
$(N_1)_{60CS} = 0.356[(q_{c1N})_{cs}]^{0.851}$ $(q_{c1N})_{cs}$ as defined in Robertson & Wride (1998)	Andrus et al. (2004)
$q_c/\sigma_{atm} = 10.6(N_{60})^{0.71}$	Souza et al. (2012)
$\frac{q_c/\sigma_{atm}}{N_{60}} = \frac{17.13D_{50}^{0.26}}{N_{60}^{0.49}(FC)^{0.27}}$	Shahien & Albatal (2014)

Finally, previous efforts also suggest linear statistical correlations between q_c and N, with different ratios according to soil type. A summary of this type of correlation is presented in Table 29.

Table 29. SPT-CPT Correlations for a Range of Soil Types

Reference	Soil Type	n Ratio
Schmertmann (1970, 1978) $n = q_t/N$ q_t in kg/cm2.	Silts, sandy silts, slightly cohesive silt-sand mixtures	2 - 4
	Clean, fine to medium sand and slightly silty sand	3 - 5
	Coarse sand and sand with little gravel	4 - 5
	Sandy gravel and gravel	6 - 8
Sanglerat (1970) $n = q_t/N$ q_t in kg/cm2.	Silts, sandy silts, slightly cohesive silt-sand mixtures	2
	Clean, fine to medium sand and slightly silty sand	3 - 4
	Coarse sand and sand with little gravel	5 - 6
	Sandy gravel and gravel	8 - 10
Robertson et al. (2022) $n = (q_t/P_a)/N_{60}$	Sensitive fine-grained (SBT zone 1)	2
	Organic soils–peats (SBT zone 2)	1
	Silty clay to clay (SBT zone 3)	1.5
	Clayey silt to silty clay (SBT zone 4)	2
	Silty sand to sandy silt (SBT zone 5)	3
	Clean sand to silty sands (SBT zone 6)	5
	Dense sand to gravelly sand (SBT zone 7)	6
	Very stiff sand to clayey sand (SBT zone 8)	5
	Very stiff, fine-grained (SBT zone 9)	1

SELECTION OF SPT-CPT PAIRS

Screening of Data Pairs

Ku et al. (2010) provided recommendations for selecting data from paired SPT-CPT tests. Figure 160 shows the procedure they followed in selecting SPT-CPT pairs. In the procedure, a range of tip resistance values (q_c) centered around an available N value is selected and averaged to have a representative q_c, which can be later correlated with N. The red circle in the q_c plot in Figure 160 represents the N location, and the vertical red lines represent the range of q_c values being considered, which correspond to the 30 cm (0.98 ft) of penetration in the SPT plus an additional 15 cm (0.49 ft) below the cone tip due to its effects, thus 45 cm (1.48 ft) in total. Ku et al. (2010) suggest considering only layers where q_c is not changing significantly. For example, the upper part of the profile in Figure 160 shows a smooth variation of q_c, whereas the lower part shows abrupt variations at some depths. They also recommend using layers where q_c does not exceed 30% of the average q_c value for the range of depths being considered.

In addition, removing outliers is also advantageous to prevent the correlations from being affected by unusual and anomalous values. Bol (2023) recommends dividing the data into bins corresponding to different ranges of I_c, then the mean and standard deviation of the variable of interest (e.g., q_c) can be calculated for each bin. Finally, values above the mean plus two standard deviations are classified as outliers and are removed from the database. The procedures recommended by Ku et al. (2010) and Bol (2023) have been implemented in selecting SPT-CPT paired results using the data collected in this project of the State of Illinois.

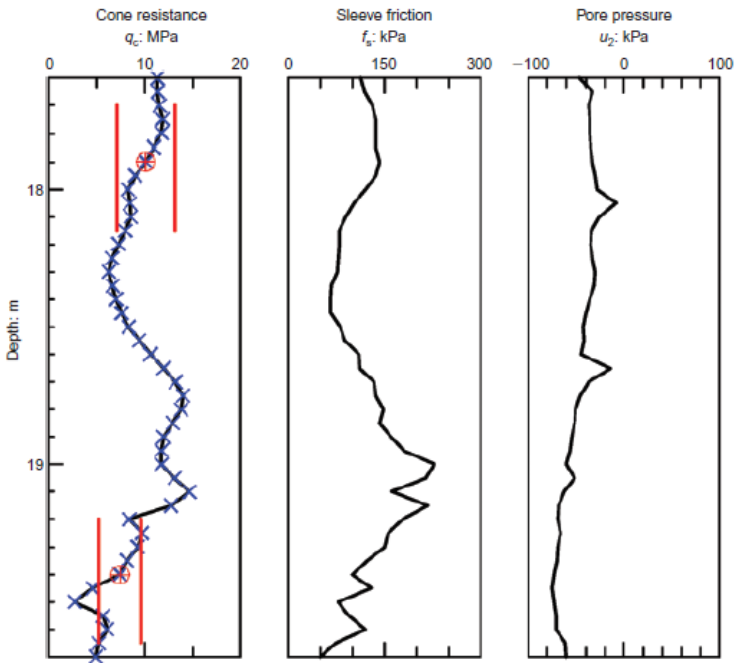

A. Screening of q_c shown in a CPT profile

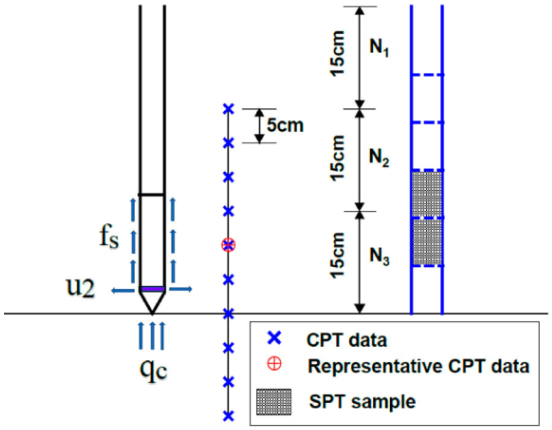

B. Location of representative q_c with respect to SPT N blow count depth

Figure 160. Pairing data points through q_c screening.

Source: Ku et al. (2010)

Processing of Illinois Data

The considered CPT data for the various IDOT districts have been presented in Chapter 4. Available SPT data were based on the information provided by IDOT from historical boring logs conducted in Illinois. CPTs and boreholes were paired based on their latitude-longitude coordinates. The boring logs were provided in non-editable formats; hence, the Georgia Tech team conducted an exhaustive manual review to compile/extract relevant information. Where possible, the N (the SPT blow count number) was energy corrected to a 60% energy efficiency. In fact, the correction energy factor (C_E) was only available for the Florence site in District 6. For other sites, C_E was assumed according to the hammer type registered in the boring logs. Of note, N values equal to zero and greater than 50 were not considered in the data processing. In addition, the soil descriptions from boring logs were compared with the index soil behavior (I_c) to identify cases where the borehole stratigraphy did not match the CPT stratigraphy, and hence the evaluated depths were not compared and included in the dataset. In cases with contrasting descriptions (e.g., sand versus clay), the SPT-CPT pairs were discarded. Finally, blow counts registered in soil layers with organic matter and peat were not considered, so the developed correlations in this project do not apply to these soil types.

After implementing the described steps, 585 data pairs (i.e., q_t and N_{60} paired values) were obtained. The next step in the processing consisted of applying the Ku et al. (2010) and Bol (2023) screening procedures previously discussed. Figure 161 shows an example of the data pairing. The location of the representative resistance tip is plotted along with the +/− 30% boundaries, so data pairs where the q_t profile exceeded these boundaries are removed from the database. In this way, only q_t values that did not show a high variation and therefore, represent a relatively homogenous layer were considered. As a result of the screening procedures, there were 304 data pairs left. The maximum distance considered in this study between a CPT sounding and a borehole is 30 m (98.4 ft). So, 73 data pairs were removed after applying the maximum distance filter. Then, the data were divided into 8 I_c bins, the mean and standard deviation were calculated for each bin, and the values

identified as outliers; 7 in total were removed. The final database was composed of 224 data pairs, and Figure 162 shows the distribution of the paired data through histograms.

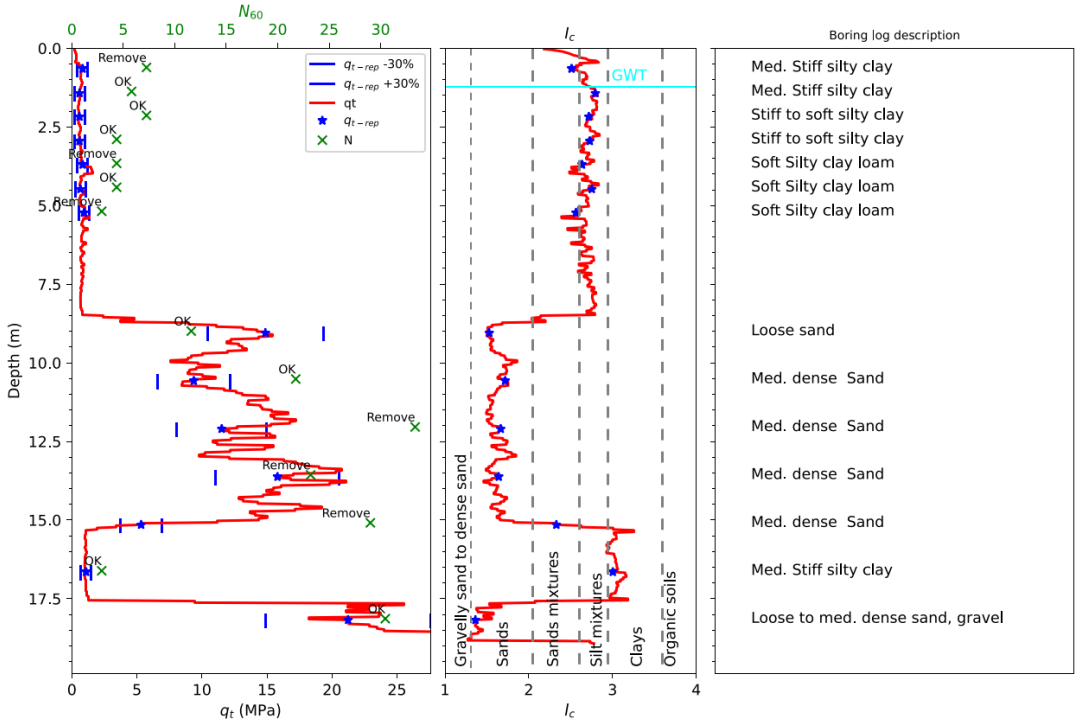

Figure 161. Screening example (CPT: D6-Site1-14 and borehole: SPT-9) for Illinois data.

Source: Georgia Tech

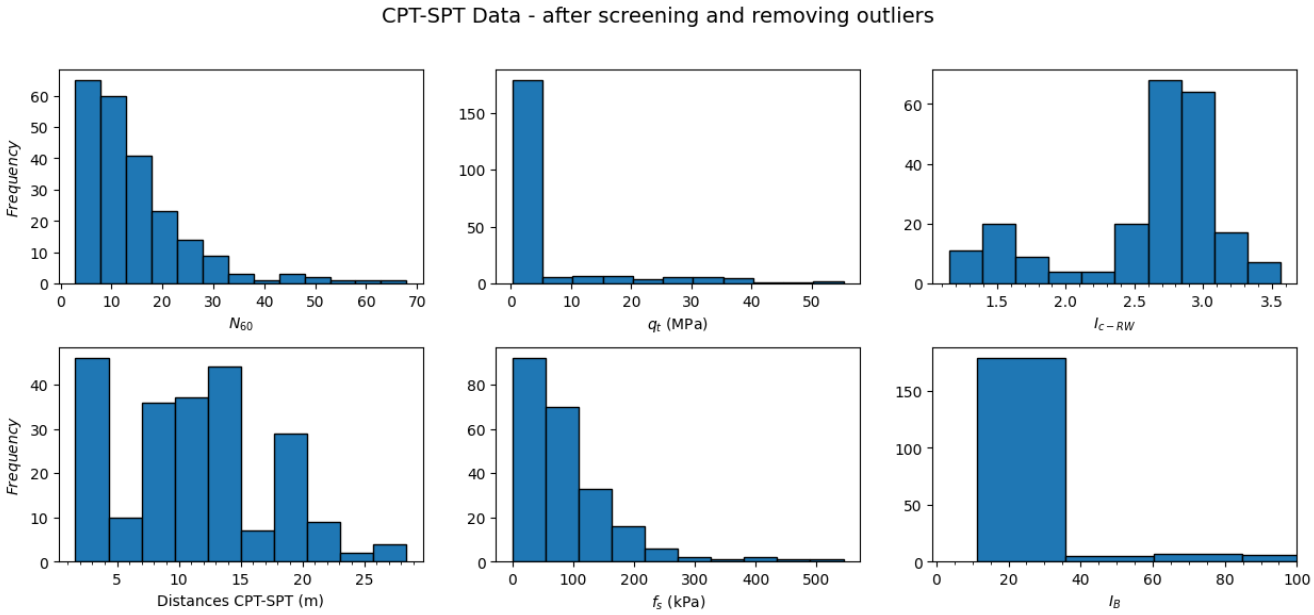

Figure 162. Pairs of CPT-SPT data from Illinois after screening and removal of outliers.

Source: Georgia Tech

SPT-CPT CORRELATIONS FOR ILLINOIS

The review of existing SPT-CPT correlations and data exploratory analyses showed that the functional forms proposed by Robertson (2012) and a power trendline fitting provided advantages (i.e., less standard deviation) compared to other functional forms shown in Table 27. The coefficients in the functional forms of Robertson (2012) were updated using the data collected in this project by conducting statistical regressions. The regressions were conducted between $(q_t/P_a)/N_{60}$ and I_{c-RW}, where I_{c-RW} is the soil behavior type material index and P_a is the atmospheric pressure, equal to 0.1 MPa if q_t units are MPa. The I_{c-RW} behavior was calculated based on Robertson and Wride (1998) and updated with Q_{tn} as modified by Robertson (2009). Table 30 shows the correlations obtained using the database built in this study for Illinois. The correlation based on a power trendline shows better performance (r^2 = 0.74) compared to the correlation based on the Robertson (2012) functional form (r^2 = 0.69); however, the two correlations show relatively high r^2 values in the context of existing correlations. Figure 163-A illustrates the fitting of the power trendline to the collected data. Figure 163-B illustrates the fitting of the functional form of Robertson (2012). The original correlation from Robertson (2012) is also shown for reference, highlighting a performance that is not ideal for the collected data. Figure 164 shows the comparison between the estimated and observed N_{60}. Both correlations have a better performance in the context of measured data when the measured N_{60} is lower than about 20, for higher values the dispersion on the estimates increase. In particular, for N_{60} values higher than 40, the correlations tend to underestimate the N_{60} values (i.e., they are conservative). In this range, based on the available data, when N_{60} is between 20 and 30, the correlation can be unconservative; hence, caution should be exerted in this range.

Table 30. SPT-CPT Correlations for the State of Illinois

Correlations	Comment
$(q_t/P_a)/N_{60} = 26.791(I_{c-RW})^{-2.808}$	Proposed correlation using a power trendline. The correlation has been derived using the database built in this project. r^2 coefficient of determination of 0.744
$(q_t/P_a)/N_{60} = 10^{(1.756-0.561I_{c-RW})}$	Proposed correlation using the Robertson (2012) functional form. The coefficients (i.e., 1.756, 0.561) have been derived through statistical regressions using the database built in this project for Illinois. r^2 coefficient of determination of 0.695.

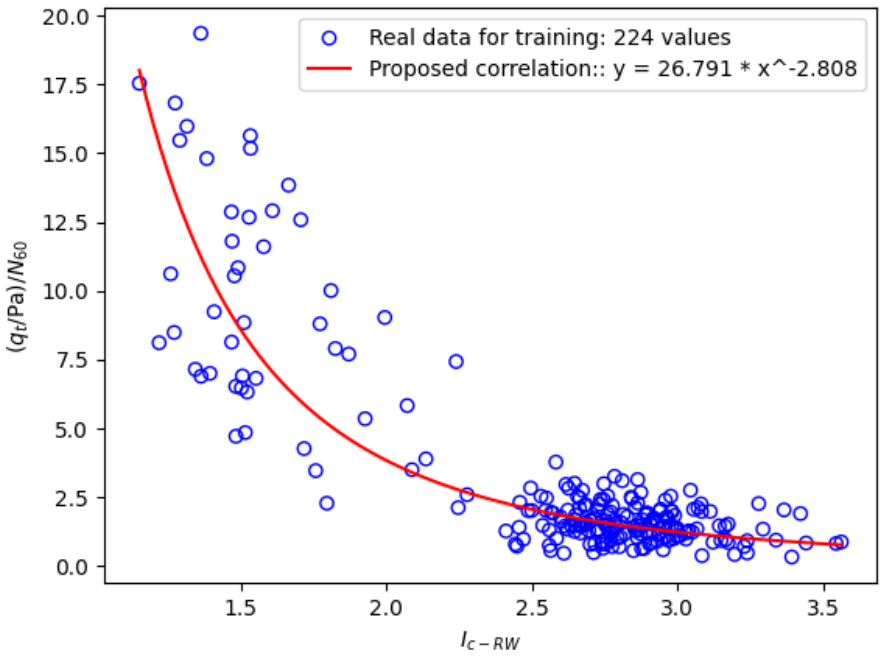

A. Proposed SPT-CPT correlation based on the compiled data, considering a power trendline fitting

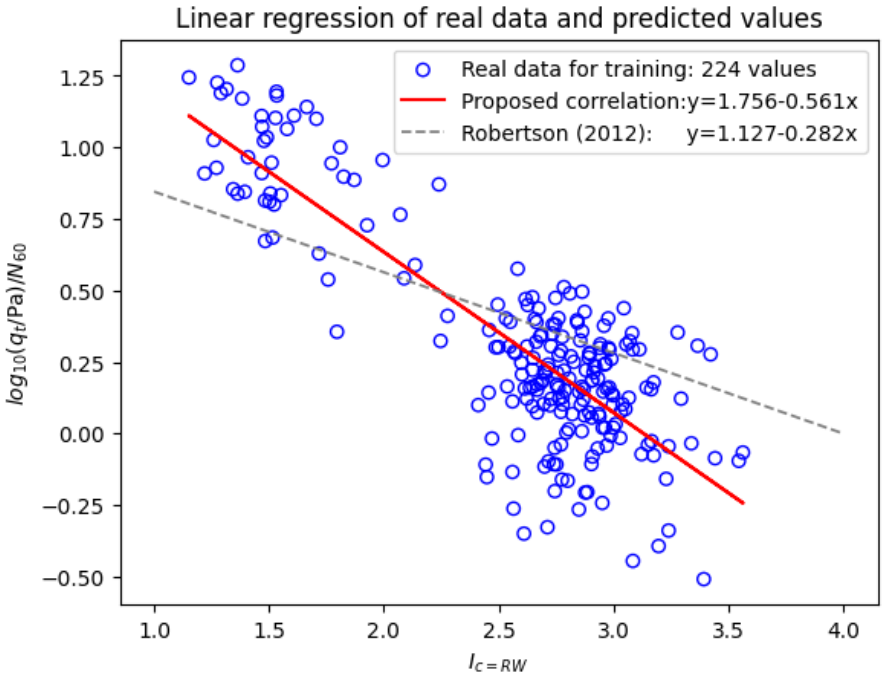

B. ICT correlation for SPT-CPT with Robertson (2012) form

Figure 163. Proposed SPT-CPT correlations considering a functional form similar to that of Robertson (2012). The coefficients of the correlation have been updated using the compiled data. The Robertson (2012) correlation is also shown for reference.

Source: Georgia Tech

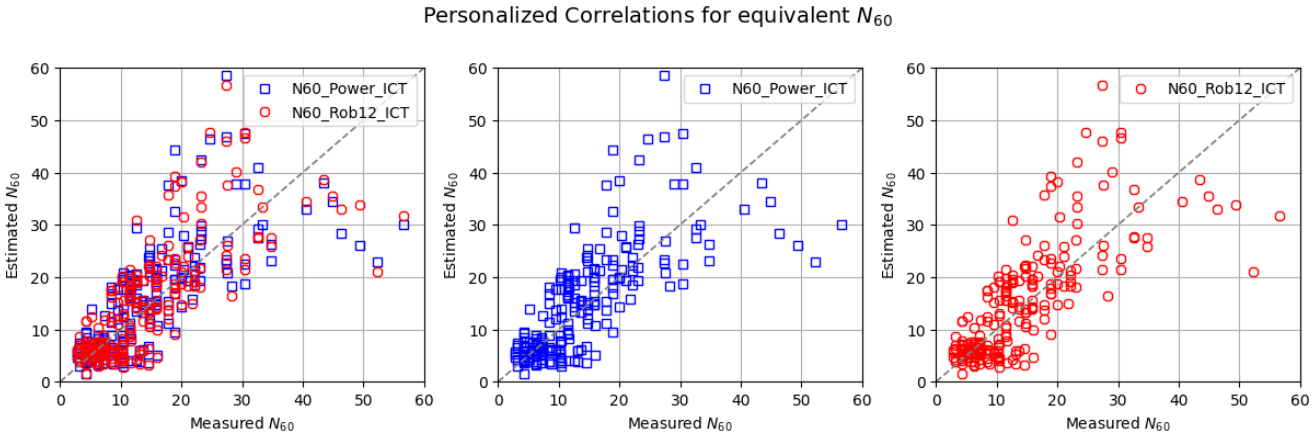

Figure 164. N_{60} estimation versus measured values from CPT using models for Illinois.

Source: Georgia Tech

CHAPTER 6: CASE STUDIES FOR CPT DATA INTERPRETATION WITH LABORATORY TESTING FROM SHELBY TUBES

In this chapter, the application of procedures discussed in Chapter 3 are showcased for sites in Illinois where "intact" samples were collected using Shelby tubes, and laboratory testing was conducted on recovered samples. Specifically, data collected on two sites, Florence and Northwestern University, is used to showcase the procedures. IDOT collected Shelby tubes at the Florence site and conducted laboratory testing. Georgia Tech also performed laboratory testing on Shelby tube samples obtained from the Florence site as an additional in-kind contribution to the project. (Laboratory testing was not part of the project scope.) In addition, data from available laboratory testing conducted on samples recovered at the national geotechnical experimentation site at Northwestern University (Finno et al., 2000) were considered.

FLORENCE SITE—DISTRICT 6

Shelby Tube Information and Laboratory Testing

Florence is located about 50 miles west of Springfield, Illinois, and was selected for a major bridge crossing the Illinois River. Figure 165 shows the boring locations where Shelby tubes were collected at the Florence site in District 6. IDOT conducted laboratory tests on samples recovered from borings drilled next to EMB-1-1, EMB-3-2, and EMB-5-2 boreholes.

Georgia Tech also performed laboratory tests on soil specimens collected as Shelby tubes near borehole EMB-1-1. The distribution of Shelby tubes between IDOT and Georgia Tech is shown in Figure 166. These laboratory test results from EMB-1-1 will be used in this chapter for the geotechnical interpretation and comparison with results from the Georgia Tech CPT Sounding D6-Site1-19 and ConeTec Sounding D6-Site1-7. A summary of the laboratory programs executed by IDOT and Georgia Tech is shown in Table 31.

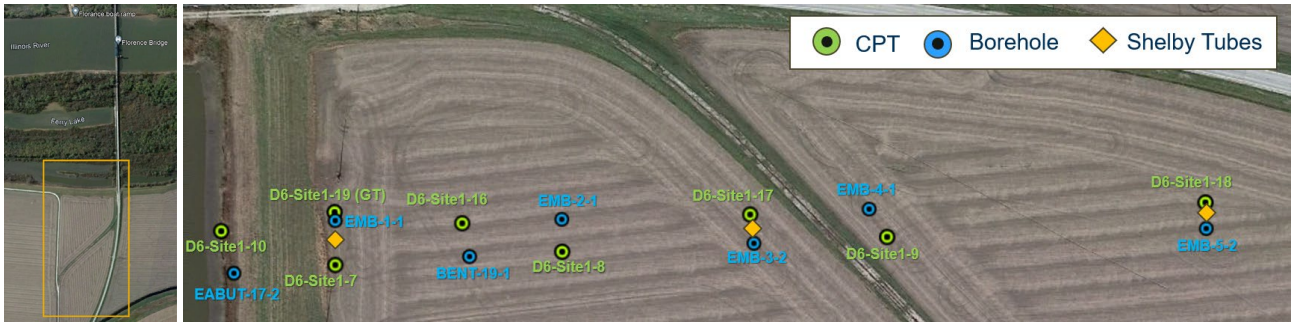

Figure 165. Photo of locations of Florence CPT soundings and borings for Shelby tube samples.

Source: Georgia Tech

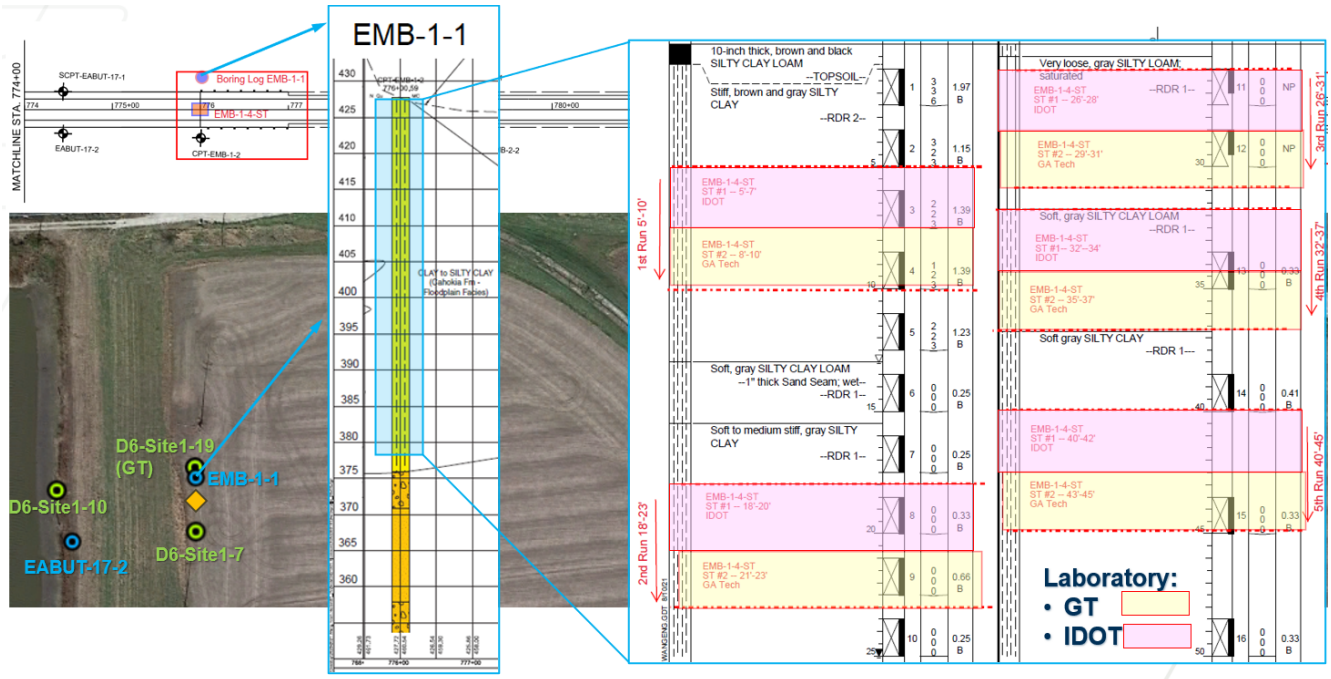

Figure 166. Shelby tubes distribution for laboratory testing by both IDOT and GT.

Source: Georgia Tech

Table 31. Laboratory Testing Performed in Shelby Tubes Next to Borehole EMB-1-1

IDOT Tests	Georgia Tech Tests
Grain size distribution (5)	*Laser diffraction analysis (grain size distribution) (5)*
Plasticity limits (5)	*Sieve analysis (5)*
Sieve analysis	*Methylene blue adsorption (5)*
Specific gravity (5)	*Fall cone test (5)*
Moisture content (19)	*Index analysis (5)*
Consolidation test (5)	*Moisture content (5)*
Unconfined compression test (UU)	*Unit weight (5)*
Unit weight (19)	*Thermal gravimetric analysis (5)*
Multistage triaxial shear test – unconsolidated undrained (UU) (5)	*Consolidation tests with shear wave measurements (5)*
Multistage triaxial shear test – consolidated undrained (CU) (1)	

Note: The number of tests is included in parentheses.

A summary of the classification and consolidation testing at the specified Florence location is presented in Table 32. The Atterberg limits of the recovered samples are also plotted in the plasticity chart (Figure 167). Based on the ASTM classification system, most of the samples are classified as lean clay (CL), except for the sample from depth 8′ to 10′ (2.4 to 3.0 m), which is identified as fat clay (CH). Similarly, IDOT laboratory test results identify the samples as silty clays (5′ to 7′ and 40′ to 42′), silty loam (26′ to 28′), and silty clay loams (18′ to 20′ and 32′ to 34′) based on the Illinois Division of Highways classification.

Table 32. Summary of Soil Classification Testing and Consolidation Test at Florence Site (EMB-1-1)

Depth (ft)	Depth (m)	Lab	Silt (%)	Clay (%)	PL (%)	LL (%)	PI (%)	e_0	σ_p' (kPa)	c_r	c_c
5′–7′	1.5–2.1	IDOT	62.21	34.97	22	41	19	0.753	276.4	0.023	0.235
8′–10′	2.4–3.0	GT	57.1	16.3	44	59.5	15.5	0.837	200.0	0.014	0.099
18′–20′	5.4–6.0	IDOT	69.52	26.76	15	33	18	0.828	87.8	0.021	0.235
21′–23′	6.3–6.9	GT	64.2	12.8	27	46.8	19.8	0.788	157.0	0.01	0.128
26′–28′	7.8–8.4	IDOT	78.96	19.03	8	28	20	0.918	203.8	0.012	0.193
29′–31′	8.7–9.3	GT	61.5	10.7	15.8	39.9	24.1	0.952	65.0	0.006	0.091
32′–34′	9.6–10.2	IDOT	71.7	27.3	16	38	19	0.957	70.0	0.018	0.265
35′–37′	10.5–11.1	GT	69.4	14.6	21.5	43.5	22	0.791	70.0	0.01	0.062
40′–42′	12.0–12.6	IDOT	58.53	41.27	25	49	24	1.333	98.1	0.058	0.486
43′–45′	12.9–13.5	GT	54.6	10.5	25.6	44.4	18.8	1.035	125.0	0.009	0.154

*Notes:

e_0: Initial void ratio for consolidation test

σ_p': Pre-consolidation stress

c_r: Recompression index

c_c: Virgin compression index

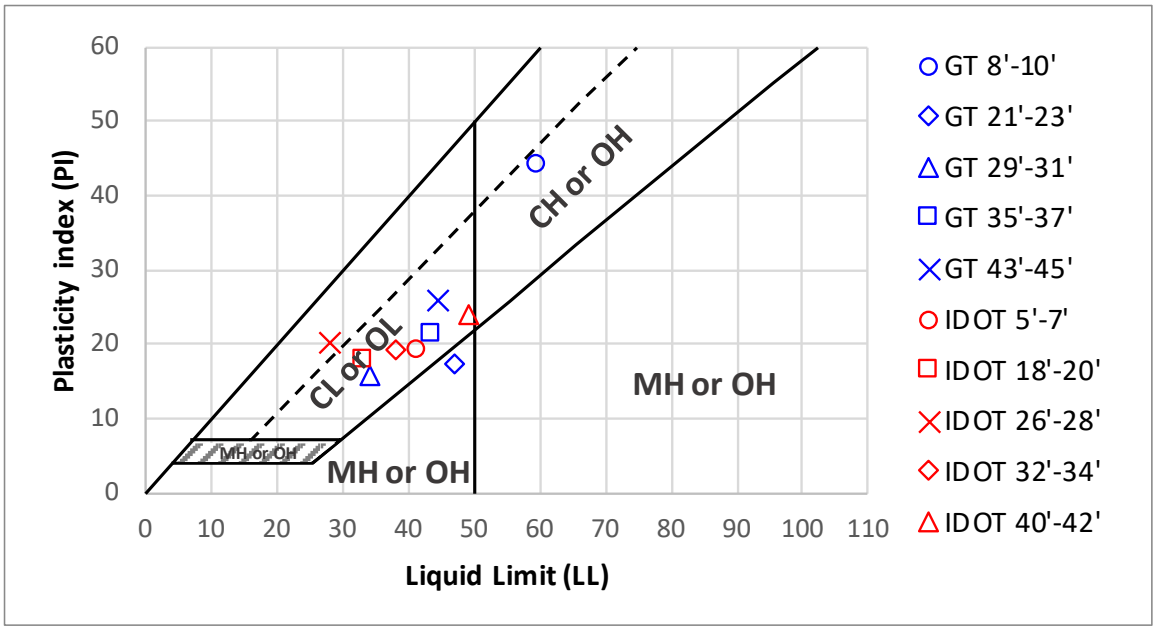

Figure 167. Plasticity chart.

Source: Georgia Tech

The following section presents a detailed assessment of representative SCPTu data at the considered site in Florence (EMB-1-1) in the context of the available laboratory information.

Data Interpretation

At the Florence site, the selected CPT test locations near EMB-1-1 are roughly 500 m (0.31 miles) from the Illinois River, as indicated by Figure 165. The soundings are located within a field on the east side of a dike that separates farmland from the river. Field SCPTu soundings in this area were conducted by Georgia Tech and ConeTec. Figure 168 compares results from the SCPTu test performed by Georgia Tech (D6-Site1-19) and ConeTec (D6-Site1-7, D6-Site1-8, and D6-Site1-16), considering the first 15 m (49.2 ft) where Georgia Tech stopped the penetration as a dense layer of gravelly sand was encountered. Overall, the readings show consistency between the corrected tip resistance (q_t), sleeve friction (f_s), and pore pressure (u_2). The collected data illustrate the good repeatability that can be achieved with the SCPTu, even when considering different operators. In addition, the soundings were performed in a soybean field in which the surface conditions and soil saturation change depending on the time of year. So, because the soundings were conducted at different times, seasonal-related additional differences can be expected, but again, the general patterns are consistent. The readings show a low q_t for the upper 15 m (49.2 ft) (< 5 MPa [725 psi]) of material as well as low f_s (< 70kPa [10.1 psi]), which was the general pattern for the investigated Illinois clays. The water table was interpreted to be located at a depth of about 3 m (9.8 ft) from the results of dissipation tests. Figure 169-A shows an example of a typical dissipation test in the upper 15 m (49.2 ft), considering the CPTu D6-Site1-10 data. The typical responses in the dissipation tests show positive porewater pressures that tend to dissipate but under considerable time. For this reason, most tests were not conducted until reaching equilibrium. Conversely, in the case of the deeper layer below 15

m (49.2 ft), the dissipations occur faster than in the upper layers (see Figure 169-B, which uses the CPTu D6-Site1-10 data).

The SBTn chart of Robertson (2009) shows the upper 15 m (49.2 ft) is composed of silt mixtures (zone 4) and clays (zone 3), as indicated by Figure 170. Similarly, in Figure 171, the SBT chart from Jefferies and Been (2015) shows the presence of clayey silts and silty clays to clays for CPT D6-Site1-7, but also suggests the presence of organic soils according to CPT D6-Site 1-19. The collected data indicate at least 2 units of clay-like soil. The upper 4.2 m (13.8 ft) is stiffer, and the lower portion extends to 16 m (52.5 ft), where a dense gravelly sand layer is encountered.

The CPT charts developed by Robertson (2009), shown in Figure 170, indicate that most of the material behaves as clays ("clay to silty clay") and silt mixtures ("clayey silt to silty clay"). On the other hand, Robertson (2016) shows a noticeable difference between the dilative behavior and contractive behavior of the upper and bottom layers of fine-grained soils (see Figure 172). The CPT-based characterization is consistent with the standard laboratory soil classification, but it is worth noticing that CPTu provides a continuous profile, and the SBT charts provide additional information related to the expected soil behavior under loading.

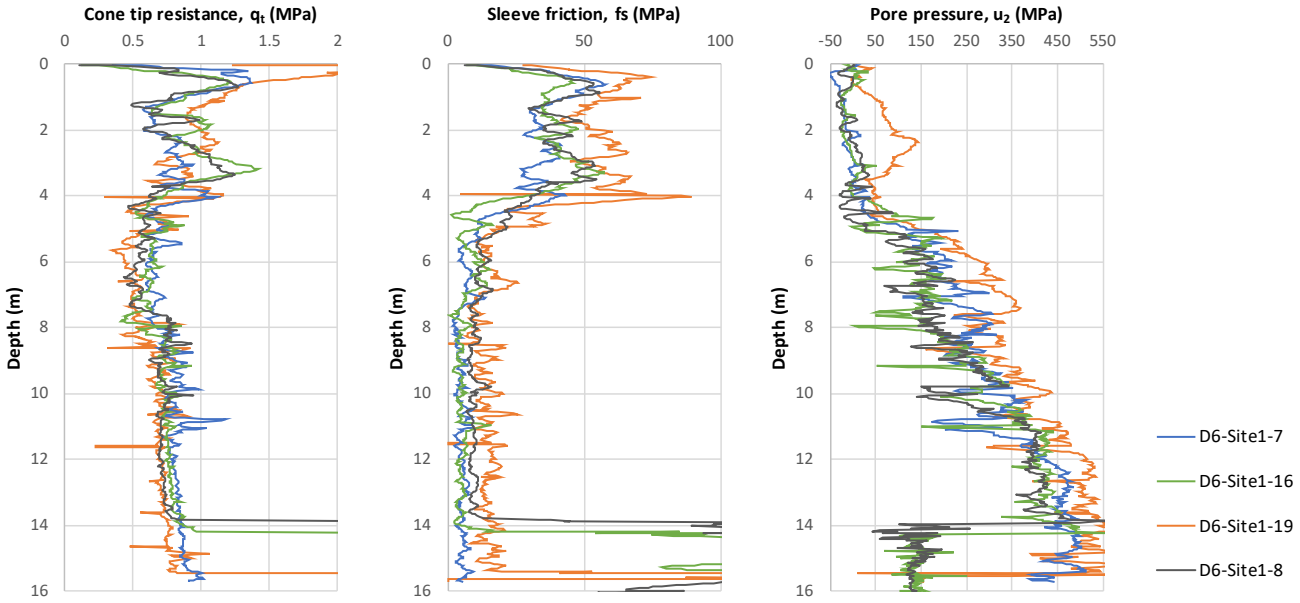

Figure 168. Comparison of piezocone tests at the Florence site performed by Georgia Tech and ConeTec.

Source: Georgia Tech

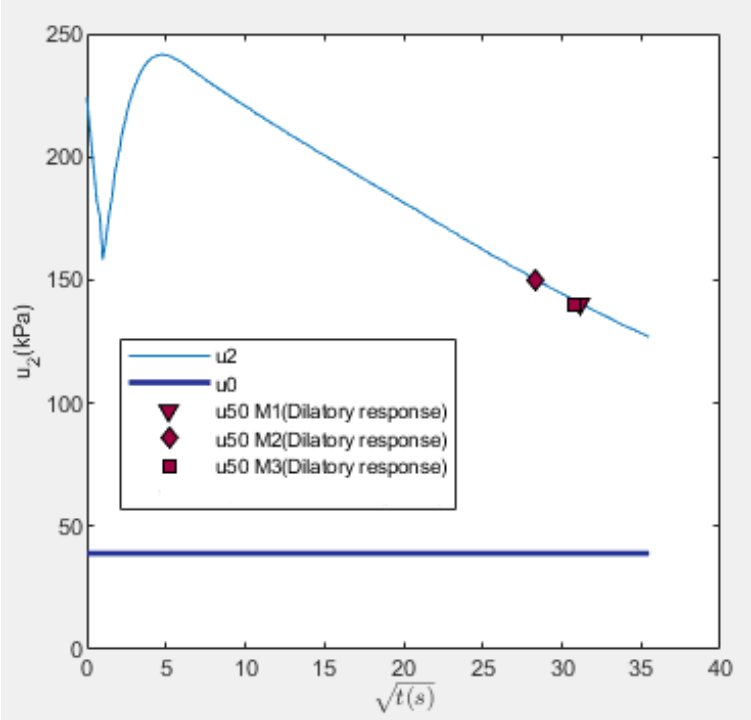

A. Typical response in the dissipation tests in the upper fine-grained soil layer

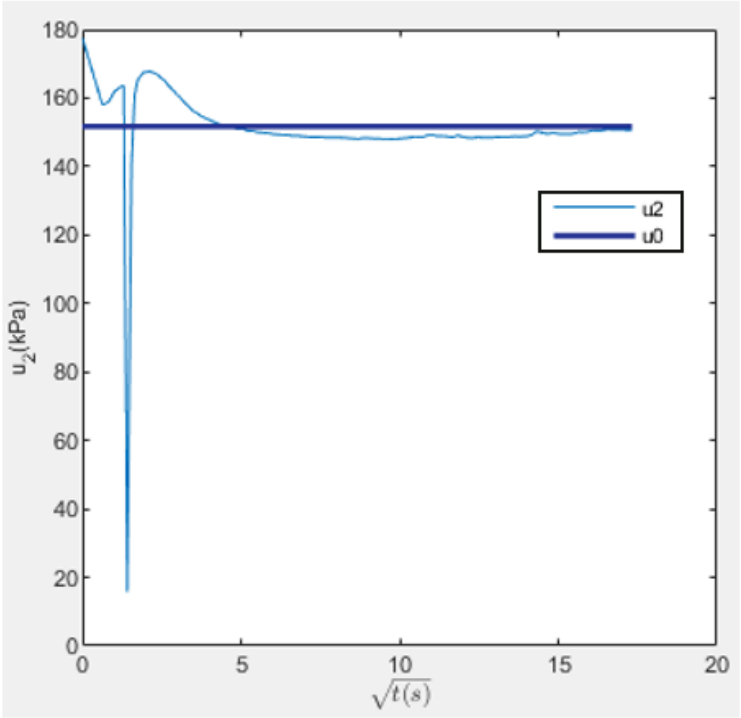

B. Typical response in the dissipation tests in the bottom sandy soil layer

Figure 169. Example of dissipation tests conducted in Florence.

Source: Georgia Tech

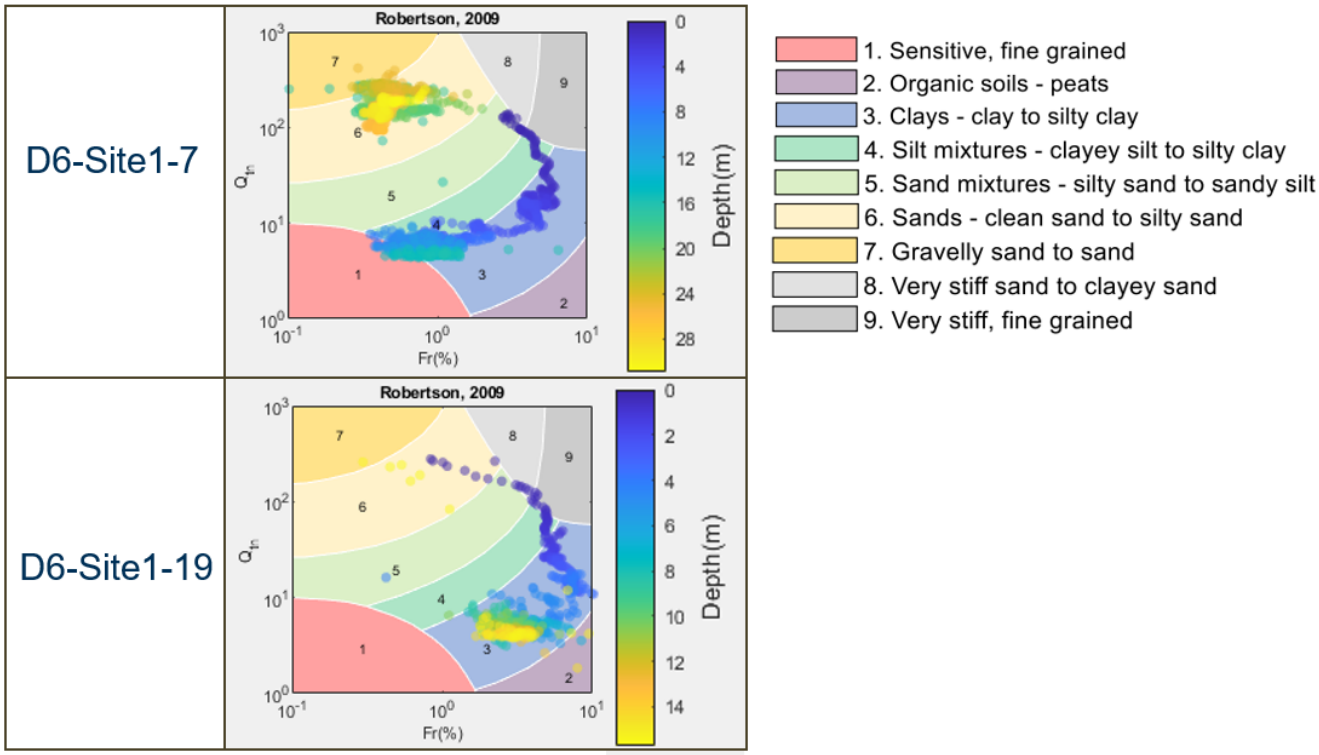

Figure 170. Florence data on CPT soil behavior type (SBTn): Q_{tn}-F_r chart of Robertson (2009).

Source: Georgia Tech

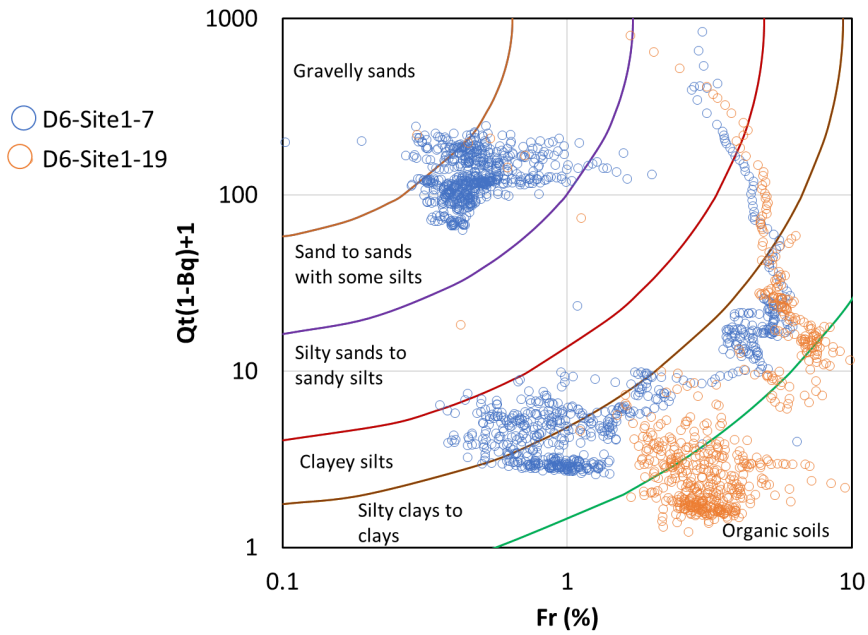

Figure 171. Florence data on CPT soil behavior type (SBTn): $Q_t(1 - B_q)$ +1 vs F_r (%) chart of Jefferies and Been (2015).

Source: Georgia Tech

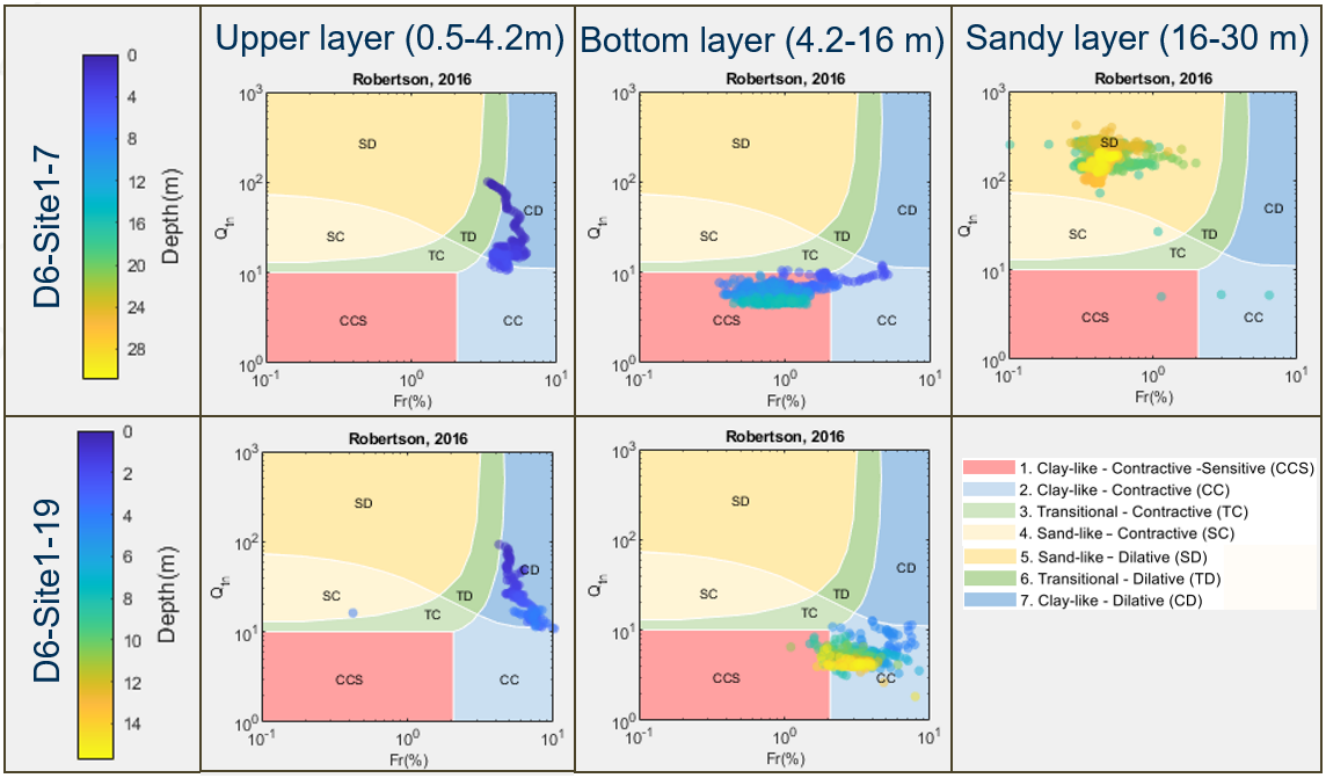

Figure 172. Florence data on CPT soil behavior type (SBTn): Q_{tn} vs F_r chart of Robertson (2016).

Source: Georgia Tech

The unit weight effective stress friction angle, undrained shear strength, over-consolidation ratio, and pre-consolidation pressure are interpreted using the procedures discussed in Chapter 3. Figure 173, Figure 174, and Figure 175 show the variation of key geoparameters for representative CPTs close to the borehole location. The available laboratory-based geoparameters are also plotted along the SCPTu-based estimations.

Unit Weight

IDOT conducted 19 tests to determine the total unit weight. The results were plotted alongside the unit weight values from correlations with CPT. Laboratory results were underestimated in most cases. However, the correlation proposed for normal consolidated to lightly over-consolidated clays, presented in Chapter 3, shows a better agreement with the laboratory testing, as observed in Figure 173. This suggests that the clays from this site have a higher unit weight than those estimated by common CPT unit weight correlations (Table 3), and the discussed correlations for normal consolidated to lightly over-consolidated clays discussed in Chapter 3 seem to work better for Illinois soils.

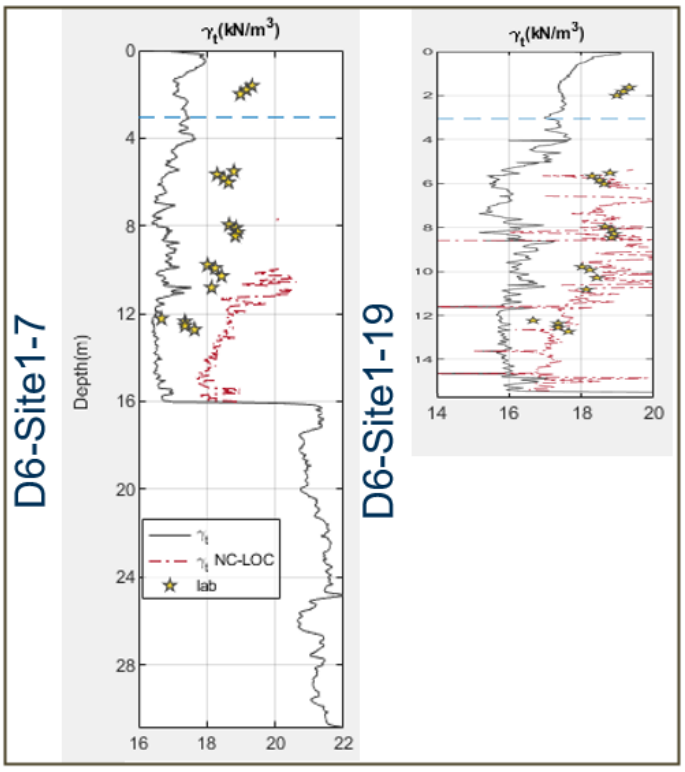

Figure 173. Interpretations unit weight from GT SCPTu at Florence, Illinois.

Source: Georgia Tech

Pre-Consolidation Stress (σ_p) and Yield Stress Ratio (YSR)

The pre-consolidation stress (σ_p') has been estimated considering the Agaiby and Mayne (2021a) screening procedure as $0.33\ (q_t - \sigma_{vo})$, $0.53(u_2 - u_o)$, and $0.6(q_t - u_2)$, with results presented in Figure 174-A. Notice that $0.53(u_2 - u_o) < 0.33\ (q_t - \sigma_{vo}) < 0.6(q_t - u_2)$ for the upper 4 m as well as other instances, suggesting the presence of either desiccated OC clays or organic clays according to Agaiby and Mayne (2021a). The thermal gravimetric analyses (TGA) on recovered samples do not suggest the presence of organics; hence, it is likely that the observations are associated with desiccation effects. Regarding the yield stress ratio (YSR) or over-consolidation ratio (OCR), if clays are identified as sensitive or insensitive according to the screening procedure presented in Chapter 3 ($a_q > 0.5$ and $a_q < 0.5$), YSR is determined using the SCE-CSSM solutions by Burns and Mayne (2002). If clays were identified as organic clays based on the Agaiby and Mayne (2021a) screening procedure (Table 8), the generalized equation form is used (Figure 59). Also, the YSR formulation for clean sands was used if the criteria $I_c < 2.6$ is met. The profile appears to show over-consolidated clays (OCR or YSR > 2) within the upper 4.2 m (13.8 ft) and lightly over-consolidated clays (OCR < 2) for the deeper soils from 4.2 to 16 m (13.8 to 52.4 ft). The larger OCRs at shallower depths may be associated with desiccation processes due to seasonal changes and possibly farming activities (e.g., surcharge from farming equipment). In contrast, the rest of the profile corresponds to normal consolidated (NC) to lightly over-consolidated material (LOC). Figure 174 also shows the resulting OCR estimates using the generalized CPT procedure (Agaiby & Mayne, 2021a).

The laboratory results follow a similar trend to the profiles of YSR and pre-consolidation stress with depth, yet their magnitudes are lower than the CPT values in most cases. This is likely associated with sample disturbance effects. In this context, both the NGI criterion (Lunne et al., 2005) and the SQD criterion (Terzaghi et al., 1996; DeGroot et al., 2005) were used to evaluate the degree of specimen disturbance. Seven out of 10 samples used for the consolidation tests qualify as poor to very poor quality according to SQD criterion, while 5 samples qualify as good to fair quality and 3 samples qualified as poor and very poor based on the NGI criterion. Thus, sample disturbance effects may likely explain the laboratory-assessed values of YSR < 1, since, considering the geology of this region, the soft clays should at least be normally consolidated (YSR ≈ 1).

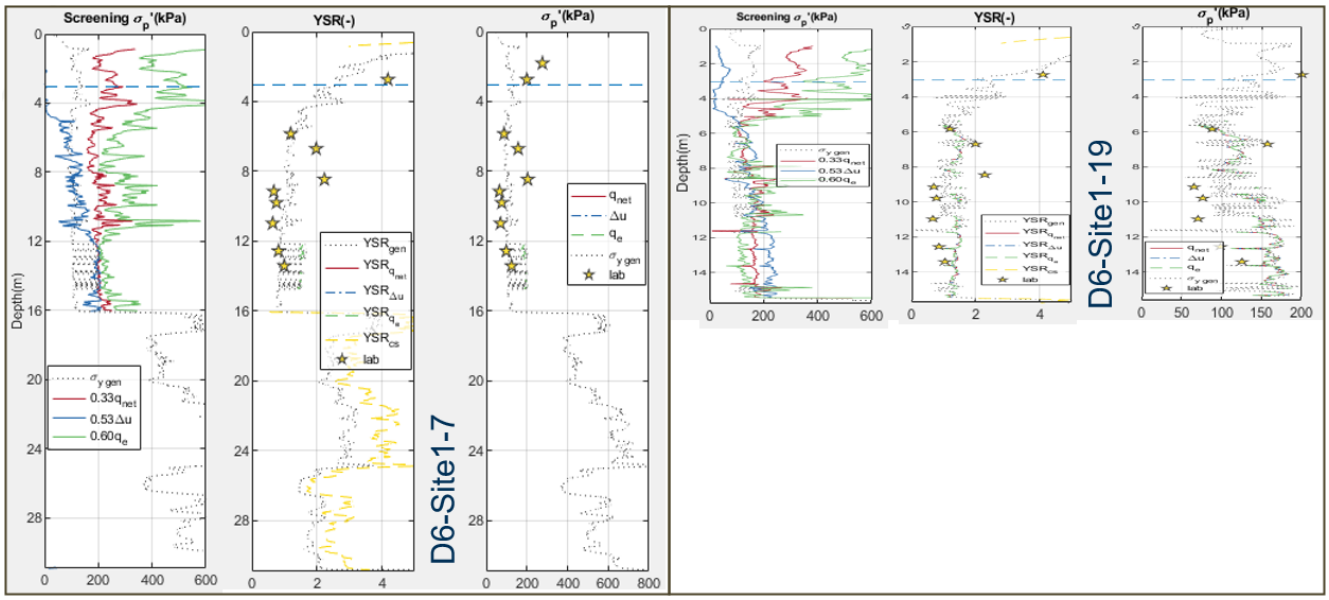

Figure 174. Interpretations of yield stress ratio (YSR) and pre-consolidation stress (σ_p') from GT SCPTu at Florence, Illinois.

Source: Georgia Tech

Effective Friction Angle and Undrained Shear Strength

For the CPT-evaluation of effective friction angle, the method by Kulhawy and Mayne (1990) is used for drained behavior ($I_c \leq 2.6$), corresponding to sands and silty sands. If the soil is classified as fine-grained ($I_c > 2.6$), the NTH approximations for undrained penetration (Mayne, 2007b) are utilized. For fissured over-consolidated clays with $B_q < 0.05$, a modification of the NTH solution is used (Ouyang & Mayne, 2019).

Specifically at the Florence site, as illustrated by Figure 175, CPTu D6-Site1-19 shows an interpreted effective friction angle of ϕ' = 22° for $B_q > 0.05$, below 1 m (3.3 ft) depth where positive porewater pressure started to be recorded. CPTu D6-Site1-19 shows higher friction angle values because $B_q <$ 0.05 for the whole upper layer. These differences might be due to seasonal changes since both soundings were performed at different times of the year. For the lower fine-grained layer, a friction angle between 28° and 33° was obtained in both soundings. Sensitive clays were identified under the

criteria a_q > 0.5 (slope parameter introduced in Chapter 3) in CPT D6-Site1-19. Thus, the modified version of the NTH solution was used to calculate ϕ_1(i.e., friction angle for the maximum deviator stress), while the original version will provide a value for ϕ_2 (i.e., friction angle for the maximum obliquity). The undrained shear strength is assessed from CPTu data using the Mayne and Peuchen (2018) approach. The upper clayey layer (0–4.2 m [0–13.8 ft]) shows a strength that varies from 25 to 60 kPa (3.6–8.7 psi). The underlying clay layer (4.2–16 m [13.8–52.5 ft]) shows an increasing undrained strength between 25 and 50 kPa (3.6-7.3 psi). The laboratory testing results for friction angle (ϕ') and undrained strength (s_u) are also plotted in Figure 175 for comparison. The friction angle was obtained from a set of three multiaxial consolidated undrained (CU) triaxial compression shear tests, while the S_u values were obtained from multistage unconfined compression tests (UC) and the CU testing. CPT-based friction angles show a good fit with the laboratory data with $\phi' \approx 31°$. However, S_u values look more scattered, probably because of sampling effects and because S_u is more sensitive to shearing mode and fabric. Moreover, although rather easy and quick to perform, UC tests do not provide the best means for assessing clay strength (Mayne, 2008).

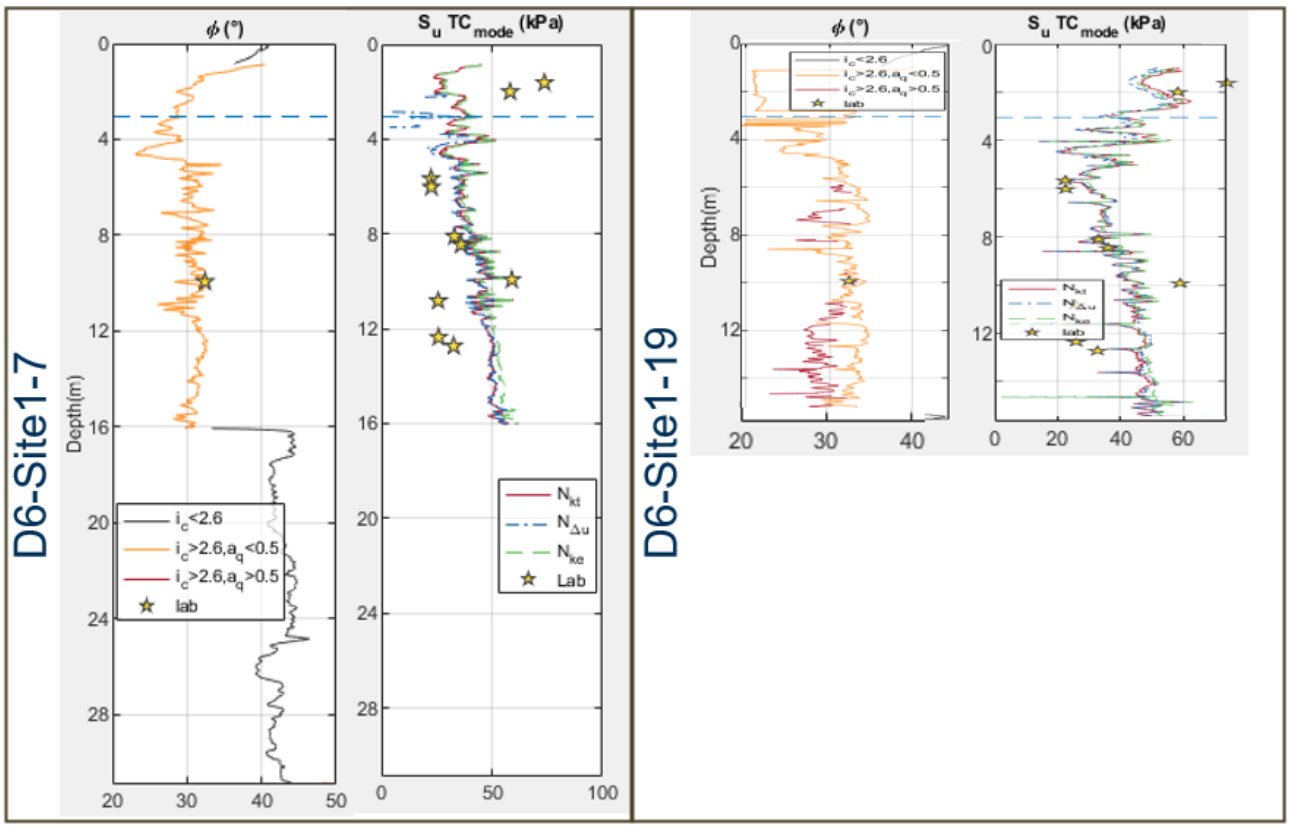

Figure 175. Interpretations of effective friction angle and undrained shear strength from GT SCPTu at Florence, Illinois.

Source: Georgia Tech

Shear Wave Velocity

Figure 176 shows the measured wavelet signatures at different depths and the interpreted shear wave velocities (V_s) from the GT sounding at the Florence test location under discussion. The field

shear wave velocity (V_s) data were interpreted using the cross-correlation method discussed in Chapter 3. Results show V_s increasing with depth in the clay layer from about 135 m/s (443 ft/s) at 3 m (9.8 ft) to around 210 m/s (689 ft/s) at 15 m (49.2 ft) depth. These values are compared against laboratory-based measurements of V_s taken during consolidation testing using bender elements (the setup used for the measurements is shown in Appendix B for reference). The consistency of the laboratory-based and CPT-based V_s estimates is remarkable.

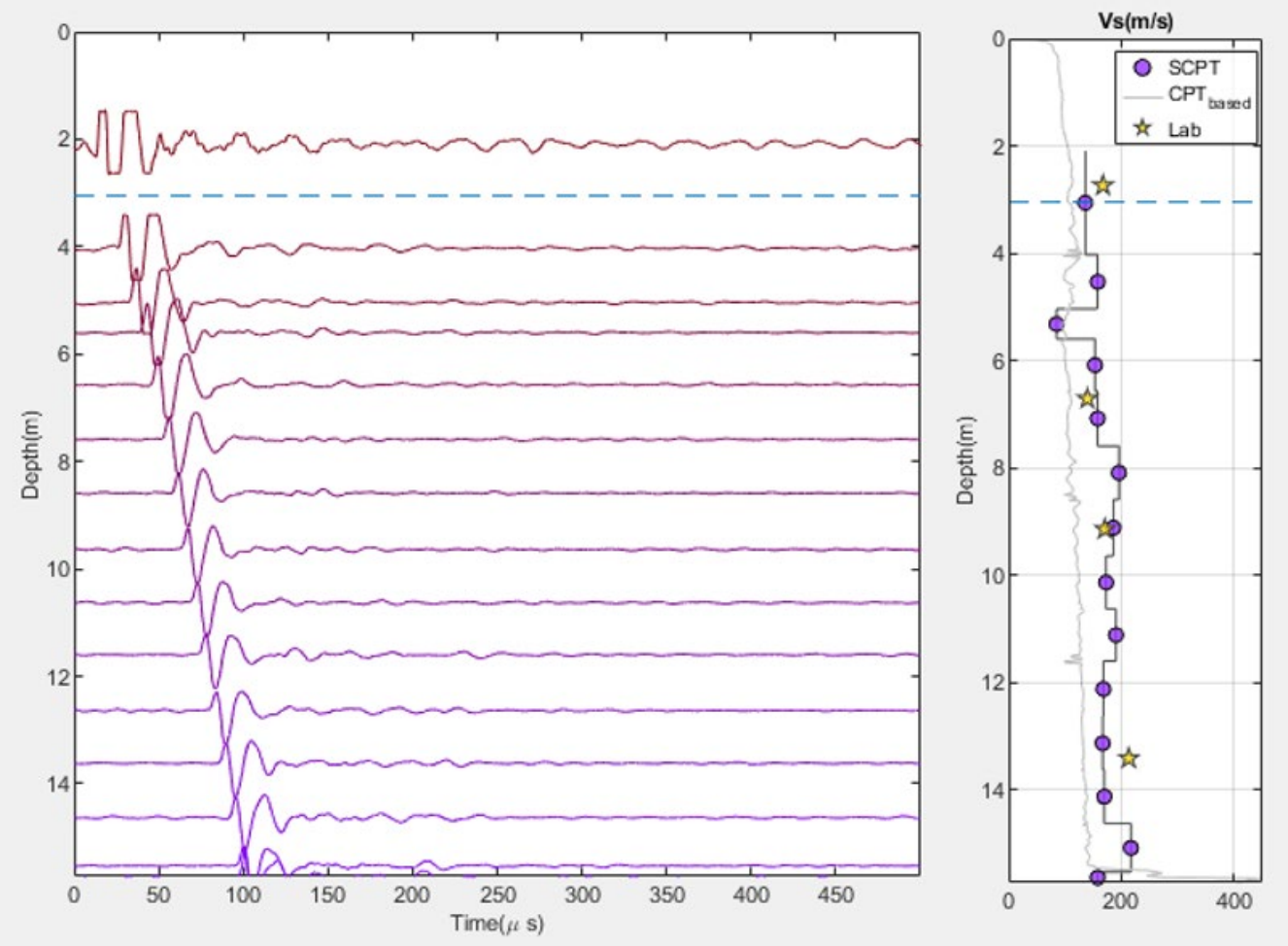

Figure 176. Florence site: (a) seismic wavelets throughout depth in clay layer, (b) interpreted in situ V_s of soil profile with lab data from Georgia Tech SCPTu D6-Site1-19.

Source: Georgia Tech

Equivalent N_{60}

Finally, given that the current geotechnical engineering practice in Illinois relies on the SPT, the CPT data were also "transformed" into equivalent SPT data using the correlations developed for Illinois. The results are presented in Figure 177, which compares the CPT-equivalent N_{60} values against measured SPT data. An energy ratio (ER = 86%) was used to correct the SPT values based on calibration results supplied by Wang Engineering (2021). Two boreholes (EMB-1-1 and EABUT-17-2, see Figure 165) are used for the comparison between measured N_{60} and CPT-equivalent N_{60}.

In borehole EMB-1-1, most of the soft clays between 5 and 15 m (16.4–49.2 ft) registered a blow count of 0. The developed correlations cannot predict zero values, but the estimates based on CPTs D6-Site1-7 and D6-Site1-7 are quite low (~5 between 5–10 m [16.4–32.8 ft] and below 10 for deeper locations). For the rest of the blow counts higher than 0, the Robertson (2012) form-based correlation and the power trendline show good agreement except for the most superficial value (depth < 1 m [3.3 ft]). In the case of the borehole EABUT-17-2, the CPT D6-Site1-10 is considered to estimate N_{60} values with results in Figure 177 (right plot). In this case, the measured and estimated N_{60} values are in reasonable agreement.

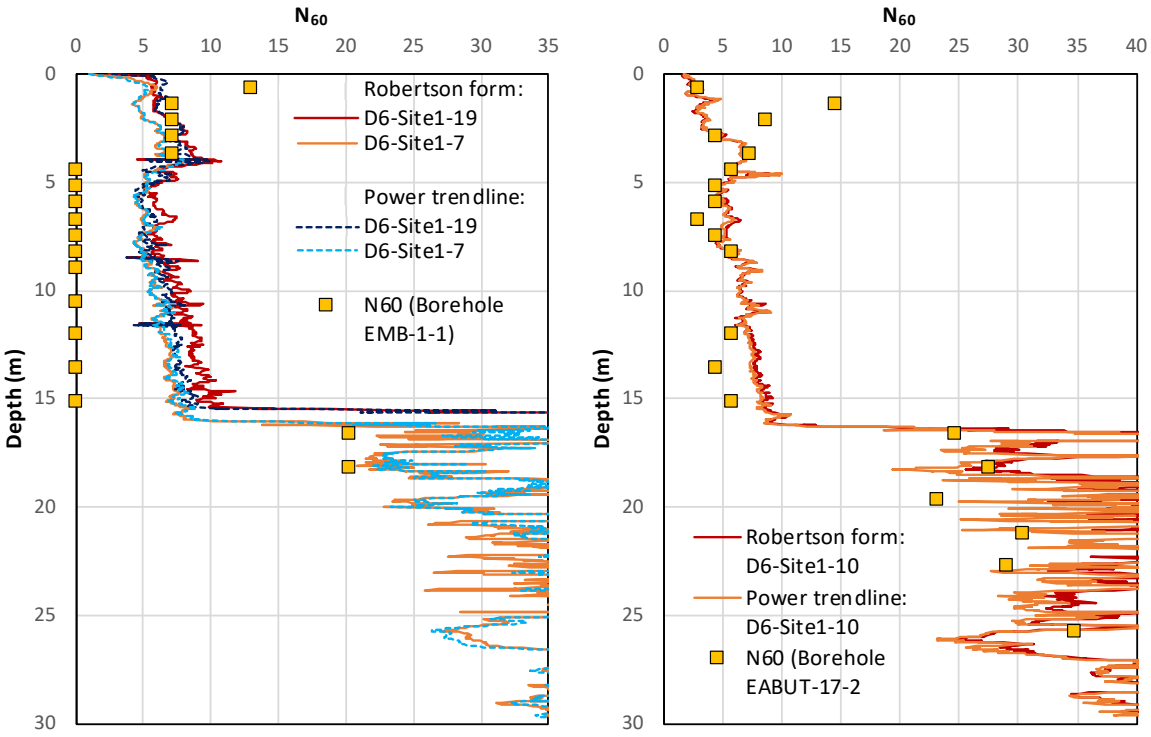

Figure 177. Comparison of measured N_{60} values and equivalent N_{60} estimated values from Georgia Tech SCPTu D6-Site1-19.

Source: Georgia Tech

TESTING AT NORTHWESTERN UNIVERSITY SITE

The second site shown as an application example is the testing site at Northwestern University (NWU) in Evanston, Illinois, which is in District 1. The CPT sounding was performed by Georgia Tech in 2003 (Mayne, 2005, 2007a). Because the NWU is a national experimentation site, there are references available with laboratory results, which provide the basis for comparisons with CPT data, including unit weights, index, grain size, consolidation, and triaxial compression tests (Blackburn & Finno, 2007; Finno et al., 2000).

Figure 178 shows the CPT used in this section, as well as the variations of q_t, f_s, u_2, and B_q, versus depth and the soil stratigraphy. The first 9 m (29.5 ft) correspond to a sand material, which is

followed by about 3 m (9.8 ft) of Blodgett clay; then, a soft clay material is apparent up to 18 m (59 ft), which is underlined by the Park Ridge clay. The upper sand and bottom clay layers show remarkable differences in the CPT response. The soft clay between 12 and 18 m (39–59 ft) shows q_t, f_s, u_2, and B_q values in the range of 0.8–1 MPa (116–145 psi), 10–12 kPa (1.45–1.74 psi), 400–650 kPa (58–94.3 psi), and 0.7–0.75, respectively. Blodgett clay layer shows similar values; however, there is a peak in the values of q_t and f_s, and a drop of u_2 due to the presence of an interbedded sandy layer. The Park Ridge clay, located below 18 m (59 ft), shows q_t, f_s, u_2, and B_q values in the range of 1.2–1.5 MPa (174–217 psi), 20–22 kPa (2.9–3.2 psi), 750–800 kPa (109–116 psi), and 0.5–0.65, respectively. On the other hand, the upper sand layer is characterized by higher q_t and f_s values and u_2 agrees very well with the hydrostatic pore pressure (u_0), and B_q values are close to 0.

Figure 179 shows the soil profiles based on the processed CPT data and the soil behavior type charts presented in Chapter 3. Based on the Robertson SBT (2009), the first layer is composed of clean sands to silty sands with an interbedded layer of sand mixtures between 3 and 5 m (9.8–16.4 ft). Then, a clay-type behavior prevails until 24 m (78.7 ft) depth, where silt mixture layers are encountered. The Robertson (2016) SBT profiles show the upper 9 m (29.5 ft) sandy layer as dilative, followed by a contractive to sensitive clay-like material until 22 m (72.2 ft) depth when a dilative clay-like and transitional dilative layer are encountered. In general, these SBT profiles match very well with the soil stratigraphy presented in Figure 178. In addition, Robertson (2016) SBT chart shows the contrast in behavior between Deerfield soft clay (CC and CCS) and Park Ridge clay (CD).

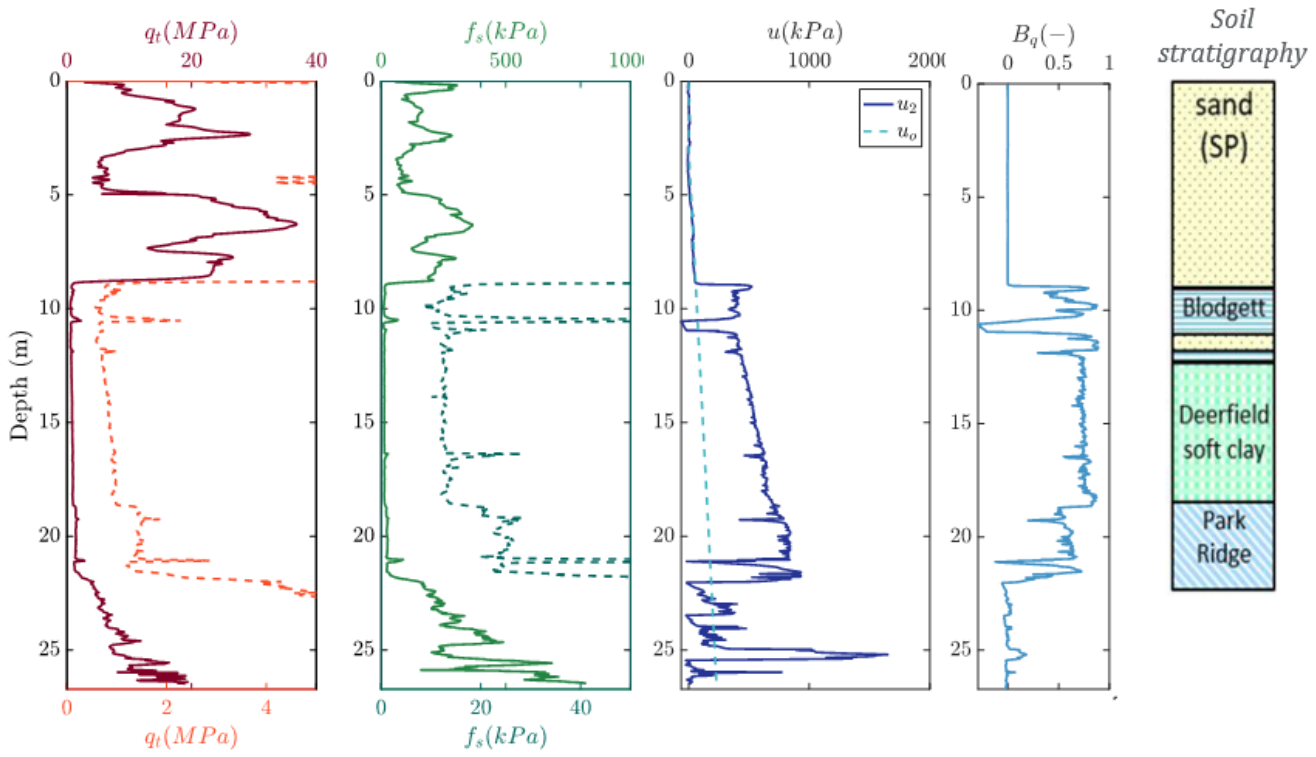

Figure 178. Typical CPT sounding at the Northwestern University site.

Source: Georgia Tech and Agaiby & Mayne (2021b)

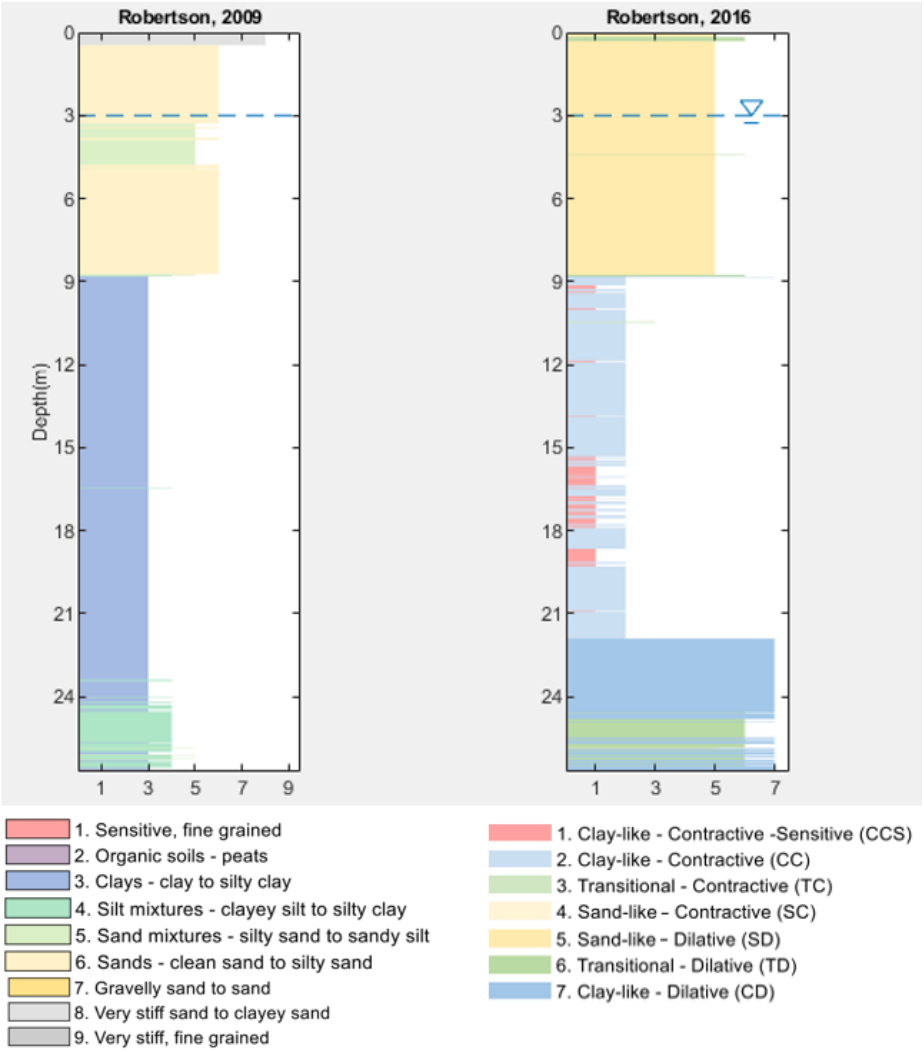

Figure 179. Experimentation site at Northwestern University: soil behavior type profiles based on Robertson (2009, 2016).

Source: Georgia Tech

Comparison between the CPT-estimated geoparameters and measured laboratory data are shown in Figure 180. Results from unit weight correlation Mayne et al. (2023b) slightly underestimate the values measured on undisturbed samples in the laboratory. On the other hand, the correlation proposed for NC-LOC slightly overestimates the measured values (Table 4 in Chapter 3). The pre-consolidation stresses (σ_p') and yield stress ratios (YSR) from one-dimensional consolidation tests are in excellent agreement with the correlative methods with the CPT data, probably because of minimized disturbance during sampling. Also, results of laboratory undrained shear strengths determined from anisotropically-consolidated undrained triaxial compression tests (CK_0UC) are very well represented by the CPTu data. Finally, the NTH solution using the CPTu data gave ϕ' = 28.8°, which is in excellent agreement with the triaxial series of tests that show ϕ' = 28.3° (Agaiby & Mayne, 2021b). This site shows that when sampling and testing is conducted carefully, the correspondence between CPT-based estimates and laboratory data is quite reasonable.

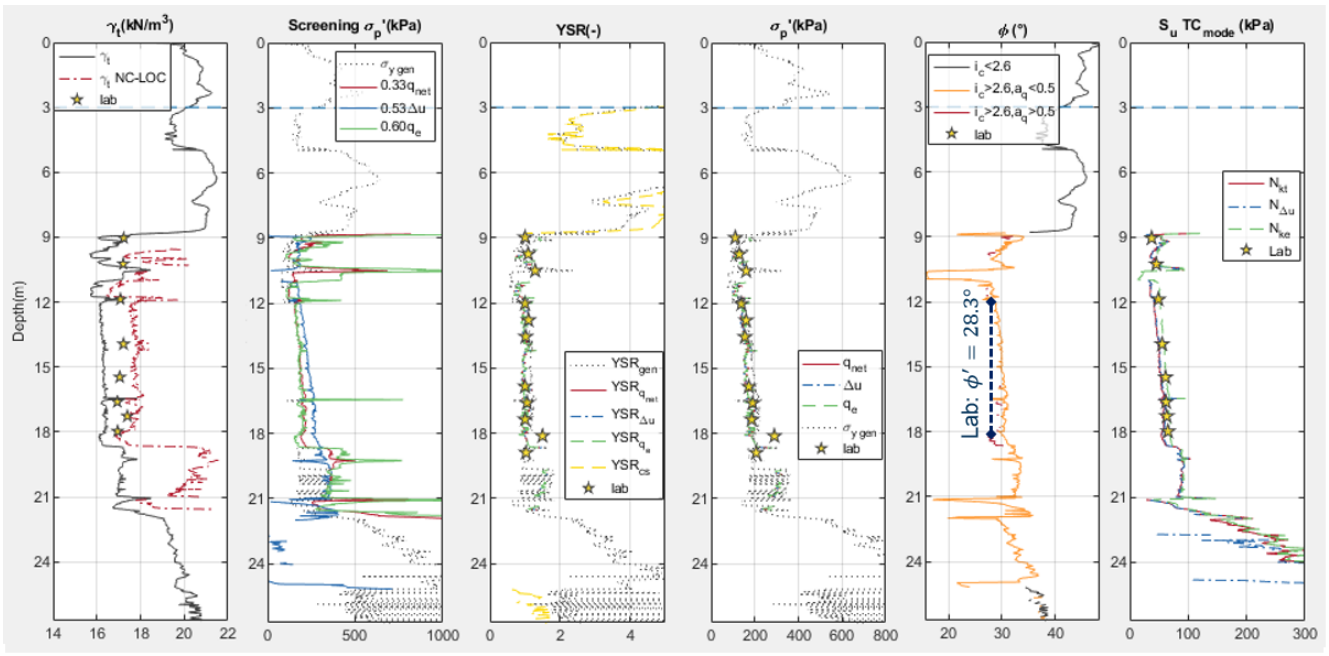

Figure 180. National geotechnical experimentation site at Northwestern University: CPT interpretations and laboratory test comparison.

Source: Georgia Tech

CHAPTER 7: CONCLUSIONS AND RECOMMENDATIONS

This study sets the stage for implementing a CPTu/SCPTu practice in the state of Illinois, providing recommendations for using and interpreting CPT soundings in subsurface investigations. This study also contributes to modernizing IDOT policy to current practices, moving the department to current CPT-related practices adopted in other departments of transportation, which is consistent with recommendations from the Federal Highway Administration.

The continuous nature and multiple measurements in CPTu/SCPTu tests provide valuable information about soil variability that is difficult to match with typical borehole sampling and laboratory testing. A CPTu collects at least three readings with depth: q_t, f_s, and u_2, which are all continuously recorded and available in digital format during the sounding. As soon as the sounding reaches the intended depth, the results can be analyzed fully, plotted or shown graphically on computer monitors, and relayed wirelessly back to the chief engineer at the main office.

A production CPT rig can conduct as many as 300 to 600 ft/day (100 to 200 m/day) of vertical soundings, compared to only 50 to 100 ft/day (15 to 30 m/day) of drilling using conventional rotary borehole and sampling methods. Moreover, the CPT has higher repeatability and reliability compared to SPT tests. In round numbers, SPT, even with energy measurements and subsequent corrections, is four to five times less repeatable than the CPT. A SCPTu sounding can provide additional measurements of shear wave velocities and pore pressure dissipations at selected depths, thus offering five independent readings from the same sounding. Hence, several independent, fast, and reliable measurements can be made cost-effectively in a SCPTu sounding. As a result, CPT is increasingly being preferred for in situ testing, and their adoption at IDOT is a positive step forward and consistent with the best practices at other US DOTs.

As part of this study, CPT/SCPTu testing was conducted at more than 21 sites. A database of 156 CPT/SCPTu distributed across the nine districts in the State of Illinois has been generated. The database also includes shear wave velocity profiles at 28 locations and pore pressure dissipation tests at 45 locations. The CPT/SCPTu data have been processed in a uniform manner (Appendix A), and recommendations for interpreting CPT/SCPTu data in the context of subsurface characterization and geotechnical design have been provided. General and detailed examples of interpreting CPTu/SCPTu data were also provided, which may be beneficial for IDOT engineers as they transition into implementing a long-term CPTu/SCPTu practice.

Of additional note, information (editable and non-editable) provided by IDOT has been carefully examined. The provided information consisted of boreholes with SPT data and laboratory tests on collected Shelby tubes. This information has been used to develop SPT-CPTu correlations that can be applied in the State of Illinois and to provide examples of interpreting SCPTu data in the context of laboratory testing.

The following recommendations are provided to further this study and advance the CPTu/SCPTu practice in the State of Illinois:

- The principal investigators are aware that some districts have (or are planning to) acquire CPT/SPTu equipment for local subsurface investigations. This is a significant step forward, and involving as many districts as possible in this initiative is encouraged. If such implementation is difficult, increased interactions between IDOT engineers and independent CPTu contractors are recommended.

- Integrate the information provided in this report into Chapter 4 of the IDOT *Geotechnical Manual*.

- Keep collecting SPT-CPTu paired data in the state of Illinois. The principal investigators understand that soil borings with SPT will continue to be used in several districts, at least in the short term. In this context, due to the efficiency of collecting CPTu data, it is encouraged to collect as much paired CPTu data as possible so the proposed correlations in this study can be refined further.

- When collecting paired data, depending on local access and site conditions, target the paired data at a boring-to-sounding distance of less than 3 m (9.84 ft). A great example of a successful CPT/SCPTu subsurface investigation program is the exploration study conducted at the Florence Bridge over the Illinois River in District 6. It is recommended to promote more efforts like the one at Florence.

- District 6 currently has most of the available CPTu/SCPTu data. Consequently, it is recommended that other districts work with District 6 to expedite the transition into a CPTu/SCPTu practice.

- Generate more paired sets of laboratory-CPTu data that would allow the development of region-specific soil property correlations for the State of Illinois. The laboratory data available during this project were limited in this context. However, as the CPTu practice is implemented in the State of Illinois, the generation of additional data is encouraged.

- Provide continuum training to IDOT personnel on using and interpreting CPTu/SCPTu tests. In particular, the CPTu/SCPTu is an evolving technology, and significant advances are expected in the short and long term. For example, artificial intelligence is expected to be gradually more active, thus offering improved interpretations to reduce risk and increase reliability in geotechnical engineering practice.

REFERENCES

Abu-Farsakh, M. Y., Yu, X., & Gautreau, G. (2011). *Control of embankment settlement field verification on PCPT prediction metho*ds. Louisiana Transportation Research Center.

Abu-Farsakh, M., Zhang, Z., Tumay, M., & Morvant, M. (2008). *Development of MS-Windows CPT Soil Classification Software*. 87th Transportation Research Board Annual Meeting.

Agaiby, S. S. (2018). Advancements in the interpretation of seismic piezocone tests in clays and other geomaterials. PhD dissertation, School of Civil & Environmental Engineering, Georgia Institute of Technology.

Agaiby, S. S., & Mayne, P. W. (2018). Evaluating undrained rigidity index of clays from piezocone data. In *Cone Penetration Testing,* 65-71.

Agaiby, S. S., & Mayne, P. W. (2019). CPT evaluation of yield stress profiles in soils. *Journal of Geotechnical and Geoenvironmental Engineering*, *145*(12), 04019104. https://doi.org/10.1061/(ASCE)GT.1943-5606.0002164

Agaiby, S. S., & Mayne, P. W. (2020). Indirect estimation of fines content using the modified CPT material index. *Proc. GeoCongress 2020: Modeling, Geomaterials, and Site Characterization,* (Minneapolis, GSP 317), ASCE, Reston, VA: 569-582. https://doi.org/10.1061/9780784482803.061

Agaiby, S. S., & Mayne, P. W. (2021a). CPTU identification of regular, sensitive, and organic clays towards evaluating preconsolidation stress profiles. *AIMS GeoSciences*, *7*(4), 553–573.

Agaiby, S. S., & Mayne, P. W. (2021b). Analytical evaluation of CPTU soundings in soft Chicago clay. *Proc. 6th International Conference on Site Characterization* (ISC-6, Budapest, Paper ID 104).

Alshibli, K., Okeil, A. M., & Alramahi, B. (2008). *Update of correlations between cone penetration and boring log data.* Louisiana Transportation Research Center.

Anagnostopoulos, A., Koukis, G., Sabatakakis, N., & Tsiambaos, G. (2003). Empirical correlations of soil parameters based on cone penetration tests (CPT) for Greek soils. *Geotechnical & Geological Engineering*, *21*, 377–387.

Andrus, R. D., & Youd, T. L. (1989). Penetration tests in liquefiable gravels. *Proc., 12th International Conference on Soil Mechanics & Foundation Engineering (ICSMFE)*, Rio de Janero, Brazil, 679–682.

Andrus, R.D., Piratheepan, P., Ellis, B.S., Zhang, J. & Juang, C.H. (2004). Comparing liquefaction evaluation methods using penetration-VS relationships. *Soil dynamics and earthquake engineering,* 24(9-10), 713-721.

Andrus, R. D., Mohanan, N. P., Piratheepan, P., Ellis, B.S., Holzer, T. L. (2007). Predicting shear-wave velocity from cone penetration resistance. *4th International Conference on Earthquake Geotechnical Engineering* (ICEGE), Thessaloniki, Greece, no. 1454.

Ansari, Y., Merifield, R., & Sheng, D. (2014). A piezocone dissipation test interpretation method for hydraulic conductivity of soft clays. *Soils and Foundations*, *54*(6), 1104–1116. https://doi.org/10.1016/j.sandf.2014.11.006

API, R. (2011). Geotechnical and foundation design considerations. *American Petroleum Institute RP*

2GEO.

Ardalan, H., Eslami, A., & Nariman-Zadeh, N. (2009). Piles shaft capacity from CPT and CPTu data by polynomial neural networks and genetic algorithms. *Computers and Geotechnics*, *36*(4), 616–625. https://doi.org/10.1016/j.compgeo.2008.09.003

Arnold, C., Macedo, J., Mayne, P., Vergaray, L., Zhao, Y., Dai, S., ... & Laningham, B. (2023). Towards implementing SCPTU geotechnical design guidelines for the state of Illinois. In *Geo-Congress 2023* (pp. 104–113).

ASTM D 4254 (2002). Standard test method for minimum index density and unit weight of soils and calculation of relative density. *Annual Book of ASTM Standards, West Conshohocken, PA, 1-9*.

ASTM D 2487 (2006). Standard Practice for Classification of Soils for Engineering Purposes (Unified Soil Classification System). *Annual Book of Standards*, Vol. 04.08, ASTM International.

ASTM D 7400 (2019). Standard test methods for downhole seismic testing. *Annual Book of Standards*, Vol. 04.08, ASTM International.

ASTM D 5778 (2020). Standard test method for electronic friction cone and piezocone penetration testing of soils. *Annual Book of Standards,* Vol. 04.08, American Society for Testing & Materials.

Azizi, F. (1999). *Applied analyses in geotechnics*. CRC Press.

Baez, J. I., Martin, G. R., & Youd, T. L. (2000). Comparison of SPT-CPT liquefaction evaluations and CPT interpretations. *Innovations and Applications in Geotechnical Site Characterization*, (GSP 97), ASCE, Reston, Virginia: 17–32. https://doi.org/10.1061/40505(285)2

Baldi, G. (1989). Modulus of sands from CPTs and DMTs. *Proc. 12th ICSMFE, Rio de Janeiro, 1989*, Vol. 1, 165–170.

Barentsen, P. (1936). Short description of field testing method with cone shaped sounding apparatus. *Proc. 1st ICSMFE*, Cambridge, Massachusetts: 6–10.

Been, K. (2016). Characterizing mine tailings for geotechnical design. *Australian Geomechanics Journal*, *51*(4), 59–78.

Been, K., Crooks, J. H. A., Becker, D. E., & Jefferies, M. G. (1986). The cone penetration test in sands: Part I, state parameter interpretation. *Géotechnique*, *36*(2), 239–249. https://doi.org/10.1680/geot.1986.36.2.239

Been, K., & Jefferies, M. (1992). Towards systematic CPT interpretation. *Predictive Soil Mechanics*, (Proc. Wroth Memorial Symposium, Oxford), Thomas Telford, London: 121–134.

Been, K., Jefferies, M., Crooks, J., & Rothenburg, L. (1987). The cone penetration test in sands: Part II, general inference of state. *Geotechnique*, *37*(3), 285–299.

Begemann, H. (1953). Improved method of determining resistance to adhesion by sounding through a loose sleeve placed behind the cone. 16–27.

Begemann, H. P. (1963). The use of the static soil penetrometer in Holland. *New Zealand Engineering*, *18*(2), 41–49.

Begemann, H. (1965). The friction jacket cone as an aid in determining the soil profile. *Proceedings,*

International Conference on Soil Mechanics & Foundation Engineering, Vol. 1, Montreal: 17–20.

Blackburn, J. T., & Finno, R. J. (2007). Three-dimensional responses observed in an internally braced excavation in soft clay. *Journal of Geotechnical and Geoenvironmental Engineering,* 133(11), 1364–1373.

Bol, E. (2023). A new approach to the correlation of SPT-CPT depending on the soil behavior type index. *Engineering Geology*, 314, 106996.

Boulanger, R. W., & Idriss, I. M. (2014). *CPT and SPT based liquefaction triggering procedures* (Report No. UCD/CGM-14/01). Center for Geotechnical Modeling, University of California at Davis.

Briaud, J.-L. (2013). *Geotechnical engineering: Unsaturated and saturated soils*. John Wiley & Sons.

Broms, B. B., & Flodin, N. (1988). History of soil penetration testing. *Penetration Testing 1988*, Vol. 1 (Proc. ISOPT, Orlando), Balkema Publishers, Amsterdam: 157–220.

Burland, J. B., & Burbidge, M. C. (1985). Settlement of foundations on sand and gravel, *Proc. Inst. Civil Engineers*, Part 1, Vol. 78, London, 1325-1381

Burns, S. E., & Mayne, P. W. (1998). Monotonic and dilatory pore-pressure decay during piezocone tests in clay. *Canadian Geotechnical Journal*, *35*(6), 1063–1073.

Burns, S. E., & Mayne, P. W. (2002). Analytical cavity expansion-critical state model for piezocone dissipation in fine-grained soils. *Soils and Foundations*, *42*(2), 131–137. https://doi.org/10.3208/sandf.42.2_131

Cambefort, H. (1963). Forages et sondages; leur emploi dans les travaux publics.

Campanella, R., & Robertson, P. K. (1984). A seismic cone penetrometer to measure engineering properties of soil. *SEG Technical Program Expanded Abstracts 1984* (pp. 138–141). Society of Exploration Geophysicists.

Chai, J., Sheng, D., Carter, J. P., & Zhu, H. (2012). Coefficient of consolidation from non-standard piezocone dissipation curves. *Computers and Geotechnics*, *41*, 13–22. https://doi.org/10.1016/j.compgeo.2011.11.005

Chen, S., & Liu, K. (2018). Advanced modelling of piezocone penetration test using cavity expansion theory and interpretation simulator development. United States Department of Transportation.

Chin, C.T., Duann, S.W. & Kao, T.C. (1988). *SPT-CPT correlations for granular soils. 1st Int'l Symposium on Penetration Testing*, 1(335-339).

Clausen, C., Aas, P., & Karlsrud, K. (2005). Bearing capacity of driven piles in sand, the NGI approach. *Frontiers in Offshore Geotechnics* (ISFOG, Perth), 574–580.

Dagger, R., Saftner, D., & Mayne, P.W. (2018). *Cone penetration test design guide for state geotechnical engineers* (Report No. 2018-32). Minnesota Department of Transportation. http://www.dot.state.mn.us/research/reports/2018/201832.

Danziger, F. A. B., Almeida, M. S. S., & Sills, G. C. (1997). The significance of strain path analyses in the interpretation of piezocone dissipation data. *Geotechnique*, 47(5), 901–914.

DeGroot, D. J., S. E. Poirier and M. M. Landon (2005). Sample disturbance-Soft clays. *Studia*

Geotechnica et Mechanica 27(3-4), 91-105.

DeJong, J., Jaeger, R., Boulanger, R., Randolph, M., & Wahl, D. (2012). Variable penetration rate cone testing for characterization of intermediate soils. *Geotechnical and Geophysical Site Characterization 4*, Vol. 1, (Proc. ISC-4, Pernambuco), Taylor & Francis Group/CRC: 25–42.

DeJong, J., & Randolph, M. (2012). Influence of partial consolidation during cone penetration on estimated soil behavior type and pore pressure dissipation measurements. *Journal of Geotechnical & Geoenvironmental Engineering*, *138*(7). https://doi.org/10.1061/(ASCE)GT.1943-5606.0000646

Eslaamizaad, S., & Robertson, P. (1996). Cone penetration test to evaluate bearing capacity of foundation in sands. *Proceedings of the 49th Canadian Geotechnical Conference,* 429–438.

Eslami, A., & Fellenius, B. H. (1997). Pile capacity by direct CPT and CPTu methods applied to 102 case histories. *Canadian Geotechnical Journal*, *34*(6), 886–904. https://doi.org/10.1139/t97-056

Fear, C. E., & Robertson, P. K. (1995). Estimating the undrained strength of sand: A theoretical framework. *Canadian Geotechnical Journal*, *32*(5), 859–870. https://doi.org/10.1139/t95-082

Fellenius, B. H. (2009). *Basics of Foundation Design*, electronic edition. www.fellenius.net

Finno, R. J., Gassman, S. L., & Calvello, M. (2000). The NGES at Northwestern University. *National Geotechnical Experimentation Sites* (NGES), 130–159. https://doi.org/10.1061/9780784404843.ch06

Fowler, J. A., Arduino, P., Holtz, R. D., Mayne, P. W., & Poulos, H. G. (2001). Approximate displacement influence factors for elastic shallow foundations. *Journal of Geotechnical and Geoenvironmental Engineering*, *127*(1), 99–102. https://doi.org/10.1061/(ASCE)1090-0241(2001)127:1(99)

Frank, R., & Magnan, J. (1995). Cone penetration testing in France: National report. *Proceedings, International Symposium on Cone Penetration Testing*, Vol. 3, (CPT'95, Linköping), Swedish Geotechnical Society: 147–156.

Hegazy, Y., & Mayne, P. W. (1995). Statistical correlations between V_S and cone penetration data for different soil types. *Proceedings, International Symposium on Cone Penetration Testing* (CPT'95), Vol. 2, Linköping, Swedish Geotechnical Society: 173–178.

Idriss, I. M., & Boulanger, R. W. (2006). Semi-empirical procedures for evaluating liquefaction potential during earthquakes. *Soil dynamics and earthquake engineering*, *26*(2-4), 115–130.

Idriss, I. M., & Boulanger, R. W. (2008). *Soil Liquefaction During Earthquakes*. EERI Monograph MNO-12, Earthquake Engineering Research Institute. www.eeri.org

Illinois State Geological Survey. (1961). Guide to the geologic map of Illinois. *Educational Series 7*.

ISGS Staff (2005). Quaternary deposits: Illinois State Geological Survey, ISGS 8.5 × 11 map series.

ISO 22476-1 (2022). Geotechnical investigation and testing – field testing – part 1: electrical cone and piezocone penetration test.

Jamiolkowski, M., Ladd, C. C., Germaine, J. T. & Lancelotta, R. (1985). New developments in field and

lab testing of soils. *Proceedings, 11th International Conference on Soil Mechanics & Foundation Engineering*, San Francisco, Vol.1: 157–154).

Jamiolkowski, M., Lo Presti, D., & Manassero, M. (2001). Evaluation of relative density and shear strength of sands from CPT and DMT. *Soil Behavior and Soft Ground Construction*, GSP 119, ASCE, Reston, Virginia: 201–238.

Janbu, N., & Senneset, K. (1974). Effective stress interpretation of in situ static penetration tests. *European Symposium on Penetration Testing*, Vol. 2, Stockholm: 181–193.

Jardine, R., Chow, F., Overy, R., & Standing, J. (2005). *Imperial College Procedure (ICP): Design methods for driven piles in sands and clays* (Vol. 112). Thomas Telford.

Jarushi, F., AlKaabim, S., & Cosentino, P. (2015). A new correlation between SPT and CPT for various soils. *International Journal of Geological and Environmental Engineering*, 9(2), 101-107.

Jefferies, M. G., & Davies, M. P. (1991). Soil classification by the cone penetration test: Discussion. *Canadian Geotechnical Journal*, *28*(1), 173–176.

Jefferies, M., & Davies, M. (1993). Use of CPTu to estimate equivalent SPT N_{60}. *Geotechnical Testing Journal*, *16*(4), 458–468. https://doi.org/10.1520/GTJ10286J

Jefferies, M., & Been, K. (2006). *Soil liquefaction—A critical state approach*. Taylor & Francis.

Jefferies, M. G., & Been, K. (2015). *Soil liquefaction: A critical state approach*. *2nd Edition*. CRC Press.

Kolk, H., Baaijens, A., & Senders, M. (2005). *Design criteria for pipe piles in silica sands*. 711–716.

Konrad, J.-M., & Law, K. T. (1987). Undrained shear strength from piezocone tests. *Canadian Geotechnical Journal*, *24*(3), 392–405.

Krage, C. P., Broussard, N. S. & DeJong, J. T. (2014). Estimating rigidity index (IR) based on CPT measurements. In *Proceedings of the 3rd International Symposium on Cone Penetration Testing*, Las Vegas 2014 May, 727–735.

Ku, C. S., Juang, C. H., & Ou, C. Y. (2010). Reliability of CPT Ic as an index for mechanical behaviour classification of soils. *Géotechnique*, *60*(11), 861–875.

Ku, T., Mayne, P. W., & Cargill, E. (2013a). Continuous-interval shear wave velocity profiling by auto-source and seismic piezocone tests. *Canadian Geotechnical Journal*, *50*(4), 382–390. https://doi.org/10.1139/cgj-2012-0278

Ku, T., Weemees, I., Cargill, E., Mayne, P. W., & Woeller, D. (2013b). Post-processing continuous shear wave signals taken during cone penetrometer testing. *Geotechnical Testing Journal*, *36*(4), 20120013. https://doi.org/10.1520/GTJ20120013

Kulhawy, F. H., & Mayne, P. W. (1990). *Manual on estimating soil properties for foundation design*. Report EL-6800, Electric Power Research Institute.

Lee, J., & Salgado, R. (2005). Estimation of bearing capacity of circular footings on sands based on cone penetration test. *Journal of Geotechnical and Geoenvironmental Engineering*, *131*(4), 442–452.

Lees, A., King, D. A., & Mimms, S. (2013). Palm Jumeirah, Dubai: Cone penetrometer testing data from the carbonate sand fill. *Proceedings of the Institution of Civil Engineers - Geotechnical Engineering*,

166(3), 253–267.

Lehane, B. M. (2012). Relating foundation capacity in sands to CPT q_c. *Geotechnical & Geophysical Site Characterization 4*, Vol. 1 (Proc. ISC-4, Pernambuco), Taylor & Francis Group/CRC Press: 63-81.

Lehane, B. M. (2019). CPT-based design of foundations. E.H. Davis Memorial Lecture (2017), *Australian Geomechanics Journal*, 54(4), 23–48

Lehane, B., Bittar, E., Lacasse, S., Liu, Z., & Nadim, F. (2022a). New CPT methods for evaluation of the axial capacity of driven piles. *Cone Penetration Testing 2022,* (Proc. CPT'22, Bologna), Taylor & Francis Group/CRC Press, 3–15.

Lehane, B., Liu, Z., Bittar, E., Nadim, F., Lacasse, S., Bozorgzadeh, N., Jardine, E., Ballard, J.-C., Carotenuto, P., & Gavin, K. (2022b). CPT-based axial capacity design method for driven piles in clay. *Journal of Geotechnical and Geoenvironmental Engineering.*

Lehane, B., Liu, Z., Bittar, E., Nadim, F., Lacasse, S., Jardine, R., Carotenuto, P., Jeanjean, P., Rattley, M., & Gavin, K. (2020). A new unified CPT-based axial pile capacity design method for driven piles in sand. *Proceedings Fourth International Symposium on Frontiers in Offshore Geotechnics*, 463–477.

Lehane, B., Schneider, J. A., & Xu, X. (2005). The UWA-05 method for prediction of axial capacity of driven piles in sand. *Frontiers in Offshore Geotechnics.* (Proc. ISFOG, Perth), Taylor & Francis Group: 683–689.

L'Heureux, J.S., & Long, M. (2017). Relationship between shear-wave velocity and geotechnical parameters for Norwegian clays. *Journal of Geotechnical and Geoenvironmental Engineering.* 143(6), 04017013.

Liao, T., & Mayne, P. (2006). Automated post-processing of shear wave signals. *Proc. 8th US National Conference on Earthquake Engineering*, San Francisco, Paper 1-460.10: 460–461.

Low, H. E., Landon Maynard, M., Randolph, M. F., & DeGroot, D. J. (2011). Geotechnical characterisation and engineering properties of Burswood clay. *Géotechnique*, *61*(7), 575–591. https://doi.org/10.1680/geot.9.P.035

Low, H., Lunne, T., Andersen, K., Sjursen, M., Li, X., & Randolph, M. (2010). Estimation of intact and remoulded undrained shear strengths from penetration tests in soft clays. *Géotechnique*, *60*(11), 843–859.

Lunne, T., Powell, J. J. M., & Robertson, P. K. (1997; 2002). *Cone Penetration Testing in Geotechnical Practice.* EF Spon/Routledge/CRC Press. https://doi.org/10.1201/9781482295047

Lunne, T., Randolph, M., Chung, S., Andersen, K., & Sjursen, M. (2005). *Comparison of cone and T-bar factors in two onshore clay sediments*. Frontiers in Offshore Geotechnics. (Proc. ISFOG, Perth), Taylor & Francis Group: 981–989.

Mahmoodzadeh, H., & Randolph, M. F. (2014). Penetrometer testing: Effect of partial consolidation on subsequent dissipation response. *Journal of Geotechnical and Geoenvironmental Engineering*, *140*(6), 04014022. https://doi.org/10.1061/(ASCE)GT.1943-5606.0001114

Massarsch, K. (2014). Cone penetration testing—A historic perspective. *Proceedings, 3rd Intl. Symp. Cone Penetration Testing*, (CPT'14, Las Vegas): 98–134.

Mayne, P. W. (1991). Determination of OCR in clays by piezocone tests using cavity expansion and critical state concepts. *Soils and Foundations*, *31*(2), 65–76.

Mayne, P. W., Robertson, P. K., & Lunne, T. (1998). Clay stress history evaluated from seismic piezocone tests. *Geotechnical Site Characterization*, Vol. 2, (Proc. ISC-1, Atlanta), Balkema, Rotterdam: 1113-1118.

Mayne, P. W. (2001). Stress-strain-strength-flow parameters from enhanced in-situ tests. *Proceedings, International Conference on In-Situ Measurement of Soil Properties & Case Histories* (In-Situ 2001), Bali, Indonesia: 27–47.

Mayne, P. W. (2005). Integrated ground behavior: In-situ and lab tests. *Deformation Characteristics of Geomaterials, Vol. 2* (Proc. IS Lyon'03), Taylor & Francis Group, 155–177.

Mayne, P. W. (2007a). In-situ test calibrations for evaluating soil parameters. *Characterization & Engineering Properties of Natural Soils,* Vol. 3, Taylor & Francis Group: 1601–1652.

Mayne, P. W. (2007b). *NCHRP Synthesis 368: Cone Penetration Testing*. Transportation Research Board, National Academy Press.

Mayne, P. W. (2008). Piezocone profiling of clays for maritime site investigations. *Geotechnics in Maritime Engineering*, Vol. 1 (Proceedings, 11th Baltic Sea Geotechnical Conference, Gdansk), Polish Committee on Geotechnics: 333–350.

Mayne, P. W. (2014). Interpretation of geotechnical parameters from seismic piezocone tests. *Proceedings, 3rd International Symposium on Cone Penetration Testing*, (CPT'14, Las Vegas): Omnipress, Madison/WI: 47–73. www.usucger.org

Mayne, P. W. (2016). Evaluating effective stress parameters and undrained shear strengths of soft-firm clays from CPT and DMT. *Australian Geomechanics Journal*, *51*(4), 27–55.

Mayne, P. W. (2019). Settlement of 16-story office tower on raft foundation situated on Piedmont residuum. *Proceedings GeoCongress 2019: Foundations* (8th International Conference on Case Histories in Geotechnical Engineering, Philadelphia, GSP 307), ASCE: 412–425. https://doi.org/10.1061/9780784482094.037

Mayne, P. W. (2020). Use of in-situ geotechnical tests for foundation systems. *Proceedings of the Széchy Károly Emlékkonferencia*, Hungarian Geotechnical Society, Budapest, Hungary, 12–73.

Mayne, P. W. (2022). Dissipation Testing. Flow Parameters: Permeability and Coefficient of Consolidation. Geosystems Engineering, Civil and Environmental Engineering, Georgia Institute of Technology, Atlanta, GA.

Mayne, P. W., Coop, M. R., Springman, S. M., Huang, A.-B., & Zornberg, J. G. (2009). State-of-the-Art Paper (SOA-1): Geomaterial behavior and testing. *Proc. 17th International Conference on Soil Mechanics & Geotechnical Engineering,* Vol. 4 (ICSMGE, Alexandria, Egypt), Millpress/IOS Press Rotterdam: 2777-2872.

Mayne, P.W., Dasenbrock, D.D., & Budge, A.S. (2023a). Axial response of driven steel pile at Clearwater MN using elastic solution and seismic piezocone. *Proc. GeoCongress 2023: Foundations, Retaining Walls, and GeoSynthetics* (GSP 341, Los Angeles), ASCE: 260–269.

Mayne, P. W., Cargill, E., & Greig, J. (2023b). *The Cone Penetration Test: Better Information, Better Decisions* (A CPT Design Manual), ConeTec Group, Burnaby, B.C. www.conetec.com.

Mayne, P. W., & Illingworth, F. (2010). *Direct CPT method for footing response in sands using a database approach*. *Proceedings of the 2nd International Symposium on Cone Penetration Testing*, Vol. 3, (CPT'10, Huntington Beach, California), Omnipress, Madison, WI: 315-322.

Mayne, P. W., & Kulhawy, F. H. (1982). K_o—OCR Relationships in Soil. *Journal of the Geotechnical Engineering Division*, *108*(6), 851–872. https://doi.org/10.1061/AJGEB6.0001306

Mayne, P. W., & Peuchen, J. (2013). Unit weight trends with cone resistance in soft to firm clays. *Geotechnical and Geophysical Site Characterization 4*, Vol. 1, (Proc. ISC-4, Pernambuco), CRC Press: 903–910.

Mayne, P. W., & Peuchen, J. (2018). Evaluation of CPTU N_{kt} cone factor for undrained strength of clays. *Proc. 4th Intl. Symposium on Cone Penetration Testing* (CPT'18, Delft), CRC Press/Balkema: 423–430.

Mayne, P. W., Peuchen, J., & Baltoukas, D. (2015). Piezocone evaluation of undrained strength in soft to firm offshore clays. *Frontiers in Offshore Geotechnics III*, Vol. 2 (Proc. ISFOG, Oslo), Taylor & Francis Group: 1091–1096.

Mayne, P. W., & Poulos, H. G. (1999). Approximate displacement influence factors for elastic shallow foundations. *Journal of Geotechnical and Geoenvironmental Engineering*, *125*(6), 453–460. https://doi.org/10.1061/(ASCE)1090-0241(1999)125:6(453)

Mayne, P. W., & Rix, G. J. (1995). Correlations between shear wave velocity and cone tip resistance in natural clays. *Soils and Foundations*, *35*(2), 107–110. https://doi.org/10.3208/sandf1972.35.2_107

Mayne, P. W., & Woeller, D. J. (2014). Generalized direct CPT method for evaluating footing deformation response and capacity on sands, silts, and clays. *Geocharacterization for Modeling and Sustainability* (GSP 234: Proc. GeoCongress 2014, Atlanta), ASCE: 1983–1997.

McGillivray, A.V. (2007). Enhanced integration of shear wave velocity profiling in direct-push site characterization systems. PhD Dissertation, School of Civil & Environmental Engineering, Georgia Institute of Technology, Atlanta, GA: 383.

Muromachi, T., & Kobayashi, S. (1982). Comparative study of static and dynamic penetration tests currently in use in Japan, *Proceedings of the 2nd European Symposium on Penetration Testing*, Vol. 1, (ESOPT, Amsterdam), Balkema Publishers, Rotterdam: 297-302.

Niazi, F. S. (2021). *CPT-Based Geotechnical Design Manual, Volume 1: CPT Interpretation—Estimation of Soil Properties* (Report No. FHWA/IN/JTRP-2021/22). Joint Transportation Research Program, Purdue University.

Niazi, F. S., & Mayne, P. W. (2013). Cone penetration test based direct methods for evaluating static axial capacity of single piles. *Geotechnical and Geological Engineering*, *31*(4), 979–1009.

Niazi, F. S., & Mayne, P. W. (2015). Enhanced UniCone Expressions for Axial Pile Capacity Evaluation from Piezocone Tests. *Proc. International Foundations Conference & Equipment Expo* (IFCEE'15,

San Antonio, GSP 256), ASCE, Reston/VA: 202-216. https://doi.org/10.1061/9780784479087.021

Niazi, F. S., & Mayne, P. W. (2016). CPTu-based enhanced UniCone method for pile capacity. *Engineering Geology*, *212*, 21–34. https://doi.org/10.1016/j.enggeo.2016.07.010

Ouyang, Z., & Mayne, P. W. (2019). Modified NTH method for assessing effective friction angle of normally consolidated and overconsolidated clays from piezocone tests. *Journal of Geotechnical and Geoenvironmental Engineering*, *145*(10), 04019067.

Pane, V., Brignoli, E., Manassero, M., & Soccodato, C. (1995). Cone penetration testing in Italy. *Proceedings, Symposium on Cone Penetration Testing*, Vol. 1 (CPT'95), Swedish Geotechnical Society, Linköping: 101-114.

Papamichael, S., & Vrettos, C. (2018). CPT interpretation and correlations to SPT for near-shore marine Mediterranean soils. *Cone Penetration Testing 2018*, (Proc. CPT'18, Technical Univ. Delft). CRC Press.

Perret, D., Charrois, E. & Bolduc, M. (2016) Shear wave velocity estimation from piezocone test data for Eastern Canada sands (Quebec and Ontario)–Extended version with appendices. *Geological Survey of Canada*, 48.

Piskin, K., & Bergstrom, R. E. (1975). Glacial drift in Illinois: Thickness and character. Circular no. 490.

Pineda, J. A., Suwal, L. P., Kelly, R. B., Bates, L., & Sloan, S. W. (2016). Characterisation of Ballina clay. *Géotechnique*, *66*(7), 556–577. https://doi.org/10.1680/jgeot.15.P.181

Plewes, H., Davies, M., & Jefferies, M. (1992). CPT based screening procedure for evaluating liquefaction susceptibility. Proc 45th Canadian Geotechnical Conference, Toronto: Vol. 4: 1–9.

Poulos, H. G., & Davis, E. H. (1980). *Pile Foundation Analysis and Design*. John Wiley & Sons.

Randolph, M. F. (2003). Science and empiricism in pile foundation design. *Géotechnique*, *53*(10), 847–875. https://doi.org/10.1680/geot.2003.53.10.847

Randolph, M. F., & Wroth, C. P. (1978). Analysis of deformation of vertically loaded piles. *Journal of the Geotechnical Engineering Division*, 104(12), 1465–1488.

Randolph, M. F., & Wroth, C. P. (1979). A simple approach to pile design and the evaluation of pile tests. *Behavior of Deep Foundations*, (STP 670), ASTM, 484–499.

Reid, D. (2015). Estimating slope of critical state line from cone penetration test—An update. *Canadian Geotechnical Journal*, *52*(1), 46–57. https://doi.org/10.1139/cgj-2014-0068

Rix, G. J., Mayne, P. W., Wainaina, N., Ebrahimi, A., Bachus, R. C., Limas, M., Sancio, R., & Fait, B. (2019). *NCHRP Manual on Subsurface Investigation, Web Document 258,* National Cooperative Highway Research Board.

Robertson, P. K., Wride, B. H. (1988). Cyclic liquefaction and evaluation based on the SPT and CPT. *Proceedings edited by Youd and Idriss*, 41-88.

Robertson, P. K. (1990). Soil classification using the cone penetration test. *Canadian Geotechnical Journal*, *27*(1), 151–158.

Robertson, P.K. (1991). Closure to Soil classification using the CPT. *Canadian Geotechnical Journal*.

Robertson, P. K. (2009). Interpretation of cone penetration tests—A unified approach. *Canadian Geotechnical Journal*, *46*(11), 1337–1355. https://doi.org/10.1139/T09-065

Robertson, P. K. (2010a). *Estimating in-situ soil permeability from CPT & CPTu*. Memorias del 2nd International Symposium on Cone Penetration Testing, California State Polytechnic University Pomona, CA. http://www. cpt10. com/PDF_Files/2-51Robehc. pdf.

Robertson, P. K. (2010b). Estimating in-situ state parameter and friction angle in sandy soils from CPT. *Proceedings of the 2nd International Symposium on Cone Penetration Testing* (CPT'10, Huntington Beach, California), Omnipress.

Robertson, P. K. (2012). Interpretation of in-situ tests—some insights. *Geotechnical & Geophysical Site Characterization 4*, Vol. 1 (Proc. ISC'4, Pernambuco, Brazil), Taylor & Francis Group/CRC Press, 1–22.

Robertson, P. K. (2016). Cone penetration test (CPT)-based soil behaviour type (SBT) classification system—An update. *Canadian Geotechnical Journal*, *53*(12), 1910–1927. https://doi.org/10.1139/cgj-2016-0044

Robertson, P. K., & Cabal, K. (2010). Estimating soil unit weight from CPT. *Proceedings of the 2nd International Symposium on Cone Penetration Testing*, Vol. 2, (CPT'10, Huntington Beach, California), Omnipress: 447–454. PDF proceedings available at: www.usucger.org

Robertson, P. K., & Cabal, K. (2015). *Guide to Cone Penetration Testing for Geotechnical Engineering.* Gregg Drilling & Testing.

Robertson, P. K., & Cabal, K. (2022). *Guide to Cone Penetration Testing*. Gregg Drilling & Testing, Inc, 7th Edition.

Robertson, P. K., Campanella, R. G., & Wightman, A. (1983). SPT–CPT correlations. *Journal of Geotechnical Engineering*, *109*(11), 1449–1459.

Robertson, P. K., & Wride, C. (Fear). (1998). Evaluating cyclic liquefaction potential using the cone penetration test. *Canadian Geotechnical Journal*, *35*(3), 442–459. https://doi.org/10.1139/t98-017

Saftner, D., Mayne, P.W., & Dagger, R. (2018). Cone Penetration Test Design Guide for State Geotechnical Engineers, Report No. 2018-32, Minnesota Dept. of Transportation, St. Paul, MN.

Sakleshpur, V. A., Prezzi, M., Salgado, R., & Zaheer, M. (2021). *CPT-Based Geotechnical Design Manual, Volume 2: CPT-Based Design of Foundations—Methods* (Report No. FHWA/IN/JTRP-2021/23). Joint Transportation Research Program, Purdue University. https://doi.org/10.5703/1288284317347

Sanglerat, G. (1972). The penetrometer and soil exploration. Elsevier, Amsterdam: 488.

Schmertmann, J.H. (1970). Static cone to compute static settlement over sand. *Journal of the Soil Mechanics and Foundations Division*, 96(3), 1011-1043.

Schmertmann, J. H. (1978). *Guidelines for Cone Penetration Test: Performance and Design* (Report FHWA-TS-78-209). Federal Highway Administration.

Schmertmann, J. H. (1986). Dilatometer to compute foundation settlement. *Use of In-Situ Tests in Geotechnical Engineering* (Proc. In-Situ'86, Virginia Tech, Blacksburg), GSP 6, ASCE, Reston,

Virginia: 303–321.

Schnaid, F., Sills, G.C., Soares, J.M. & Nyirenda, Z. (1997). Predictions of the coefficient of consolidation from piezocone tests. *Canadian Geotechnical Journal*, 34(2),315-327.

Schneider, J. A., & Hotstream, J. N. (2011). *Cone Penetrometer Comparison Testing* (Report No. WHRP 0092-10-10). Wisconsin Highway Research Program, prepared by Univ. Wisconsin, Madison.

Schneider, J. A., Hotstream, J. N., Mayne, P. W., & Randolph, M. F. (2012). Comparing CPTU $Q - F$ and $Q - \Delta u_2 / \sigma_{v0}'$soil classification charts. *Géotechnique Letters*, *2*(4), 209–215. https://doi.org/10.1680/geolett.12.00044

Schneider, J. A., Mayne, P. W., & Rix, G. J. (2001). Geotechnical site characterization in the greater Memphis area using cone penetration tests. *Engineering Geology*, *62*(1–3), 169–184. https://doi.org/10.1016/S0013-7952(01)00060-6

Schneider, J. A., Randolph, M. F., Mayne, P. W., & Ramsey, N. R. (2008a). Analysis of factors influencing soil classification using normalized piezocone tip resistance and pore pressure parameters. *Journal of Geotechnical and Geoenvironmental Engineering*, *134*(11), 1569–1586. https://doi.org/10.1061/(ASCE)1090-0241(2008)134:11(1569)

Schneider, J. A., Xu, X., & Lehane, B. M. (2008b). Database assessment of CPT-based design methods for axial capacity of driven piles in siliceous sands. *Journal of Geotechnical and Geoenvironmental Engineering*, *134*(9), 1227–1244.

Seed, H. B., & De Alba, P. (1986). Use of SPT and CPT tests for evaluating the liquefaction resistance of sands. *Use of In-Situ Tests in Geotechnical Engineering* (Proceedings of In Situ '86, Geotechnical Special Publication No. 6), ASCE, Reston, Virginia: 281-302.

Seed, H.B., & Idriss, I.M. (1971). Simplified procedure for evaluating soil liquefaction potential. *Journal of the Soil Mechanics and Foundations division*, 97(9), 1249–1273.

Senneset, K., & Janbu, N. (1985). Shear strength parameters obtained from static cone penetration tests. *Strength Testing of Marine Sediments: Laboratory and In-Situ Measurements*. ASTM STP 883, American Society for Testing and Materials: 41–54.

Senneset, K., Sandven, R., & Janbu, N. (1989). Evaluation of soil parameters from piezocone tests. *Transportation Research Record 1235*.

Shahien, M. M., & Albatal, A. H. (2014). SPT-CPT correlations for Nile Delta silty sand deposits in Egypt. *Proc. 3rd International Symposium on Cone Penetration Testing*, (CPT'14, Las Vegas, Nevada), Omnipress: (pp. 2–43).

Souza, J. M. S., Danziger, B. R., & Danziger, F. A. B. (2012). The influence of the relative density of sands in SPT and CPT correlations. *Soils and Rocks*, *35*(1), 99–113.

Stern, A. N., & Fox, P. J. (2011). *Evaluation of cone penetration testing (CPT) for use with transportation projects.* Ohio. Dept. of Transportation. Office of Research and Development.

Sully, J. P., Robertson, P. K., Campanella, R. G., & Woeller, D. J. (1999). An approach to evaluation of field CPTU dissipation data in overconsolidated fine-grained soils. *Canadian Geotechnical Journal*, *36*(2), 369–381.

Suzuki, Y., Sanematsu, T., & Tokimatsu, K. 1998. Correlation between SPT and seismic CPT. *Geotechnical Site Characterization*, Vol. 2 (Proc. ISC-1, Atlanta), Balkema, Rotterdam: 1375–1380. PDF proceedings at: www.usucger.org

Tand, K. E., Funegard, E. G., & Briaud, J.-L. (1986). Bearing capacity of footings on clay CPT method. *Use of In-Situ Tests in Geotechnical Engineering* (Proceedings of In Situ '86, Geotechnical Special Publication No. 6), ASCE, Reston, Virginia: 1017–1033.

Teh, C. I., & Houlsby, G. T. (1991). An analytical study of the cone penetration test in clay. *Géotechnique*, *41*(1), 17–34.

Terzaghi, K., Peck, R.B., & Mesri, G. (1996). *Soil mechanics in engineering practice (Third Edition).* John Wiley & Sons Inc.

Titi, H. H., & Abu-Farsakh, M. Y. (1999). *Evaluation of bearing capacity of piles from cone penetration test data*. Louisiana Transportation Research Center.

Torstensson, B. A. (1975). *Pore pressure sounding instrument*. *In-Situ Measurement of Soil Properties*, Vol. II, (Proc. Conference at North Carolina State University, Raleigh), ASCE: 48–55.

Uzielli, M., & Mayne, P. W. (2019). Probabilistic assignment of effective friction angles of sands and silty sands FROM CPT using quantile regression. *Georisk: Assessment and Management of Risk for Engineered Systems and Geohazards*, *13*(4), 271–275.

Wang Engineering (2021). Preliminary geotechnical assessments: east approach embankment at Illinois Route 100106 over the Illinois River, Florence (Document ID-D-96-018-12, PTB Ref. 191/010; and Wang ID: 314-13-01) submitted to Parsons Brinkerhoff, Chicago; 129 pages.

Wissa, A. E., Martin, R. T., & Garlanger, J. E. (1975). *The piezometer probe*. *In-Situ Measurement of Soil Properties*, Vol. I, (Proc. Conference at North Carolina State University, Raleigh), ASCE: 536–545.

Wroth, C. P. (1984). Rankine Lecture: The interpretation of in situ soil tests. *Geotechnique*, *34*(4), 449–489.

Youd, T. L., Idriss, I. M., et al. (2001). Liquefaction resistance of soils: Summary report from the 1996 NCEER and 1998 NCEER/NSF Workshops on evaluation of liquefaction resistance of soils. *Journal of Geotechnical and Geoenvironmental Engineering*, 127(10): 817–833.

Yu, F., & Yang, J. (2012). Base capacity of open-ended steel pipe piles in sand. *Journal of Geotechnical and Geoenvironmental Engineering*, *138*(9), 1116–1128.

Zhang, G., Robertson, P., & Brachman, R. W. (2002). Estimating liquefaction-induced ground settlements from CPT for level ground. *Canadian Geotechnical Journal*, *39*(5), 1168–1180.

APPENDIX A

Appendix A includes relevant information for the generated CPTs in this project. It can be accessed through the following link: https://gatech.box.com/s/tsnunyfl5fdc7ub9b6o7wqggg6in9vr1

- The file "*1.CPTInformation.xlsx*" includes general information on the generated CPT data. The name of each CPT is as follows "District Name-Location –CPT number." For example, "D6-Site1-1" indicates district 6, location "Site 1" and CPT 1.

- The folder "*2.EditableCPT_DissipationData*" has editable information for the CPT and dissipation data. Please read the included "readme.txt" file for how the data is organized.

- The folder "*3.PDFsProcessed_data*" has PDF files for the process data. A merged PDF file for all CPTs is included as well as processing for individual CPTs.

- The file "*4.ShearWaveVelocityResults.xlsx*" includes the results of the shear wave velocity measurements in an editable format.

APPENDIX B

As requested by IDOT, the figures below show (1) schematic setup for the Georgia Tech shear wave measurement apparatus and (2) photo showing the Georgia Tech apparatus:

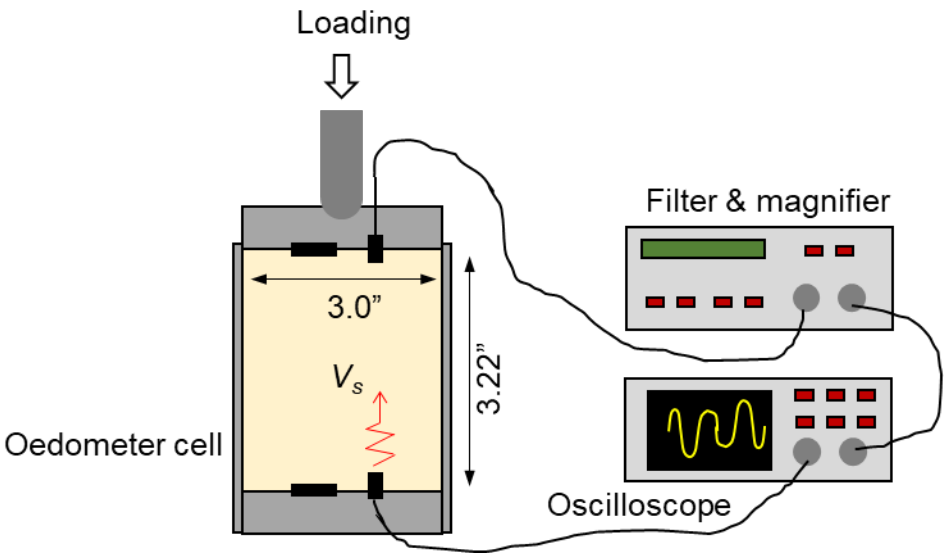

Figure 181. Schematics of the laboratory shear wave measurement setup.

Figure 182. Laboratory shear wave measurement Photos: consolidation cell with wave measurement settling on an oedometer (left); inside view of the top cap showing bender element for shear wave velocity measurement. This setup can also measure compressive wave through piezoelectric pads (right).

APPENDIX C

Additional notes on settlement calculations for shallow foundations:
https://gatech.box.com/s/lpuwn6x18kiyaqw2d2dtku2nuvjgfvl9


Illinois Department
of Transportation


ILLINOIS